A Study of the Adaptation of the Mechanical Properties of Bone Material using Raman Spectroscopy

Thesis submitted for the degree of Ph.D.

Kevin Buckley

Institute of Orthopaedics and Musculoskeletal Science

University College London

Declaration

I, Kevin Buckley, confirm that the work presented in this thesis is my own.

Where information has been derived from other sources, I confirm that this has been indicated in the thesis.

_____

Kevin Buckley

Abstract

Bone is a composite material comprising an organic collagen scaffold surrounded by mineral platelets. The weight ratio of mineral to collagen is not constant, and hence the mechanical properties of the material can vary. In this thesis, the analytical technique Raman spectroscopy (which uses inelastically scattered photons to probe chemical composition) is used to explore the hypothesis that the mechanical properties of bone material are adapted in differently loaded regions by a subtle tuning of the collagen chemistry, which controls the mineral to collagen ratio. The question is first approached by looking at Raman spectra of a range of bony materials which are adapted to different functions. Bone material composition in different loading environments within individual bone organs is then examined, and finally, collagen Raman band *profiles* from a range of bony material are examined to search for variations which would signify differences in collagen chemistry.

The results of the experiments show that for the functionally adapted bony materials a correlation exists between the Raman spectra and mechanical properties. Raman data from further experiments show that there are anatomical regions near the ends of long bones where the mineral to collagen ratio is lower than average (that this may be another adaptation of mineral/collagen ratio to function is discussed). Finally, analyses of Raman band *profiles* are presented which show that there are differences in the collagen chemistry of the various functionally adapted bony materials.

The work furthers our understanding of the relationship between the mechanical properties of bone material and its Raman spectrum, a relationship which is of great importance if Raman spectroscopy is to be developed as an *in vivo* technique. Understanding the regional variations in mineral to collagen ratio will be vital if Raman spectroscopy is to be utilised to measure the mechanical integrity of whole bone organs. The elucidation of the band *profile* differences may provide a therapeutic target for the management of bone conditions i.e. enabling the control of the mechanical properties of bone; further research is required to determine what specific aspect of the collagen chemistry they represent, and to establish the causal relationship from the spectra to mechanical properties.

Acknowledgements:

I'd like to thank my mother and father for their support and for their patience throughout the *long* time I spent at university. I'd also like to thank them for sending me to St. Patrick's Boys' National School and St Finbarr's College, Farranferris where I was taught to love learning; both times they could have taken easier options. I would also like to thank Monika for her support.

I would like to thank my supervisors, Professor Pavel Matousek, Professor Tony Parker and Professor Allen Goodship. Pavel showed great patience when I knocked on his office door everyday for three years. I'd like to apologise to him in advance for the next four years when it's going to happen again. I'd like to thank Tony for all the thoughtful comments and feedback he gave me when I was preparing this thesis. I didn't even know what a protein was when I started at UCL yet Allen always gave me encouragements like "Don't panic Mr Mainwaring! ...Time for a group brainstorm."

I'd like to thank some of the scientists who helped me with my work. I am grateful to Professor John Currey for providing sample materials, for his helpful comments and discussions, and for his hospitality when we visited him at his home in York. I'd like to thank Dr. Ian McCarthy for showing me how to use the pQCT machine and for helping me analyse the results. I would like to thank Andrew Allan, Chantal Fowler and Dr. David Clarke of the Research Complex at Harwell for their help in creating the electron micrographs presented in Chapter Four. And I'd like to thank Dr. Tony Deeney and Dr. Simon Osborne at University College Cork and the Tyndall National Institute for helping me to stick with science at a time when I was close to giving it up.

I would like to thank the Science and Technology Facilities Council's Biomedical Network and University College London for their support.

Abbreviations, Conventions and Formulae

Abbreviations

NMR – Nuclear Magnetic Resonance

NCP – Non-collagenous proteins

ECM – extracellular matrix

EM – electromagnetic radiation

C.T. – Computed Tomography

pQCT – peripheral Quantitative Computed Tomography

DXA – Dual x-ray absorptiometry

BMD – Bone Mineral Density (BMD)

aBMD – areal Bone Mineral Density

DNA – Deoxyribonucleic acid

QUS – Quantitative ultrasound

MRI – magnetic resonance imaging

PET – Positron emission tomography

E.M. – Electron Microscopy

SEM – Scanning Electron Microscopy

T.E.M. – Tunnelling Electron Microscopy

EDX – Energy-dispersive X-ray spectroscopy

SAS – Small Angle Scattering

SAXS – Small Angle X-ray Scattering

SANS – Small Angle Neutron Scattering

IR – Infrared electromagnetic radiation

UV – Ultraviolet electromagnetic radiation

THz – Terahertz

N.A. – Numerical Aperture

CCD – Charge Coupled Device

Formulae

Stress = Force / Area

Strain = (Elongated length – Original length) / Original length

Total energy of a molecule = Electronic energy + Vibrational energy + Rotational energy + Translational energy

- $E_{Total} = E_{Electronic} + E_{Vibration} + E_{Rotation} + E_{Translation}$

Boltzmann Distribution: Number molecules in the upper state / Number of molecules in the lower state = $e^{(-\text{Difference in energy/Boltzmann constant x Temperature})}$

- $N_{upper}/N_{lower} = e^{(-\Delta E/kT)}$

Energy of a Photon = Planck's constant x Frequency of the photon

= Planck's constant x (Velocity of the photon / Wavelength of the photon)

- $E = v_2 - v_1 = h\nu = h\,c/\lambda$

Depolarisation ratio = Intensity of the parallel polarised light / Intensity of the perpendicularly polarised light

- $\rho = I_{\perp} / I_{\parallel}$

Abbe diffraction limit: Diameter of smallest spot = Wavelength of light / 2 x Numerical Aperture

- $d = \lambda / (2 \times N.A.)$

Numerical Aperture = Refractive index x Sin (Acceptance angle)

- $N.A. = n \times \sin(\theta)$

Conventions

Bone Material - The hard material from which bones are made (i.e. arrangements of mineralised collagen fibrils).

Matrix - The contiguous material which surrounds the reinforcing material in a composite material, i.e. in reinforced concrete, the steel rebars are the reinforcing material and the concrete is the matrix.

Raman Spectra – Only Stokes shifted spectra are shown. They are plotted with shift (in wavenumber) increasing from left to right.

Publications and Presentations Produced During the Work for this Thesis:

Peer Reviewed Publications

- **Buckley K.**, Matousek P., Parker A.W., Goodship A.E., Material analysis of the third Equine Metacarpal by Raman Spectroscopic serial scans, *In Preparation*
- **Buckley K.**, Matousek P., Parker A.W., Goodship A.E., Differences in Mineral Volume Fraction are Associated with Changes in the Collagen Chemistry; a Raman Spectroscopy Study, *In preparation*
- **Buckley K.** & Matousek P., Recent Advances in the Application of Transmission Raman Spectroscopy to Pharmaceutical Analysis, *Journal of Pharmaceutical and Biomedical Analysis*, **55**:645-652, (2011)
- **Buckley K.** & Matousek P., Non-invasive Analysis of Turbid Samples using Deep Raman Spectroscopy, *Analyst*, **In Press**
- **Buckley K.,** Goodship A.E., Macleod N.A., Parker A.W. & Matousek P., Technique for Enhancing Signal in Conventional Backscattering Fluorescence and Raman Spectroscopy of Turbid Media, *Analytical Chemistry*, **80(15):**6006–6009, (2008) - *This paper was featured as a news article on the www.spectroscopyNOW.com website*

Book Chapters

- **Buckley K.** & Matousek P., Non-invasive Detection of Concealed Liquid and Powder Explosives using Spatially Offset Raman Spectroscopy, Chapter **X** of Edwards H.G.M., Hargreaves M.D., Chalmers J.M., (Eds.) *Infrared and Raman Spectroscopy in Forensic Science*, (John Wiley & Sons Ltd, Chichester, U.K., **2011**)
- **Buckley K,** & Matousek P., Non-invasive Detection of Illicit Drugs using Spatially Offset Raman Spectroscopy, Chapter **X** of Edwards H.G.M., Hargreaves M.D., Chalmers J.M., (Eds.) *Infrared and Raman Spectroscopy in Forensic Science*, (John Wiley & Sons Ltd, Chichester, U.K., **2011**)

Reports

- **Buckley K.**, Macleod N.A., Parker A.W., Matousek P. & Goodship A.E., A Novel Technique for Enhancing Signal in Conventional Fluorescence and Raman Spectroscopy of Diffusely Scattering Media, *Central Laser Facility Annual Report*, **2008-2009**

Conference/Meeting Presentations

- **Buckley K.**, Matousek P., Parker A.W. & Goodship A.E, Can Raman Spectroscopy be used to Measure Qualitative Differences in the Organic Phase of Bone with very Different Mineral Volume Fractions?, Poster Presentation, *3rd Joint Meeting of the Bone Research Society and the British Orthopaedic Research Society*, Cambridge, United Kingdom, June 27-29, **2011**

- **Buckley K.**, Matousek P., Parker A.W. & Goodship A.E., Collagen Chemistry is Altered in Bones with Different Mineral Volume Fractions; a Study using Raman Spectroscopy and Bony Materials with Different Functions, Oral Presentation, *Orthopaedic Research Society Annual Meeting*, Long Beach, California, U.S.A., January 13-16, **2011**

- **Buckley K.**, Matousek P., Parker A.W., McCarthy I.D. & Goodship A.E., Raman Spectroscopy used for Non-Destructive Assessment of Material Properties in Mineralised, Poster Presentation, *British Orthopaedics Society Annual Meeting*, Cardiff, United Kingdom, June 12-13, **2010**

- **Buckley K.**, Matousek P., Parker A.W., McCarthy I.D. & Goodship A.E., Development of Raman Spectroscopy as a Technique for Non-Invasively Monitoring Bones *In Vivo*, Poster Presentation, *Lasers for Science Facility User Meeting*, Abingdon, United Kingdom, April 27-29, **2010**

- **Buckley K.**, Matousek P., Parker A.W., McCarthy I.D. & Goodship A.E., Development of Raman Spectroscopy as a Technique for Non-Invasively Monitoring Bones *In Vivo*, Poster Presentation, *The (191th) Infrared and Raman Discussion Group Meeting*, London, United Kingdom, December 17, **2009**

- **Buckley K.**, Goodship A.E., Macleod N.A., Parker A.W. & Matousek P., New Technique for Enhancing Raman and Fluorescence Spectroscopic Signals from Diffusely Scattering Media, Poster Presentation, *The (191th) Infrared and Raman Discussion Group Meeting*, London, United Kingdom, December, 17, **2009**

- **Buckley K.**, Matousek P., Parker A.W., McCarthy I.D. & Goodship A.E., Development of Raman Spectroscopy as a Technique for Non-Invasively Monitoring Bones In Vivo, Poster Presentation, *British Orthopaedics Society Annual Meeting*, Newcastle, United Kingdom, June 22-23, **2009**

- **Buckley K.**, Goodship A.E, Macleod N.A., Parker A.W. & Matousek P., New Technique for Enhancing Raman and Fluorescence Spectroscopic Signals from Diffusely Scattering Media, Poster Presentation, *Pittcon,* Chicago, U.S.A. March 08-13, **2009**

Table of Contents

Introduction and Summary

"it would be impossible to build up the bony structures of men, horses, or other animals so as to hold together and perform their normal functions if these animals were to be increased enormously in height; for this increase in height can be accomplished only by employing a material which is harder and stronger than usual, or by enlarging the size of the bones"

Galileo Galilei[1]

The human skeleton comprises over 200 bones. These bones have many functions; they shield and protect sensitive organs from damage, they act as a reservoir for mineral ions, they transmit acoustic vibrations and they house the bone marrow which is responsible for producing blood cells. The other main function of bones is to transmit muscular forces, i.e. they are the levers of bodily mechanics. The factors which determine whether bones can withstand the forces put on them, and thus perform their functions, can be divided into two broad categories; structural/architectural properties and material properties. The structural/architectural properties of a bone are dependent on the quantity of material from which it is made and its three-dimensional arrangement. This thesis is concerned with the latter category and will use Raman spectroscopy (a spectroscopic technique in which inelastically scattered photons are collected and analysed), to probe the chemical composition of the bone material itself.

Bone is a composite material comprising a collagen fibril scaffold surrounded by crystals of a hydroxyapatite-like mineral. The relative proportions of mineral and collagen in bone are not constant and their ratio largely determines the bone material's mechanical properties,[2,3] even small changes in its composition can lead to a rapid changes in the mechanical properties.[4,5] Thus, measuring the relative ratio of mineral to collagen and understanding the biochemical processes which control it, are vitally important. The main advantage of using Raman spectroscopy to study bone material is that, unlike x-ray techniques, it can provide information from both its mineral and collagen phases.

The thesis begins with a description of the composition of bone material and some important concepts related to its mechanical behaviour, some of the most widely used methods for imaging and analysing bone material will then be introduced. The next chapter gives an introduction to Raman spectroscopy, starting from the theory which underlies it and progressing onto the general description of a Raman instrument. An overview of the many Raman studies of bone material in the literature is given; they include emerging developments (such as Spatially Offset Raman Spectroscopy) which have enabled the retrieval of chemically specific information from bone non-invasively through the skin.

The third chapter begins with a technical description of the Raman instrument which was used to record the data presented in this thesis and an outline of the experimental methodology. A technological advance in Raman spectroscopy which was developed during the course of thesis research is then described. The technique can be used to improve sensitivity when probing turbid media and may be of use to those who are developing Raman spectroscopy as a tool for analysing bone material *in vivo*.[6]

Chapters Four, Five and Six give the main results stemming from the research on bone material, they begin with the well established premise that each bone in the skeleton has a mineral to collagen ratio which is adapted to produce mechanical properties that suit the specific bone's function.[7] The research question that drives the work is:

Are the mechanical properties of bone material adapted in differently loaded regions by a subtle tuning of the collagen chemistry which controls the mineral to collagen ratio?

This question is approached by forming three related and null hypotheses and exploring each of them in its own chapter:

- No correlation exists between Raman bands and mechanical properties for bony materials that differ widely in mineral volume fraction
- The mineral/collagen ratio does not vary in any ordered way along the cortices of long bones
- The collagen in bone materials with different mineral volume fractions is identical and varies only in quantity

In order to explore the hypotheses, Raman studies are performed on a wide variety of functionally adapted bony materials whose mineral/collagen ratio span the range found in nature; it is this feature that sets this work apart from many of the Raman studies of bone in the literature. Chapter Four explores the first hypothesis, the results in the chapter show that mineral to collagen ratio as measured with Raman, accounts for a much of the mechanical property difference between different bony materials.

Chapter Five explores the second hypothesis; it reports the variation in the mineral to collagen ratio occurring in bone material occurring at different points in the cortex of long bones, specifically along main axes. The changes were first seen in metacarpal bones from equine cadavers and afterwards in other long bones. In the past, many studies have measured differences in the mechanical properties of the bone material along the proximodistal axis suggesting that the findings presented here may be

relevant to all long bones. The work will be of interest to orthopaedic scientists and to biologists or zoologists interested in the anatomy of bones.

Since Raman spectroscopy can provide information on both the mineral and collagen phases of bone material, there are two important questions that it may shed light on; what are the biochemical processes by which the mineral to collagen ratio is controlled? And, how are the mineral crystals and collagen fibrils bound together? Subtle changes in the Raman spectra of extreme bone materials are presented in Chapter Six that may illuminate the collagen chemistry relevant to these questions. If one could interpret the Raman spectral changes in the functionally adapted bones and engineer the subtle collagen chemistry they represent, then one could possibly produce bone materials with particular mechanical properties, this would obviously be of great interest to medical science. The work forms the basis of the paper "Collagen Chemistry is Altered in Bones with Different Mineral Volume Fractions; a Study using Raman Spectroscopy and Bony Materials with Different Functions" which was presented at the Orthopaedic Research Society Annual Meeting in Long Beach, California in January 2011.

Finally, the thesis concludes with a general discussion of the questions which the research has raised.

1. Bone Material & Bone Imaging/Analysis

This chapter will introduce the major concepts relevant to this study; the first section will describe, from the molecular to the macroscopic levels, the substance from which the bones are made (the bone material). The second section will describe techniques which have been used to assess bone material at the different hierarchical level in the past. The multidisciplinary nature of the research means all concepts are introduced from first principles.

1.1 Composition of Bone Material

Bone material has remarkable mechanical properties and the structures made from it (the bone organs) remain rigid even after being subjected to many thousands of cycles of immense force, e.g. the stresses (force per unit area) in the long bones of a horse's forelimb can easily exceed 40 MNm^{-2} during each stride.[8] Bone is able to sustain these immense forces repeatedly because it is a composite material with two phases which both contribute to its performance; they are a fibrous scaffold of collagen fibrils (which give the bone material its toughness) and a stiff solid matrix of tiny hydroxyapatite crystals (which give the bone material its stiffness).

Collagen

The organic scaffold of bone material consists of the fibrillar protein collagen; it is secreted along with other non-collagenous proteins by bone cells, becomes mineralised and develops as bone material. The mineralisation has two stages; primary mineralisation (first few days) in which the mineral content increases rapidly to over 50% of its final value and secondary mineralisation, the long slow gradual increase to 100%.[9] Collagen type I, which accounts for 95% of the collagen in bone[10] is coded as three polypeptide chains; two identical peptide chains (alpha one chains) and one other similar chain (an alpha two chain). One end of each alpha chain terminates in an amino functional group ($–NH_2$) group and the other end terminates in a carboxyl group (–COOH).[11] In humans, the alpha one chain and alpha two chains are encoded by genes on chromosome 17 and chromosome 7 respectively.[12] Each chain is roughly 1000 amino acids long and consists of a repetitive triplet pattern, defined by the presence of glycine (Gly) at every third position, along most of its length.[13] Usually the second (X) and often the third (Y) position in the collagen triplet (Gly-X-Y) are occupied by proline (Pro).[10]

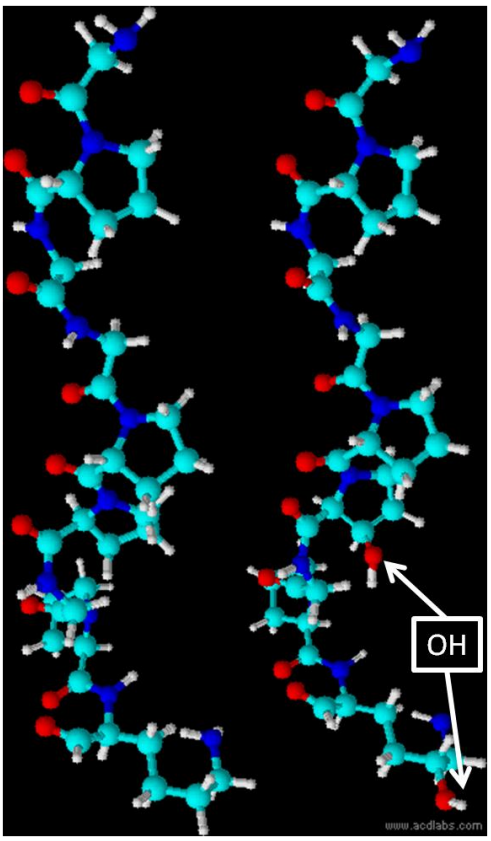

Figure 1.1 Two sections of collagen α_1 chain. The amino acid triplet-sequences in both chains are (from the top) Gly-Pro-Gly_Gly-Pro-Pro_Gly-Pro-Lys but in the right hand chain the third proline and the lysine have been hydroxylated.

After the polypeptide chains have been translated, some of the proline acids present in the X and (more usually) the Y positions are hydroxylated; a hydroxyl (-OH) group is added to the gamma carbon. The lysine (Lys) residues in the alpha peptide chains can also have one of the carbons in their side chains hydroxylated (Figure 1.1). The hydroxylation of proline and lysine is a distinctive feature of collagen.

The presence of glycine at every third position along the alpha chain causes them to fold and form left-handed helixes along most of their length (there are non-repetitive, non-helical regions at each end). The three helical chains aggregate and intertwine to form a quaternary structure, a right-handed super helix called a tropocollagen.[14] These tropocollagen molecules are about 300 nm long and 1.5 nm in diameter. The tropocollagen aggregate to form bundles called micro-fibrils and the micro-fibrils aggregate to form fibrils.[15] These collagen fibrils have typical diameters of 50 to 200 nm and are the fibrous structural unit in the bone material composite.[16] The tropocollagen to collagen-fibril aggregation is an ordered process with the adjoining 300 nm long tropocollagen molecules being offset from each other by 67 nm along the long axis. Since the 300 nm is not divisible by the 67 nm, a periodic banding pattern is created along the long axis where the ‘remainders’ line up, these holes are

called gap regions, and are thought to be where most of the mineral crystal nucleation occurs in bone. Figure 1.2 shows a cross section of a collagen fibril with the gap regions illustrated in red (the figure is from a paper which used x-ray diffraction data of rat tail tendon to produce a computer model of a collagen type I (tendon) fibril).[17]

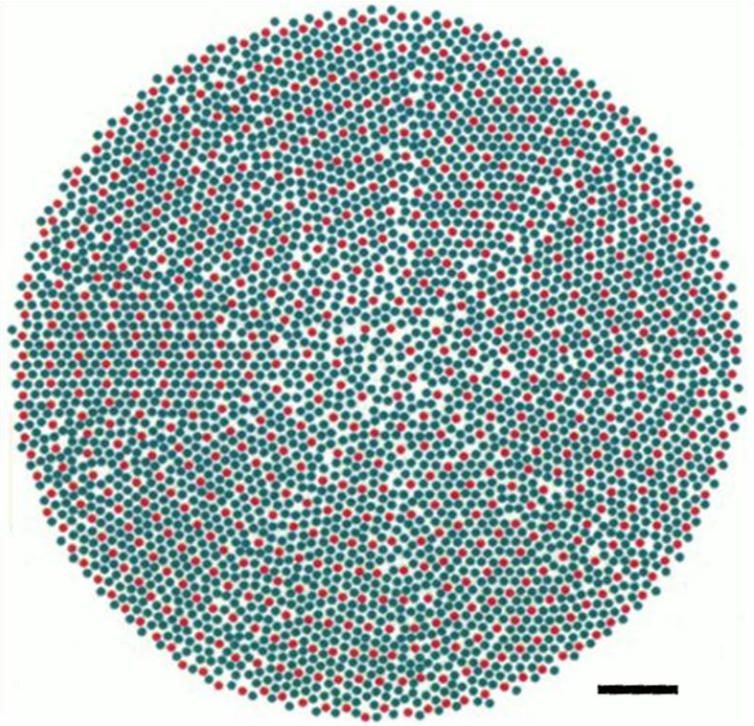

Figure 1.2 Computer model of a rat tail tendon collagen fibril (cross section), the 67 nm stagger is illustrated with colours, cross-sections of tropocollagen are green and cross-sections of gaps are red. The scale bar is equal to approximately 15 nm. This figure is from Ref. 17.

The neighbouring tropocollagen molecules are joined together by covalent cross-links found within and between the micro-fibrils. They are formed when one lysine residue in a tropocollagen's helical region joins with a lysine residue from the non-helical ('non-repetitive') region of another tropocollagen. These linked lysyl groups form an initial keto-imine cross-link which can then mature into various other types of cross-link.[18] The cross-links are of vital importance and when their formation is inhibited using drugs, the bone material loses most its strength.[19] Collagen cross-links will be discussed again in later chapters.

Mineral

The collagen fibrils are surrounded by a solid matrix of tiny, closely packed mineral crystals. The morphology of the crystals has been contentious but it is now widely accepted that in mature bone they are platelet shaped, with thickness in the range of 2 to 7 nm, a length of 15 to 200 nm and a width of 10 to 80 nm.[20] The mineral is analogous to naturally occurring hydroxyapatite, $(Ca_{10}(PO_4)_6(OH)_2)$, but the small size of the crystals (and thus their large surface to volume ratio) mean substitutions readily occur; cations such as Mg^{2+}, Sr^{2+}, Fe^{2+}, Pb^{2+}, Na^{+}, K^{+} take the place of calcium, and anions such as CO_3^{2-}, F^{-}, HPO_4^{2-}, H_2PO^{4-} take the place of phosphate groups or hydroxyl groups. Carbonate ions $(C0_3)^{2-}$ are often substituted for phosphate groups, hydroxyl groups, or for both.[21]

The exact relationship between the mineral crystals and the collagen fibrils at the molecular level has not yet been fully clarified. The situation at the nanoscale is clearer; the mineral platelets are found within and between the collagen fibrils, and that they are mostly orientated in the same direction with their faces parallel to each other and their long axes parallel to the long axis of the collagen fibrils (Figure 1.3).[22] The outer surfaces of the collagen fibrils are also coated in hydroxyapatite.[23,24]

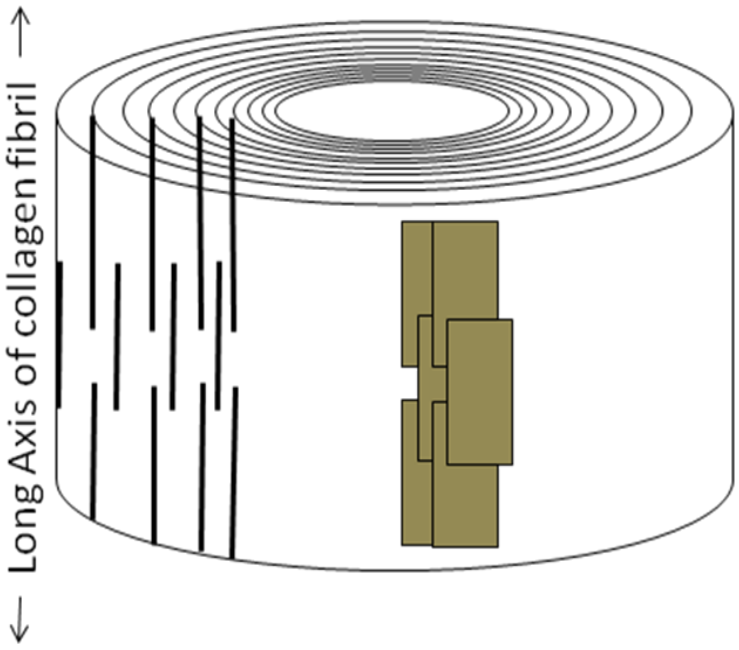

Figure 1.3 Schematic sketch of the 3-D arrangement of a mineralised collagen fibril. The mineral crystals platelets (in yellow) are staggered, the thick black lines are an attempt to show the stagger in side profile. The figure is adapted from Ref. 22.

Water

Water can account for 5-20% of the weight of bone material (Figure 1.4).[2,3] Water fills pores where it acts as an interstitial fluid, diffusing nutrients, removing waste, etc.[25] Many studies of this fluid have been reported and it has been implicated in many aspects of whole bone organ behaviour, including the mechanosensory system.[26] Water affects the mechanical properties of bone, with dry bone being more brittle than wet bone even if the ratio of organic material to mineral remains the same.[27] It is probable that this is because dried collagen is more brittle than wet collagen (observable in any sample of dried tendon). The removal of water from bone causes the average spacing between the collagen molecules to decrease (e.g. from ~1.24 nm to ~1.16 nm for cow tibia).[2,28]

At smaller (molecular) scales, Nuclear Magnetic Resonance (NMR) spectroscopy techniques have been used to observe water molecules in, and between, the bone mineral crystals and at the interface between the mineral and the organic phase of the bone material composite, however, the water's exact structural role and how it contributes to the mechanical properties of the material are still unclear.[25,29]

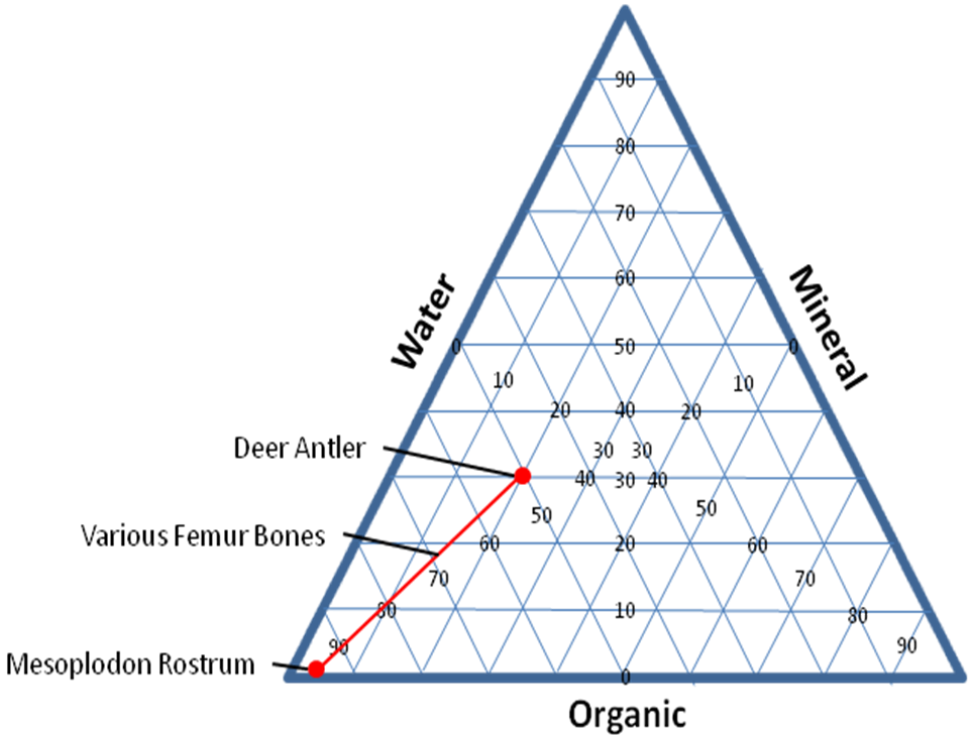

Figure 1.4 Schematic representation of ternary diagrams adapted from references 2 and 3, the references give the weight fractions of mineral, water and organic material for dozens of bone samples, they all lie along this red line.

Non-Collagenous Proteins

Collagen constitutes 80-90% of the organic material mass in bone but it is not the only protein with an essential role. A number of non-collagenous proteins (NCPs) have been shown to be important for controlling the mechanical properties of bone material and maintaining the performance of the skeleton.[10] For example, fibronectin, one of the most abundant NCPs in bone, is thought to have critical roles in bone development and bone function; in particular it may regulate the mineralisation of bone by binding to other matrix proteins and it may regulate and control the cells which create the bone material. Another NCP, Osteonectin, is found throughout the body, particularly at sites of bone remodelling and matrix assembly. Osteonectin has a strong affinity for both collagen and mineral, and it has been theorized that it regulates mineralisation.[10] Yet another NCP, Thrombospondin-2, has been shown to inhibit the production of bone producing cells (by modulating cell-extracellular matrix interactions) and to affect mineralisation (it can bind to calcium and interact with type I collagen). Mice born without the gene necessary to produce it have bones with thicker cortices (0.304 vs. 0.279 mm) and denser bone material (523.13 vs. 464.73 mg cm^{-3}) than age matched controls.[30,31,32]

Collagen is far more abundant than the NCPs and they are composed of many of the same amino acids. Conventional Raman spectroscopy does not have sufficient sensitivity to measure trace quantities (For example, it has a sensitivity of ~0.1%, at best, when used in pharmaceutical applications, and those applications are not even limited by the problems of identical amino acid composition[33]). Hence, the molecular vibrations of the NCPs are not easy to discern using the technique. However, there have been Raman studies of bone material from mice lacking certain NCP genes, they will be discussed in the next chapter.

1.2 Bone at Higher Levels of Organisation

Bone Microstructure

The mineralised collagen fibrils which constitute the basic unit of bone can be arranged in many different ways to create bony materials which differ at the micro-scale and are better suited to particular functions. The study of bone at the micro-scale is a large field and many types of microstructure have been reported.[34,35] In broad terms, the microstructure of standard limb bone material can be classified into a few types. And which of these microstructures is found in a particular at a particular anatomical point is constrained by time. In circumstances where bone needs to be created very quickly such as in very young animals or at fracture calluses, the bone cells can lay down collagen fibres without regard to its structural order.[36] This woven bone (thus named because of unordered appearance of the fibres) is inefficient, being highly mineralised yet having relatively poor mechanical properties.

At the other extreme is lamellar bone in which the mineralised collagen fibrils line up in one direction to form an ordered sheet (2-6 μm thick) of bone. As alternate sheets, called lamellae, are laid down their fibril axes are tilted so the material takes on a plywood-like arrangement.[37] Lamellar bone can be found in large cylinders running circumferentially around the long axes of bones, in smaller concentric cylinders running around blood vessels (primary or secondary osteons), or layered in small depressions (1 mm long and 50 μm thick)[38] surrounded by older bone.[I] Lamellar bone takes longer to form than woven bone but has superior mechanical properties.

Bone in which the fibres are aligned in one direction but not formed into neat lamellae (i.e. an intermediate form between woven and lamellar bone) is called parallel fibered bone.

In many large animals, whose bones have to grow in diameter rather quickly, a micro-structural arrangement called fibrolamellar bone, which combines regions of woven bone and lamellar bone, can be found. In fibrolamellar bone, the woven bone scaffold grows quickly leaving large cavities near blood vessels, which are filled in by slower growing lamellar bone. In many species, including humans, this fibrolamellar bone is replaced with purely lamellar bone over time (this process is described below).

[I] The circumferential lamellar bone and primary osteons are primary bone, whilst bone packets and secondary osteons are secondary bone; these terms will be described in the Modelling and Remodelling section.

Macroscopic Structure

At the next level of organisation, the macroscopic scale, the bone material can be seen to be arranged in one of two distinct architectural states; cortical bone and cancellous bone. Cortical bone is compact solid bone material such as that found in the shafts of long bones. Cancellous bone on the other hand is a network of struts and plates (called trabeculae) of bone material that is porous on the millimetre-scale. The trabeculae can be few and sparse, can be densely packed system of highly interconnected plates, or can be somewhere on the continuum in-between. Cancellous bone is found throughout the body, usually beneath a thin layer of cortical bone, e.g. in the ends of long bones, and in the vertebrae. Cortical bone and cancellous bone contribute 80% and 20% of the skeletal mass respectively but as one would expect the cancellous bone contributes a large percentage (61%) of the bone surface area (excluding surfaces related to micro-porosities and canaliculi).[38]

Modelling and Remodelling

The larger scale structures made from cortical and cancellous bone, i.e. the whole bone organs, do not have fixed shapes but can be **modelled** and sculpted into new forms when they grow, or when they need to adapt to new loading patterns.[39] The bone material itself does not grow or shrink; it is added to and removed from existing surfaces by specialised bone cells.[II]

Even when the shape of the whole bone is static the bone material itself can be turning over (constantly being reformed), this process is called **remodelling**. The remodelling cycle is thought to begin when cells (osteocytes) living in small cavities (lacunae) in the bone material sense damage in their surrounding area (possibly with their extended cell processes which run through narrow tunnels called canaliculi), undergo apoptosis and release signalling molecules.[38] These signalling molecules activate and summon large multi-nucleated cells called osteoclasts which arrive and burrow into the bone surface by releasing H^+ ions and dissolving the bone material. Next, the resorption cavity is filled in with lamellar bone by teams of specialised bone building cells called osteoblasts.

The remodelled units on the surfaces of trabeculae are called bone packets (1 mm long and 50 μm thick).[38] In the case of cortical bone, where the osteoblasts and osteoclasts can reach internal bone surfaces via blood vessels, the remodelling can manifest itself as small concentric cylinders of lamellar running around blood vessels. These units of remodelled bone are called a Haversian system or secondary osteon. If a new Haversian system is formed by replacing an older Haversian system, the remnants of the older system are called interstitial lamellae.

[II] The cells which add bone are called Osteoblasts and the cells which remove it are called Osteoclasts.

Mechanical Behaviour of Bone Material

When bone material is subjected to a force it deforms. As the force increases, the deformation increases, until it reaches the point where the material breaks. For some forces, the removal of the applied force will allow it to go back to its original shape (i.e. it will behave elastically) but for other, larger forces, the material will remain deformed even after the force has been removed; the transition point between the two types of behaviour is called the yield point.[40] Figure 1.5 shows a diagram representing this behaviour; the force, or load, on the sample is plotted on the x-axis and deformation on the y-axis.

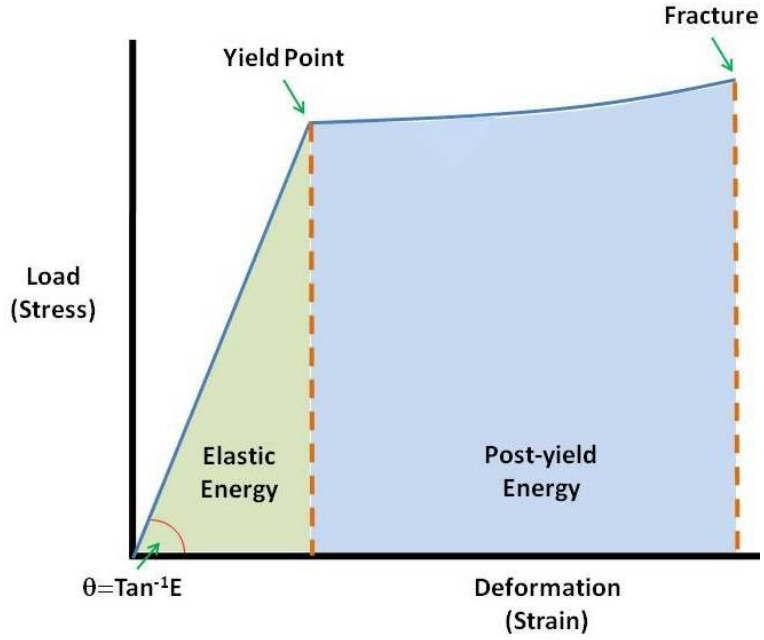

Figure 1.5 Schematic representation of a load-deformation curve for bone material tested in tension.

The 'stress' and 'strain' labels refer to concepts from material science (defined in Figure 1.6) which allow comparison between samples of different sizes and shapes. The area under the stress-strain curve can be integrated to give an energy; the area under the whole curve gives the amount of energy the sample can withstand before breaking (the toughness of the material) and the area under the curve, before the yield point, is the elastic energy (for obvious reasons). The Young's modulus of elasticity of a material is defined as stress/strain in the elastic (pre-yield) region of the curve.[III] The stiffer a sample, the less it will deform when experiencing a force and larger the slope will be, thus the Young's modulus is a measure of stiffness. The ultimate strength of the bone material is the stress it undergoes at the point of fracture.

[III] Therefore the units of Young's modulus are Nm^{-2} or Pa.

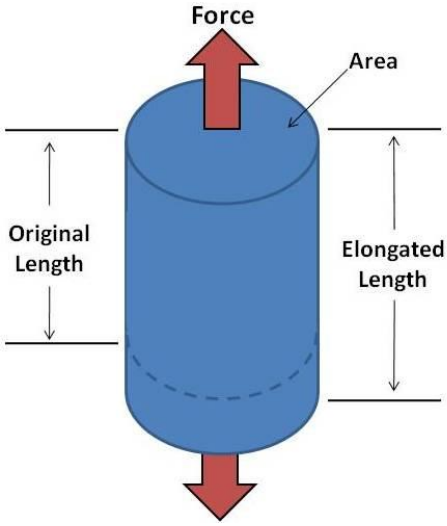

$$Stress = \frac{Force}{Area}$$

$$Strain = \frac{elongated\ length - original\ length}{original\ length}$$

Figure 1.6 Formulae for Stress and Strain, thus, the units of stress are N/m² and strain is unit-less.

1.3 Bone Imaging and Analysis

From the constituent molecules all the way up to the macrostructure of whole bone organs, bone has been imaged and probed using many hundreds of analytical techniques. A full description of every instrument which has been used to study bone is beyond the scope of this thesis (and perhaps beyond the scope of any single book). Instead, a few important techniques will be described and techniques which can probe the *chemical* composition of bone, or its mechanical properties will be discussed. It will be stated whether the techniques are used to study whole bones, specific regions of individual bones or small samples of bone material. These techniques will be classified into four general (and sometimes overlapping) categories: radiographic techniques, other clinical *in vivo* techniques, *ex vivo* imaging techniques and spectroscopic techniques.

Radiographic Techniques

X-ray radiation is the name given to electromagnetic (EM) radiation with wavelength in the range of 0.1-10 nm. When a quantum of x-ray radiation (a photon) is incident on a material the chance of it being absorbed (the absorption coefficient) depends on the material's composition (especially its density, molecular/electronic structure). X-ray photons easily pass thorough soft bodily tissues but are stopped by the mineral phase of bone material, they have long been used to make *in vivo* images of bone. The simplest x-ray technique is **projection radiography** in which an x-ray source is placed at one side of the limb/bone and a detector is placed at the other. As the x-rays are absorbed by the different tissues, an image (analogous to a shadow) is created at the detection equipment. The bone mineral shows up most clearly because it is much denser than the surrounding tissue and absorbs more of the incident x-rays. Though this method of imaging bone is widely used to image whole bones, it does have a major limitation in that it produces 2-D images of 3-D objects and hence objects

which are spatially offset from each other in reality, become superimposed on the image. This limits the usefulness of projection radiographs and means interpreting the images is a specialised skill.

This limitation is overcome with **x-ray computed tomography (CT)**.[41] Early C.T. scanners had an x-ray source (an x-ray tube) which was aligned so as to be incident on the part of the body to be imaged e.g. the chest, and a detector was used to measure the x-ray signal (the attenuation) at the other side of the chest. The source and detector was then moved along the axis parallel to the original measurement and another reading was taken. This was repeated until data from a full 'slice' of the chest was collected. The source and detector were then rotated through a small angle (i.e. the imaginary line connecting the source and detector is rotated) and the same slice is imaged from a slightly offset angle. This was repeated until the equipment had rotated through 180°. This process resulted in a large number of cross-sectional attenuation paths which cross at all angles and the mathematical manipulation of the data set (using integral transforms) enabled a model to be created of the slice. In such a model the chest becomes a grid of 3-D boxes (called voxels), each with uniform density. A colour scaled plot of these voxels gives a 2-D cross-sectional image of the chest i.e. a 2-D image of a 2-D object.

Modern C.T. scanners operate in slightly different manner; in order to speed up the measurement (and hence reduce problems associated with patient movement, patient breathing, patient heartbeat, etc), the x-ray source and the detector are constantly moving through a helical path around the patient and the lying patient is moving headfirst through the helix in the opposite direction. The data are taken as one long set meaning the stop-start drawback of earlier scanners is overcome.

Peripheral Quantitative Computed Tomography (pQCT) instruments have workings that are very similar to those of the older style C.T. scanners described above but they have a smaller sample space between x-ray source and detector. They are designed to create images of thin cross-sections of the bones of the appendicular skeleton and can give quantitative values for the amount of bone mineral present. Using computer algorithms, the images can be divided into trabecular and cortical regions and by averaging the density across the different topographic regions the density of the trabecular or cortical bone (or both) can be obtained.

Dual-Energy X-ray Absorptiometry (DXA) is another radiographic technique that is used by clinicians to assess the bones *in vivo*.[42] Compared to computed tomography, the technique is relatively simple (the equipment is much simpler) and the dose of radiation is relatively small (~1 μSv for absorptiometry and ~30 μSv for computed tomography)[43]. In a DXA scan, an x-ray beam is sent through the bone to be examined and the attenuation is measured, a second x-ray beam with a different wavelength (different energy) is sent along the same path through the same bone and its

attenuation is also measured. Since x-ray attenuation-coefficient depends on atomic number and photon energy, the measurement of the transmission coefficient at two different energies enables the mass per unit projected area of bone and soft tissue to be inferred by solving a pair of simultaneous equations.

DXA is the most widely used method to measure the density of bones. It is the gold standard test for the diagnosis of osteoporosis, has high resolution and good precision. It is however limited by its inherent planar nature, the density values it produces, called Bone Mineral Density (BMD) or areal Bone Mineral Density (aBMD) is a measure of the x-ray absorption along the path of travel of the x-ray; a thin slab of highly mineralised material would stop as many photons as a thicker slab of poorly mineralised material, but the two slabs could have very different mechanical properties. In addition to this, DXA measurements cannot be resolved into separate measurements for trabecular and cortical bone.[44] DXA-measured aBMD accounts for 60–70% of the variation in whole bone strength.[45]

Radiographic techniques are extremely useful and are very widely used, however, they do have some drawbacks and limitations, the main one being the x-rays themselves are inherently harmful. The relatively high energy photons can ionise the molecules they collide with and can create free-radical particles in the body which can damage DNA and/or destroy cells. This makes radiography more harmful to children or pregnant women. C.T. scans expose patients to higher doses of radiation than other radiographic techniques because each scan is made up of a large number of individual measurements and because during the course of each scan the x-rays are incident from all directions. This symmetric dose of radiation is more harmful than, for instance, a projection radiograph, because in projection radiographs some of the body is ‘shielded’ by another part of the body (known as a radiation gradient). This radiation gradient is much reduced for a C.T. scan. These issues limit applicability and make certain radiographic techniques unsuitable for screening large numbers of healthy people.

The other important limitation to note about radiographic techniques is that they practically blind to the organic phase of the bone material. Since the organic phase can account for up to 30% of the weight of the bone material (Figure 1.4) and is an integral part of the composite, it could explain some of the variation in whole bone strength that is not accounted for by DXA-measured aBMD.[45]

Alternative Clinical (*in vivo*) Techniques

Ultrasound is the term given to acoustic vibrations with frequencies above the hearing threshold, (audible frequencies are of the range 20 Hz – 20 kHz). Ultrasound vibrations can be used as a medical tool, the sound wave sent through the body-part to be probed and the reflected or transmitted sound (echo) is collected and analysed. Quantitative ultrasound (QUS), which looks at the percentage of the signal that was transmitted (transmission coefficient) and at the time the vibration took to propagate (transmission delay) has been extensively used to study osteoporosis. Authors have reported moderate (but statistically significant) correlation coefficients with bone mineral density and numerous studies have shown that its ability to predict fracture is similar to DXA.[46] Several authors have suggested that QUS may measure qualities of bone architecture rather than bone material density.[47] In addition to osteoporosis, QUS has been used in studies of osteogenesis imperfecta and hyperparathyroidism (a glandular problem which affects the skeleton).[47] Ultrasound has also been used to make images of the surfaces of bone though no images of the internal structure of a bone can be obtained as the components of the sound wave which penetrates the bone and reflects from trabeculae cannot be collected efficiently and resolved into an image. Ultrasound techniques, like the radiographic techniques discussed above, primarily probe the mineral phase of the bone material and are not chemically specific.

Another non-radiographic technique which is used to image bones and other internal organs is **magnetic resonance imaging (MRI)**.[48,49] MRI uses the distinctive magnetic properties of protons in different environments to distinguish between differing tissues. To create an MRI image, the patient (or a part of the patient) is placed in a strong magnetic field (produced by sending a large electrical current through a supercooled coil). The field exerts a force on the charged particles and magnetic dipoles within it. Atomic nuclei which have nuclear spin (such as hydrogen, phosphorus, sodium, and fluorine) become aligned parallel or anti-parallel to the field. Since hydrogen is a constituent of water and is thus found in every kind of tissue, it is the most commonly studied (its nucleus is a single proton with spin ½).

When the atomic nuclei are aligned parallel (or anti-parallel) to the field, they precess about their spin axis (analogous to a child's spinning top precessing in the earth's gravitational field). These precessing protons are then given a predetermined amount of energy with an incident pulse of radio-wave electromagnetic radiation (radio-wavelength radiation is resonant with the precession). The time it takes the agitated nucleus (or proton for hydrogen) to return to its original position depends on its electric shielding and its local magnetic field (i.e. on the atoms and molecules surrounding it) and thus differs for each kind of tissue. By sending radio wave pulses of specific energies, pulse lengths and wavelength, the contrast between the different tissues can be maximised.

The varying magnetic fields produced by the relaxing nuclei in the different tissues are recorded by measuring the electric currents they induce in coils of metallic wire called receiver coils. In order to spatially resolve the edges of bones, organs, etc, different fields with varying strengths are applied. These variations in the magnetic field and in the radio frequencies can be used to divide the body into the voxels from which the MRI images are made. MRI scanners can be used to probe different connective tissues, e.g. bone, tendon, ligament, cartilage etc, and the images they produce can give information about the structure, function and pathology of joints.[50] Recently, smaller MRI scanners have been developed which have higher magnetic fields and produce more localised scans e.g. of a limb. The use of these smaller scanners (**Magnetic Resonance Microscopy (μM.R.)**) has enabled investigators to create in-vivo images of bone microarchitecture and discriminate individual trabeculae.[51] From these images, it is possible to calculate various structural properties of a bone e.g. the mean trabecular spacing.

The process of magnetically inducing precessions, using radio-waves to induce an agitation, and electromagnetically observing the relaxation of nuclei, can also be used for chemical analysis. If the precession and recovery characteristics of a certain nucleus in a certain biochemical are known, then one can look for it *in vivo*. **M.R. spectroscopy** has already been used to investigate tumours of the breast, prostate and cervix among others and the presence of certain chemicals which can help differentiate between malignant and benign growths has been confirmed.[52,53,54] The technique has also been applied to tumours in bone; in one study the presence of a biochemical (choline) was determined and used to diagnose malignancy, its success at was notable (sensitivity: 95%, specificity: 82%, accuracy: 89%).[55]

None of the variants of magnetic resonance analysis outlined here expose a patient to harmful ionizing radiation and hence may become useful for screening for bone disease. However, presently the M.R.I. scanning procedure is time-consuming (much slower to perform than a C.T. scan) and expensive (a single scanner can cost millions of pounds). There are some safety issues associated with the intense magnetic fields utilised in M.R.I., metallic objects can be subjected to strong forces and may become projectiles if they are brought to close to the scanner. This is especially dangerous to patients with implanted metallic or electronic devices, e.g. pacemakers.[56]

Positron emission tomography (PET) is a medical imaging technique that can be used to create 3-D images of internal organs and tissues.[57] In PET a bio-compound is labelled with radioactive markers, injected into the patient and its distribution around the body is measured as function of time. The radioactive markers (or radiopharmaceuticals) are manufactured in special nuclear reactors and decay relatively quickly (half-life in the region of ~20 minutes). The atoms employed are ones which decay via positron emission. Once the decaying atoms are inside the body and are emitting positrons, a

secondary sub atomic event begins to occur inside the body. The emitted positrons combine with electrons present in the surrounding tissues and are annihilated, this annihilation results in the creation of two high energy (short wavelength) gamma-ray photons.

The two gamma-ray photons travel in opposite directions (conservation of momentum law) and when detectors arrays 180° apart detect two photons at the same time the event is recorded as a count. In practice the angle is allowed to deviate slightly from 180° to allow for some scattering events and there is a small time window that is considered the 'same time' (of the order of nanoseconds). When the count is measured an imaginary line is recorded connecting the two detectors. An image is created by a computer out of millions of these lines.

PET is a quantitative technique; the differing amounts of radiopharmaceuticals which accumulate in different parts of the body are measured as units of radioactivity per volume. The quantitative data complements other imaging techniques well (even those with better resolution such as CT or magnetic resonance imaging) and it plays an increasing role in the assessment of possible tumours and infections in bone.[58] PET studies of bone formation and bone diseases have also been reported.[59] However, PET also has some severe limitations: it is a complex undertaking, requiring a concerted effort of chemists, radiopharmacists, physicists and physicians. Add to this the equipment and chemical costs and it is clear why PET scans are quite expensive. PET scans are also time-consuming because not only can a scan can take several hours but it can take hours or days for radiopharmaceuticals to accumulate in the part of the body being studied. The availability of radiopharmaceuticals is a major problem, by necessity they decay relatively quickly and only last for a few hours (to limit the release of ionising radiation) so the scanner needs to be near a facility with expertise and capability to make the radioactive tracers and the scans need to be well planned.

***Ex Vivo* Imaging Techniques**

Powerful analytical techniques have been used to probe every aspect of excised bone material and image it at each of its hierarchical scales of order. In the following chapters data related to and obtained from a number of different analytical techniques will be presented, some of those techniques are described here.

Atomic force microscopy (AFM)[16] is a technique in which the tip of a tiny probe needle (usually made of silicon) mounted on a springy arm (called a cantilever) interacts with the surface of the sample. Topographic features will mean the tip has to travel difference distances to measure the same force at the different points on the surface (the up and down movement of the tip is usually measured by reflecting a laser off the back of the cantilever and onto a quadrant photodiode). The data are then processed by a computer and turned into a visual image. The technique is not limited by the optical

diffraction limit (spatial resolution of ~1 nm have been reported)[60] and AFM has been used to image hydroxyapatite crystals and the surfaces of mineralised/demineralised collagen fibrils. AFM has also been used to image bone at the micro-level with studies of resorption cavities and lamellae being reported.

AFM instruments can also be used to measure the mechanical properties of samples, this technique in which the displacement is measured as a stiff AFM tip is driven into the sample at a defined loading (and unloading) rate is called **nanoindentation**. From the unloading portion of the curve, the elastic modulus and the hardness of the sample can be calculated. Many nanoindentation studies of bone have been reported. They include an investigation of the mechanical properties of bone material as it develops in growing rats,[61] of the anisotropy/heterogeneity of bone material, of the effects of genetic mutations, and of low protein diet.[16] The nanoindentation study of developing rat bone showed the tissue properties increased rapidly in the first several days of bone formation and thereafter increased only slightly through 70 days (0 – 4 day old bone material was less stiff (~5 GPa vs. ~30 GPa) and less hard (~0.3 GPa vs. ~1.5 GPa) than bone material that was 29–70 days old). Nanoindentation has also been used measure the reduced stiffness and hardness in diseased bone material and bone material from ovariectomy-induced osteoporotic rats[16] and in bone material which has had mineral removed with acid.[62]

Another non-optical technique which has been used to image the constituents of bone material is **Electron Microscopy (E.M.)**. An electron microscope uses a beam of electrons in place of photons to image the sample. Since the electrons in the beam have much shorter wavelengths than visible light, electron microscopes are capable of much higher resolution than optical microscopes (TEM - ~1 nm, spatial resolution similar to AFM, SEM – 1-10 nm, not as high as TEM)[60,]. The electrons can be passed through a thin section of sample and collected on the transmitted side (**Transmission Electron Microscopy**) or the signal they produce when they interact with the sample surface can be collected (**Scanning Electron Microscopy**). The electrons are usually emitted from a tungsten filament and the sample is usually housed in a vacuum chamber for imaging. For scanning electron microscopy the sample must be electrically conductive, for biological samples, such as bone, this means they are usually coated in a thin layer of metal before imaging. Both transmission[63] and scanning[64] electron microscopy have been used to analyse collagen fibrils, bone microstructure, hydroxyapatite crystal structure and bone cells.

Scanning Electron Microscopes can be used to perform elemental analysis. The technique is called **Energy-dispersive X-ray spectroscopy** (EDX) and relies on the fact that when SEM probe-electrons collide with the sample atoms, an electron can be ejected from an inner shell. If an outer shell electron falls in to replace it, the lost energy can be emitted as an x-ray photon. Each element has a

characteristic electronic structure and thus a characteristic x-ray emission spectrum. EDX can be used to probe bone material, e.g. one study of functionally adapted bony materials showed that the bone mineral composition (as measured using Ca/P molar ratios) did not differ between samples with a wide range of densities.[65]

Another class of laboratory techniques which have been used to study the structure of the hydroxyapatite crystals and collagen fibrils in bone are the small angle scattering (SAS) techniques; **Small Angle X-ray Scattering** (SAXS) and **Small Angle Neutron Scattering** (SANS). In SAS studies of bone material, the probe particles (be they x-ray photons or neutrons) are usually generated by a synchrotron/particle accelerator (or sometimes a nuclear reactor). They impact on the sample and the majority of them pass thorough to the detector without interaction. However, some of the probe particles elastically scatter from the bone and deviate slightly from their original path, the resultant diffraction patterns can be analysed mathematically. The data obtained from each technique are complimentary; for example, neutrons scatter from atomic nuclei and hence scatter strongly from materials with high hydrogen content (water, organic compounds) whilst x-ray photons scatter from electron clouds and hence scatter strongly from materials with relatively large electron densities (metals, mineral crystals).

Much important information that is known about the nanostructure of bone material's mineral phase comes from SAXS; it has been used to study the thickness and orientation of the hydroxyapatite crystals in both bone and dentin, in diseased bone (osteogenesis imperfecta) and mineralising turkey leg tendon.[17,20,28,66] Investigations of the bone-cartilage interface in joints and of bone archaeological science have also been reported.[67,68] SANS has been used to study the organic (collagen) phase of the bone material; it has been used to measure the distance between the tropocollagen molecules in the collagen fibrils in cortical bone (distance along the radii and from end to end).[69] It has also been used to look at the lateral spacing of collagen fibrils in healthy (cortical) bone and diseased (osteoporotic cancellous and osteoarthritic cancellous) bone.[70] The collagen spacing in the osteoporotic bone was larger than normal and the spacing in osteoarthritic bone was smaller, though neither measurement was statistically powered.

Optical Spectroscopy Techniques

Optical spectroscopy techniques use radiation from the infrared (IR) to the ultraviolet (UV) region of the EM spectrum to probe molecular energy levels. Every molecule has a total energy which can be split into four components; the electronic energy, related to the occupancy of the molecule's electron orbitals; the vibrational energy, related to the movement of the constituent of atoms relative to each other; the rotational energy, a measure of atomic movement about the molecule's internal axes and the translational energy, the kinetic energy of the molecule as it travels through space.

$$E_{Total} = E_{Electronic} + E_{Vibration} + E_{Rotation} + E_{Translation}$$

The first three components of the total energy, the 'internal' components, are distinguishable from the translational energy in that they are quantised; they have discrete values and a minimum non-zero value which is called the ground state. The molecule's velocity through space does not have similar discrete values, and hence its translational energy is not quantised in the same way.

The electronic, vibrational and rotational energies can usually be considered separately because they are not of the same magnitude;[IV] the electronic energy is roughly three orders of magnitude greater than the vibrational energy which is in turn three orders of magnitude greater than the rotational energy.[71] At room temperature and standard pressure, the majority of molecules are in their electronic and vibrational ground states.[V] Figure 1.7 shows a schematic representation of the vibrational and electronic energy levels of a molecule, the rotational energy levels are omitted for clarity but if they were present they would be drawn as smaller graduations between each vibrational state. In real molecules, vibrations of different orders and involving different atoms have characteristics energies and the exact spacing between the energy levels is affected by the local chemical and molecular environment in which the vibration occurs.

[IV] Born-Oppenheimer approximation

[V] The proportion of molecules in a given population which exist in the ground state can be calculated using the Boltzmann distribution [$N_{upper}/N_{lower} = e^{(-\Delta E/kT)}$]. If $-\Delta E$ (the energy difference between (for instance) the first two vibrational states of a molecule is 11.5 kJ mol^{-1} (a typical energy value), then N_{upper}/N_{lower} = ~0.01 at 300K, meaning the first excited state is about one percent of the ground state.[71]

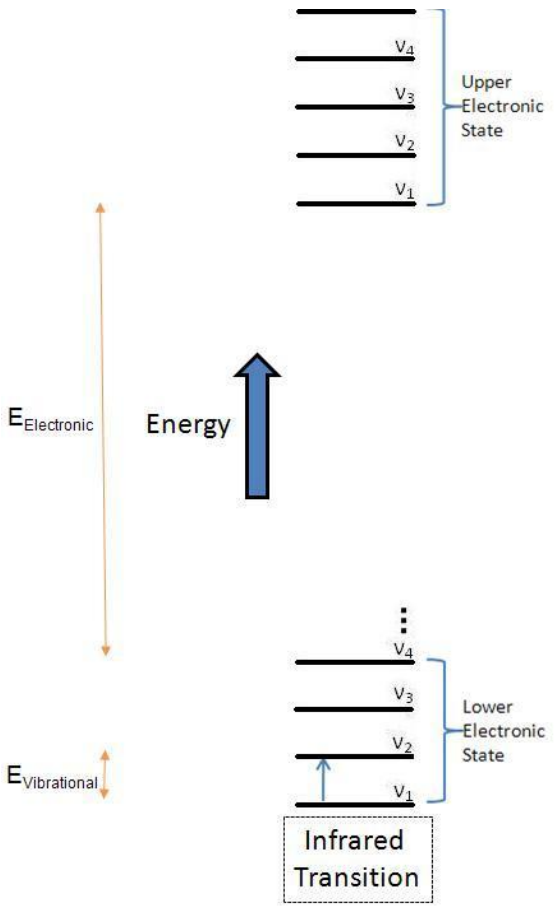

Figure 1.7 Schematic representation of the vibrational and electronic energy levels of a molecule. The rotational energy level would be found in between the vibrational levels if they were shown. The arrow starting at the ground electronic/vibrational state shows the molecule being excited into an excited vibrational state by the absorption of an infrared photon.

Infrared Absorption Spectroscopy

Infrared absorption spectroscopy is a technique in which light with a range of wavelengths is sent through a sample and the transmitted light is analysed. Those photons with energies that match energy-level transitions absorb more strongly than those which do not and hence the transmitted light will show absorption bands at certain energies. Figure 1.7 shows a sample molecule absorbing a photon and being raised from the ground energy level; if a range of wavelengths (i.e. a range of energies) were incident on this molecule then an absorption band would exist at the wavelength corresponding to energy v_2-v_1.* The typical energies between vibrational levels of a molecule mean

* The frequency and wavelength of this photon are related to the energy difference between the vibrational states by the simple relations [$E = v_2\text{-}v_1 = h\,\nu = h\,c/\lambda$] where energy difference (E) between the ground state (v_1) and the final state level (v_2), h is Planck's constant = 6.626068×10^{-34} m^2 kg s^{-1} and ν is the frequency of the photon, λ is the wavelength of the light and c is the speed of light = 299,792,458 m s^{-1}.

that these absorbed photons will usually be from the infrared (I.R.) part of the electromagnetic spectrum (i.e. between visible light and microwaves {λ = ~750 nm to λ = ~0.1 mm}).

Infrared absorption spectroscopy has been extensively used to analyse bone material and many of the studies described in the Raman literature review section below (pg 52) have analogues in the I.R. literature (for example, studies of biocompatibility of implants, the composition of bone mineral, mineralisation, aged and diseased bone).[72] Indeed, most of the spectral band assignments used in Raman spectroscopy came from the older field of infrared spectroscopy. If some spectral feature is measured with I.R. (or Raman) at many different points on a sample surface, images (maps of chemical composition) can be created.

I.R. spectroscopy has some advantages over Raman spectroscopy; it generally offers better signal to noise ratio than Raman and fluorescence is much less of a problem (for reasons that will become clear after the discussion of Raman theory).[72,73] However, there are also limitations that are not associated with Raman; there is significant interference from water and the technique requires that the sample be transparent to infrared (I.R.) light; for bone material this means the samples typically need to be cut into sections less than 10 μm thick and mounted on I.R. transparent slides.

Other Optical Absorption Spectroscopy Techniques

The infrared spectral region is bordered on the low wavelength side (boarder ~750 nm) by the visible region which itself borders (~390 nm) the ultraviolet (U.V.) region (this extends to the start of the x-ray spectrum (~10 nm). A **UV/Vis absorption spectroscopy** experiment is conceptually similar to the infrared absorption technique described above but the radiation's higher energy means it is used to probe the *electronic* energy levels of molecules (Figure 1.8). Although UV/Vis absorption spectroscopy is not widely used to study bone material, it has been introduced here because it is related to fluorescence spectroscopy. Fluorescence is an important concept for Raman spectroscopists and will be described in detail in the next chapter.

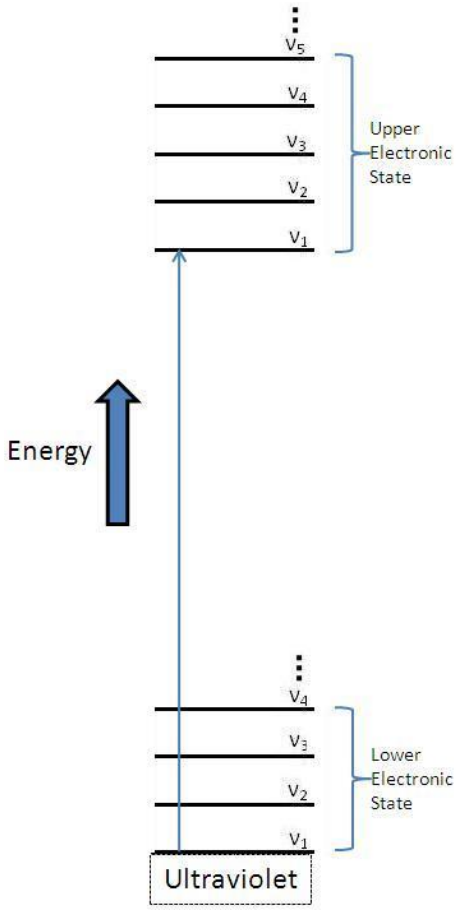

Figure 1.8 shows a shows a molecule being excited into an excited electronic state by an ultraviolet absorption.

The spectral region on the other side of the infrared (i.e. the longer wavelength, lower energy region that borders the microwave region) is called the **Terahertz** (THz) region (~0.1 mm - ~1 mm), beyond that is the microwave region. Obtaining suitable sources and sensitive detectors for THz radiation have historically been problematic and have limited its use as an analytical tool. THz spectrometers are currently being introduced to the market but very few reports of its use to analyse bone material have been published. Stringer et al. attempted to use THz to measure the mechanical properties of bone material but they had limited success.[74] The energies associated with THz radiation are resonant with inter-molecular vibrations and thus it may prove useful for studying cross-linked collagen molecules and for studying the relationship between collagen and mineral, indeed a recent study concerning biological tissues stated "terahertz radiation is sensitive to covalently cross-linked proteins".[75] It is conceivable that THz radiation could become a useful for examining excised bone samples, however, THz radiation has a property that will limit its development as an *in vivo* technique; it is absorbed by water and hence will not easily pass through skin or other human tissues.

1.4 Conclusions from Chapter One

This chapter has introduced some of the terms and concepts which will be used in the rest of the thesis. It has described the chemical composition of the organic scaffold (mostly collagen) and the hydroxyapatite crystals which surround it. Some of the techniques which have been used to image and analyse bone material in the past have also been described. From these discussions it is apparent that the most widely used (esp. radiographic) techniques for probing bones *in vivo* are blind to the organic phase of the bone composite and that those technique which *are* good at probing both phases are not readily employed *in vivo*. Since organic phase can account for up to 30% of the weight of the bone material (Figure 1.4), this is far from ideal.

The organic phase does not just account for a large percentage of the mass the bone material but also contributes to its mechanical properties. It has already been stated that DXA-measured aBMD accounts for only 60–70% of the variation in whole bone strength,[45] the importance of the organic phase to the mechanical properties can be further illustrated with experiments that utilise ionizing radiation. The ionizing radiation damages the organic phase much more than the mineral phase,[76,77,78] and has a severe effect on the fracture properties of bone material. In particular, it reduces the energy absorption, as measured by work to fracture.[78,79]

The next chapter will describe the analytical technique which is the main focus of the present work and which can probe both organic and mineral phases of the bone material, Raman spectroscopy. Reports from the literature of its use in analysing bone material, and of its potential to be developed as an important *in vivo* technique[VI] will also be reviewed.

[VI] It should be noted that an aBMD measurement combines contributions from two different types of information, the nature of the bone material (i.e. its density) and the quantity of bone material present. Raman measurements only contain information relating to the first, the nature of the bone material.

2. Raman Spectroscopy and its Use in the Analysis of Bone Material

2.1 Raman Spectroscopy

Origins

The inelastic scattering of light from matter is named the Raman effect after the Indian scientist Chandrasekhara Venkata Raman who first observed it. Raman, along with his students at the Indian Association for the Cultivation of Science in Calcutta, studied the scattering of filtered sunlight from various liquids during the 1920s. The experiments culminated on the 28th February 1928 when they passed monochromatic light from a quartz mercury lamp through bulbs containing a series of liquid samples. Raman reported the results of this experiment to the South Indian Science Association on the 16th March 1928 in a talk titled 'A New Radiation',[80] he stated "most liquids showed in the spectrum of the scattered light, a bright line in the blue-green region of the spectrum, whose position was practically the same for chemically similar liquids such as pentane, hexane and octane for instance. There was, however, a recognizable difference in the position of the modified line when other liquids such as benzene or water were used".[81,82] He was awarded the Nobel Prize in Physics for his discovery in 1930, he was so sure of winning that he had booked his travel four months before the prize was announced.[83]

Scattering

The absorption processes discussed in the previous chapters are not the only possible result when light is incident on a molecule. The light can also scatter from the molecule, the scattering can be an elastic process (no energy is exchanged between the photon and the molecule, e.g. Rayleigh scattering) or an inelastic process (energy is exchanged between the photon and the molecule, e.g. Raman scattering). Figure 2.1 shows energy level diagrams of these scattering processes, they consist of two steps. First, the photon and the molecule combine to excite the molecule to a higher energy 'virtual' state (this step is represented by the upwards part of the arrows). This virtual state exists for a very short time (~10^{-15} s, the virtual states are represented as stationary points on the arrows) before the second step occurs; a new photon is released and the molecule is returned to a vibrational state. It is evident that the only differences between the three scattering diagrams (one Rayleigh and two Raman) in Figure 2.1 are the vibrational energy level from which the molecule begins the scattering process and the level where it ends up after the process is complete.

If the molecule ends up at the original energy after the scattering event, the released photon will have the same energy as the original one (Figure 2.1 - the arrow will be the same length) and the process is called Rayleigh scattering. If the molecule ends up at a different energy level, the photon released will

have a different energy (Figure 2.1 - the arrow will be a different length) and the process is Raman scattering. A Raman scattering event that creates a photon with less energy (longer wavelength) is called Stokes scattering and a Raman scattering event that creates a photon with more energy (shorter wavelength) is called anti-Stokes scattering.[84] Changes of $\Delta v = 0 \ \pm 1, \pm 2\ldots$ are possible (which is the same as infrared absorption spectroscopy) though the probability of $\Delta v = \pm 2, \pm 3\ldots$ decreases rapidly. In order for an anti-Stokes scattering to occur (change in photon energy Δv = +ve) the molecule must be in an excited energy state before the scattering event, it was already noted that unless the scattering material is very hot, most of the molecules will occupy the vibrational ground state; hence in normal conditions anti-Stokes scattering events will be much less numerous than Stokes scattering events.[VII]

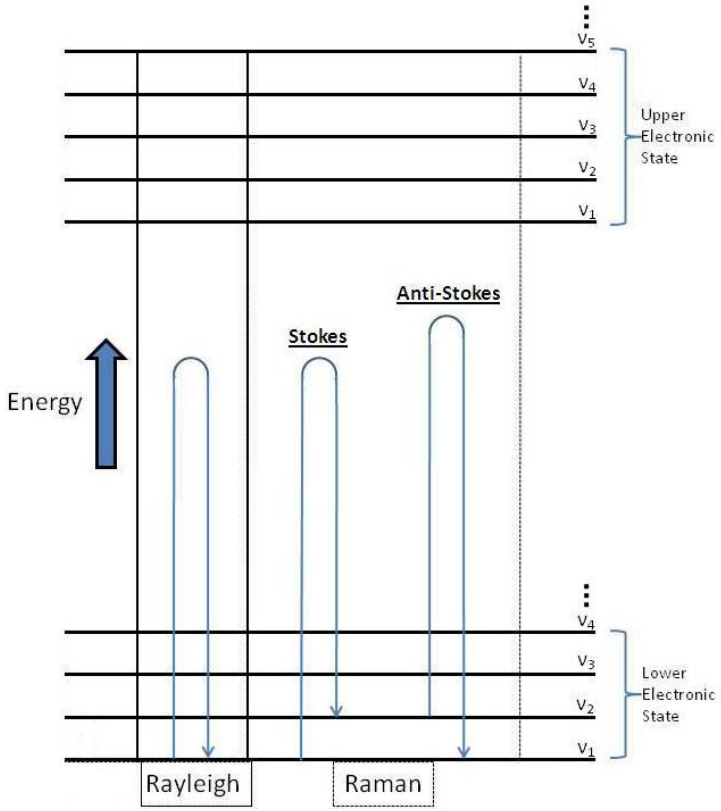

Figure 2.1 shows the elastic and inelastic scattering processes. The difference between scattering and absorption is evident, for scattering the energy of incident photon does not have to match the energy level difference (cf. absorption in Figure 1.7 on pg 37).

[VII] This, again, can be calculated with the the Boltzmann distribution [$N_{upper}/N_{lower} = e^{(-\Delta E/kT)}$]. That is, if $-\Delta E$ (the energy difference between (for instance) the first two vibrational states of a molecule is 11.5 kJmol^{-1} (a typical energy value), then N_{upper}/N_{lower} = ~0.01 at 300K, meaning the first excited state is about ~1% of the ground state.[71]

A scattering event from a molecule in its ground state can lead to Rayleigh scattering or to Stokes shifted Raman scattering but the probability of each event occurring is very different. Rayleigh scattering is 10^6-10^8 times more likely to occur; hence the number of inelastically scattered Raman photons is comparatively tiny and Raman signal is very weak.[85] If a molecule has a centre of symmetry[VIII] then Raman active vibrations are infrared inactive (and vice versa), this is called the mutual exclusion principle. If there is no centre of symmetry then some (but not necessarily all) vibrations may be both Raman and infrared active.

The Intensity of the Scattered Radiation

The energy level (Jablonski-type, Figure 2.1) diagrams above describe some the features of Raman scattering but they say little about the intensity of the scattered light and little about how the nature of the incident light affects the process. To address these issues, more formal mathematical descriptions are required; such descriptions can be formed in several ways. Classical mechanical models can be formed which treat radiation as an electromagnetic wave and the scattering material as an assembly of rotating/vibrating 'balls and sticks'. These classical models can be used to explain some aspects of Raman scattering, such as the frequency dependence of the scattered light, but they are silent on many others. The other extreme is to form a full description of all the relevant physics using a quantum electrodynamical approach, i.e. treat both the energy of the radiation and the energy of the scattering system as fully quantised (as they are in the diagrams above). This approach is difficult, results in unwieldy equations and is unnecessary for the purposes at hand. A third approach is to combine aspects of both the classical and the quantum electrodynamical approaches, specifically; to consider the radiation as a classical electromagnetic wave and the scatterer as a material system with quantised energy levels. This is the method presented here.[86]

[VIII] If a straight line can be projected from an atom A through another atom L and on again to identical atom A, and if the length of |AL| is identical to |LA| then L is a centre of symmetry of the molecule.

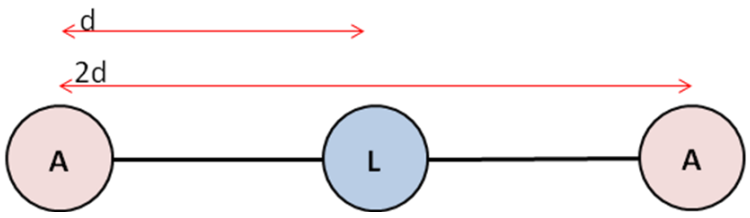

If electromagnetic radiation is incident on a scattering material which starts at a ground state G, passes through a virtual state r, and finishes at a final state F, then the intensity (I) of the scattered light:

$$I = K\,(v_0 \pm v_{GF})^4 I_0 \sum_{\sigma\rho} \left|(\alpha_{\sigma\rho})_{GF}\right|^2$$

Equation 2-1: Intensity of scattered Raman radiation.

where K is a constant, ν_0 is the frequency of the incident radiation, ν_{GF} is extent of the frequency shift and I_0 is the intensity of the radiation incident on the scatterer i.e. the number of photons per unit area per second. The subscripts σ and ρ each represent a Cartesian coordinate x, y or z (σ can be equal to ρ) meaning that after the summation operator there are nine versions of the transition polarisabilty tensor $\alpha_{\sigma\rho}$. These transition polarisabilty tensors have the form:

$$(\alpha_{\sigma\rho})_{GF} = \frac{1}{h}\sum_r \left(\frac{\langle F|\mu_\rho|r\rangle\langle r|\mu_\sigma|G\rangle}{v_{rG} - v_0 + i\Gamma_r} + \frac{\langle F|\mu_\sigma|r\rangle\langle r|\mu_\rho|G\rangle}{v_{rF} + v_0 + i\Gamma_r} \right)$$

Equation 2-2: Transition polarisabilty tensors.

As before the ground state is G, the virtual state is r and the final state is F, and again there is a constant (1/h) before the summation operator. The description now diverges from the picture outlined in the discussion of the energy level diagrams above, there, it was implied that the virtual state was a definite state, with energy equal to the energy of the incident photon plus the energy of the initial vibrational state; this is now revealed as a simplification. In reality, many virtual states must be considered, one for each of the possible quantum mechanical states (vibrational or electronic) of the actual molecule.[IX] The two descriptions can be best reconciled if the situation in the energy level diagram is considered to be the most *probable* occurrence, but it must be remembered that in a fuller quantum mechanical/mathematical treatment all the other possibilities must also be accounted for.

[IX]The interaction is un-quantised but Heisenberg's uncertainty principle means that conservation laws are not broken, i.e. the virtual states are extremely short lived, $\Delta E\,\Delta t \geq \hbar$.

The numerator and the denominator of the remaining terms will be considered separately. The denominators have one new term, Γ_r, which is a damping constant and takes into the account the finite lifetime of each molecular state. It is small compared with ν_{rG}, ν_{rF} or ν_0. The numerators are written in Dirac notation and are so similar that only one needs to be elaborated. The term

$$\langle F|\mu_\rho|r\rangle$$

Equation 2-3: one term of a Transition polarisabilty tensor along the ϱ-axis.

gives the amplitude of the electric dipole transition moment where μ_ρ is electric dipole moment operator operating on F along the ρ axis, the wave functions of the virtual state and the excited state are given by r and F respectively.

From the consideration of these equations it becomes clear that the factors which are important in determining the intensity of the Raman radiation from a material with vibrational ground state G and excited state F are the ***intensity of the incident radiation***, the ***wavelength of the scattered radiation*** (to the power of four), and the ***properties of the molecular vibration*** in question. These properties include the geometry of the molecule (which will determine which of the nine 'Cartesian' terms are important) and the values of the electric dipole moment for each quantum mechanical state.

Generalizations on Raman Intensities

The mathematical description shows that Raman scatter is determined by the properties of the incident light and the transition polarisabilty tensor. In order to use the equations to determine how intense the scattering would be from a particular chemical bond one would need to include many terms, the transition polarisabilty tensor includes terms related to all the possible quantum mechanical states of the molecule and hence it is not feasible to do full mathematical investigations of every scattering system in the laboratory. The mathematics however can be summed up by the statement, "any molecular vibrations which affect the *ability* of a molecule to become polarized by an electromagnetic wave will be a (relatively) strong Raman scatterer". This leads to some generalisations which prove to be useful in practice:

- Stretching vibrations should scatter more than deformation vibrations
- Multiple bonds i.e. double bonds and triple bonds should scatter more than single bonds, e.g. C=C scatters more than C-C
- Raman scatter is more intense when molecules are symmetric and have many conjugated electrons e.g. cyclic compounds are intense scatterers but molecules with a strongly electronegative atom are not

Polarisation Effects

A beam of electromagnetic radiation consists of electric and magnetic fields oscillating at right angles to each other and at right angles to the direction of propagation. For the scattering processes which are concerned with the electrons orbiting a molecule, it is the electric field component of the radiation which is most important. If we imagine the electromagnetic wave to be travelling towards us (with axis of propagation labelled z), the electric component of the light will be oscillating along a line on the x-y plane and the line will be randomly changing its orientation about the z-axis. We can imagine a case where the electric field component is fixed on the x-y plane (i.e. its orientation about the z-axis is fixed) this is called linearly polarised light.

When linearly polarised light is incident on a molecule, it interacts with the molecule's various chemical bonds in a distinct way; interactions with bonds that lie in the same plane as the electric field will be stronger than those which lie perpendicular to the electric field of the incident light. If the light is incident on the same molecule but the polarisation angle is different, the bonds will experience different electric fields. Hence, scattering is affected by the orientation of a molecule's bonds with respect to the electric field component of the incident radiation.

This dependence of Raman band intensity on the polarisation of the incident light provides spectroscopists with the ability to check band assignments. If unpolarized light (whose electric component is randomly changing its orientation about the direction of propagation, the z-axis) is incident on a molecule (e.g. a methane molecule), the scattered light may have some degree of polarisation (Equation 2-4). The degree of polarisation (the depolarisation ratio) of a Raman band is a measure of the symmetry of a vibration. Symmetric vibrations have the lowest depolarisation ratios. For example, in the case of methane, the totally symmetric vibration gives rise to a completely polarized Raman line whereas the non-symmetric vibrations give depolarized lines.

$$\rho = \frac{I_{\perp}}{I_{\parallel}}$$

Equation 2-4 When scattered light is passed through a piece of polaroid (or other analyser), its intensity will have a maximum ($I_{\perp}$) for some polaroid angle (X°) and a minimum ($I_{\parallel}$) at some angle (X+90°). This is called the depolarisation ratio.

This description of polarisation and the depolarisation ratio is rooted in the classical description of light as a plane wave and unlike the theory section above there is no mention of photons. A quantum mechanical description of Raman scattering which included the intensity terms above (such as the transition polarisabilty tensor) and also included polarisation effects would be very challenging to formulate and would be beyond the scope of this thesis. It is however possible to bridge the

conceptual gap between the discussions if it is recalled that electromagnetic waves comprise a large number of photons, and if the phenomenon of circularly polarised light is considered. In the case of circularly polarised light, the electric component, instead of travelling along a line, travels around a circular path on the x-y plane (about the z-axis). The electric component can rotate clockwise or anti-clockwise (as the light comes towards us) and this corresponds to left-circularly and right-circularly polarized light respectively.

This circularly polarised light is closely related to the spin angular momentum quantum number of individual photons: each photon carries spin angular momentum which has two possible values (+1 and -1) and does not depend on its frequency. The spin angular momentum has three orthogonal components and the component measured along the axis of propagation is called the helicity. The two possible values of the helicity correspond to left-circularly polarized and right-circularly polarized light.

Raman Instrument

In light of these discussions of Raman scattering theory, it is helpful to now consider the workings of a Raman instrument. The principles behind its operation will be outlined here; more technical descriptions of the apparatus will follow in the methodology sections below (pg 69).

A Raman instrument consists of three main components:

1. A light source. The availability of bright monochromatic light sources was one of the factors preventing the widespread adoption of Raman spectroscopy for many decades. However, since the latter half of the twentieth century, the filtered sunlight and gas-discharge lamps of the early days of Raman spectroscopy have been superseded by the development of cheap efficient laser light sources. Modern lasers (Acronym - **L**ight **A**mplification by **S**timulated **E**mission of **R**adiation) can emit light at a single wavelength from the ultraviolet (UV) to the near infrared (NIR) and beyond, can deliver high intensities and can maintain their performance for many thousands of hours.

2. A wavelength discriminator. A Raman instrument must have a component for separating the Raman signal from the light that has been elastically scattered from the sample; the much weaker Raman signal would otherwise be obscured. The instrument must also be able to separate the different wavelength Raman photons in order to record a spectrum. Originally, sets of filters and later monochromators were used for both tasks. Modern instruments use holographic notch filters, made by imprinting inference patterns in optical media with laser beams, to remove the elastically scattered laser light. These filters are very efficient and their recent development has aided the widespread use of Raman spectroscopy. In modern

instruments the Raman signal is separated into its constituent wavelengths using dispersive techniques (diffraction gratings) or interferometry techniques (interferometer & computer running a Fourier transform program).

3. A detector. In the original experiments C.V. Raman detected the photons with his eyes and the first Raman spectra were recorded spectra using photographic plates. The later application of photomultiplier tubes to Raman spectroscopy meant that weaker signals could be measured and better spectra obtained. As with the first two components of the Raman instrument (i.e. the light source – laser, and wavelength discriminator - notch filter) advances in technology mean modern detectors are faster and easier to use. The current detector of choice for widely used dispersive systems is the charge coupled device or CCD camera. A CCD camera consists of a semiconductor chip which builds up electrical charge when electrons are incident on it; the charge is then read off by electrodes and recorded on a computer. The chip can have millions of electrodes on it and are designed so as to be most sensitive in the optical region of interest.

The Appearance of a Raman Spectrum

In a Raman spectrum the energy of the scattered photons is recorded along the x-axis and the intensity of the Raman signal is recorded on the y-axis, an example is shown in Figure 2.2. The energy of the axis is represented as a wavelength shift from the laser wavelength, rather than in absolute wavelengths; this enables the comparison of spectra recorded with different instruments and with lasers of different wavelength. The units are inverse centimetres (cm^{-1}), they enable comparison between spectra recorded with different excitation wavelengths. The spectrum in Figure 2.2 shows the Stokes shifted side of the laser line, the anti-Stokes spectrum is be found on the opposite side of the vertical axis and is much less intense (as discussed above – pg 42). Some spectroscopists prefer to keep the Stokes shifted spectrum on the left (negative) side of the vertical axis as it shows that those photons have lost energy. The spectra in this thesis will follow the former convention and will resemble the spectrum in Figure 2.2.

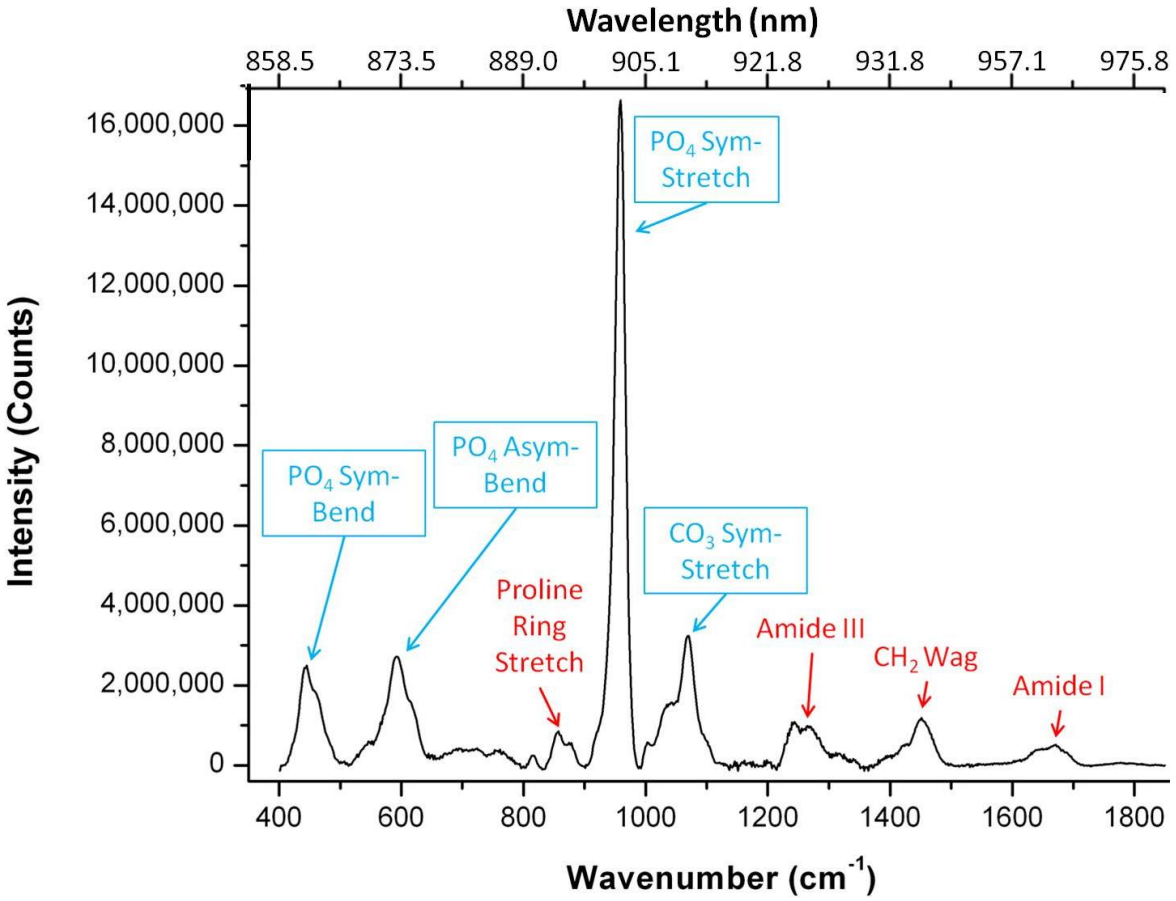

Figure 2.2 An example of a (Stokes shifted) Raman spectrum of bone material from the midshaft of an ovine femur. The top x-axis shows the spectrum in nm and the bottom in standard Raman spectroscopy units (Wavenumbers).

The intensity of the light in Figure 2.2 is measured in detector counts; this has to do with the charge coupled device (CCD) chip in the detector and will be explained later in the description of the experimental apparatus (3.1 Raman Instrument Section – pg 69). Since Rayleigh scattering is so much more intense than Raman scattering there is often a massive detector-saturating peak at the wavelength of the laser (wavelength shift = 0 cm^{-1}). Typically, the filter is used to remove this elastically scattered (Rayleigh) light also removes some of the Raman signal in that region of the electromagnetic spectrum and consequently the 'start' of the spectrum may be missing (e.g. the Raman spectrum Figure 2.2 starts at 400 cm^{-1}). The Raman spectrum in the example stops at ~1850 cm^{-1} because the sensitivity of the detector decreases after this point, again this is a determined in this instance by the CCD chip and will be explained below (pg 69).

The Raman theory to this point can be summarised as "an energy exchange occurs between a photon and a molecule, the energy lost (or gained) by the photon causes a change in the vibrational state of the molecule". It has been explained that Raman spectra comprise a number of Raman bands (and that

each band is an envelope containing a number of peaks). The physical relevance of the Raman spectra can be summarised as "each band has a frequency, and thus signifies an energy at which a vibrational transition (or a lattice vibration) takes place in the scattering molecule". In the stokes shifted Raman spectrum in Figure 2.2 the dominant band is the symmetric ν_1 phosphate stretch at ~960 cm^{-1}, this means that laser photons with energy X inelastically scattered from the sample, during the scattering process the photons lost an amount of energy corresponding to 960 cm^{-1} and were collected by the instrumentation. The other bands correspond to different molecular vibrations; their shape, position and intensity are different for each scattering molecule and hence Raman gives a unique chemical fingerprint.

Advantages & Disadvantages of Raman Spectroscopy

Advantages

- As water is a weak Raman scatterer, it does not interfere strongly with the recording of Raman spectra. This distinguishes Raman spectroscopy from some other spectroscopic techniques (e.g. infrared absorption spectroscopy or THz spectroscopy) and makes it amenable to many biological applications, including the spectroscopy of bone

- Since laser beams are fairly easy to manoeuvre onto the sample, the technique is easy to apply to a wide range of experimental setups. This makes it a very useful analysing a whole range of samples, be they solids, liquids or vapours in hot or cold states

- Lasers can be focused to very small points and hence photons can be scattered from well defined areas or from small volumes of sample. Theoretically, the spatial resolution is only constrained by the diffraction properties of the light (typical limit of 0.5 – 1 μm)[X]

- As mentioned above, the fact that the light from typical Raman laser wavelength is in the visible to infrared region (i.e. non-ionising) means that it is inherently safer for some applications than x-ray techniques

[X] Abbe diffraction limit: diameter of smallest spot, $d = \lambda / (2 \times N.A.)$, e.g. (830 nm / 2 x 0.08) = 5.19 x 10^{-6} m = ~5 μm. (Numerical aperture, N.A., is a measure of the light-gathering power of the system and is defined as $N.A. = n \times \sin(\theta)$, where n is the refractive index of the surrounding medium (~1 for air) and θ is the acceptance angle (the half-angle of the acceptance cone of the system, e.g. of an optical fibre). N.A. can vary between 0 and 1, the figure used in the example is for a collimated beam filling a full lens with diameter 2.5 cm and focal length 300 mm.

- Unlike many other analytical techniques, there is often no requirement for sample preparation with Raman

- The technique is non-destructive and once care is taken to avoid burning the sample with the laser, even valuable samples can be analysed

- Specialised Raman techniques can be used non-invasively to depths of several millimetres with biological tissues (e.g. Spatially Offset Raman Spectroscopy or Transmission Raman Spectroscopy) and can be highly chemical selective (e.g. Resonance Raman)

Disadvantages

- It was stated in the theory section above (Scattering – pg 41) that the for every 10^6-10^8 photons scattered form a sample only one is likely to be scattered inelastically and hence Raman signals are very weak. The inherent weakness of the Raman Effect means that conventional Raman spectroscopy cannot be used to measure trace quantities and that can be overwhelmed by other sources of light

- Related to the weakness of the effect is the fact that it cannot be used on samples which exhibit strong fluorescence in the spectral region. Fluorescence will be described in more detail below (pg 62); essentially it is the excitation of the target molecule into one of the upper *electronic* states accompanied by a subsequent emission of a photon. When the photon and the molecule's electronic gap have matching energies this interaction is much more favourable than Raman scattering and the resultant fluorescent emission drowns out the Raman signal. Its effects can be reduced by using probe photons with energies as far below the electronic excitation energy gap as possible

- Raman is unsuitable for pure metallic samples and not readily deployable with highly absorbing samples

- If care is not taken the laser can change the sample while it is being probed. If the intensity of the laser light at the sample is too high or if the laser energy is coincident with an absorption band then it can increase the temperature of the sample to undesirable levels. This can lead to sample degradation. If the energy of the probe photons is too high (i.e. the wavelength is too short) it may affect the chemistry of the sample

2.2 Use of Raman Spectroscopy to Study Bone

Raman spectroscopy of bone is a relatively young field; "the feasibility of obtaining Raman spectra from intact calcified tissue" was first demonstrated by Walton et al. in 1970.[87] Some sporadic reports of closely related subjects followed (bone proteins,[88] natural and synthetic hydroxyapatites,[89,90] bone implant interfaces[91]) but it was not until the mid-1990s that the field began to burgeon. As the interest in the Raman spectroscopy of bone has grown, it has been reviewed a number of times (the most recent review being published in 2010).[73,92,93,94,95,96] This section will not reiterate all the findings of those reviews, but will give an overview of the field.

Figure 2.3 shows the spectrum of ox tibia which was reported by Walton et al. in 1970 along with a spectrum of equine metacarpal bone from our laboratory.[87] The axes of the metacarpal spectrum have been set so as to aid comparison between the two, the full height of the phosphate band at 960 cm^{-1} can be seen in Figure 2.2 (pg 49). The interpretation of the data relies on knowing which molecular vibration in the bone is associated with each band in the spectrum and as was stated above much of this information comes from the older field of infrared absorption spectroscopy.[72] Roughly speaking, the bands below 1150 cm^{-1} are associated with the mineral phase of the bone material and those above are associated with the organic phase. The features at ~445 cm^{-1}, ~590 cm^{-1} and ~960 cm^{-1} are the symmetric bending (ν_2), asymmetric bending (ν_4) and symmetric stretch (ν_1) vibrations of the phosphate (PO_4^{3-}) group. The peak at ~1070 cm^{-1} is the carbonate (CO_3^{2-}) symmetric stretch and in the lower part of that band is the asymmetric stretching mode (ν_3) of the phosphate.[97]

The mineral phase of bone has been repeatedly and thoroughly studied with Raman spectroscopy since the mid 1990s. Many studies have focused on the comparison between the Raman spectra of natural and synthetic hydroxyapatites [References include: 98,99,100,101,102] and on analysing materials which could be used by surgeons for filling bone defects.[103,104,105] There has also been intense interest in the nature of the hydroxyapatite crystals themselves; Raman spectroscopy has been used along with other techniques to resolve the extent of substitutions at the hydroxyl group site in bone[106,107] and to study the maturation of the crystals.[108,109,110]

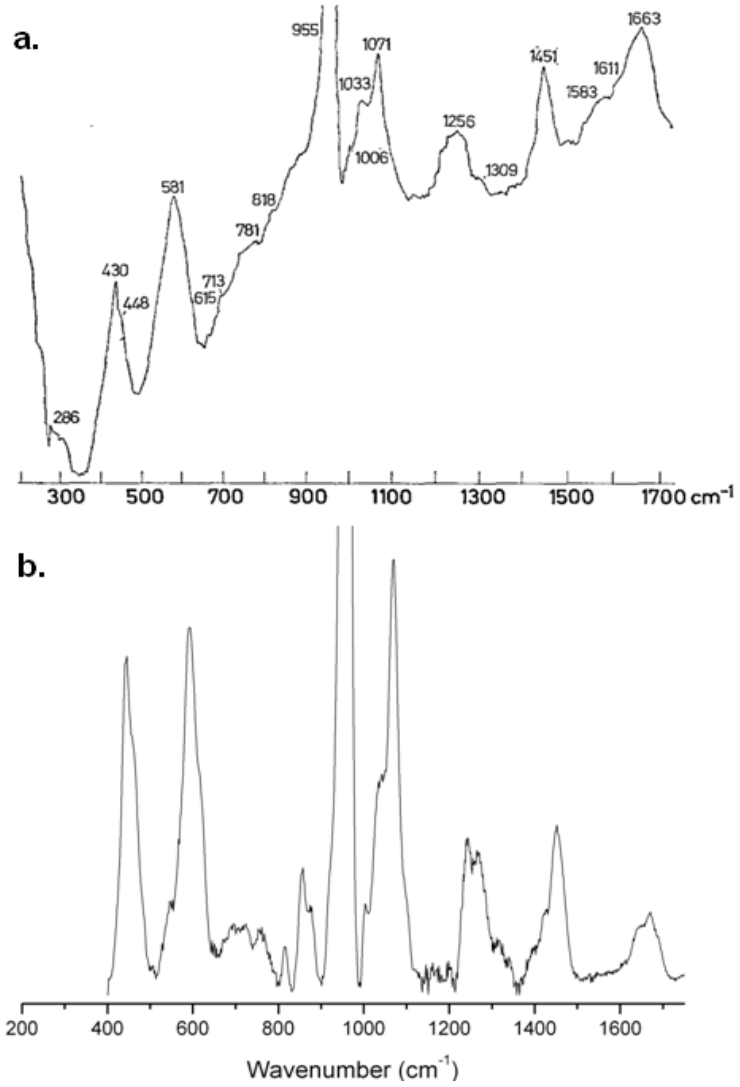

Figure 2.3 (a) First Raman spectrum of bone (Ox tibia) reported by Walton et al. in 1970.[87] The tops of the bands are missing where the detector has been saturated. [Laser, λ = 488 nm] 5(b) A spectrum of ovine femur bone from our laboratory. The bands have been plotted so as to aid comparison. Apart from the removal of the fluorescence background in the bottom spectrum (described below – pg 77), the main difference is in the proline/hydroxyproline region near 865 cm^{-1}.

What sets Raman spectroscopy apart from x-ray techniques however, is its ability to also probe the organic phase of the bone. It was discussed above how DXA-measured aBMD accounts for only 60-70% of the variation in whole bone strength[45] and how selectively damaging the organic phase of bone[76,77,78] has a severe deleterious effects on the fracture properties of bone material[78,79] so this capability is of obvious importance for understanding the mechanical properties of bone material. Raman can also be used to probe the bone material at different points on a whole bone and may offer insights into the interaction between the mineral and collagen phases.

Most of the molecular-vibrational Raman band assignments for collagen also come from the more established field of infrared spectroscopy; the small band with peaks at ~855 cm^{-1} and ~875 cm^{-1} are associated with the Proline and hydroxyproline residues on the collagen polypeptide chains (C-C and C-N ring stretches). The band between ~1230 cm^{-1} and ~1280 cm^{-1} is the amide III band; it involves the stretching of C-N along the backbone of the polypeptide chain, stretching of C-N at right angles to the backbone, and also some N-H in-plane bending. The band at ~1450 cm^{-1} is the CH_2 'wagging' mode (two H atoms vibrating out of the plane in unison). The amide I band centred at 1670 cm^{-1} is assigned to the C=O stretches in collagen molecules.

Raman Studies of Bone Material

Mineralisation and Development of Bone Material

Raman spectroscopy has been used to study the mineralisation and development of bone material for a number of years. A 1995 study of pathological growths in the ear used Raman spectroscopy to study the demineralisation and remineralisation of synthetic bone material that had been implanted in rats.[111] The hypothesis was that the mechanism of bone destruction associated with cholesteatoma (a type of skin cyst) was demineralisation; this was confirmed using Raman spectroscopy by measuring the narrowing of the PO_4^{3-} symmetric stretch (ν_1, ~960 cm^{-1}). *In vitro* studies using Raman techniques combined with other techniques have looked at the mineralisation of collagen obtained from fish bone, and at bone material produced by (rat) bone cells; in the latter case the network of mineralised fibres produced after 14 days had a chemical composition (as measured with Raman) that were similar to that of mature rat femur bone.[112,113]

The complicated self-assembly of collagen and hydroxyapatite into the hierarchical materials has been studied with combinations of light and electron microscopy, synchrotron x-ray diffuse scattering and Raman spectroscopy; these types of studies have begun to produce insights into the protein-control of biomineralisation,[114] and to the elucidation of a collagen self-assembly model mechanism (silica nano-tubes which self-organize into highly ordered centimetre-sized fibres).[115] The former study looked at the mineralisation of collagen type I scaffolds and used changes in the width of the PO_4^{3-} symmetric stretch (ν_1, ~960 cm^{-1}) to show that the transformation of amorphous calcium phosphate into crystalline hydroxyapaitite was controlled by DMP1 (Dentin matrix protein 1 - a non-collagenous protein present in the mineral phase of bone and dentin).

A prominent series of experiments used Raman to look at the ontogenetic development (from the embryonic stage to six months after birth) of bone material and cells in murine skulls. The experiments showed a variety of apatite mineral environments are present in the material during its development (by looking at the changes in the phosphate ν_1 region ~960 cm^{-1}).[116,117] The same murine

model was then used to study force-induced fusion of the bones of the skull at a premature state of development and it was found that the mineral to collagen ratio was decreased in the prematurely fused skulls (i.e. those fused by the experimenters) compared with controls.[118]

The mechanical properties of the collagen fibres at different levels of demineralisation,[119] and the chemical etching (demineralisation) process itself have also been studied with Raman spectroscopy.[120] The individual collagen fibres (obtained from teeth) were found to decrease in modulus from 1.5 GPa to 50 MPa (as measured by AFM-nanoindentation) with the removal of mineral (by acid etching). The demineralisation study contained a calibration curve based on the Raman spectra of known powder mixtures of hydroxyapatite and collagen constructed by looking at the hydroxyapatite Raman band at 960 cm^{-1} and the collagen Raman band at 2937 cm^{-1}. The detection limit for hydroxyapatite and collagen were found to be 2.8 % and 0.6 % weight respectively. The collagen figure may not be relevant to many of the other studies described here because although the high wavenumber bands (e.g. 2937 cm^{-1}) are very intense, they lack chemical specificity (they are due to C-H stretches) and hence are not often measured.

Effect of Age and Exercise on Bone Material

The age-related compositional changes of bone material are of great importance in trying to understand fragility fractures in the elderly. Raman spectroscopy is well placed to study subtle chemical changes in bone material; information that complements the well documented density and architectural changes which have been measured with x-ray techniques. A 2001 study showed that the crystallinity of the hydroxyapatite phase i.e. the degree of order and size of the crystals (measured using the width of the ν_1 phosphate band) and brittleness of the bone material increased with age in mouse femora.[121] The same paper also reported spectral and mechanical property changes associated with the incorporation of fluoride into the mineral crystals; the crystallinity increased more than normal but the brittleness *decreased* (The ν_1 phosphate band also shifted from 961 cm^{-1} to 964 cm^{-1}, possibly due to exchange of F^- and OH^- in the lattice).[121] Another Raman study which looked at the changes in the mechanical properties of bone material that accompany age found increased crystallinity (width of ν_1 phosphate band), increased type-B carbonate substitution (carbonate symmetric stretch {~1070 cm^{-1}} to ν_1 phosphate ratio) and increased mineral to collagen ratio (ν_1 phosphate to amide I band ratio) in bone material from the femora of aged rats.[122] It is now known from infrared absorption studies of age-related changes that crystallinity and crystal maturity are two different traits of the hydroxyapatite crystals (the former being related to a crystal's degree of order and its size, and the latter its thickness).[123]

Age-related changes of the organic phase of bone material have also been investigated using Raman spectroscopy, it has been found (using deep-ultraviolet Raman spectroscopy - excitation laser 244 nm) that the amide I band increases in intensity (relative to the other organic bands) with donor age. The spectral changes were also correlated with decreased fracture toughness, it has been hypothesized that the data reflected changes in collagen cross-linking.[124] The same deep-ultraviolet Raman technique has been used to study the increasing fragility of human teeth with age.[125] The results were similar to the bone studies, the amide I band increased in intensity (relative to the other organic bands) with donor age.

When trying to understand fragility fractures it is also necessary to consider the aging process of whole bones (rather than just the aging of smaller volumes of bone material); in one study, of cortical bone from the femora of healthy male donors (aged 17-73), investigators used Raman spectroscopy to look at (1) primary lamellar bone material (that can survive turnover for decades), (2) secondary osteons (product of remodelling) that represent relatively younger bone material, and (3) homogenized bone material (i.e. milled into small particles).[126] It was found that (1) the mineralisation of the primary lamellar bone material (amide I/phosphate ν_1) increased for the first three decades of life and then plateaued, (2) that the secondary osteons had an increased mineralisation (decreased amide I/phosphate ν_1, borderline statistical significance of $p = 0.07$), and (3) the mineralisation (amide I/phosphate ν_1) did not change with age. These interesting results indicate that Raman spectroscopy is useful for investigating *localised* mineralisation differences.

On average, older people do less exercise than younger people, thus it is important to investigate the effect exercise has on bone material if one is interested in fractures in the elderly. Recently, the effects of exercise on the size, composition, mechanical properties and damage resistance of bones from mice of various ages, background strains and genetic make-up were assessed.[127] Raman spectroscopy was used to show that exercise caused *compositional* changes in the tibial bone material; The mineralisation (ν_1 phosphate band to the proline/hydroxyproline band at ~855 cm^{-1}/~875 cm^{-1}) was significantly increased in exercised bones relative to controls. The carbonate/phosphate ratio (reduced) and the profile of the amide I band (hypothesized to be due to differing crosslinking) also showed significant differences. A recent study of the humeri and femora of rats that had been given spinal cord injuries showed that severe bone loss *and* compositional changes (longitudinally decreasing mineralisation as measured by the ratio of ν_1 phosphate/CH_2 wag) accompanied paralysis.[128] That study saw no change in the carbonate/phosphate ratio.

Influence of Mechanical Loading on Bone Material

Since it is fairly easy to manoeuvre a laser beam onto a sample, experiments can be performed in which the bone material is subjected to a force and probed at the same time, or subjected to the force and then probed at the point where the force was applied. These experiments, which were reviewed recently,[129] are interesting because certain Raman bands in a material can shift when a material is under stress (termed the 'piezo-spectroscopic effect').

An early example of this type of study was the recording of a Raman spectrum of a sample of pure calcium hydroxyapatite (and a sample of calcium fluoroapatite) through a diamond-anvil cell whilst it was under high external pressure. The phosphate ν_1 in the hydroxyapatite spectrum shifted frequency linearly (from ~962 cm^{-1} to ~967 cm^{-1}) when pressure was applied until ~2 GPa when a (reversible) jump (to ~970 cm^{-1}) was seen in the shift. The jump suggested a structural change in the crystal at this pressure and was not seen in fluoroapatite.[130]

The response of the chemical structure of bone to large mechanical stresses has also been studied with Raman spectroscopy. In one study,[131] pressure was seen to induce large shifts in the positions of collagen bands; the CH_2 bands shifted towards higher wavenumbers (CH_2 stretch shifted from ~2935 cm^{-1} to ~2970 cm^{-1} and the CH_2 wag shifted from ~1460 cm^{-1} to ~1490 cm^{-1}) whilst the amide I band shifted towards lower wavenumbers (from ~1655 cm^{-1} to ~1645 cm^{-1}). The CH_2 shifts were reversible but the amide I shifts were not. The phosphate and carbonate Raman bands broadened under pressure and they also shifted position, though the shift was smaller than those associated with the collagen phase (from ~960 cm^{-1} to ~977 cm^{-1} and from ~1070 cm^{-1} to ~1082 cm^{-1} for phosphate and carbonate respectively). All the mineral band shifts were reversible. It has been suggested irreversible shifts in the amide I band are associated with changes in protein secondary structures, e.g. cross-linking and helix pitch. The reversibility of the mineral Raman bands has been taken as evidence that it is very hard for water to move out of the crystal lattice.

Carden et al. permanently deformed bovine cortical bone specimens using a cylindrical indenter and measured the spectrum in and around the indent, the application of forces to bone material manifested itself in the Raman spectrum with spectra from the edge of the indents showing changed in the band profiles. The intensity of the low-frequency edge of the amide III band increased and so did the high-frequency part of the amide I band. It was stated that the spectral changes were indicative of rupturing of the collagen crosslinks.[132] The response of bone to elastic deformation in the physiological range has also been probed, the centre of gravity of phosphate bands have been seen to shift on tensional loading (from ~963 cm^{-1} to ~962 cm^{-1}) indicating that bone mineral may not be "a passive contributor

to tissue strength. The mineral active response to loading may function as a local energy storage and dissipation mechanism, thus helping to protect tissue from catastrophic damage."[133]

These findings were related to those from another study which looked at the influence of mechanical loading on the Raman spectrum using 'double-notch' specimens; pieces of bone with two identical U-shaped notches cut into them.[134] These specimens were subjected to four-point bending and they broke at the base of one of the notches leaving areas of undamaged (far from the notches), strained (unbroken notch) and failed bone (broken notch). Raman spectra were used to make stress maps (by measuring the shift of the phosphate ν_1 band at different points) in the undamaged, failed and strained areas. The undamaged regions all showed stress of less than 0.01 MPa.

For two of the three specimens the corners of the unbroken notches had stresses between 80 and 165 MPa, and broken notches had regions near the cracks with stresses of between 135 and 235 MPa. However, a third specimen had different stress patterns in both the unbroken and broken notches, with regions of higher than average stress occurring across the top of the notch, but the maximums being lower than before in both the strained and failed regions (26 MPa and 43 MPa respectively). The third specimen came from an older horse (6 yrs compared with 4 yrs and 2 yrs respectively) and had a lower breaking force (54.9 N as opposed to 63.8 N and 66.5 N). It was hypothesized that the third sample had a different failure mechanism and a poorer performance because the horse was passed the age of peak bone mineral content, this hypothesis was supported by the fact that its average mineral to collagen ratio (phosphate ν_1 to proline band) was 11.8 ± 1.6 compared with 13.9 ± 1.1 and 13.8 ± 1.1 for specimens one and two).

Effect of High Energy Radiation on Bone Material

Raman spectroscopy studies which look at the effect of ionizing radiation (x-rays and gamma rays) on bone material have shown that the organic phase suffers much more damage than the mineral phase. For example, one study[77] which irradiated sections of adult bovine femur showed that doses of gamma radiation greater than 100 kGy cause "great changes in the organic part of the bone" (measured as CH_2 band wavenumber shifts) whereas for even larger doses (of up to 1 MGy) no changes are observed in the mineral phase (no phosphate ν_1 wavenumber shifts). A different gamma irradiation study[135] also found changes in the Raman bands positions of mineral component of bone to be much smaller than those observed for the organic component. It was also reported that irradiation did not affect the CO_3^{2-}/PO_4^{3-} ratio or the crystallinity (phosphate ν_1 width). This study reported that doses higher than 100kGy affected the majority of bands assigned to organic component of bone (including the amide I band, which became narrower and shifted towards higher wavenumbers).

It was mentioned above (the end of Chapter One - pg 40) that the damage caused to the organic phase by ionizing radiation has a severe effect on the fracture properties of bone material. A recent study[78] which used Raman spectroscopy to investigate this phenomenon, evaluated the strength, ductility and fracture resistance (both work-of-fracture and resistance-curve fracture toughness) of human cortical femur bone following their exposure to x-ray synchrotron-source radiation (0.05 - 630 kGy). The mechanical properties of the material were severely altered (e.g. an irradiation of 210 kGy changed the bending stiffness, ultimate bending strength and work to fracture from 1.37 to 1.20 GPa, 166.9 to 65.4 MPa and 16.7 to 2.22 kJm^{-2} respectively). Deep UV (244 nm) Raman spectroscopy revealed large changes in the relative height of the amide I band compared to the CH_2 wag band, it was hypothesised that this was due to *increased* collagen cross-linking induced by the radiation damage. It was also noted that at the largest radiation dose (630 kGy), the spectral features were broadened to an extent such that individual peaks were hard to discern, it was hypothesised that this was due to the breaking of peptide bonds in the collagen backbone.

The biological effects of ionising radiation on bone material have also been studied using Raman spectroscopy, one such study[76] looked at osteoradionecrotic bone; a serious complication that results from the cells and vascular canals in an area of bone being destroyed and can arise in patients who have undergone radiation therapy for oral cancer. In the osteoradionecrotic bone, the organic phase had been damaged by the treatment radiation but the damage had not healed because the cells that would normally carry out the repairs have also been destroyed.

Raman Studies Looking at the Roles of Non-Collagenous Proteins in Bone

It was stated above (Chapter One – pg 24) that the Raman spectra of non-collagenous proteins are difficult to distinguish in bone material as they are present in relatively small amounts and have similar constituent chemical groups. However, (as it was also pointed out) studies have been reported which look at the *effect* that the loss of certain Non-Collagenous Proteins (NCPs) have on bone material, these studies normally use mutant mice who are missing a gene needed to express a certain NCP and comparing their bone with wild-type controls. One such study from 2006 looked at the NCP 'osteopontin' and the role it plays in the mineralisation process of the skull.[136] The mineral/collagen Raman band ratio was used to measure mineralisation and biochemical methods were used to measure osteopontin expression. It was found that osteopontin is present even at the earliest stages of mineral deposition. Another osteopontin study, looked at young (< 12 week old) knock-out mice and found that the hardness and elastic modulus of their bone material (as tested with nano-indentation techniques) were much lower and that the mineral content was lower (as measured with Raman) than the wild-type controls.[137]

A similar study has been reported using mice without the ability to express the NCP 'fibrillin 2'.[138] In this study nano-indentation was used to measure mechanical properties of the bone material and it was found that the femora of the mutant mice had lower hardness and lower elastic modulus than the wild-type controls but interestingly, the Raman analysis showed little difference between the mice (except for a decreased carbonate band in the endosteal region of the knock-out bones). Since the chemical constituents of bone were reported to be present in their correct proportions fibrillin 2 must play some other role in determining the mechanical properties of bone material (e.g. it may be needed to control the arrangement of collagen fibrils).

The combination of nano-indentation with Raman spectroscopy has also been used to analyse bone material from osteocalcin knock-out and wild-type controls. Osteocalcin is an NCP which is believed to play a role in bone formation and resorption. Type-B carbonate substitution decreased significantly in the absence of osteocalcin and it appeared that this affected the hardness more than the elasticity. It was suggested by the authors that osteocalcin plays a role in the growth of apatite crystals in bone by increasing the degree of carbonate substitutions.[139]

Raman Studies of Bone Microstructure

Raman spectroscopy has a theoretical spatial resolution of ~1 μm (with 700-1000 nm excitation wavelengths)[XI] and gives one the potential to preferentially probe collagen fibrils which are aligned in specific directions (using polarized light), these factors have proven to be very useful for investigating the microstructure of bone. Studies of woven bone and lamellar bone have revealed new information about the subtleties of mineral composition and collagen fibril arrangement. For woven bone for instance; Raman analysis of skulls from very young mice revealed that the earliest mineral detected was a carbonated hydroxyapatite and that some other phosphate environments were also present at lower levels,[140] and Raman analysis of induced rat fracture-calluses revealed that woven bone density increased by 80% from 7 to 14 days and that the density increase was accompanied by a 30% increase in the mineral to collagen ratio (as measured with ν_1 phosphate/2940 cm^{-1} ratio).[141]

The microstructure and spatial differences in local mineral and protein composition across individual osteons and in interstitial bone have been the subject of much inquiry.[142] Interesting findings include; the discovery of an amorphous-type calcium phosphate, which has been theorised as a precursor to hydroxyapatite, in older interstitial bone material, rather than in the recently remodelled bone near the osteon centre.[143] The observation of both phosphate (PO_4^{3-}) and mono-hydrogen phosphate (HPO_4^{2-}) species in newly formed trabecular bone.[144] And, the observation that phosphate to carbonate ratio increases towards the edge of the osteons (i.e. as the age of the bone material increases).[145] Raman

[XI] From the Abbe diffraction limit, described above (pg 50).

spectroscopy, in combination with acoustic microscopy and nano-indentation, has also been used by investigators interested in assessing the composition and mechanical properties of individual osteonal lamellae. They used the phosphate ν_1 and the amide I band to measure the spatial distributions of the mineral and collagen phase and combined this information with the acoustic microscopy images.[146] This study was one of the earlier attempts to use Raman spectroscopy to investigate the orientation of collagen fibril and mineral crystals at the level of lamellae; it did not produce evidence in support of the idea that osteons contain an alternating pattern of highly mineralised lamellae and less mineralised lamellae.[147]

Raman imaging which utilised the polarisation dependence of Raman scattering has been used to examine the distribution of mineral and collagen around osteons. Linearly polarised light will excite different molecular vibrations depending on the angle between the polarisation angle and the long axis of the collagen molecule (or the long axis of the crystal). Collagen molecules and mineral crystals are aligned with their long axes parallel, so the phosphate ν_1 band (a vibration parallel to mineral crystal long axis) and the amide I band (a C=O vibration perpendicular to the collagen fibril) are particularly sensitive to the orientation and the polarization angle of the incident light. Other bands such as amide III (with components parallel and perpendicular to the collagen axis), phosphate ν_2 and phosphate ν_4 are less susceptible to the orientation effects.[148,149] Studies which probed perpendicular faces of 3-D sections cut from human femora and turkey leg tendon have confirmed that phosphate ν_1 to amide I ratio is best for looking at the orientation of the lamellae whilst phosphate ν_2 to amide III, and, phosphate ν_2 to carbonate are best for bone material composition.[150,] These composition versus orientation methods were also used to look at anatomically identical regions of femur in mice of different ages; the results indicated that there is an evolution of both orientation and chemical composition as a function of tissue age within the same specimen. The ratios of carbonate to phosphate signal increased as the age of the mouse increased.[151] These results illustrate that both information about composition (e.g. mineral to collagen ratio) and information about the organisation of the constituents (e.g. fibril orientation information) can be gleaned from single Raman spectra.

Recently, polarisation studies of mineral and protein orientation across individual osteons have continued to provide evidence for the 'twisted plywood' model of osteon micro-organisation[152] and have looked at the profile changes in the amide III band effects caused by sample orientation.[153] Polarisation dependant Raman scattering has also been used to measure the alignment of the collagen fibrils with the bone diaphysis and of the hydroxyapatite crystals with the long bone diaphysis for both mutant mouse bone specimens (specifically oim/oim, osteogenesis imperfecta model mice), and wild type controls.[154] This was accomplished by comparing the intensity of the amide I band (vibrates perpendicular the long axis of collagen chains) with the intensity the phosphate ν_1 band (vibrates

along the long axis of hydroxyapatite crystals) for parallel polarised light and perpendicular polarised light. Using the spectral information it was calculated that the hydroxyapatite crystals are not as well aligned in oim/oim bones (28±3°) compared to wild-type bones (22±3°). This result was statistically significant and was in agreement with earlier small-angle x-ray scattering results.

Raman Spectroscopy to Probe Bone through Skin and Soft Tissue

The Raman studies surveyed so far have all been concerned with excised bone material that had laser light shone directly onto its surface. In 2005, an interesting set of experiments were reported in which investigators implanted titanium bone chambers equipped with a fused-silica optical window in the skulls of rabbits.[155] The Raman spectra from both the mineral (e.g. the phosphate ν_1 and carbonate bands) and organic (e.g. the amide I and amide III bands) phases of bone material were retrieved. The behaviour of synthetic calcium phosphate biomaterials were also observed *in vivo* over a period of 8 months (they remained in situ after that period). Although the implanted windows were well tolerated, the expansion of this technique is not feasible (especially for human subjects).

More recently techniques have been developed which allow deep, non-invasive Raman spectroscopy of bone through skin and overlying tissue, these techniques have allowed new experiments to be designed and may even be developed as diagnostic instruments. The new techniques have been recently reviewed, the finding of those reviews are outlined below.[156,157]

Kerr Gate

The excitation of a molecule from its ground state into an excited *electronic* level was discussed in the previous chapter (Figure 1.8). If a molecule that is in an excited *electronic* state relaxes back down to the *electronic* ground state and releases the energy as a photon, the process is called fluorescence; it is illustrated in Figure 2.4. If the energy gap between the electronic states is similar to the energy of the incident photons then the absorption of the photon is very probable (due to the fact that the upper electronic states are real, in contrast to the excited states in scattering which are virtual[XII]). In skin, muscle and other soft tissues there are more large biological molecules (with smaller electronic energy gaps) than there are in bone, these tissues fluoresce strongly.[XIII] The fluorescent photons, along with surface Raman signal, often saturate the detection equipment and drown out the Raman signal making transcutaneous analysis very difficult.

[XII] If the excited state in a Raman scattering process coincides with a real electronic state an enhanced Raman effect called Resonance Raman can occur.

[XIII] Examples are haemoglobin and melanin, it is probable that there are many others.

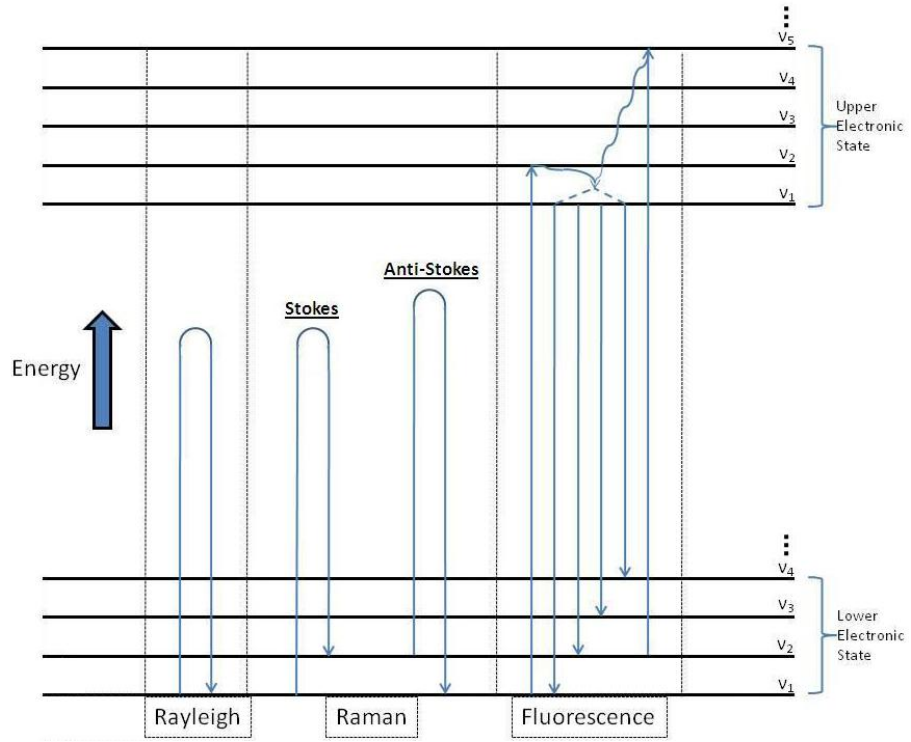

Figure 2.4 The energy level diagrams of Rayleigh and Raman scattering which were described above (pg 42) are plotted here with a diagram of fluorescent emission. Fluorescence occurs when the relaxation of a molecule to one of its lower electronic states is accompanied by the emission of a photon.

The emitted fluorescence photons themselves can be collected and used as a spectroscopic signal, however, unlike the case with Raman, a fluorescence spectrum will have wide overlapping bands and thus they have much lower chemical specificity. The property which accounts for the differing chemical specificity between Raman and fluorescence is the timescale associated which each process. As was stated above (Scattering – pg 41), the lifetime of the excited (virtual) in a scattering event is very short (~10^{-15} s), however, the excited state in the fluorescence process is a real vibronic state and thus its lifetime is much longer (in the order of nanoseconds, ~10^{-9} s). The Raman scattering event occurs so quickly that the photons capture 'snapshots' of the target molecule whereas the longer timescales associated with the fluorescence process allow time for the excited electronic state to change energy due to thermal collisions with surrounding molecules, i.e. to move vertically up and down in energy level diagram. Thus, since the gap between the excited and ground state varies during fluorescence the energy of the emitted photons varies; the emitted photons have a range of wavelengths and the spectrum has broad overlapping bands.

The temporal difference between the Raman and fluorescence processes has been exploited using Kerr-gate technology to produce fluorescence free Raman spectra.[158] The first set of experiments used

ultraviolet lasers (400 nm) which, as was discussed in the theoretical section, have a higher scattering efficiency than the near infrared lasers (785 nm and 830 nm) conventionally used; the use of these shorter wavelength lasers is often limited due to fluorescence. The experimental set-up is shown in Figure 2.5. The Raman signal and the florescence signal (which is spread over much longer time), pass through a polariser and a Kerr-gate before encountering a second crossed polariser.[XIV] In the normal case, the Kerr-gate allows the signal through without interference and none of it passes through the second polariser further along the optical path. However, if intense laser light is incident on the Kerr medium as the Raman signal passes through it, then the Raman signal can be induced to change polarisation and some of it will make its way through the second polariser. The system can be optimised by using appropriately timed short pulsed lasers (e.g. 1 ps).

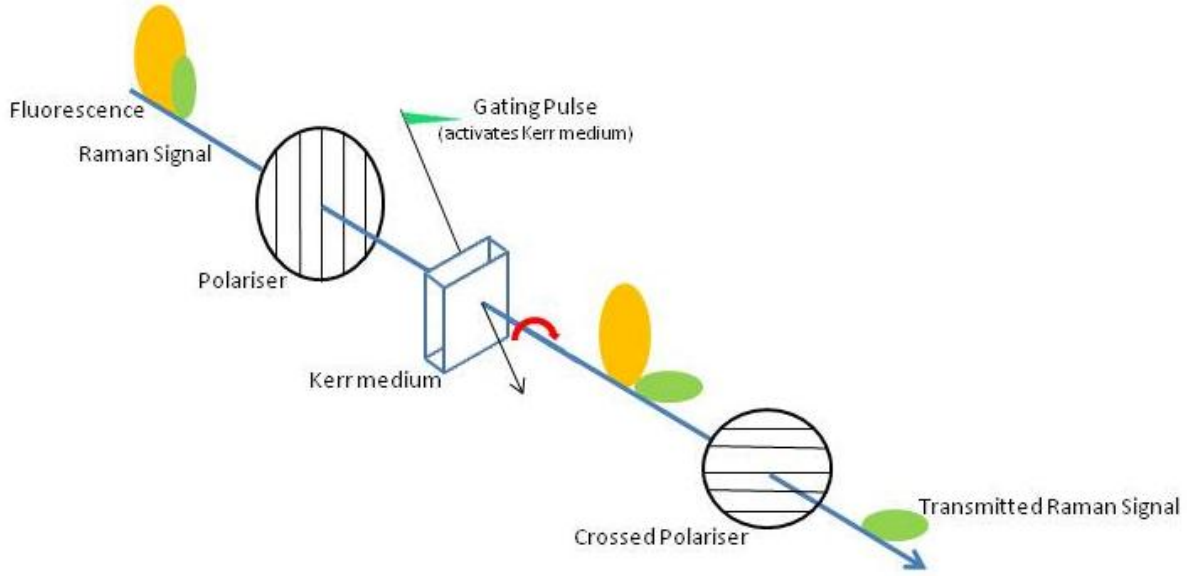

Figure 2.5 Schematic diagram of the experimental set-up used to remove the 'lagging' fluorescence signal. Adapted from Ref. 158.

The Kerr-gate technology was first used to retrieve fluorescence background-suppressed Raman spectra from excised bone material using 400 nm laser.[159,160] It was then developed to enable the retrieval of Raman spectra of bone through ~1 mm of skin and tissue, and the discrimination between healthy and pathological bone material.[161,162] The development involved removing the Raman signal of the outer skin and tissue, as well as the trailing fluorescence (Figure 2.6).[163] This process relied on different gating pulses being incident on the Kerr medium; it could be accomplished because as photons propagate through a turbid (scattering) media, they take random paths and diffuse away from

[XIV] A Kerr gate is a substance whose optical properties (nonlinear refractive index, n_2) vary depending on the electromagnetic radiation incident on it. The induced changes decay naturally with a lifetime of 2-3 ps.

the point they entered the sample. Thus, it takes a photon longer to travel deep into the sample (into the bone material in this case) and back out (and on towards the Kerr-gate) than to scatter from near the surface.

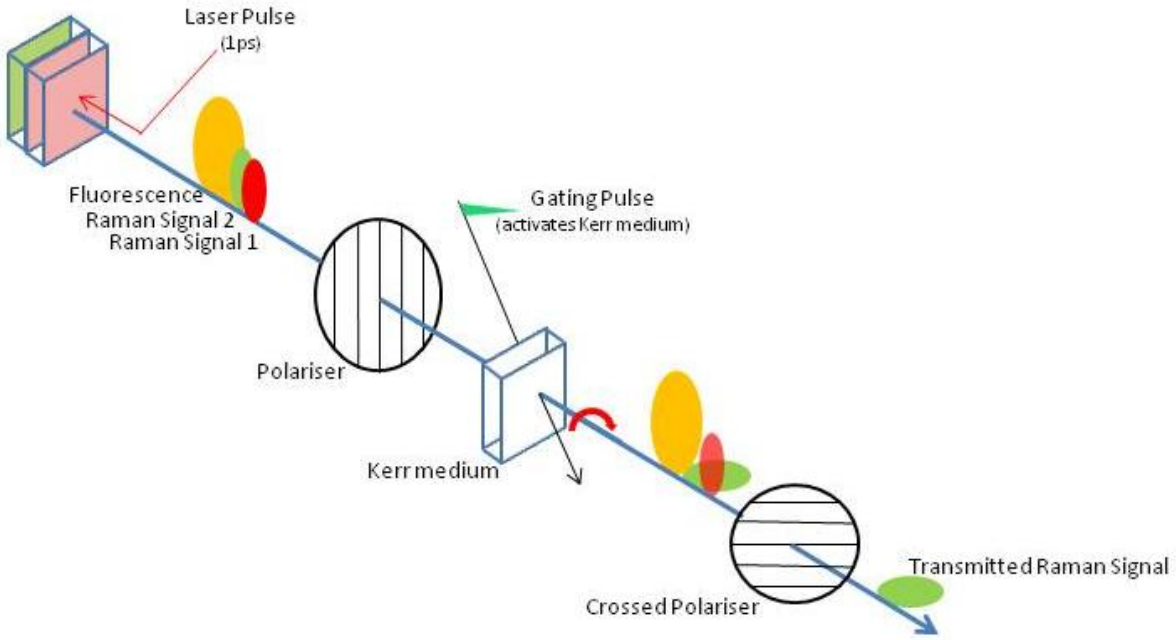

Figure 2.6 Experimental set-up for deep Raman spectroscopy (Gating pulse was 800 nm, 500 μJ, 1 ps & Kerr gate was a 2 mm cell of CS_2). The experiment works because the photons take time to diffuse from sample 2 (green sample) back out to the surface. Adapted from Ref. 156.

The discrimination between normal and defective bone material through skin and tissue using Raman spectroscopy was a major advance, but the inherent instrument complexity limited its applicability. Building on this work, Matousek and co-workers developed Spatially Offset Raman Spectroscopy which also utilises the diffuse scattering properties of photons in turbid media but because it is much simpler conceptually and technologically has the potential to be used more widely.[164]

Spatially Offset Raman Spectroscopy

Spatially Offset Raman Spectroscopy (SORS) relies on the fact that in certain media photons scatter in random directions, laser photons that enter through the surface will increasingly diffuse in lateral directions the further they travel through the medium. This means that photons returning from deep in the turbid medium will be more likely to emerge far from their entry point than photons which made only a short journey to the surface from more shallow regions. SORS of a two layer system is illustrated in Figure 2.7, unlike conventional backscattering geometry the illumination point where the laser is focused on the sample is offset some distance Δs from the collection point. The diagram shows the laser photons (blue arrows pointing down) diffusing laterally on the way down (blue lines)

and it shows the signal photons travelling back up (thinner blue arrows). The result of this is the light collected at some distance (s > 0) will contain some photons from the bottom-layer and some photons from the top layer, the photons collected s = 0 will be mostly from the top layer (with some small component from the bottom layer). A scaled subtraction of the s = 0 measurement form the s > 0 measurement will result in the Raman spectrum from the bottom layer (no *a priori* information from the top or bottom layer is required).

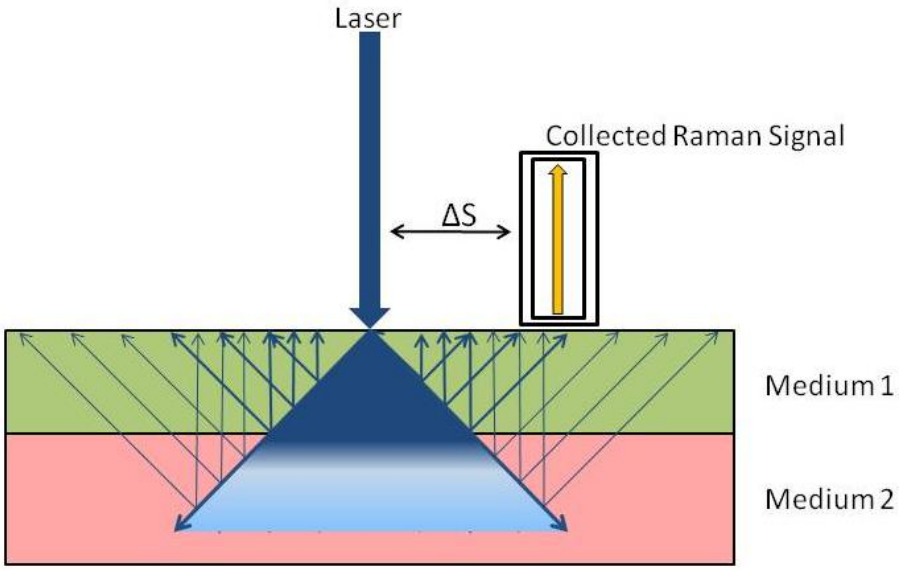

Figure 2.7 Conceptual diagram of SORS. Suppose that the injected laser light diffuses the same way in medium 1 (green) and medium 2 (red). The photons collected at larger offsets (Δs – large) will have spent a larger proportion of their time in medium two (red) than those collected at smaller offsets (Δs = 0), and hence will be more likely to have Raman-scattered from it. Adapted from Ref. 163.

Shortly after the development of SORS, it was demonstrated that Raman spectra of bone material could be retrieved through skin and other overlying tissues using animal specimens and living human subjects (depths of up to 4 mm).[165,166,167] Since then experiments looking at murine bone *in vivo* have been reported,[168] as have experimental refinements for the optics, the data analysis and the preparatory protocols.[169,170,171,172] These preparatory protocols include the application of glycerol as an optical clearing agent to reduce turbidity (i.e. reduce optical scattering) in the skin.[173]

Transcutaneous Raman spectroscopy of bone material has also been combined with x-ray computed tomography[174] and been used to develop Raman tomographic imaging.[175] This imaging technique gives spatial and chemical information, studies of tissue phantoms and animal bones have been reported.[176]

2.3 Conclusions from Chapter Two

In this chapter the theory of Raman spectroscopy and its advantages and disadvantages were introduced. The general principles which underlie a Raman instrument and the appearance of Raman spectra were explained. Novel Raman techniques (Kerr-gate and SORS) which are being developed to enable the safe, non-invasive retrieval of Raman spectra of bone material through skin and other overlying tissues *in vivo* were also described; these techniques may become important for diagnosing bone diseases or measuring mechanical properties. The longest section of the chapter detailed previous studies which utilised Raman spectroscopy as a tool for analysing bone material. Many of those studies are relevant to the central question of this thesis: Are the mechanical properties of bone material adapted in differently loaded regions by a subtle tuning of the collagen chemistry which controls the mineral to collagen ratio?

It was discussed how exercise, as well as well as altering the size and mechanical properties of bone material, alters its mineral to collagen Raman ratio (ν_1 phosphate/proline + hydroxyproline, ~855 cm^{-1} + ~875 cm^{-1})[127] and how paralysis (caused by spinal cord injury) affected the mineralisation longitudinally (the ratio of ν_1 phosphate/CH_2 wag decreased).[128] It was also discussed how age altered both the mechanical properties, and mineral/collagen ratio of rat bone (increased ν_1 phosphate/amide I band ratio)[122] and horse bone.[134] In the case of the horse bone, a study of three 'double-notch' specimens was reported in which the sample form the oldest horse had a lower average mineral to collagen ratio (phosphate ν_1 to proline band), lower breaking force, lower maximum stresses and different stress patterns after failure. The relationship between the Raman bands and bone material adaptation is explored further in Chapter Four.

In another of the studies that was discussed, the investigators attempted to understand the aging process of whole human femora (rather than aging of smaller volumes of bone material); it was found that the mineralisation (ν_1 phosphate/amide I) of the primary lamellar bone material (old material that survives turnover) increased for the first three decades of life and then plateaued, and it was found that that the average mineralisation of homogenized bone material (i.e. milled into small particles) did not change with age.[126] Chapter Five of this thesis also looks at the mineralisation of the bone material at different points in long bone cortices but the investigation is concerned with mechanical property adaptation at regions which experience different mechanical loads.

Other important findings outlined concerned the effect non-collagenous (or their absence) had on bone material and the interaction of collagen with the mineral crystals. In studies of osteopontin, the Raman mineral/collagen ratio was used to measure mineralisation. Results from those studies included the confirmation that osteopontin is present even at the earliest stages of mineral deposition

and that young (< 12 week old) osteopontin knock-out mice had less stiff bone and lower mineral content than the wild-type controls. [136,177] Raman spectroscopy was used in a study of fibrillin 2, where again it was shown that knock-out mice had less stiff bone, however, the Raman analysis showed little difference between knock-outs and wild types.[138] A Raman study of osteocalcin showed carbonate substitution decreased significantly in the absence of osteocalcin.[139] A combination of analytical techniques (including Raman) were used to show that the transformation of amorphous calcium phosphate into crystalline hydroxyapatite was controlled by an NCP called DMP1.[114]

Among the studies of collagen itself were the deep-ultraviolet Raman studies of age-related changes in bone and teeth.[124,125] They showed that the amide I band increased in intensity (relative to the other organic bands) with donor age and that this ratio changes was accompanied by decreasing mechanical properties. The results were hypothesized to reflect changes in collagen cross-linking. The study[127] (already mentioned in this summary) found that exercise, as well as well as altering the size and mechanical properties of bone material and its mineral to collagen Raman ratio, also alters the profile of the amide I band (again, it was hypothesized to be due to differing crosslinking). In Chapter Six, the amide I band will be looked at in more detail and it will be investigated if it can shed light on the tuning of the mineral to collagen ratio in bone, and thus on the tuning of mechanical properties.

Before the chapter investigating the adaptation of mechanical properties, regional mineralisation differences and collagen chemistry are presented, the Raman instrument used to record the data for will be described. The next chapter will give a detailed description of the instrument and of some experimental methodologies. A newly developed technique which can be used to enhance Raman signal from turbid media will also be presented.

3. Description of Apparatus, Methods and Technical Developments

3.1 Raman Instrument

Figure 3.1 shows the instrument used to record the spectra presented in this thesis. The light source, shown in the blue 'window' is a laser diode (i.e. a laser with a semiconductor lasing medium) made by Process Instruments (model PI-ECL-830-300-FS), which operates in continuous wave mode (as opposed to pulsed laser mode) and emits light at 830 nm (in the near infrared region of the electromagnetic spectrum). Its maximum output power is 300 mW but the amount of light reaching the sample varies depending on the optical path and the alignment of the set-up.

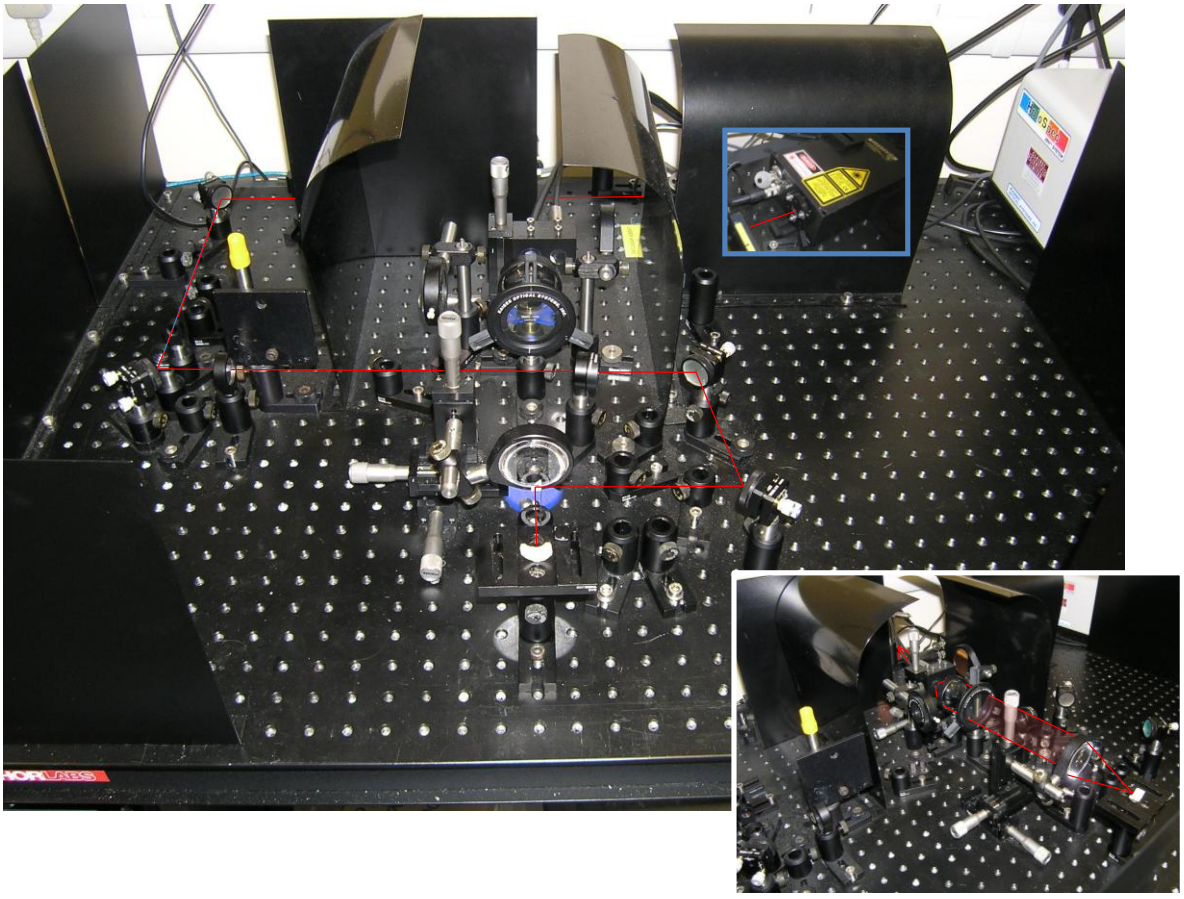

Figure 3.1 The fibre leads to the spectrograph which can be seen in the top right hand corner of the picture (grey box). The laser is behind the black shielding and can be seen the blue 'window'.

The path of the laser beam is illustrated with a red line; it is directed through two dielectric bandpass filters which 'clean' the laser line (i.e. remove wavelengths other than 830 nm) and is directed on towards the sample using mirrors (broadband dielectric mirrors) and a lens (Plano-Convex Lens, f = 250.0 mm). A fraction of the light that is scattered from the sample is collected by a lens (50 mm

diameter and a focal length of 60 mm) and collimated before reaching the holographic notch filter. [xv] The dielectric notch filter (50.8 mm diameter, manufactured by Kaiser Optical Systems) is the wavelength discriminating device which removes the Rayleigh scattered light. The dielectric notch filter comprises a substrate with a sinusoidal refractive-index variation etched through it. This refractive-index pattern (usually etched with laser beams) is designed so that for the selected wavelength (e.g. 830 nm) the light waves which reflect from the different layers are in phase and interfere with each other constructively. The remaining scattered light, the Raman signal, is now imaged by a second lens (identical to the first - 50 mm diameter and a focal length of 60 mm) onto the front face of the fibre collection probe.

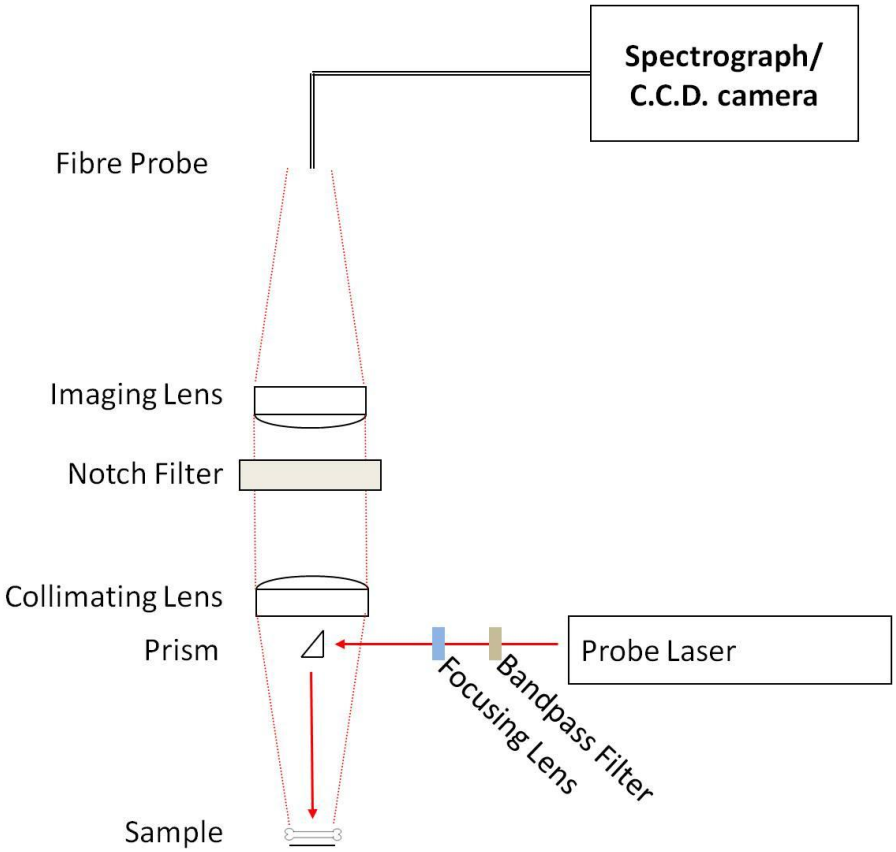

Figure 3.2 Schematic diagram of the experimental apparatus shown in Figure 3.1.

This fibre probe consists of twenty-two active optical fibres arranged in a disk, each with numerical aperture of 0.37 (acceptance angle ~35°). Each fibre is made of silica with a core diameter of 220 μm, a doped silica cladding diameter of 240 μm, and a polyimide coating diameter of 265 μm

[xv] The laser and Raman photons scatter from the sample in all directions (though there is a bias towards propagation near the normal). The percentage of scattered photons collected by the collimating lens thus depends on its radius and its focal length.

(manufactured by CeramOptec Industries, Inc). The fiber bundle length is ~2 m and at its output end the fibres are arranged in a line. This line is orientated vertically and placed in the input image plane of the spectrograph. The spectrograph (a Holospec 1.8i NIR manufactured by Kaiser Optical Technologies) contains a series of lenses (Figure 3.3); the first of which collimates the light before it is passed through another internal (Kaiser Optical Systems) notch filter, it is then focused though a slit and collimated again before passing through a diffraction grating which spatially separates the Raman photons of different wavelengths before they are imaged onto the CCD camera detector (manufactured by Andor Technology, model DU420A-BR-DD) by a final lens.

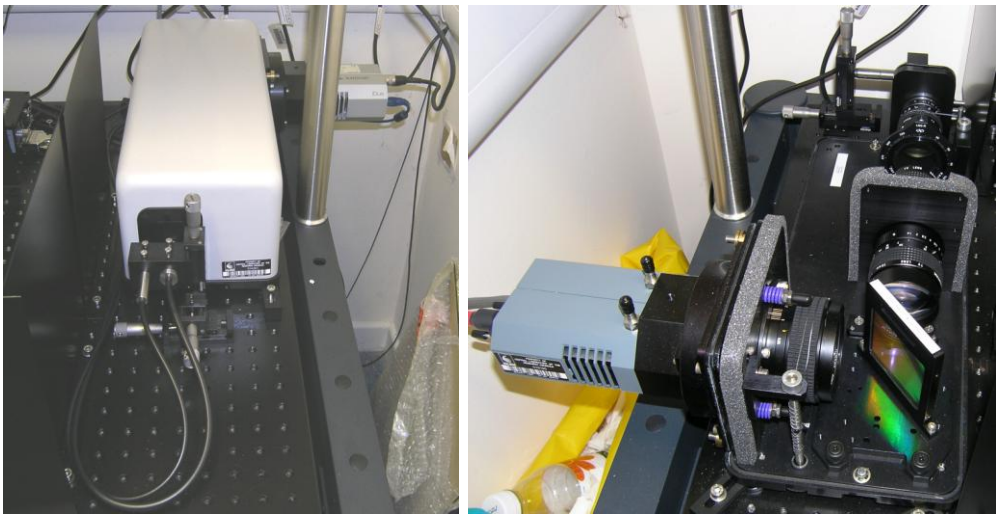

Figure 3.3 The image on the left shows the fibre carrying the Raman signal into the spectrograph. The image on the right shows the spectrograph with its lid removed (described in text).

As discussed in the theory sections above (pg 47), a CCD camera contains a semiconductor chip (in this case it is made from silicon) divided in many pixels (1024 wide × 256 high), each of which builds up an electrical charge when struck by photons. This charge is then read off and recorded on a computer. The chip is thermoelectrically cooled to 193 K to reduce the thermal noise. The variation in the apparatus' sensitivity across the spectral range (i.e. the filter blocking out light at low wavenumbers and or the CCD sensitivity decaying towards the tail of the silicon sensitivity) is not corrected for.

3.2 Methodology

Validation of Apparatus

Before the Raman instrument could be considered appropriate for assessment of bone material, a number of validation experiments had to be performed.

X-Axis Calibration (Accuracy)

The x-axis of a Raman spectrum, which measures the magnitude of the wavelength shift, should be comparable between any two instruments. The Raman bands of some chemicals are very accurately known and can be used as a standard with which to calibrate an instrument. The standard used in our laboratory is *trans*-stilbene ($C_{14}H_{12}$) which is a very strong Raman scatterer.

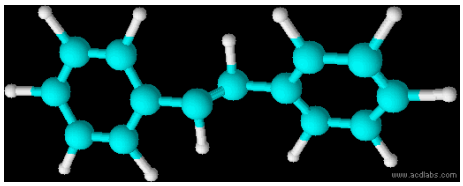

Figure 3.4 Molecular structure of *trans*-stilbene, the chemical used to calibrate the x-axis.

The spectrum of *trans*-stilbene used to calibrate the system is shown in Figure 3.5, the spectrum took 30 seconds to accumulate (30 x 1 s exposures) and the detector settings were such that the chip (with its 1024 columns and 256 rows) was read as one string of 1024 values (i.e. the 256 rows were summed to give one set of x-values). A well defined spectrum of *trans*-stilbene was obtained from a Raman atlas of organic compounds.[178] The frequencies of the four dominant bands used to calibrate the detector are shown in Figure 3.5, the final calibrated spectrum is shown in Figure 3.6.

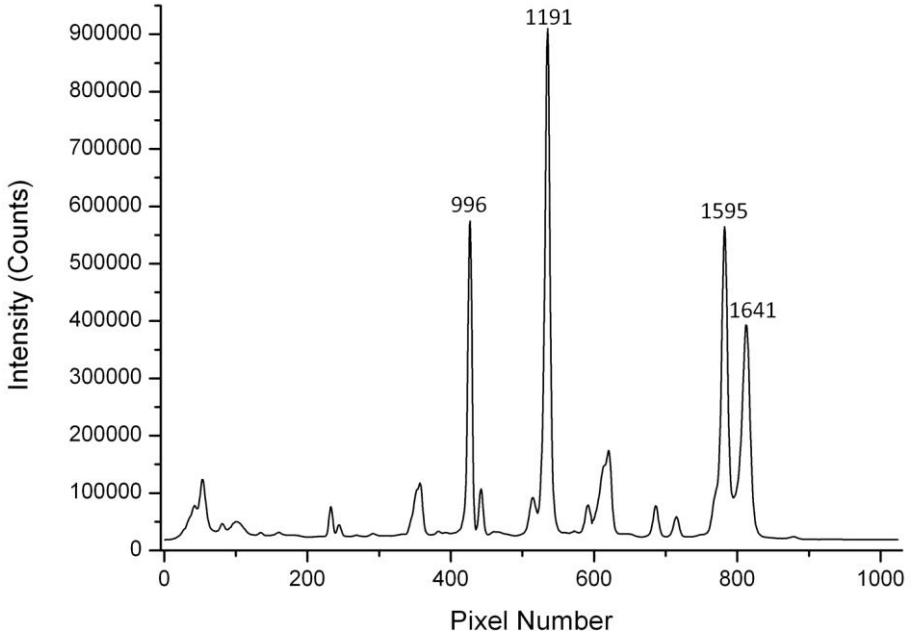

Figure 3.5 Spectrum of *trans*-stilbene used to calibrate the x-axis.

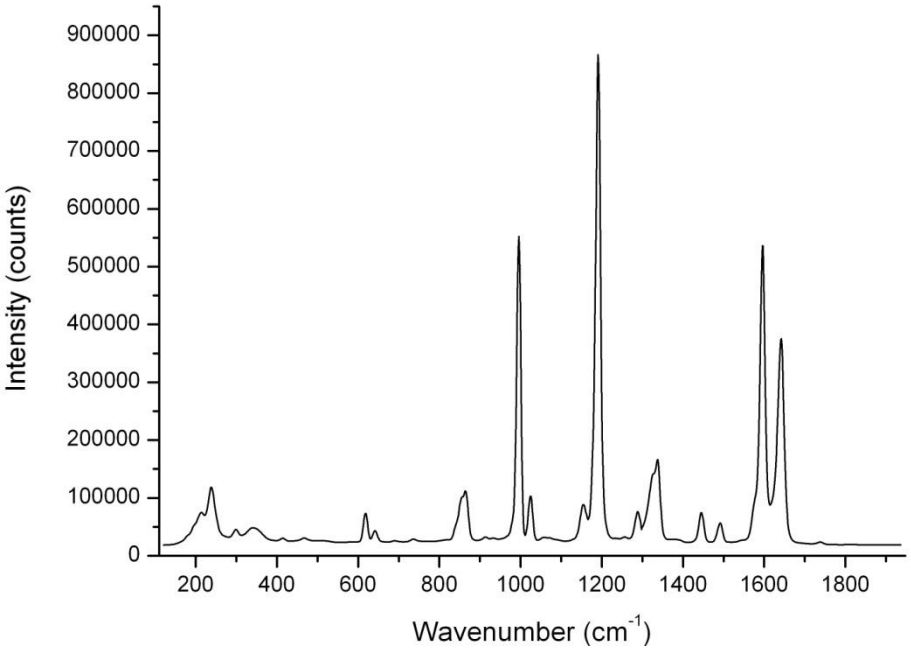

Figure 3.6 Calibrated spectrum of *trans*-stilbene.

Y-Axis - Intensity (Precision)

The y-axis of a Raman spectrum is the intensity of the Raman signal, the number of counts registered on the CCD chip in this case. Since a large number of variables (laser power at the sample, alignment of the optics, detector sensitivity, etc) affect the measurement, it is rarely possible to compare accurately the absolute intensities between different instruments. Instead, the method employed is the

comparison of different peaks within each spectrum (the area under a band, the band height, position, shape, etc). This 'self-calibration' removes the problem of instrument variation but at the same time limits the technique's applicability. Thus, it was essential to ensure that the intensities recorded across the spectral range did not vary between measurements before scientific investigations could begin.

Repeatability

In order to confirm that the instrumentation gave the same response to the same experimental conditions, repeated spectra of a sample were recorded. A piece of bone from the midshaft of on ovine femur was placed on the sample stage and a spectrum was recorded for one minute (60 x 1 s accumulation), without changing anything another spectrum was recorded. Ten spectra were recorded in this way. The fluorescence background was subtracted from each spectrum (using the routine that will be described below – pg 77) and they were plotted together (Figure 3.7). It can be seen that variation is very small (compared to the size of the signal) between each measurement and that the amide I band (shown inset) does not change shape. The average phosphate/amide I, carbonate/amide I and carbonate/phosphate ratios are given in Table 3-1, the standard deviation for each ratio is of the order of 1%.

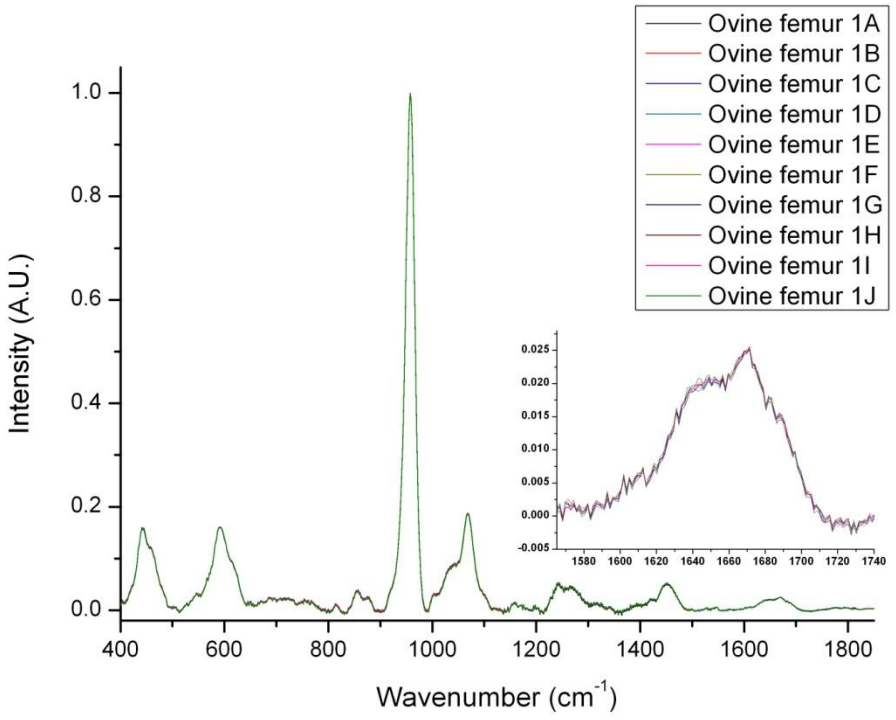

Figure 3.7 Ten spectra recorded one after another on the same piece of bone, the amide I band can be seen on a different scale (inset).

	(Repeatability) Ovine Femur
Phosphate/Amide I	*16.9 (±0.2)*
Carbonate/Amide I	*8.6 (±0.1)*
Carbonate/Phosphate	*0.507 (±0.002)*

Table 3-1 The same measurement was repeated ten times, i.e. 'record spectrum' was pressed ten times. The average ratio (and standard deviation) for the ν_1 phosphate band, carbonate sym-stretch and amide I band are shown

Reproducibility

The related issue of reproducibility was also investigated. A piece of ovine femur was placed on the sample stage and a spectrum was recorded for one minute (60 x 1 s accumulation). The sample was then removed, it was then placed back on the stage so that the laser illuminated roughly the same area and another spectrum was recorded. Since it was impossible to probe to exact same piece of bone material (i.e. to have photons scatter from the same molecules), the variation between these plots was larger than in repeatability measurements. However, the spectra were again very similar and the amide I band did not change shape (shown in Figure 3.8). To quantify the difference between Figure 3.7 and Figure 3.8, the deviation between the ten spectra was calculated for each data set. The 'amount of scatter' (the mean standard deviation of each pixel) across the spectrum was 172% of that for the repeatability measurements above (11.7×10^{-4} as opposed to 6.8×10^{-4}). The band ratios are given in Table 3-2, the standard deviations are a larger percentage of the averages.

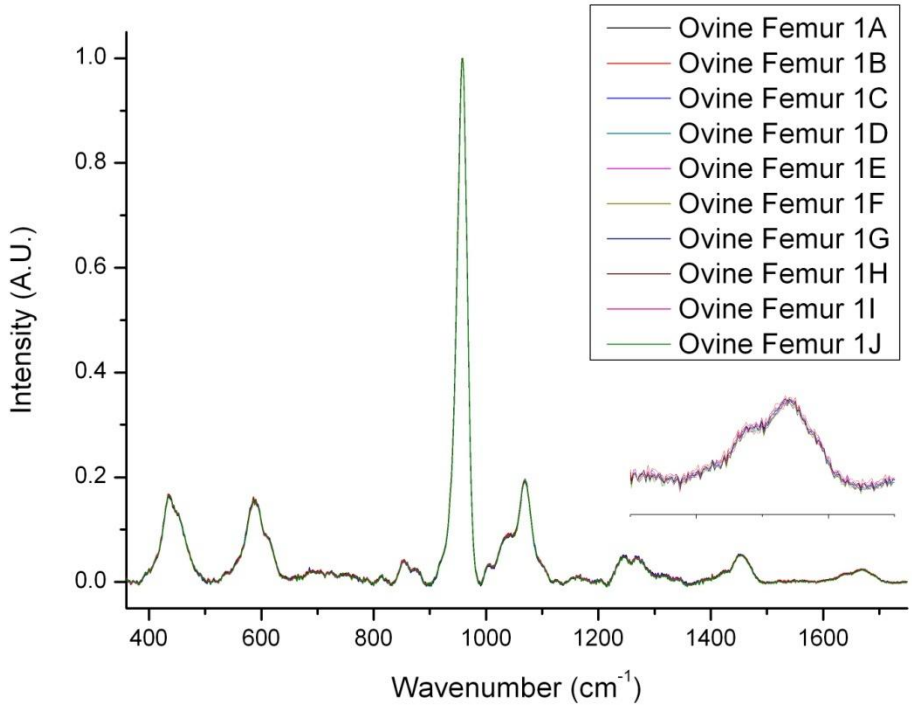

Figure 3.8 The bone sample was removed and replaced before ever spectrum was recorded.

	(Reproducibility) Ovine Femur
Phosphate/Amide I	*17.0 (±0.4)*
Carbonate/Amide I	*9.0 (±0.2)*
Carbonate/Phosphate	*0.533 (±0.003)*

Table 3-2 A sample of bone was placed in the instrument and removed after the spectrum was recorded, this was repeated ten times. The average band ratio (and standard deviations) for the ν_1 phosphate band, carbonate sym-stretch and amide I band are shown.

Background Subtraction

It was described above (Kerr Gate section – pg 62) how fluorescence can drown out weak Raman signals by flooding the detection equipment and it was stated that this is often an especially severe problem for biological samples (where the fluorescence can be several orders of magnitude more intense than the weak Raman signal). There are hardware solutions for this problem other than Kerr-gating; Fourier Transform Raman spectroscopy (which uses interferometry to separate light of different wavelengths)[179] and longer wavelength or tunable lasers (which reduce the probability of exciting the molecule into an upper electronic state)[124,125,180] have also been used by Raman investigators of bone. Methodological procedures such as photobleaching (allowing the laser to be incident on sample for a long time in order to 'bleach' out fluorescing species)[181,182] and treating the bone with chemicals[183,184] have also been reported, but since these methods may chemically modify the sample they are not ideal.

Another partial solution is to treat the data after they have been obtained to minimise the effect of the fluorescence. The spectra can be differentiated to show the positions of the (often) sharper Raman bands or a curve can be fitted to the broad fluorescence band variation and it can be subtracted from the original data. It is the latter method which was used for this thesis (see Figure 3.10). The automated "modified polyfit method", which was designed by Lieber and Mahadevan-Jansen for application to biological samples fits high-order polynomial curves to the spectrum and subtracts them away.[185] The automated process proceeds by smoothing of the spectrum in such a way that Raman peaks are automatically eliminated, leaving only the base-line fluorescence intact; this is then subtracted from the raw spectrum. It is based on a least-squares polynomial curve-fitting function. The function is modified so that all data points in the generated curve that are above the spectrum are automatically reassigned to the original intensity. This process is repeated a number of times (in our case there's a large upper limit of 10,000), gradually eliminating the higher-frequency Raman peaks (the program stops when number of reassigned pixels goes to zero). The program used was written in-house by Dr. Neil MacLeod in the Matlab programming language (The MathWorks Inc., MA) and run on a desktop computer; a screenshot from it is shown in Figure 3.9.

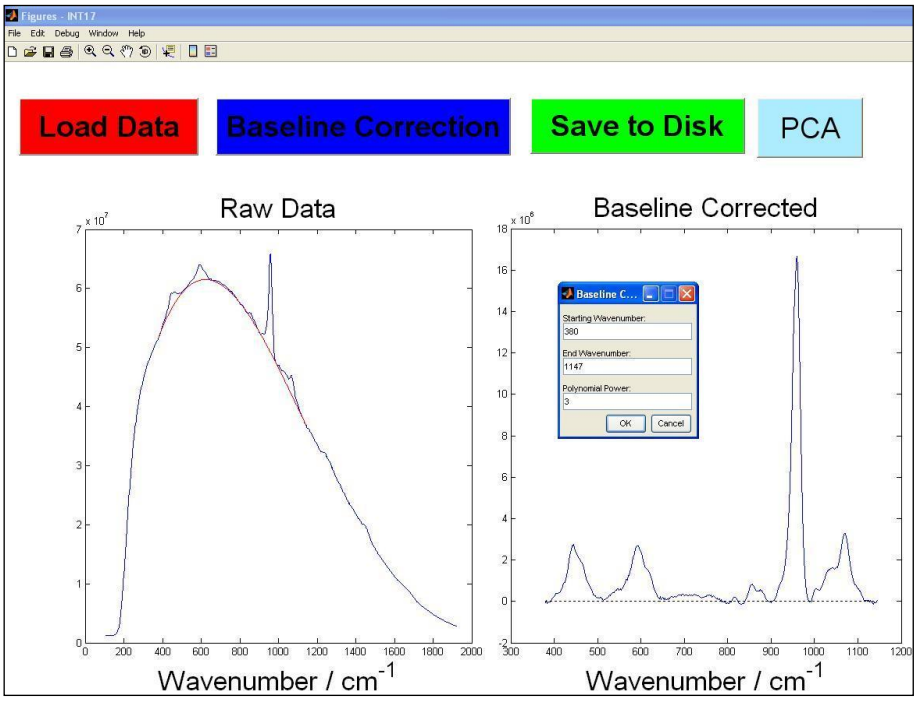

Figure 3.9 Screenshot of the Matlab program used to subtract fluorescent backgrounds.

The spectrum is loaded and the section to be corrected and order of polynomial to be fitted are chosen so as to most smoothly remove the fluorescence. Figure 3.10 shows the ovine femur spectrum with the background subtracted, it was corrected in three sections; the first from 380-1147 cm^{-1} had a 3rd order polynomial fitted (shown in Figure 3.9), the second from 1147-1515 cm^{-1} had another 3rd order curve fitted and the last section from 1515-1925 cm^{-1} had a 2nd order curve fitted. The breaking of the spectrum into pieces gave the cleanest background subtraction.

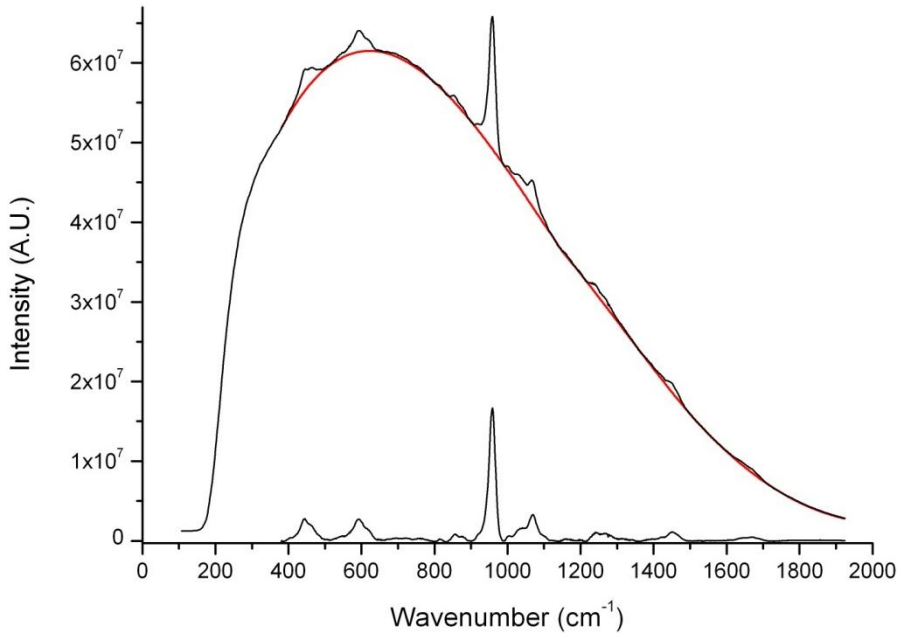

Figure 3.10 The black line with intensity of up to ~6.5 x 10^7 is the raw data (obtained from ovine femur bone). It contains the fluorescence and Raman spectra. A polynomial was fitted to it (red line) and subtracted to give the final spectrum (at the bottom). This final spectrum has already been shown in Figure 2.2 and Figure 2.3(b).

There is another problem related to fluorescence and inherent to Raman spectroscopy that should be mentioned here. Typically, the longer a Raman spectrum is accumulated for, the more photons collected, and the better the signal to noise ratio will be (assuming the laser power and laser wavelength are such that they will not damage the sample).[XVI] However, the signal to noise ratio of the Raman spectrum will be affected by the shot noise (or Poisson noise - the statistical fluctuations due to the quantised nature of light) of the (often much larger) fluorescence background signal. This shot noise (which is proportional to the square root of the number of photons collected) often determines the quality of a Raman spectrum.

[XVI] This also assumes the detector is not saturated, e.g. in the repeatability experiment above the CCD chip was read off 30 times, each after an accumulation of 1 s (i.e. 30 x 1 s) but 1 accumulation of 30 s (i.e. 1 x 30 s) would have meant that some of the pixels would hit their maximum capacity and stopped recording (saturation - Figure 2.3, pg 53).

Other Validation Experiments

The specific details of the various bone samples used in the experiments will be described in the appropriate sections but two aspects of the methodology which are relevant to Chapters Four, Five and Six, are addressed here; the variation between individuals and the affect the state of hydration of the bone material has on its Raman spectrum.

Measurement of Spectral Variation between Individuals

The Raman spectra (60 x 1 s accumulation) of mid-shaft tibiotarsus bone material (periosteal surface) from ten chickens are shown in Figure 3.11; the chickens were from the same batch on a single farm and were slaughtered at the same time. It can be seen that there are no large variations in the band intensities or band profiles between the animals. The average band ratios are given in Table 3-3, the largest standard deviation (for the ν_1 phosphate/amide I) is ~5% and this includes the difference introduced during the fluorescence background removal. This indicates that the chemical compositions of the different tibiotarsi and mineral volume fractions are very similar (since the intensity ratios of phosphate bands to collagen bands are linearly related to gravimetrically determined (ashing) mineral volume fraction[120,186]). It is not surprising that genetically similar chickens which were born on the same farm in the same year have very similar bone material; indeed it is known from the literature that the mechanical properties of bone material from the limb bones of adult mammals and birds do not vary a great deal (this is discussed further in Chapter Five).[7,38,224]

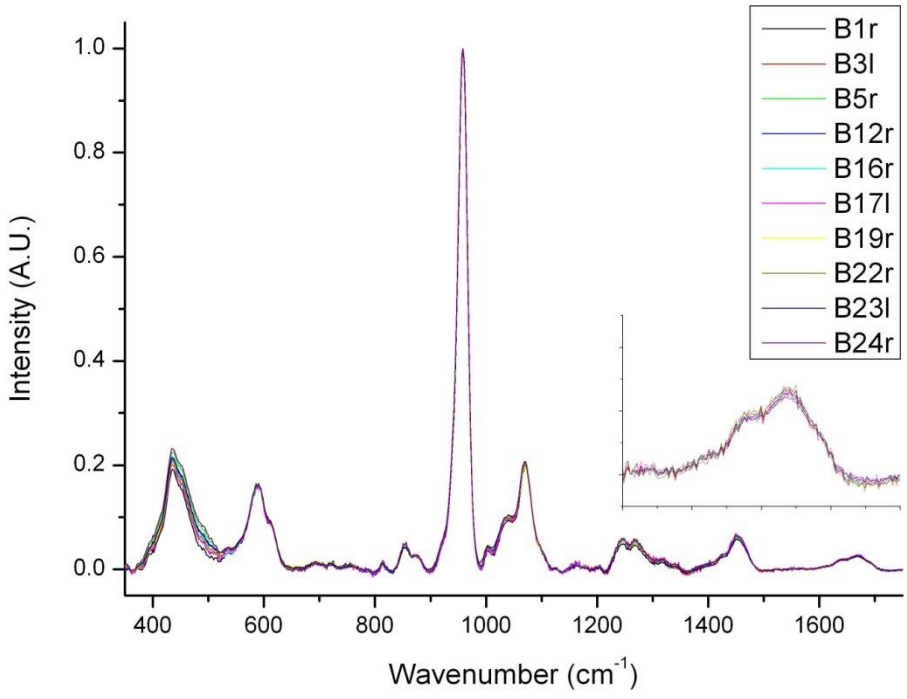

Figure 3.11 Tibiotarsus bone from ten chickens. There are no great variations in the intensities or profiles of the bands. The fluorescence background subtraction may be responsible for the largest variation observed (phosphate ν_2 at ~445 cm^{-1}).

	Individual Variation (Ten Chicken Tibiotarsi)
Phosphate/Amide I	*15.2 (±0.9)*
Carbonate/Amide I	*8.4 (±0.4)*
Carbonate/Phosphate	*0.56 (±0.01)*

Table 3-3 Spectra of tibiotarsus bone material were obtained for ten chickens. The average height ratio (and standard deviation) for the ν_1 phosphate band, carbonate sym-stretch and amide I band are shown.

Dehydration/Rehydration

It was stated above that water is a weak Raman scatterer and that this can be an advantage for Raman over other spectroscopy techniques (pg 50). However, it was also stated that water affects the mechanical properties of bone (pg 23), affects the spacing between the collagen molecules and plays a role at the molecular scale in and about the interface of the bone mineral crystals/collagen fibrils, this means the effect that the evaporation of water has on the Raman spectrum of bone material must be investigated.

In order to study how the ambient evaporation of fluid from bone material affects its Raman spectrum, the cortex was excised from the mid-shaft of a chicken-tibiotarsus bone. It was scraped to remove marrow, blood and other tissues, cleaned with phosphate buffered saline solution (PBS - GIBCO™ 7.2 (1X); liquid) and polished/dried with tissue paper. This resulted in a small sample (1 cm x 2 cm x cortical thickness [~1 mm]) of clean white cortical bone material which was stored in a jar of PBS solution. After thirteen days, the sample was removed from the jar and placed in the laser beam (at the illumination point of the Raman instrument) and a spectrum (60 x 1 s) was recorded instantly. When this accumulation finished more spectra were recorded at different intervals until the specimen had been drying for fifty hours. The spectra are shown in Figure 3.12, there are no significant changes in the band profiles (inset of Figure 3.12) and the band ratios are consistent (Table 3-4 shows the largest standard deviation between the band ratios is less than 5% and this includes the differences introduced by the fluorescence background removal).

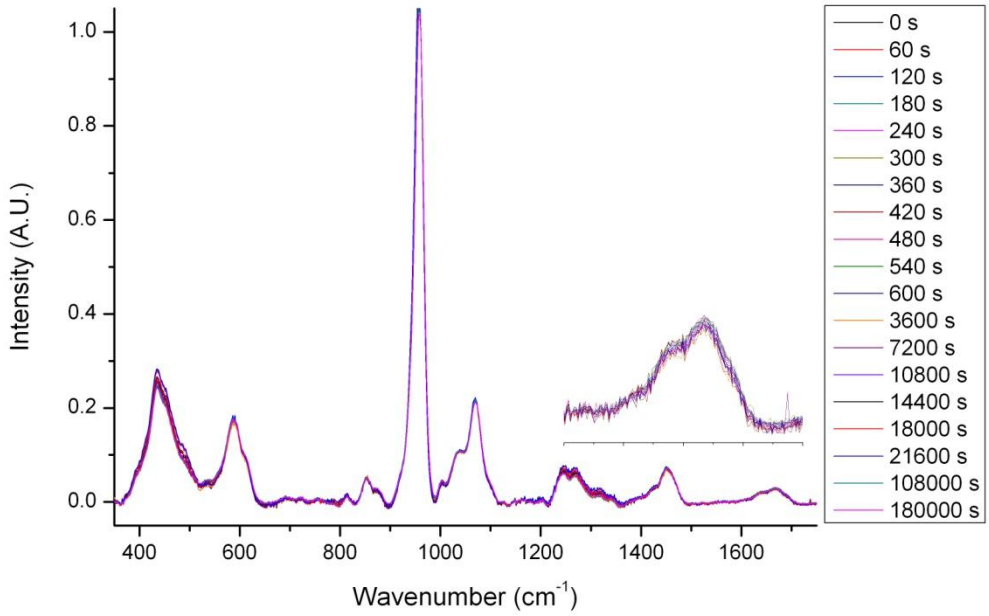

Figure 3.12 Spectra of cortical bone from a chicken-tibiotarsus, the spectra did not change even though bone was dripping wet (PBS solution) for first spectrum and had been at room temperature for 50 hours for the last. The small sharp peak at 1730 cm^{-1} in one of one of the spectra is a cosmic ray (a spurious signal due to CCD being impacted by a charged particle originating in space).

	Dehydration (One Chicken Tibiotarsus)
Phosphate/Amide I	*14.4 (±0.6)*
Carbonate/Amide I	*7.8 (±0.3)*
Carbonate/Phosphate	*0.539 (±0.003)*

Table 3-4 Spectra of bone material were recorded as it dried in ambient conditions. The average ratio (and standard deviation) for the ν_1 phosphate band, carbonate sym-stretch and amide I band are shown.

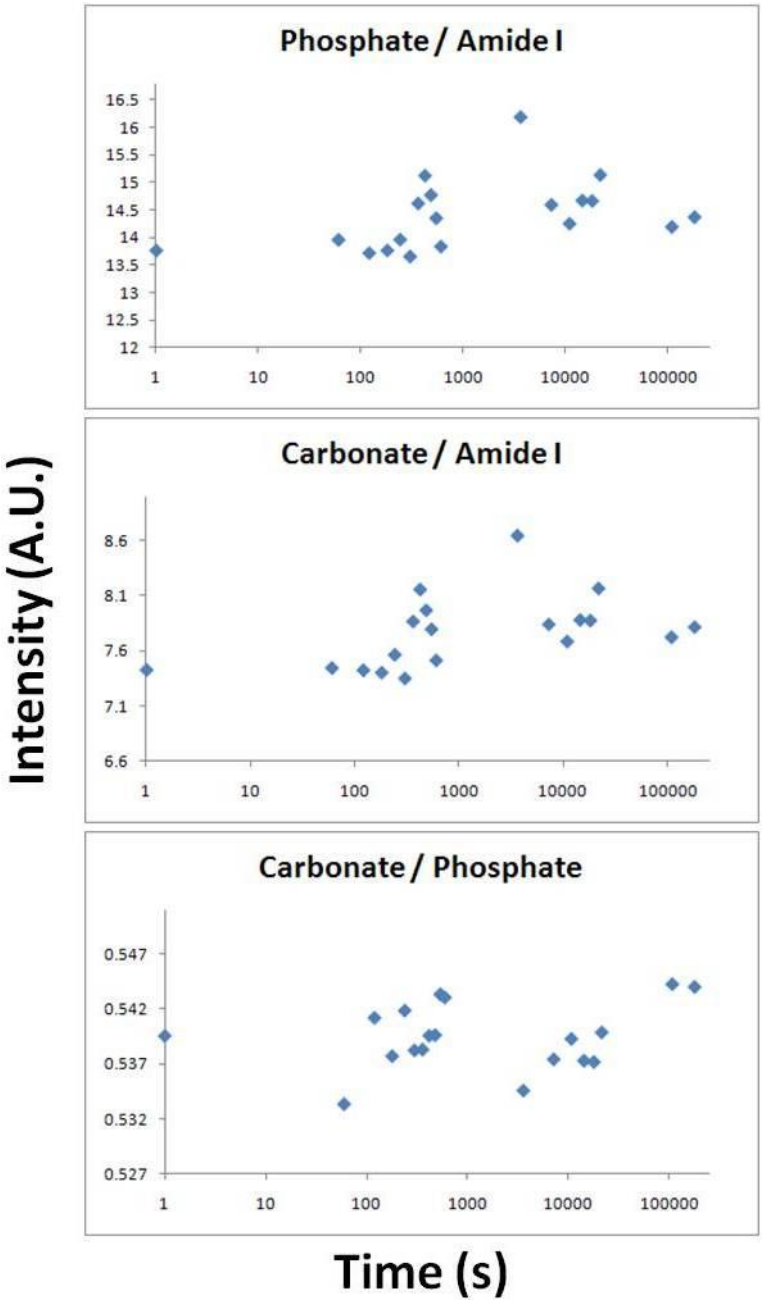

Figure 3.13 Spectra of bone material were recorded as it dried in ambient conditions. The average ratios for the ν_1 phosphate band, carbonate sym-stretch and amide I band did not vary in any systematic way over time.

3.3 Technical Developments

A Novel Technique for Enhancing Signal in Conventional Backscattering Fluorescence and Raman Spectroscopy of Turbid Media

Introduction

The research presented in this section resulted in a paper titled "Technique for Enhancing Signal in Conventional Backscattering Fluorescence and Raman Spectroscopy of Turbid Media" which was published in the journal *Analytical Chemistry* and a poster of the same name which was presented at the *Pittsburgh Conference* in Chicago in March 2009.[6] The work explores whether the Raman (and Fluorescence) signal of turbid media collected in the conventional backscattering geometry can be enhanced by inserting a dielectric filter at the laser illumination. Signal enhancements improve the spectral quality, enhance sensitivity and/or reduce acquisition times. The technique is based on the use of a dielectric filter as a 'unidirectional mirror' and was previously demonstrated using transmission Raman spectroscopy and SORS.[187,188] Described here is the first demonstration of its application with the conventional backscattering experimental geometry (where the signal that is collected is travelling in the opposite direction to the probe photons with no lateral displacement on the sample surface). Since the backscattering geometry is more common, this development makes the enhancement technique more widely applicable.

In order for Raman (or fluorescence) signal to be generated in a sample medium, the probe photons must propagate through it, once they scatter across the boundary of the medium they propagate away from the sample and are lost from the system i.e. they are wasted. For turbid media, such as living tissue and pharmaceutical products, many probe photons are lost at the point where the laser photons should be entering the system (the 'coupling interface' or 'illumination zone').[189,190] For opaque samples such as powders, over 90% of the incident laser radiation can be scattered backwards in a sample just a few millimetres thick.[191] The aim of the 'unidirectional mirror' or 'beam enhancer' technique (illustrated in Figure 3.14) is to reduce this probe-photon loss, increase the average time the probe photons spend in the sample medium and thus enhance useful signal (specifically Raman or fluorescence signals). It is applicable when the laser wavelength is not, or is only weakly, absorbed by the diffusely scattering samples. Given it is such a weak process, any method that enhances the intensity of Raman scattering is a valuable addition.

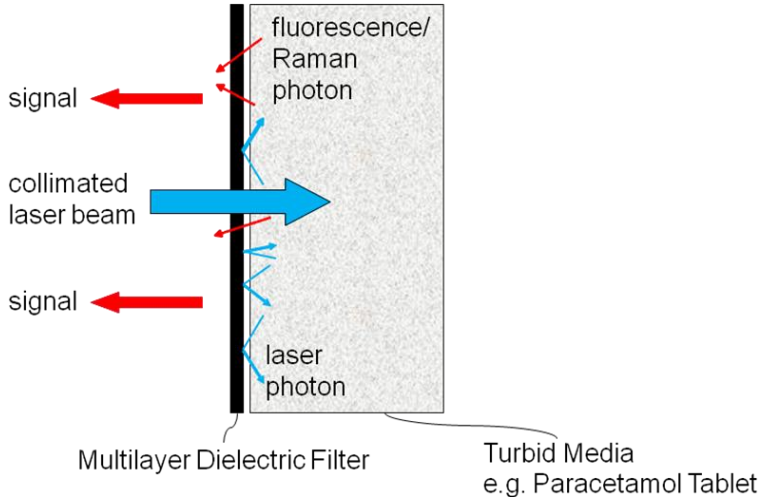

Figure 3.14 Schematic diagram of the principle for the enhancement of fluorescence and Raman signals in conventional backscattering geometry of turbid samples using a 'unidirectional' mirror.

Figure 3.14 shows the dielectric element positioned in the laser path. Similar schemes have been described by Matousek et al. in earlier theoretical and experimental work where the benefits of such filters were demonstrated using specialized variants of Raman spectroscopy (transmission Raman and spatially offset Raman spectroscopy (SORS)).[156,187,188] These studies required the spatial separation of the laser deposition and the collection areas. However, the majority of Raman and fluorescence spectrometers utilize a backscattering geometry where the illumination and collection areas are coincident. Here, the viability of this concept for the *backscattering geometry* commonly used in Raman and fluorescence spectroscopy is demonstrated experimentally for the first time, thus considerably increasing its usefulness and its applicability.

The 'unidirectional mirror' concept relies on the angular dependence property of multilayer dielectric optical filters, specifically the dependence of the transmission profile on photon incidence angle; the spectral transmission window shifts to shorter wavelength when a photon is incident from an angle greater than zero (see Figure 3.15).[192] The mechanism and the magnitude of this shift are discussed in reference 187. If the filter is designed for high transmittance of the laser wavelength at normal incidence, then it can function as a unidirectional mirror; laser photons scattered from the sample surface with angles of incidence different from normal *will be reflected back into the sample* with high efficiency. By choosing a suitable dielectric filter, photons shifted to longer wavelength (due to Raman or fluorescence scattering) are able to pass through the filter and on towards the detection system (see Figure 3.16). In addition, broadband mirrors can be used at the other sample-air interfaces to minimize the loss of photons (at all wavelengths) and further enhance the detected signal. This property will also be demonstrated experimentally.

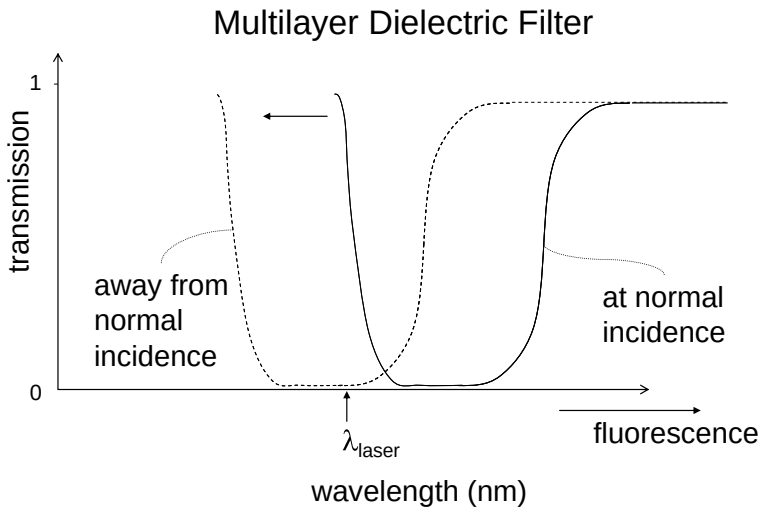

Figure 3.15 Schematic illustration of the shift of the wavelength dependence of a multilayer dielectric optical element with angle of incidence.

As discussed in earlier work[187] the enhancing mirror when used in the conventional geometry constrains the usable Raman signal to be above a certain wavenumber threshold, in our experiments the value is ~900 cm^{-1} (see Figure 3.17). This limitation stems from requirement for positioning the filter's spectral edge at a wavelength sufficiently far from the laser line; it needs to be far away in order to act as a mirror for a significant portion of laser photons emerging from sample at non-normal incidence. No such constraint exists on the spectral profile for the transmission geometry.[187] For fluorescence spectroscopy this is a lesser issue as red shifts from the laser excitation wavelength are typically much larger.

Although conventional mirrors have long been used to redirect transmitted laser light back into the sample as a way of increasing the intensity of Raman signal[193] and to reduce photon loss *near* the laser radiation coupling zone[194] such elements do not prevent the photon loss at what is often the most critical area, the delivery zone of laser radiation into the sample. This loss becomes more marked in applications where safety or other limits prevent the laser radiation from being concentrated onto a small area. Examples include the illumination of human skin or applications in explosive powder environments in pharmaceutical industry. The solution presented here is fully compatible with the defocused laser beams used in such conditions. It also means that the technique may be important for future SORS experiments which aim to obtain chemical information from bone through skin and tissue.

Materials and Methods

A schematic diagram of the apparatus used to obtain the Raman and fluorescence spectra is shown in Figure 3.16. For the Raman measurements, much of the equipment was that described above (the 830 nm laser, the collection optics, the collection fibre, the Kaiser notch filter, the spectrograph and the CCD camera). The laser beam was directed with a prism through the beam enhancer and onto the sample. The beam enhancer was an Iridian Spectral Technologies custom made filter (see Figure 3.17) with a transmission peak at the lasing wavelength and with a full transmission above 900 nm (corresponding to 930 cm^{-1} Raman shift). The dielectric filter was mounted on a translation stage in order to be able to precisely control its distance from the sample. At the sample, the laser power was 250 mW and the laser beam diameter was 1.0 mm.

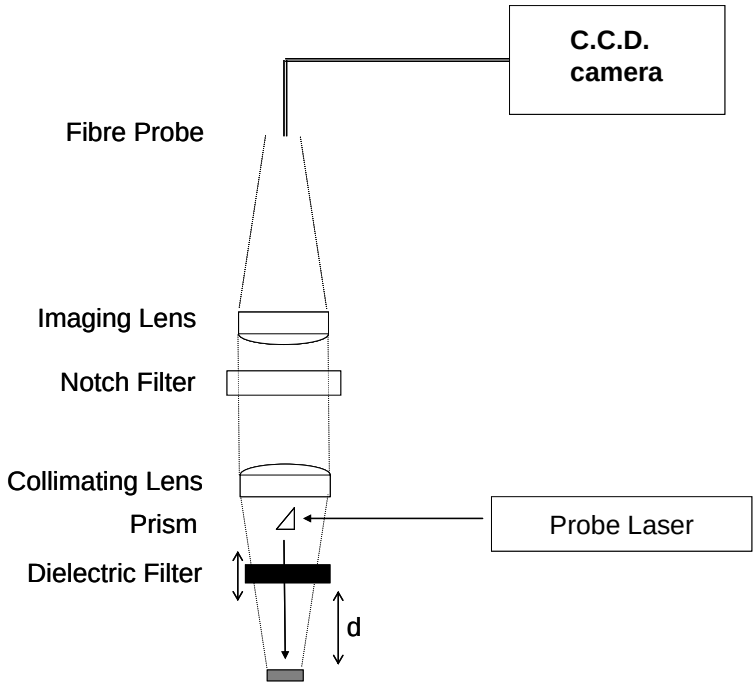

Figure 3.16 Experimental apparatus used to measure enhanced fluorescence and Raman spectra. The wavelength of the probe laser and the transmission profiles of the filters are different for each experiment.

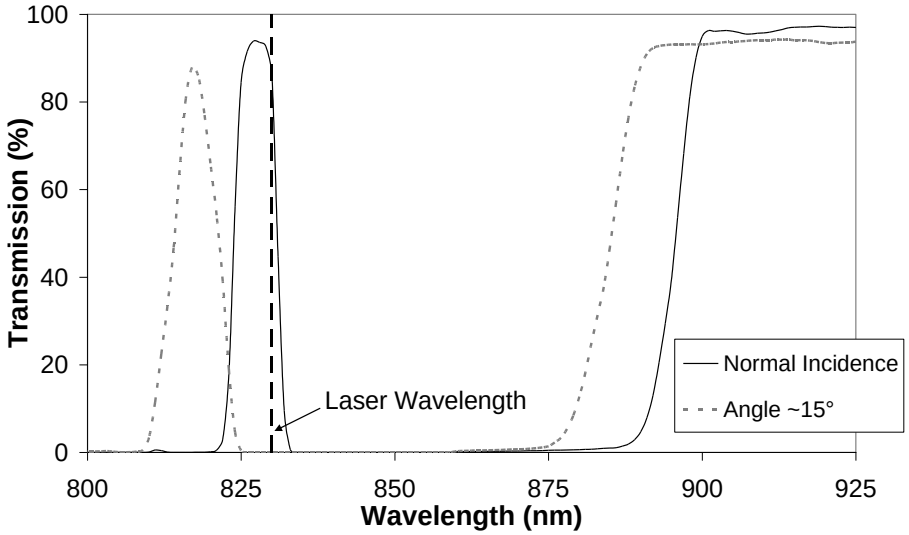

Figure 3.17 Measurement of the wavelength dependence of the 'unidirectional mirror' used to enhance the Raman spectra.

For the fluorescence measurements, the collection and detection equipment was the same as above but the probe laser was a green Helium Neon laser (543.5 nm, 0.40 mW, 1.1 mm beam diameter) equipped with a 10 nm bandpass filter centered at the laser wavelength to purify the spectrum. The beam enhancer was a (Semrock BrightLine®) dielectric single-band filter (525 nm), its transmission spectrum is given in Figure 3.18. In place of the notch filter was an edge filter (Semrock) that removed all radiation with a wavelength shorter than 900 nm.

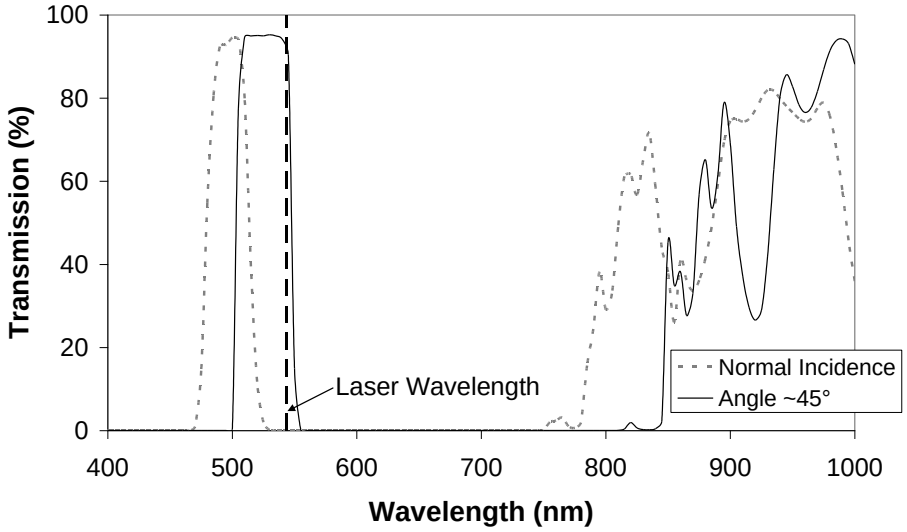

Figure 3.18 Measurement of the wavelength dependence of the 'unidirectional mirror' used to enhance the fluorescence spectra. The non-uniformity of the transmission in the 900-1000 nm range produces artefacts in the enhanced spectra.

Spectra were obtained whilst varying the distance (d in Figure 3.16) between the sample and the dielectric filter (the beam enhancer). In Raman measurements the sample was a standard 3.9 mm thick paracetamol tablet. In fluorescence studies, the same tablet was used but with a thin coating layer of fluorescent ink applied to its surface using a green highlighter pen to enhance florescence emission in the 900-1000 nm region covered by the detection system. Additional Raman experiments were performed on a 4 mm thick block of plastic (Teflon) with the dichroic mirror at the illumination site and a second mirror (Aluminum UV protected mirror, Reflectivity >90%; 400nm-10.0μm, Thorlabs) at the back end of the slab. Raman spectra were taken with no filters present, with the filter at the illumination zone, with the mirror at the back of the sample and finally with both filter and mirror.

Results of Study

The Raman and fluorescence spectra of a paracetamol tablet for different enhancer/tablet distances (d) are shown in Figure 3.19 and Figure 3.20; maximum signal is achieved when the filter is in contact with the sample and it decreases rapidly with increasing d.

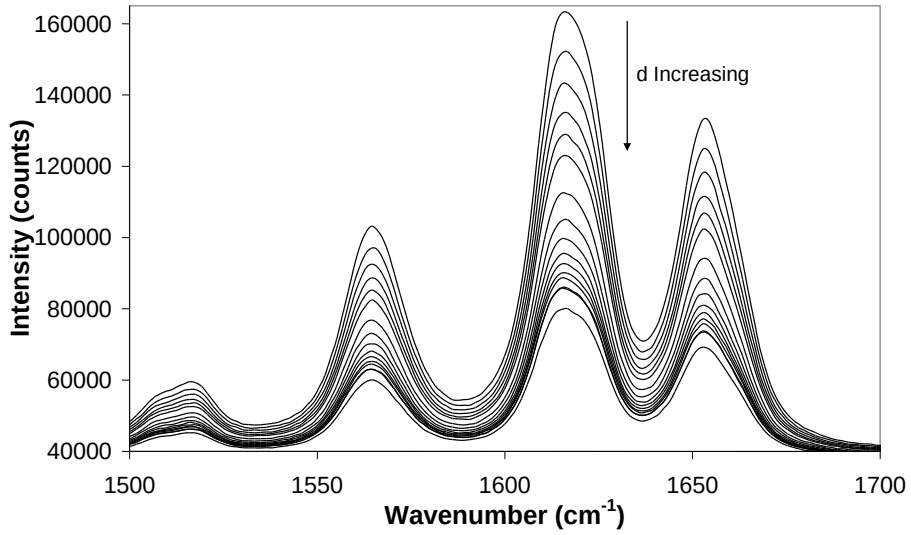

Figure 3.19 Raman spectrum of a paracetamol tablet recorded at various separations between sample and dielectric mirror (d = 0 to 2.75 mm). The filter used to enhance the Raman spectra was designed to have a flat transmission profile across the whole active spectral region thus the whole spectra sees the same enhancement.

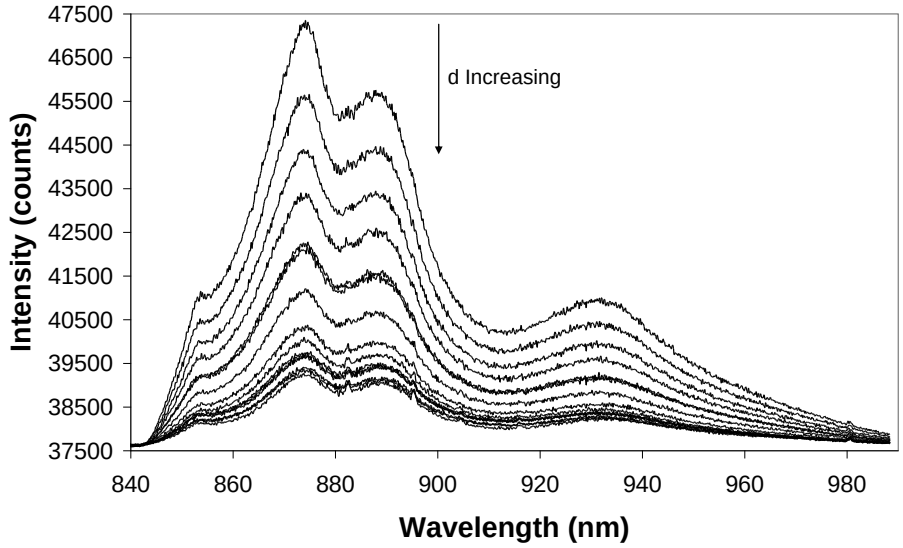

Figure 3.20 Fluorescence spectrum of a paracetamol tablet recorded at various separations between sample and dielectric mirror (d = 0 to 2.75 mm). The intensity can be seen to decrease as the filter is moved away from the tablet. The apparent structure in the fluorescence spectra is an artefact of the transmission profile of the mirror, a suitably designed filter would eliminate this.

Plots of the (approximately exponential) relationship between signal enhancement and d can be seen in Figure 3.21 and Figure 3.22. The signal is enhanced by a factor of 3 for Raman and a factor of 6 for fluorescence. When the Raman spectra were normalized so as to be the same height, the features were seen to be identical, as was expected. The enhanced signals were stable with no signs of any undue intensity fluctuations and the enhancement factors were reproducible upon successive approaches of the filter to the sample. The apparent structure in the fluorescence spectra is an artefact of the transmission curve of the beam enhancer (see the 900-1000 nm range in Figure 3.18).

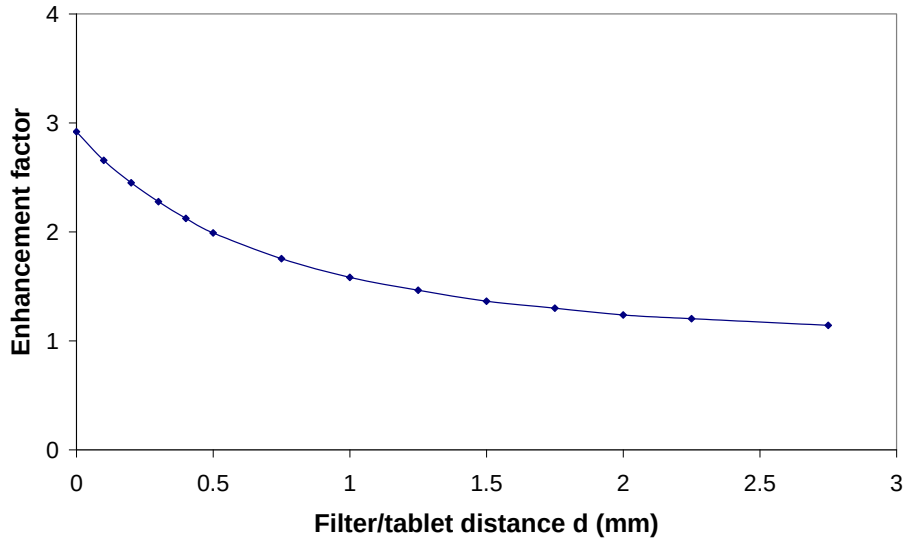

Figure 3.21 shows the dependence of the Raman signal intensity on the separation between sample (paracetamol tablet) and dielectric filter.

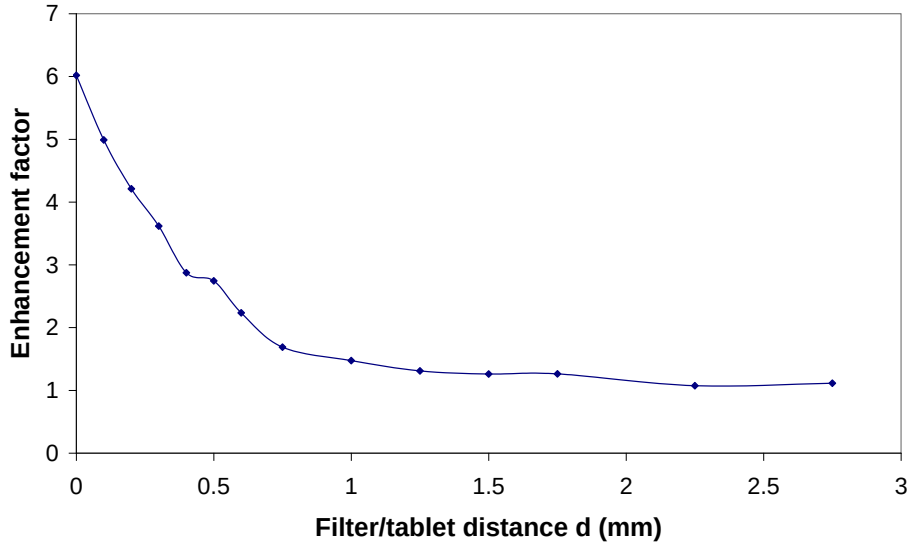

Figure 3.22 shows the dependence of fluorescence signal intensity on the separation between sample (paracetamol tablet) and dielectric filter.

In some cases, further enhancement can be obtained by the incorporating an additional broadband mirror at the "transmitted side" of the sample. For 4 mm thick Teflon slabs, a single unidirectional mirror at the illumination zone resulted in an enhancement of the Raman signal by a factor of 1.7. A single broadband mirror at the transmitted side gave an enhancement of 1.5 and the combination of the two gave an enhancement factor of 2.8 (Figure 3.23).

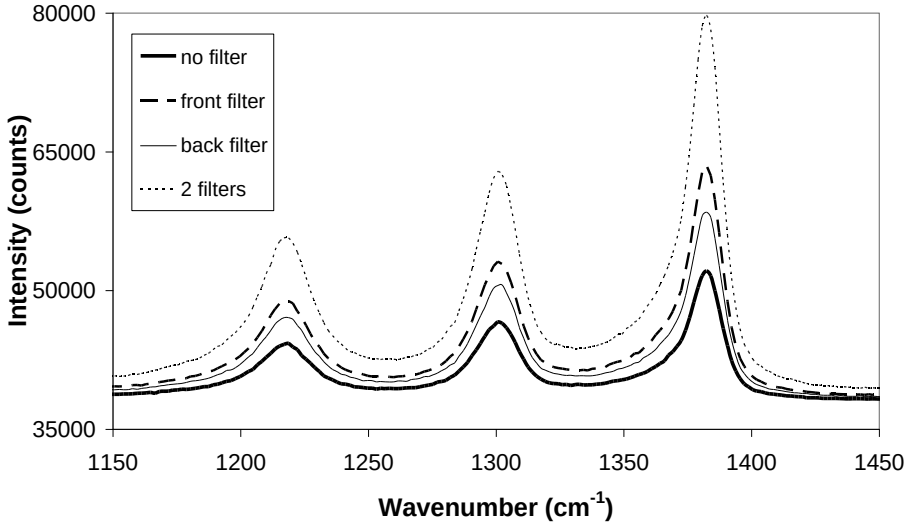

Figure 3.23 Raman spectra of a plastic slab (Teflon, 4 mm thick) with no filters present (thick line), with a single filter added to the front (dashed line) or back (thin line) of the sample and with filters at both sides of the sample (dotted line).

Discussion of Study

The beam enhancer technique presented here may be useful for investigators developing SORS as a tool for probing bone through skin and overlying tissue and has potential to become incorporated in a future SORS instrument. The enhancer could be put in contact with the skin and used to define the optical plane. However, since the precise enhancement factors achievable in each application will vary depending on the experimental parameters and the scattering/absorption properties of the probed sample, it is hard to predict how useful it will be without further experimentation. For example, the 'photon trap' experiment was also performed for a standard 3.9-mm thick paracetamol tablet, a medium of higher turbidity, and adding the extra mirror at the back, in addition to the beam enhancer at the front, only increased the overall Raman signal by a small fraction (10 %). The efficiency of coupling of laser radiation into turbid media using enhancing elements as a function of sample properties was discussed in an earlier theoretical study.[195] The final result (presented in Figure 3.23) suggests that, using suitably selected filters and mirrors, a photon 'trap' could be constructed which would be capable of increasing the Raman signal by a significant amount. In order to achieve an equivalent enhancement using other means it would be necessary to increase laser power, collection time, detector sensitivity or collection system/spectrograph throughput[196] by similar factors. However, these alternative measures may not be straightforward (or even possible) to implement for *in vivo* studies (for instance, the maximum laser power allowable on the skin is set by safety regulations).

Conclusions from Study

A concept for the enhancement of fluorescence and Raman signals from turbid media using a conventional backscattering geometry has been demonstrated. The enhancement was achieved using a custom made dielectric bandpass filters inserted at the laser illumination spot. Additional enhancement was achieved by inserting broad-band mirrors at the other sample to air interfaces. The enhancement contributes to improve signal or permits shortening of applied laser power or acquisition times and may be useful for deep, non-invasive Raman spectroscopy of bone through skin and overlying tissue in the future.

3.4 Conclusions from Chapter Three

This chapter described the instrument which was used to record all the Raman spectra in this thesis in detail. Some of the tests which were performed to calibrate and validate the instrument were also described.

A new technology which enhances Raman signal from turbid media (such as pharmaceutical tablets and plastics) was then described, and it was demonstrated experimentally. The beam enhancer would be useful in applications where safety, or other limits, prevent the laser radiation from being concentrated onto a small area, e.g. the illumination of human skin or applications in explosive powder environments in the pharmaceutical industry. The magnitude of the enhancement depends on the scattering and absorption properties of the turbid medium and can be predicted using Monte Carlo simulations or derived empirically.[187,188]

The Raman data reported in the rest of this thesis were recorded using conventional Raman spectroscopy (traditional backscattering geometry) and excised bone samples. Thus, there will be no further discussion of this beam enhancer technology until the final **'Future Work'** section, when the possibility of applying it to the study of bone material *in vivo* will be discussed (specifically the possibility of combining the beam enhancer with SORS).

The Raman spectroscopic studies of excised bone samples begin in the next chapter with a study which looks at the spectral consequences of functional adaptation.

4. Raman Spectroscopy Used for Non-destructive Assessment of Bony Materials with Widely Ranging Material Properties

4.1 Introduction

In the earlier introductory chapter, it was shown that the chemical composition of bone material could vary, with the proportions of mineral, collagen and water differing for different bone samples (see Figure 1.4 – pg 23). This compositional variation exists because of natural selection and is driven by the need to produce bone-types that have different mechanical properties in order to fulfil different functions.[7] This chapter investigates the Raman spectral signatures of this functionally induced compositional variation. Electron micrographs of this functionally adapted bone material are also presented which illustrate how large differences in mineral to collagen ratio manifest themselves at the micron scale. The aim is to determine if a correlation exists between Raman bands and material properties for bony materials that differ widely in mineral volume fraction. This work is being prepared for publication in an article titled "Differences in Mineral Volume Fraction are Associated with Changes in the Collagen Chemistry; a Raman Spectroscopy Study".

Functionally Adapted Bone

Bones are adapted through evolution to fulfil the specific functional demands placed upon them. The adaptations are evident at all levels, from the macroscopic shape, to the smaller level architecture and microstructure, and down to the basic genetically determined chemical composition of the material itself. The bone material's composition is adapted in order to 'tune' its mechanical properties; bone can have a large mineral volume fraction to maximize stiffness, can have a large relative proportion of collagen to increase toughness, or generally, can be somewhere on the continuum in between.[197] Illustrative examples of this phenomenon have been well documented for many species and many different bones with different functional roles they include: bone from deer's antler (a bone naturally selected for toughness), tympanic bulla bone from the ear of a fin whale (naturally selected for stiffness) and 'standard' bone material from the long bones of the leg, which must be both tough enough to resist fracture and stiff enough to resist deformation during physiological loading.

Deer antlers are mainly used to fight for male dominance, any deer with brittle antlers would lose the fights in which he entered, lose the chance to reproduce and pass on his genetic material, and could possibly lose his life. Hence, natural selection has ensured that the material from which antlers are made is as tough as possible; this tough material has a lower mineral volume fraction and higher collagen content than that found in the matrix of long bone diaphyses. At the other extreme, auditory bones in the skulls of mammals, e.g. the tympanic bulla, are adapted to optimize transmission of

acoustic vibrations; the bone matrix is optimised to be as stiff as possible, resulting in a brittle bone material with a high mineral volume fraction. Between these two extremes is 'standard' bone material from adult mammalian limbs. It must be tough enough to resist fracture during physiological loading, and stiff enough to resist too much deformation, for this, natural selection has produced a material with adapted material properties that are an intermediate between antler and tympanic bulla.[197,198,199] Some mechanical properties of these three types of bone material (obtained from reference 7) are given in Table 4-1.

Property	***Antler***	***Femur***	***Tympanic Bulla***
Young's modulus of elasticity (measure of stiffness)	7.4 GPa	13.5 GPa	31.3 GPa
Work to fracture (measure of toughness)	6190 J m^{-2}	2800 J m^{-2}	20 J m^{-2}

Table 4-1 Data (from reference 7) illustrating the different mechanical properties of bone with different roles. Femur in the table refers to an equine femur whereas the present study uses 'standard' bone from an ovine femur and an equine metacarpus.

The purpose of this study was to explore the premise that a correlation between Raman bands and material properties exists across a wide range of mineral volume fractions and across bones with different functional roles. In addition to Raman measurements, images of the tough, stiff and standard bone were obtained with a scanning electron microscope; these images showed how the chemical compositional changes manifested themselves at the micron level.

Relevant Raman Studies

As was shown in the literature review section above (pg 52), studies showing relationships between the Raman spectrum of bone material and its mechanical properties are well demonstrated. Amongst others, there have been studies relating Raman measurements to nano-indentation measurements within osteons,[200] studies of bone from inbred mice strains,[137,138,139,201,202] and studies of age-related changes in bone.[122,124] Crystallinity of the mineral phase of bone has also been measured with Raman spectroscopy and been related to various mechanical properties.[203] Raman studies of non-standard bony materials (i.e. bone not from the cortices adult mammal long bones) are not new either; the literature includes reports of studies of human dentine composition[204,205,206] and dentine mineralisation,[207] a study which used Raman spectroscopy to discriminate between ivories from six different species,[208] a study of fish bone[209] and a study which looked at bones from different species and found an increased collagen/mineral Raman ratio in deer antler compared with other bones.[210]

However, no comparative studies have been reported relating the Raman spectra of non-pathological bony materials which have been adapted for different physiological requirements, to their matrix composition/material properties over the wide range given here.

4.2 Materials and Methods

Bone Samples

The samples of bone material used in this study were the antler (from a red deer - *Cervus elaphus)*, 'standard' bone material from the femur of a sheep (it was from the mid diaphysis of the femur of a skeletally mature Welsh Mule domestic sheep - *Ovis aries*) and the highly mineralised tympanic bulla bone material (from a Fin Whale - *Balaenoptera physalus*) described above. In addition to these were a number of other mineralised tissues with differing functions; they were bone from the metacarpus of a thoroughbred racehorse (*Equus callabus*), both the dentine and cementum from the tusk (incisor tooth) of a narwhal (*Monodon monoceros*) and rostrum bone from the skull of a Beaked Whale (*Mesoplodon densirostris*). There was one sample (n=1) of each. Five of the samples had been used in previously published studies and hence their Young's moduli were known, the other two figures reproduced in Table 2 come from the cited literature. The samples had been stored under ambient conditions for a number of months or in some cases years and hence were dry when their spectrum were taken. Thin sections were cut from the red deer antler, ovine femur and fin whale tympanic bulla in order that they could be imaged with the electron microscope.

	Red Deer Antler	**Ovine Femur**	**Fin Whale Bulla**	**Beaked Whale Rostrum**	**Horse Metacarpus**	**Narwhal Dentine**	**Narwhal Cementum**
Young's modulus of elasticity	*7.4 GPa*	*22 GPa*	*31.3 GPa*	*46 GPa*	*15 GPa*	*10.3 GPa*	*5.3 GPa*

Table 4-2 Young's moduli of various bony materials. Note: All data from Currey 2006[7] except Ovine Femur[211] & Horse Metacarpus.[212]

Raman Data Collection

The Raman instrument used to obtain the spectra has been fully described in Chapter Three above (pg 69). The laser beam was directed onto the area of bone to be probed, the arrangement meant that signal was collected from ~1.2 mm diameter circle on the sample surface which is a relatively large collection area (in other applications using confocal Raman microscopy typical probe zone diameter would be ~1-100 micrometers) and meant that variations due to bone heterogeneity (microstructure) were largely reduced.

The spectrum of each sample was taken in turn for 60 seconds (240 x 0.25 second exposures) and this was repeated ten times; this meant that each measurement sampled a different volume of bone and the reproducibility could be quantified. Some samples comprised cortical and cancellous bone; all measurements were taken from cortical bone.

Electron Microscope Images

The micrograph images were captured with a JEOL JSM-6610LV scanning electron microscope instrument; it had a tungsten filament and was operating in high vacuum mode. The magnification was 25,000 and the voltage was 15kV. Each sample was metalized with a thin layer of platinum before imaging, the metal was sputtered (thickness <10 nm) using an Emitech K650TB (plasma technology). Cracks in the samples were not visible with the naked eye. It is probable that micron-scale defects were present in the animal's bones when they were alive but it must be pointed out that these particular cracks may have been created when the bones were being sectioned.

Data Processing

The raw Raman spectra had broad fluorescence backgrounds which were removed using the method described above (Chapter Three – pg 77). The spectra were split into two (at 1150 cm^{-1}) and a third order polynomial curve being fitted to each section before they were rejoined. These parameters were chosen to ensure the smallest collagen bands did not become distorted. The Raman spectra were then normalized to the largest band (the ν_1 phosphate band at ~960 cm^{-1}) in order to compare the relative intensities of the other bands (i.e. every pixel was divided by the intensity of the pixel atop the 960 cm^{-1} band. The intensity ratios for different bands were calculated by dividing one height by the other (specified in the results section). The noise on the height measurement was reduced by taking account of a number of pixels (averaged).

4.3 Results

Figure 4.1 shows scanning electron micrographs of micro-cracks in tympanic bulla bone (left), ovine femur bone (middle) and antler bone (right). The difference in the cracking mechanisms are dramatic, the tympanic bulla sample has a clean crack with no collagen fibrils visible, whereas the antler sample on the left shows many collagen fibrils, some of which are seen to be traversing the crack. The standard bone only has a few fibrils which still traverse the crack or jut out from the surface.

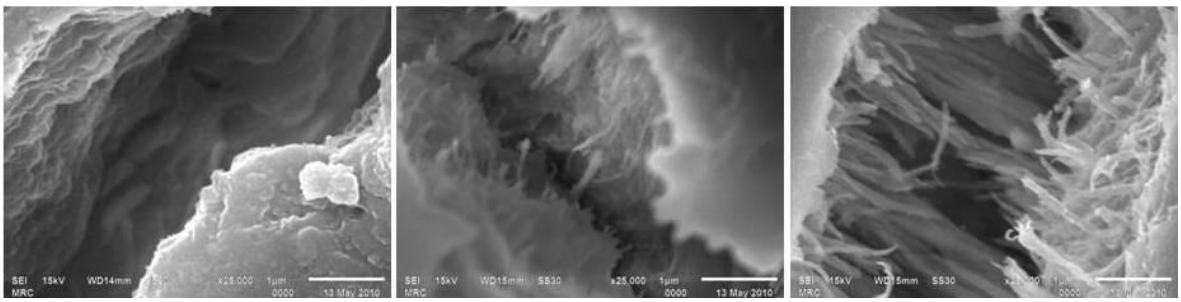

Figure 4.1 SEM pictures of the stiff tympanic bulla bone material from the ear of a fin whale, 'standard' bone material from an ovine femur and tougher bone material from a red deer antler. The density of collagen fibres is clearly different in each. The scale bar represents 1 μm.

The Raman spectra of the antler, femur and bulla are shown in Figure 4.2, the molecular mode assignments of the Raman bands of bone have already been described; below 1200 cm^{-1} the bands associated with the inorganic mineral phase of bone dominate and above it the bands associated with the organic (collagen) phase of bone dominate (there are some exceptions such as the proline/hydroxyproline bands below 900 cm^{-1}). The variation in the intensity of the collagen bands is clear in Figure 4.2; the intensity ratios for different bands were calculated and are given in Table 4-3.

What seems like broadening of the phosphate ν_1 band near its base is actually due to overlapping collagen bands in the same spectral region. The Raman spectra of all of the samples were analysed in the same way. The carbonate/phosphate band ratio showed no large variation. The ratio of mineral to collagen (main phosphate band to amide I band) varied over a relatively large range: rostrum (246.3), metacarpus (19.6), dentine (16.5) and cementum (18.0). The phosphate/amide I ratios of the mineralised tissues increased with Young's modulus; this relationship is plotted in Figure 4.3.

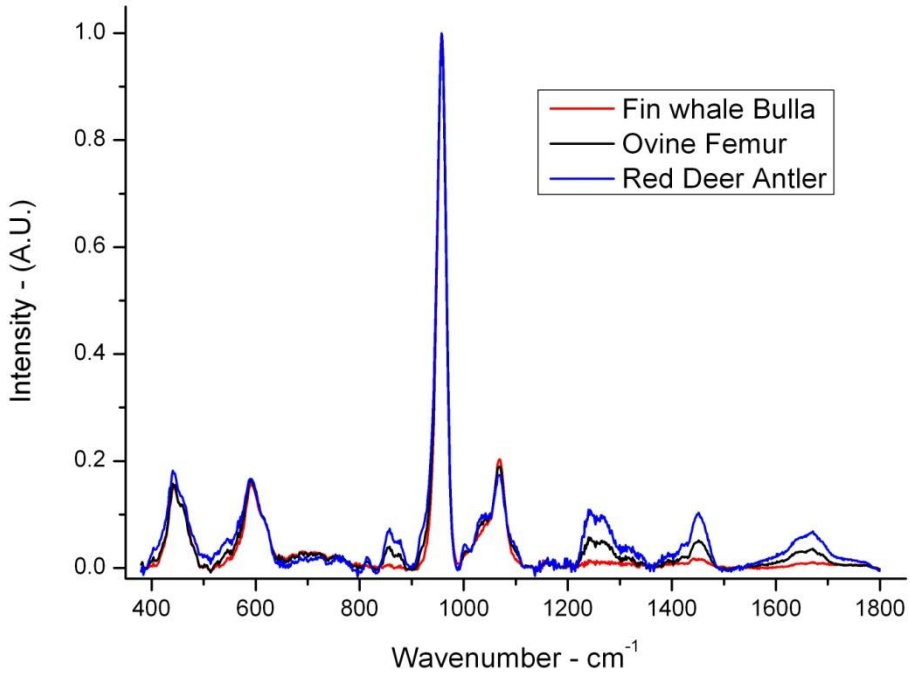

Figure 4.2 Raman spectra of the stiff tympanic bulla, 'standard' femur and the tough antler. The spectra have been normalised to the ν_1 phosphate band (960 cm^{-1}); the other major mineral bands are all the same height (small differences occur near where there are broad underlying collagen bands) and the collagen bands have large differences.

	Antler	**Femur**	**Tympanic Bulla**
Phosphate/Amide I	*13 (±1)*	*24.7 (±0.7)*	*95 (±9)*
Carbonate/Amide I	*2.5 (±0.3)*	*5.2 (±0.2)*	*20 (±2)*
Carbonate/Phosphate	*0.197 (±0.007)*	*0.212 (±0.004)*	*0.214 (±0.005)*

Table 4-3 Compositional differences of the three main bone samples. Ten different measurements were made of each sample (10 X 3 = 30 spectra), the average result is given along with the standard deviations in parentheses.

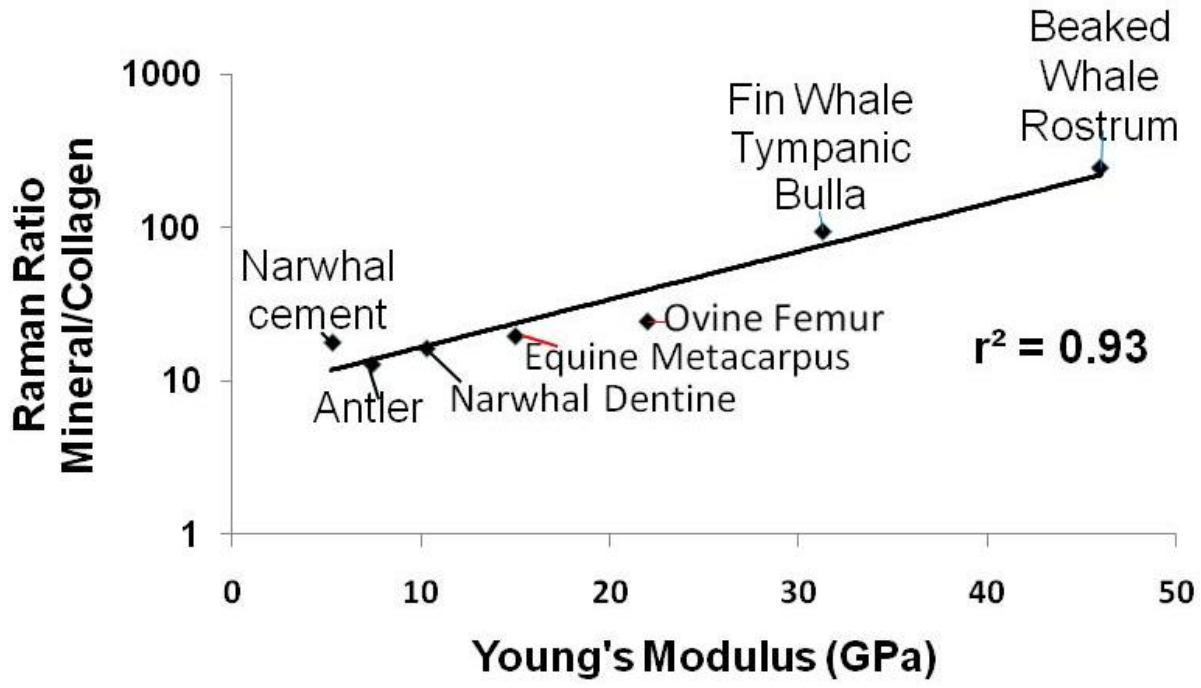

Figure 4.3 The relationship between mineral/collagen ratio (log_{10} scale) derived from Raman measurements, and the Young's modulus for seven types of bony tissue. The Young's moduli are all from Currey 2006[7] except Ovine Femur[211] & Horse Metacarpus.[212]

4.4 Discussion

The correlation of Raman spectroscopic measurements of the mineral to collagen ratio with Young's moduli has been demonstrated for a number of different mineralised tissue types, the range of moduli is much wider than previously demonstrated in the literature. The correlation coefficient is 93% (Figure 4.3) and is statistically significant ($\mathbf{p} < 0.05$)[XVII]. SEM images of three types of bone material with widely differing functions have also been presented; the images compliment the Raman measurements of chemical composition by illustrating how the variation of mineral volume fraction affects the material at the micron level. The tympanic bulla bone which has a work to fracture (this is the amount of work to drive a crack through the material and is a measure of toughness) of 20 J m^{-2} had sheer cracks in the SEM images and no collagen fibres were visible. The phosphate/amide I band ratio was 95 for this material. This was in stark contrast to the antler bone material which has a work to fracture of 6190 J m^{-2}, it had a dense array of fibres in its SEM image and a phosphate/amide I of 13.

Previous studies have shown that the phosphate/amide I band ratios are polarisation sensitive.[148, 149] Unlike the instruments used in those studies, the instrument in the present study was not designed to

[XVII] $\mathbf{p} = 0.0004$ - Result of an **r** to **p** calculation for $\mathbf{N} = 7$ and $\mathbf{r}^2 = 0.9326$ ($\mathbf{r} = 0.9657$).

be polarisation sensitive; it had no polarizer (half wave plate) to filter the laser light before it impacted on the sample (i.e. laser light was not perfect linearly polarised), the spot size at the sample was >1 mm in diameter (introducing polarization-destroying scattering effects and meaning information was averaged over many lamellae) and the collected scatter was fed through optical fibres (meaning some polarisation information was destroyed). In addition, the numerical aperture of the fibre probe was low (N.A. 0.37); Raghavan et al. have shown that polarisation effects are reduced for instruments with such low numerical apertures[154] because the light penetrates through several lamellae and smears the orientation out.[92]

Visual inspection of Figure 4.2 shows that the ν_2 phosphate to amide III ratio (which is polarization and orientation insensitive)[149] also increases in the order bulla-femur-antler, as one would expect if the measurements were due to composition rather than orientation. The large differences in mineral to collagen band ratios remained when the results were reproduced with two orthogonal laser polarizations.

This study was limited by our inability to access large numbers samples and by the fact that the exact history of each specimen was unknown. The latter was somewhat mitigated by the fact that the Raman spectral features reported are more than eighty times larger than subtle effects associated with dehydrating/rehydrating bone samples (Chapter Three) and by the fact that the antler, tympanic bulla, narwhal dentine, narwhal cementum and the rostrum bone were the *actual specimens* whose properties were measured in the cited literature.[7]

Gravimetric methods such as ashing have long been used to measure the amount of organic material and mineral in bone samples, they give absolute amount results and not the relative ratios obtainable with Raman spectroscopy. For example, for the specimens in Currey 1990[198] the mineral content (mg of Calcium per mg of bone) predicts 93% of Young's modulus (in agreement with the Raman data presented here). Ashing is convenient and easily executed with excised samples, but it has an obvious drawback in that it cannot be used without destroying the sample.

Perhaps the most interesting of the various bone materials probed was from the rostrum of Blainville's Beaked Whale (*Mesoplodon densirostris*); it is very highly mineralised and is the stiffest bone yet documented with a Young's modulus of 46 Gpa.[3,213,214] Its purpose is not known but it has been hypothesized that it plays a role in echolocation or as a weight for ballast.[215] The Raman measurements showed a large phosphate/amide ratio (phosphate/amide I = 234), much higher than any of the other bony tissues. Tympanic bulla bone and rostrum bone have a higher mineral volume fraction and stiffness than femur bone material but they are much less tough, a femur made from these materials would be very susceptible to fracture and therefore not fit for purpose. This consideration of

extreme bone materials is useful for illustrating the strengths and limitations of different analytical techniques, and their potential to analyse and predict the mechanical properties of whole bones. An ideal technique would take into account both the structural properties of the bone (the amount of material and its architectural arrangement) and the material properties of the bone (the mechanical properties of the bone material). Since the mechanical properties of bone material are to a large degree determined by its collagen to mineral ratio[216] and can be very sensitive to small changes,[5] an ideal measurement technique would obtain information from the organic phase and the mineral phase of the bone.

X-ray techniques, which measure the amount of bone mineral (and thus the amount of bone) present along the direction of radiation propagation, are well suited to measure structural properties, they can be used to measure the amount of bone in a given volume and its arrangement in space. However, since x-ray techniques are blind to the collagen in the bone; they cannot directly measure the ratio collagen to mineral; a thin cortex of 'rostrum-type' bone would absorb as much radiation as a thicker slab of 'standard' bone. Raman spectroscopy on the other hand can give chemically specific information about the material that is present but cannot measure the quantity of bone material. [This distinction is blurred when analysing sectioned bone samples of known thickness: x-ray techniques[217,218] and spectroscopic techniques[186]]. As was shown in Chapter Two, it may be possible to obtain compositional information non-invasively with Raman spectroscopy in the future[162,172,219] which could be combined with the structural data from x-ray or other techniques (e.g. ultrasound).

4.5 Conclusions from Chapter Four

A correlation exists between the intensity-ratios of certain Raman bands and the mechanical properties of bone material across a wide range of mineral volume fractions and in bone materials with different functional roles. The effects of compositional changes on bone material mechanical properties become clear when one examines micron-scale cracks.

The central thesis is concerned with the mechanical properties of bone material being adapted in differently loaded regions by a subtle tuning of the collagen chemistry which controls the mineral to collagen ratio. The data presented in this chapter show that Raman spectroscopy can be used to study this adaptation of bone material mechanical properties and so the central thesis can now be broken down into two sections:

- Are the mechanical properties tuned at the whole bone (or regional) level?

And

- Is mechanical property tuning controlled by the collagen chemistry?

The next chapter will look at the first of these two questions by looking for regional variation in the cortices of long bones from large animals.

5. Changes in the Composition of Cortical Bone along the Proximodistal Axis of Long Bones

5.1 Introduction

As was discussed in the previous chapter, bone is a class of materials with different proportions of mineral and collagen and hence it has a range of mechanical properties. The chapter also discussed *why* evolution has produced these different types of bone material, i.e. they fulfil different functions. In this chapter, mineral to collagen tuning of cortical bone within single bone organs will be investigated. The material comprising long bones will be probed with Raman spectroscopy at different points on the cortex; it is hypothesised that the bone material will have differences in mineral/collagen ratio in regions where it is subjected to different mechanical loads. First; another more widely known example of mineral/collagen variation within individual bone organs will be discussed.

Cancellous and Cortical Bone Material

Cancellous bone material is 20-30% less stiff than cortical bone material (i.e. the *material* the plates and struts are composed of is less stiff than the material that solid cortices are made of).[220] The cancellous bone material also has a lower mineral volume fraction than cortical bone[221,222] (although microstructure may explain some of the mechanical property differences)[220]. A recent Raman study comparing cortical and trabecular bone from standard laboratory mice in physiological conditions reported that the mineral to collagen ratio (phosphate v_4/amide III) was significantly greater in cortical bone than in trabecular bone.[223] The Raman study ascribed the changes observed to differences in the tissue-age stemming from slower turnover rates but in general small rodents have little or no bone remodelling.

There could be another age related explanation as to why cancellous bone material has lower mineral volume fraction than cortical bone; bones grow from the growth plates near their ends, so the cancellous bone material first formed after the midshaft of the bone where the cortical samples were taken from. However, Hodgskinson et al. measured the mineral content of cortical bone and cancellous bone taken from *adjacent* sites and still found differences.[222] It may be impossible to deduce if cortical and cancellous bone material's mineralisation level would differ when they were fully mature but the fact is they are different when measured; these points will be elaborated further below.

Cortical Bone

Cortical bone found in the limbs of adult mammals has to be both stiff, and resistant to fracture. Studies have shown that its mechanical properties do not vary greatly between species (for example, a variety of human, bovine, leopard, brown bear, roe deer, king penguin, polar bear and wallaby limb bones have the Young's modulus in the range 16.7-22.9 GPa)[7] and that it has a composition of roughly 65% mineral and 35% organic material/water.[38,224] However, studies on larger animals have shown that within single bones the mechanical properties of the bone material can have measurable differences, and that these differences can be dependent on anatomical position. Mechanical and ultrasonic studies of elastic moduli and various fracture stresses have been reported for many bone samples including human, canine and bovine femora, equine metacarpal bones and bovine tibiae. These studies have shown that some mechanical properties of cortical bone have local extrema in the midshaft; for example, elastic moduli have a local maximum and decay in both directions along the proximodistal axis.[212,225,226,227,228]

In addition to mechanical testing, some of these studies used Archimedes principle and/or gravimetric techniques to measure changes in the density, and/or mineral content, of the bone material at different points along the length of the bone in question. They found lower densities and lower mineral content towards the ends of the diaphyses. Some of these studies ascribed the mechanical property-variations to the anisotropic manner in which the osteons are orientated in the bone material and to regional micro-structural changes.[226,227]

The main focus of these studies was the variation of mechanical properties along the cortex and the compositional differences were measured as supporting data. However, there have also been investigations which focused solely on density variations; Archimedes principle has been employed to show the density of the human femoral cortex varied from midshaft to metaphysis,[229] x-ray techniques have been used to study mineral density distributions in the femora of various primates[230] and ultrasound measurements have shown regional changes in human tibia.[231] Investigators have also used x-ray tomographic techniques, chemical and gravimetric analysis of the bone material to show gradients of decreasing bone density towards the distal end of rat femoral diaphyses.[232,233]

Recently, a paper has been published which used peripheral quantitative computed tomography to examine the structure of the human tibia at different points along its length.[234] The purpose of the study was to look at the adaptation of structure and architecture, to function along a bone's long axis, they found that the long bone (human tibia) had a complex internal structure, and that its architectural design, and thus structural strength, varies profoundly along its length. The results showed that the

cortical mineral content and cortical thickness were largest near middle of the bone and decayed in both directions along the long axis, they stated "the tibia anatomy is closely adapted to the mechanical requirements derived from the different stress patterns to which every bone region is subjected by body weight-bearing and customary mechanical usage of the bone […] regardless of the gender and anthropometric characteristics of the individual". In the present study, the density of the bone material at different points is also probed with peripheral Quantitative Computed Tomography (pQCT) and the results are very similar to those published in the tibia-architecture study. However, in this study, the chemical composition of the material along the major axes of long bones is also probed (using Raman spectroscopy) and the possible adaptation of the bone material composition to its function is discussed.

Relevant Raman Studies

As mentioned in the literature review chapter above (pg 52), Raman spectroscopic techniques have been used to spatially map chemical changes in bones in a number of different studies; they include studies of undamaged, strained, and failed regions of bone, developing murine skulls and across individual osteons.[116,134,142] Raman spectroscopy has also been used to study variation within the cortices of individual bones; a study looking the mechanical property variation between anterior and posterior quadrants of a murine femur found that the Raman spectra between the two did not vary but that the orientation of the collagen fibrils did,[235] other studies looked at the mechanical-property and Raman-spectral differences between newly formed bone near the periosteum and older bone at greater distances[61] and the differences between cubes of metaphyseal bone and diaphyseal bone. These studies typically mapped smaller areas than those in the study reported here. Raman tomographic imaging of large, intact sections of a canine limb bone has also been reported; but to the best of our knowledge variations at the macroscopic scale, along the proximodistal axis has not.[175]

5.2 Materials and Methods

Bone Samples

The long bones probed in this study were cannon (third metacarpal) bones from the cadavers of skeletally mature (6-12 years old) thoroughbred racehorses (*Equus callabus*), and femurs from the cadavers of a skeletally mature (approximately 5-6 years old) Welsh Mule domestic sheep (*Ovis aries*). Some of the bones (with their soft tissue and periosteum removed) were divided along their proximodistal axes (metacarpal bone – sagittal plane, femur – coronal plane) exposing the whole length of the cortex for the spectroscopic examination (shown in Figure 5.1 and Figure 5.2). The samples were frozen after being excised and stored in a freezer (253 K) when not being used.

Figure 5.1 Equine metacarpal bone divided along sagittal plane.

Figure 5.2 Ovine femur divided along coronal plane.

Raman Data Collection

The Raman instrument used to record the spectra was described in Chapter Three. The beam, with a 1.2 mm diameter at the sample, was directed onto the point on the cortex which was to be probed. That such a large illumination point was used, along with the fact that a large number of spectra taken at many different points, help reduce the Raman signal variation due solely to the heterogeneity of the bone material at the micro-scale. The spectrum collection process was automated by loading the bones on a motorised translation stage, which was controlled by Labview software (using a program that was written in house). The control software acquired a Raman spectrum, moved the stage by 1 mm, took another spectrum and repeated this process over a specified distance. Each Raman spectrum was collected with a 30 s acquisition time (30 x 1 s accumulations).

X-ray Measurements

The pQCT data were obtained with an XCT 3000 scanner, (Stratec, Pforzheim, Germany) with the cortical density threshold set at 700 mg cm^{-3}. The bone sections were placed in the sample holder and the density was recorded at 1 cm intervals along their lengths from the proximal end (starting from where the cortex became discernable).

Data Processing

The raw Raman spectra had broad fluorescence backgrounds which were removed using the polynomial fitting routine described above (pg 77).[185] The band heights were determined by averaging a number of pixels across the band and different bands were compared by calculating the ratio of the two heights. In order to make the trend plots, the average value of the measurement was obtained (e.g. the average value of proline/phosphate ν_2), all the values recorded were then divided by this average (this normalised to measurements to one), and these numbers were then multiplied by 100 to give a percentage. The trend plots were smoothed with the use of rolling averages (each data point is the average of a spectrum and three neighbours on either side).

5.3 Results

Equine Metacarpus

Spectra comparing the diaphysis and metaphysis of the horse metacarpal bone are shown in Figure 5.3. The spectra are very similar and differences cannot be discerned easily by visual inspection. However, the inset plots of the proline and amide II regions show that there are measurable differences between the two spectra.

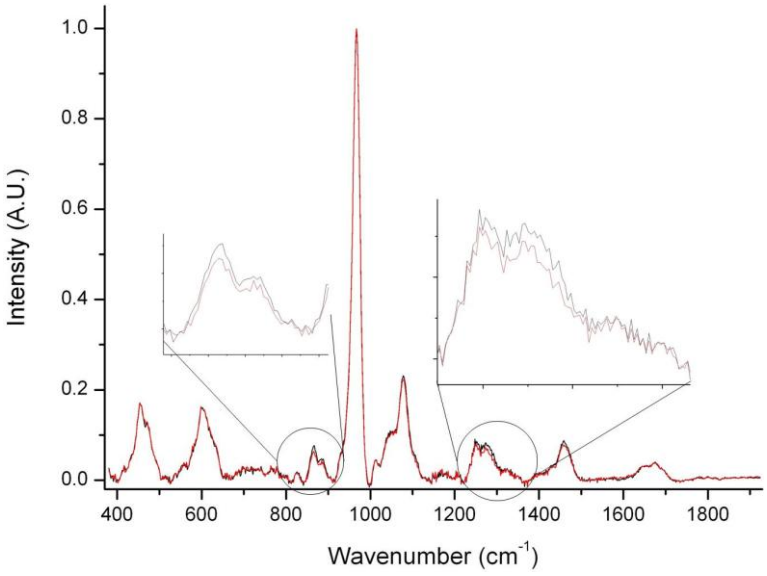

Figure 5.3 Spectra of equine mid-diaphysis metacarpal bone (red) and distal metaphysis bone (black).

Figure 5.4 shows the systematic changes in the mineral to collagen ratio that were measured along the equine metacarpal cortices. The data points represent the spectra which were taken at one millimetre intervals along the exposed anterior surface. It can be seen that the bone material has a fairly steady proportion of mineral along most of the length of the diaphysis and the proportion of mineral decreases towards the metaphyses. Figure 5.5 shows a similar plot of mineral to collagen ratio for the cut surface (exposed cortex) of the same metacarpal bone; this plot shows the amide III/ν_2 phosphate (symmetric stretch at ~450 cm^{-1}) band ratio. As discussed above (Raman Studies of Bone Microstructure - pg 60), the amide III/ν_2 phosphate is a good measure of composition (as opposed to, for instance, the amide I/ν_1 phosphate band ratio which is sensitive to polarisation and orientation effects).[150] The bone was moved along in the straight line by the mechanical stage, this in effect meant the laser 'walked' a straight line along the cortex. The straight line scan and the fact that metacarpal cortices have a varying thickness along their length created the jagged pattern along the diaphysis as the laser moved between the endosteal and periosteal surfaces.

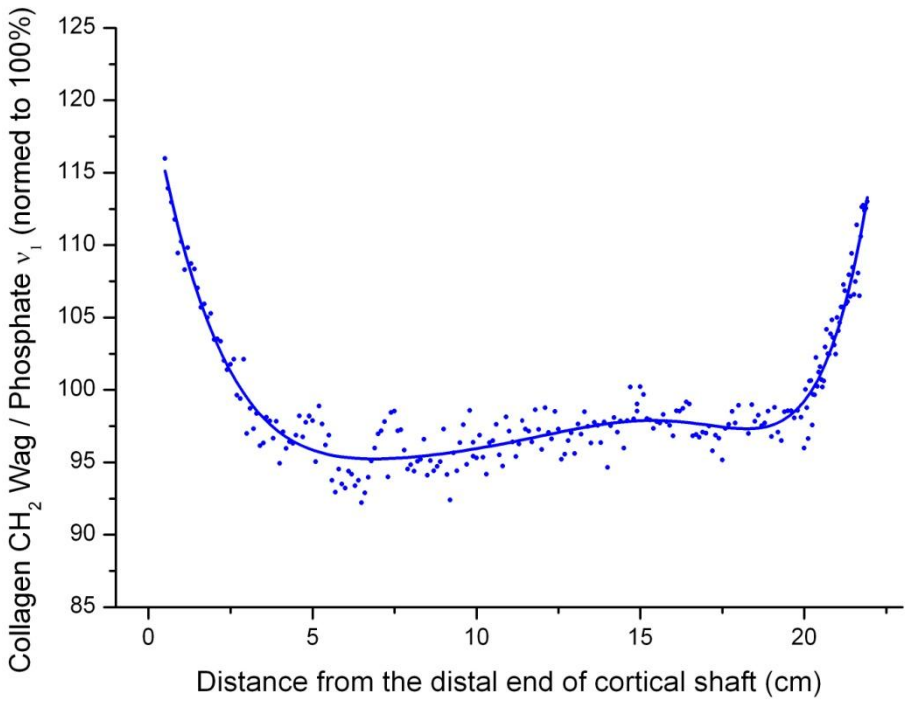

Figure 5.4 Relative proportion of collagen to mineral along the length of the equine metacarpal bone. The measurements were taken along the anterior surface.

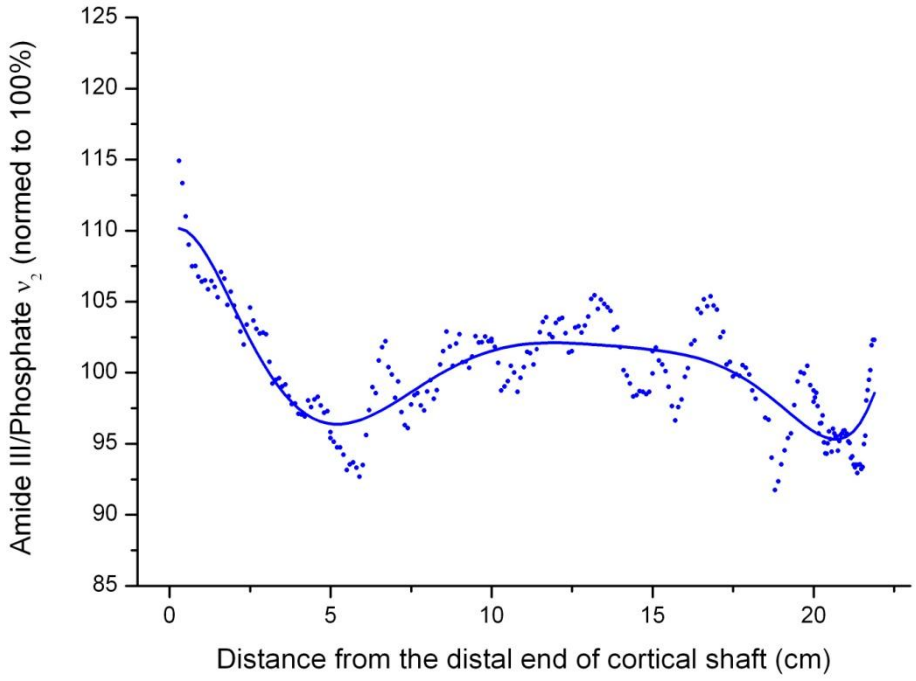

Figure 5.5 Relative proportion of collagen to mineral along the length of the equine metacarpal bone measured with the polarisation and orientation insensitive amide III/ν2 phosphate band ratio.

The proline band near 860 cm^{-1} does not overlap with any other major/relevant band and is relatively insensitive to changes in the collagen secondary structure,[92] for these reasons a plot of proline/ν_2 phosphate band ratio is presented in Figure 5.6. The trend is similar to the previous graphs with a decreasing proportion of mineral towards the ends of the bone.

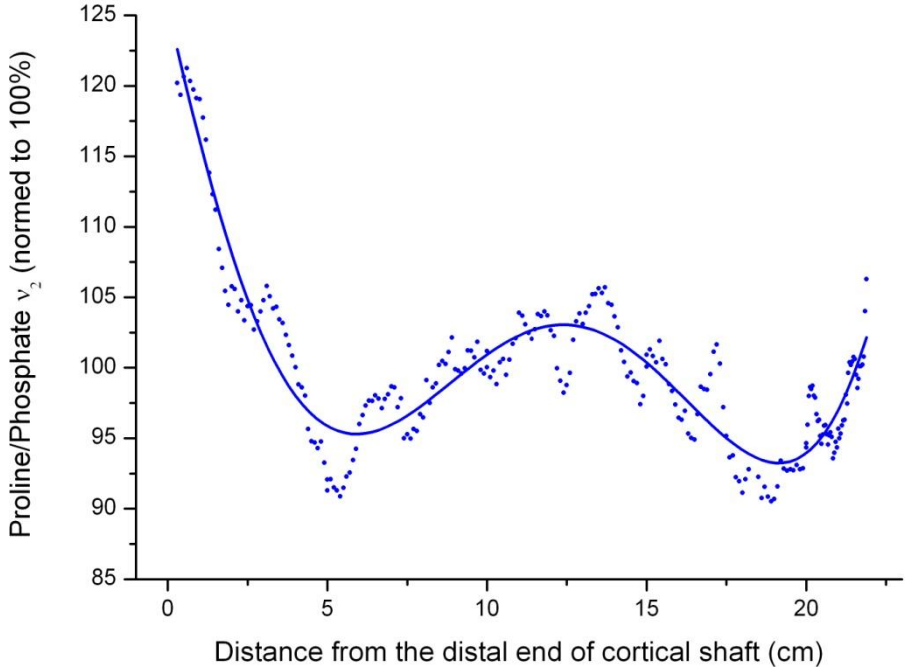

Figure 5.6 Relative proportion of collagen to mineral along the length of the equine metacarpal bone. Measured by comparing the structure-insensitive proline band with the polarisation-insensitive ν2 phosphate band.

Raman data from the exposed anterior surfaces of three more equine metacarpal bones are shown in Figure 5.7. For each of these samples, only one metaphysis was probed. As before each data point represents a whole spectrum and the measurements were taken at one millimetre intervals along the proximodistal axis. Again there are differences in the mineral to collagen ratio between the (proximal) metaphyses and diaphyses; the bone material has a fairly steady proportion of mineral along most of the length of the diaphysis with a decreasing proportion of mineral towards the proximal metaphysis.

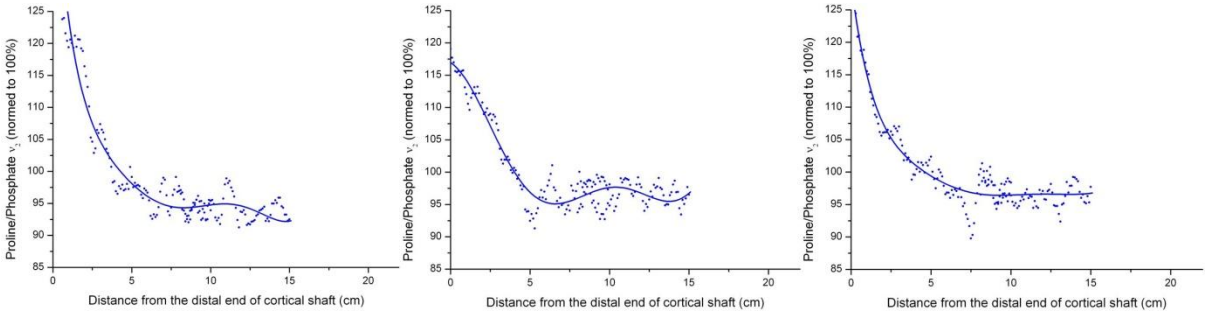

Figure 5.7 The difference in mineral to collagen ratio between the proximal metaphysis and the diaphysis for the third metacarpal bone of three thoroughbred racehorses.

The pQCT measurements taken along the proximodistal axis of an equine metacarpal bone are shown in Figure 5.8. The volumetric density (as measured with the pQCT instrument) plateaus along most of the length of the diaphysis and decreases towards the metaphysis. The density changes occur at similar anatomical regions to the compositional changes (Raman collagen/mineral ratio - which are inverted to aid comparison).

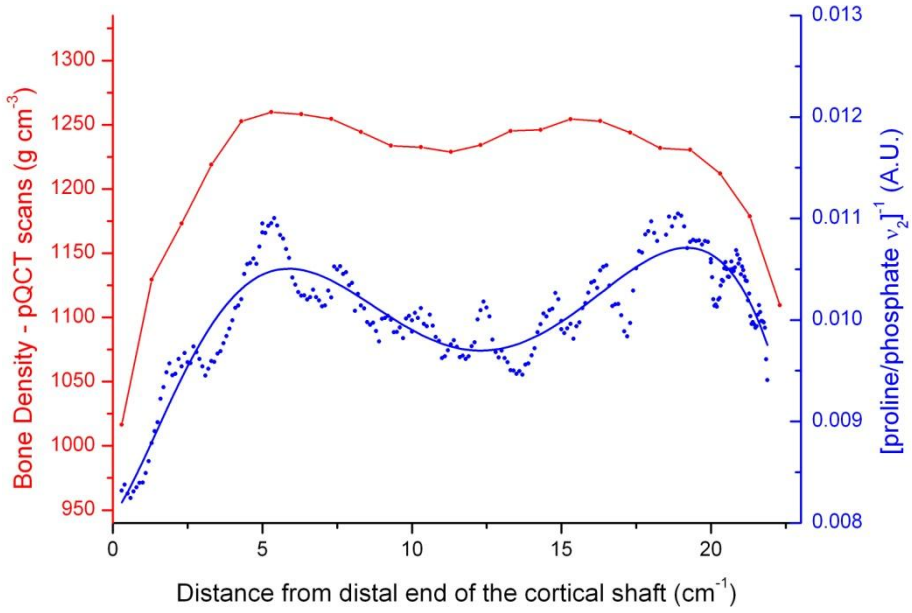

Figure 5.8 the volumetric density (red line and red scale) decays occur towards the ends of the equine metacarpal bone diaphysis. The trend is similar to the Raman spectroscopic (collagen/mineral ratio) measurements (blue line and blue axis).

Ovine Femur

The proline/phosphate ν_1 ratio measured along the lateral surface of the ovine femoral cortex is shown in Figure 5.9, it shows similar trends to the equine metacarpal bone, with the maximum mineral content being found towards the middle of the diaphysis and the mineral content decreasing as towards the ends of the bone. The proline/phosphate ν_1 ratio measured along the cut edge of the cortex is shown in Figure 5.10, as was the case with equine metacarpal bone the jagged pattern along the diaphysis is the result of the laser 'walking' in a straight line between the endosteal and periosteal surfaces. The pQCT measurements are shown in Figure 5.11. The density plateaus along most of the length of the diaphyses and decreases towards the ends. Again, the density changes occur at similar anatomical regions to the compositional changes (Raman collagen/mineral ratio).

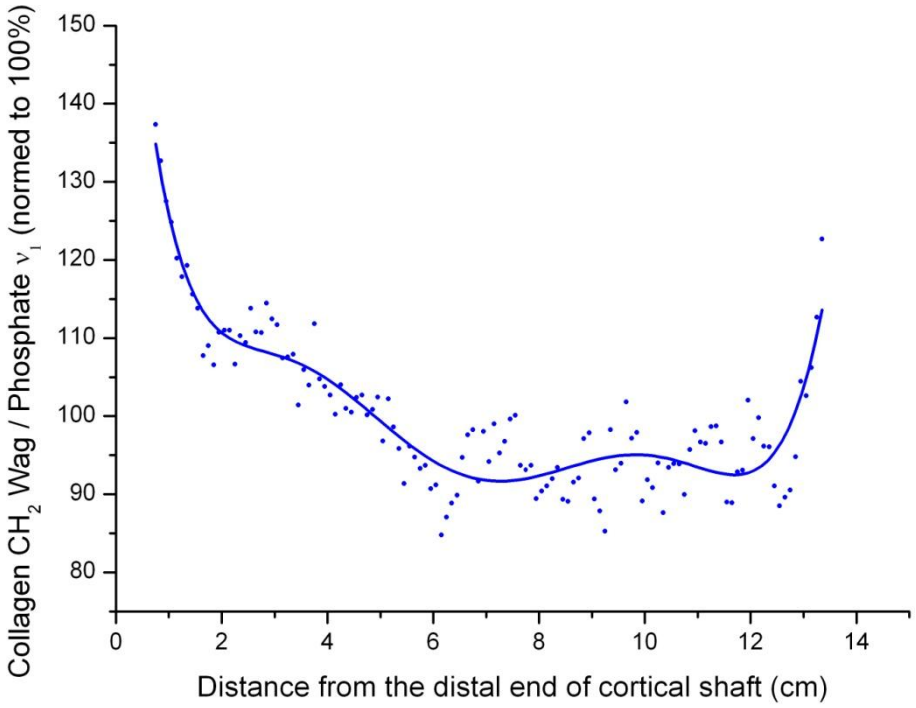

Figure 5.9 Relative proportion of collagen to mineral along the length of the ovine femur. The measurements were taken along the lateral surface of the bone.

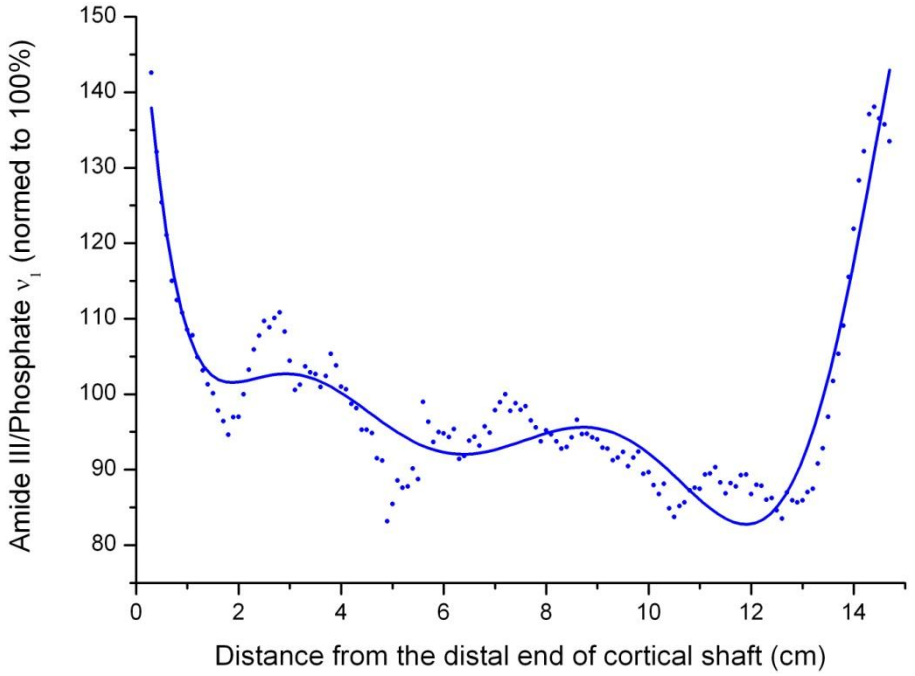

Figure 5.10 Relative proportion of collagen to mineral along the length of an ovine femoral cortex. Measured by comparing the structure-insensitive proline band with the dominant ν1 phosphate band.

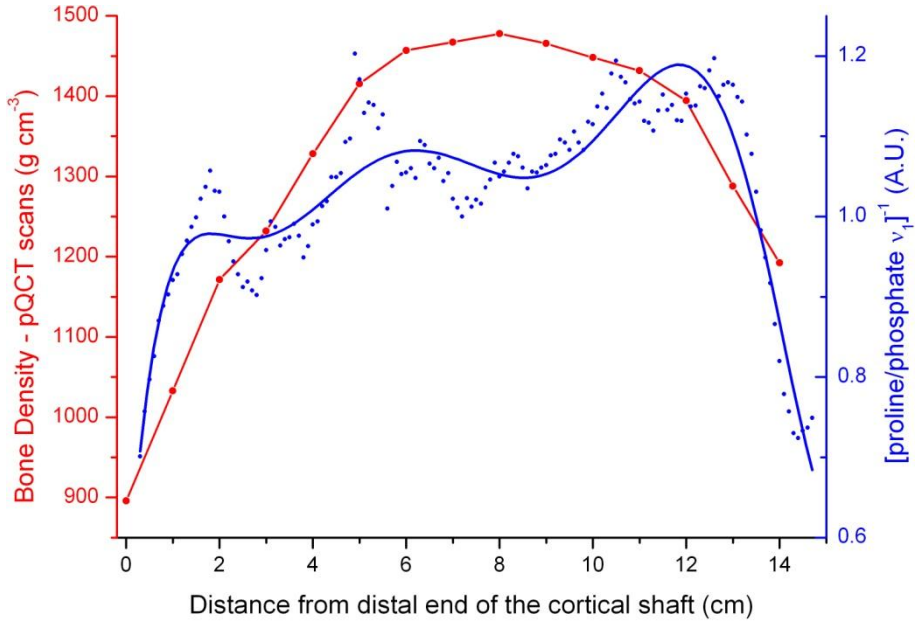

Figure 5.11 The volumetric density (red line and red scale) decays occur towards the ends of the ovine femur diaphysis; in a similar manner to the Raman (collagen/mineral) variation (blue line and blue axis).

Similar compositional trends have been measured for other long bones (e.g. the cervine (red deer) metacarpal bone shown in Figure 5.12), however less spectra and shorter accumulation times were collected and the data needs to be repeated. Further work will be needed to reproduce the trend-plots above for more long bones and from more species.

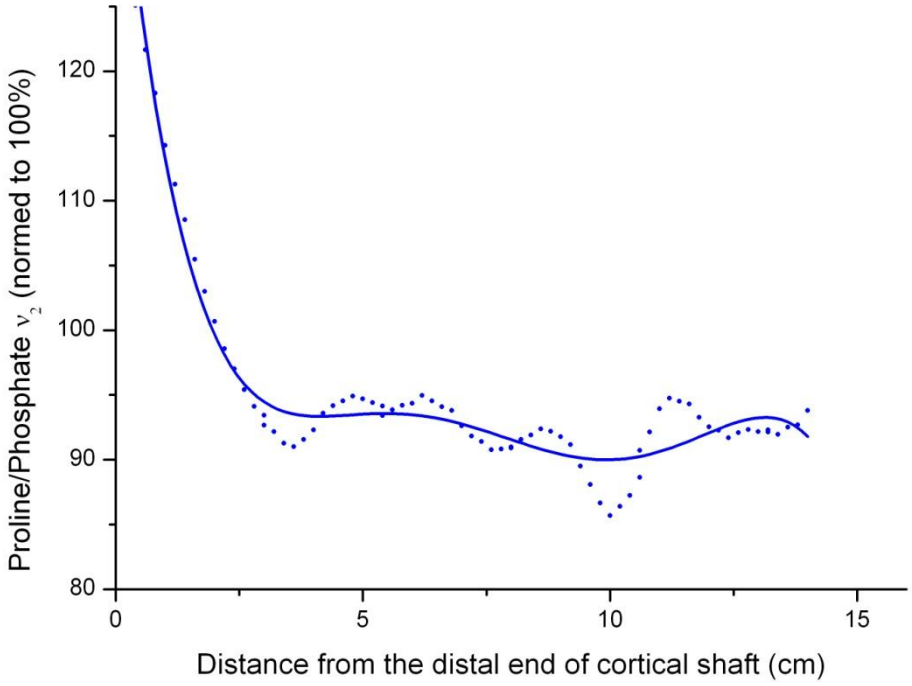

Figure 5.12 Raman measurement along the proximodistal axis of a Cervine metacarpal bone, the proximal metaphysis has a lower mineral to collagen ratio than the diaphysis.

5.4 Discussion

The bone material which comprises the cortices of long bones is not a uniform material. Its mineral/matrix ratio, as measured with Raman spectroscopy changes as a function of position along the proximodistal axis. The volumetric mineral density (as measured with pQCT) also shows distinguishable changes along the length of the bone, decreasing at the ends of the cortex; this is in agreement with earlier studies. [212, 225, 226, 227, 228, 229, 230, 231, 232, 233] It was noted above, that some previous studies have ascribed the variation along the proximodistal axis to the anisotropic manner in which the osteons or collagen fibres are orientated at different points (bone material's mechanical properties[226, 227] & Raman spectral properties[151]). However, the instrument used to record the data presented here was relatively insensitive to polarisation effects (no polarizer, large spot size, use of optical fibres, low numerical aperture[154]), the Raman bands were specifically chosen to measure composition[150] and the pQCT measurements should not have been affected by collagen fibre orientation. When added to previous gravimetric studies, such as those reported by Kim and Walsh,[227]

the most obvious conclusion is that at least some of the variation in the mechanical properties of the bone material along the proximodistal axis are due to a variation in the level of mineralisation.

Bones grow from the growth plates at each end, bone material which is furthest from a growth plate has (if we neglect remodelling for the present) existed longest. Hence, this bone has had longer to mature and should have reached a later stage of mineralisation. These bone material-age differences have been used to explain findings from an x-ray tomographic study of mineralisation gradients in the femora of 6-9 week old rats[233] and a Raman study which showed differences between metaphyseal bone and diaphyseal bone from the femora of 2-12 week old mice.[151] However, the investigators in the x-ray study discounted this explanation for density variations seen in bones which undergo continual remodelling; in these bones the proximal end of bones and bones from older subjects may not necessarily be made of older bone. This caveat is relevant to the data presented here; the bones were from skeletally mature specimens (sheep 5-6 years old, horses 6-12 years old) and from animals which are known to undergo remodelling.

The other factor which affects the age of bone material is remodelling; if more remodelling were to occur near the ends of long bones, the bone material there *would* on average, be younger than the mid-diaphysis bone (and the associated resorption cavities would also contribute to lowering the density). Marotti and others have shown that for some animals, it is certainly the case that more remodelling occurs towards the ends of long bones.[236] In the cited study, skeletons of stray dogs were collected and various long bones (metacarpal bone, metatarsal bone, femur, ulna, rib, etc) were sectioned and histologically examined. There were more secondary osteons per unit area near the ends of the bones than nearer the midshaft. Figure 5.13 and Figure 5.14 show micrographs of sections cut from the midshaft and metaphysis of the ovine femur cortex from which the data were obtained; the images show no glaring disparity in the number of resorption cavities present i.e. there are no large cavities in either of the 4 mm^2 boxes. More work is needed to rigorously quantify histological differences along the length of the bone.

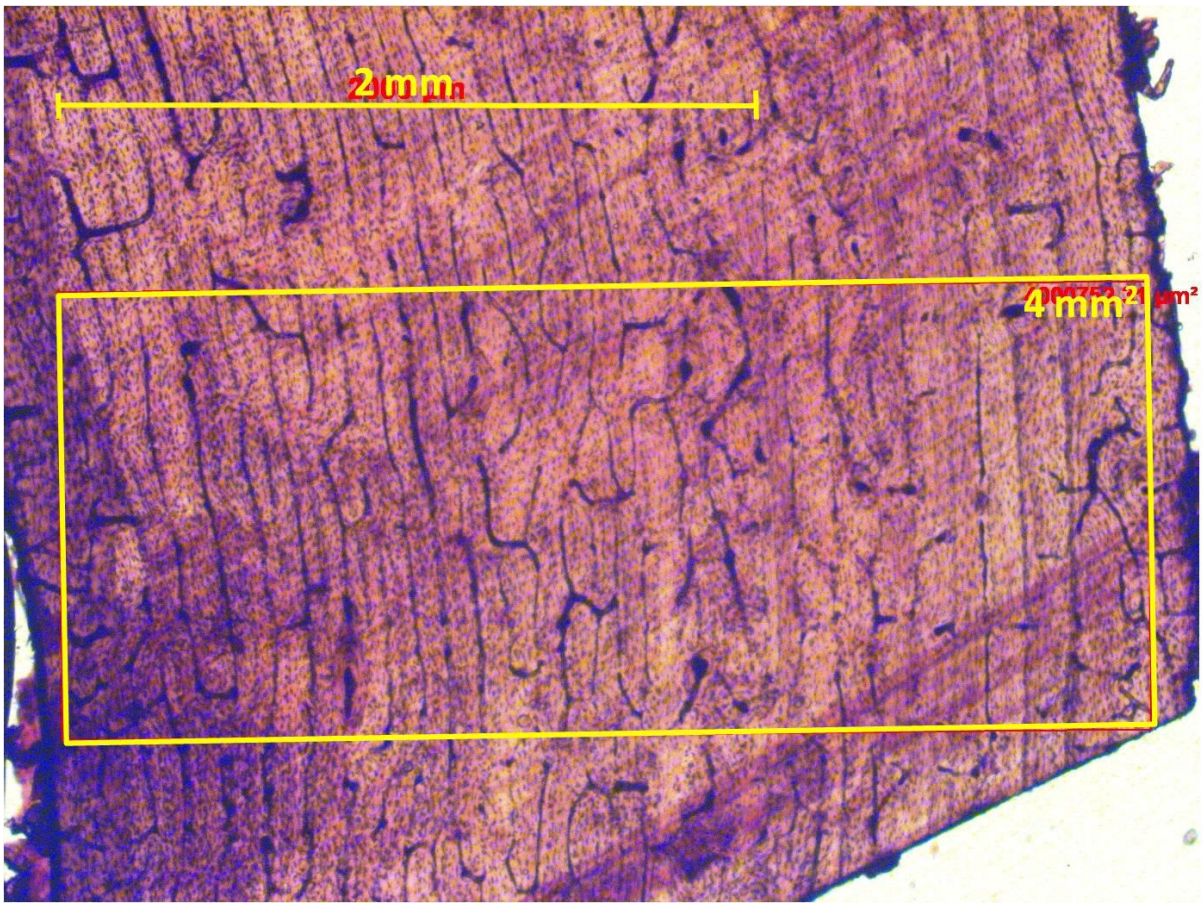

Figure 5.13 A 150 μm thick transverse section of cortex from the mid-diaphysis of an ovine femur, it was cut with a Leica SP 1600 Saw Microtome and stained with Paragon. The scale bar is 2 mm and the box has an area of ~4 mm².

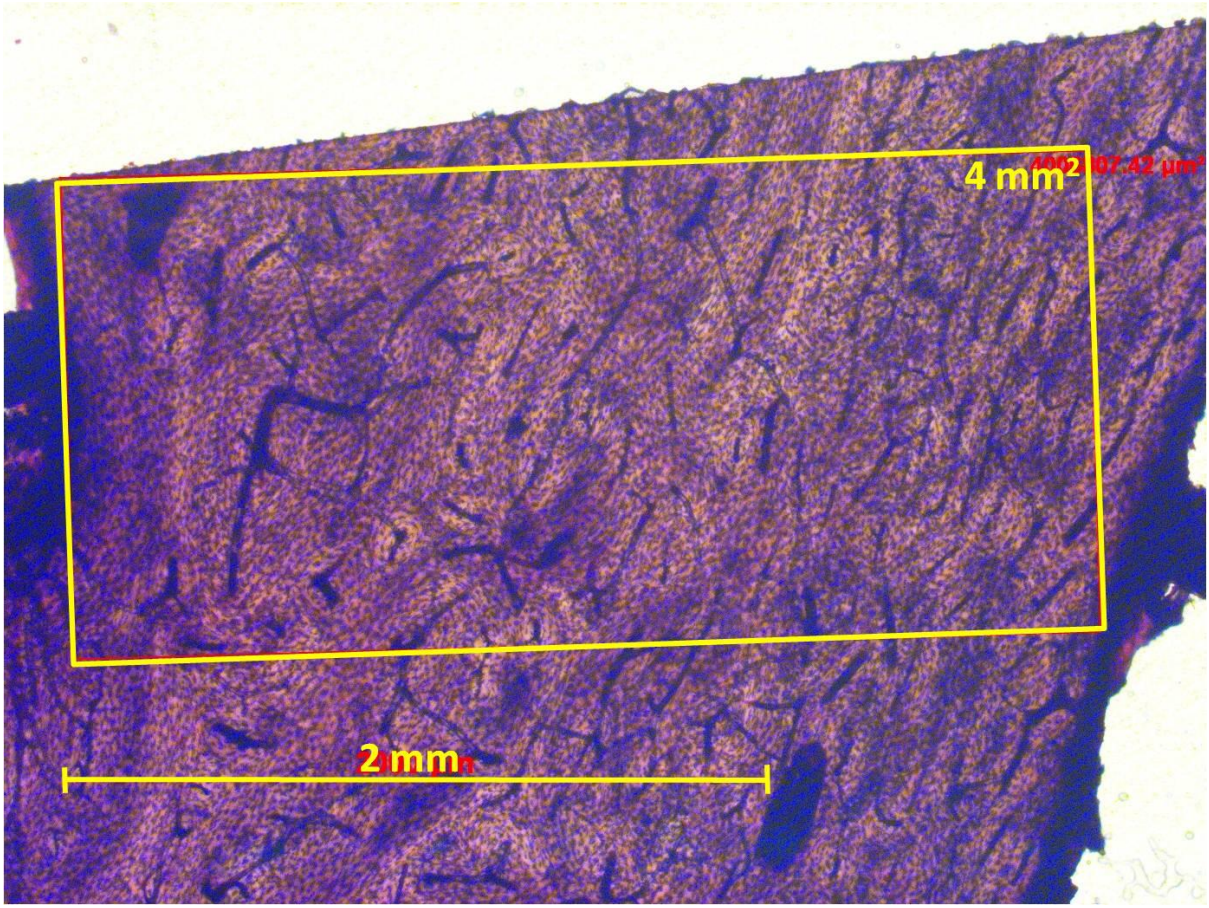

Figure 5.14 A 150 µm thick transverse section of cortex from the mid-diaphysis of an ovine femur, it was cut with a Leica SP 1600 Saw Microtome and stained with Paragon. The scale bar is 2 mm and the box has an area of ~4 mm².

Thus, there are at least two ways the observed variation in chemical composition, density and mechanical properties along the proximodistal axis of long bones can be explained by differences in the *age of the bone material*. There are also other factors which are not related to the age of the bone material and which may partly explain the trends. For example, it could be that the trends are an adaptation to mechanical loading. In the case of the human femur (a bone which does undergo remodelling) it has long been proposed that the density patterns are a structural feature of developmental origin, with density increasing where the greatest load is applied.[229] Les et al., looking at the distribution of material properties in equine metacarpal bones, stated that the variation served to enhance and modulate sagittal bending. They stated that they were unable to address whether the proximodistal variation was "the result of adaptation to applied loads or [was] genetically determined, independent of exercise regimes".[212]

The latter possibility, that the mechanical properties of cortical bone vary at different points because they are adapted through evolution to cope with different forces is interesting to consider. Long bones

experience different forces at different regions and their shapes are adapted through evolution to withstand the loads without experiencing too much strain (stiffness) or without breaking (toughness). It may be that, where the bending stresses are highest, near the mid-shaft, stiff material (highest mineral/collagen ratio) is needed to resist deformation (and thus reduce strain). Where loads are transferred from one bone to the next and cartilage must be protected from destructive forces, it would be the more desirable for both the cortical bone material and the cancellous bone material to be pliant and to absorb energy (toughness); bone materials would need to be less mineralised (i.e. have a lower mineral/collagen ratio) in order to have these properties. A tapered transition from the stiffer (midshaft) bone to the less stiff bone (near the ends) would mean that there would be no sharp interfaces between materials of very different Young's modulus and thus no large stress discontinuities.

If the gradual compositional trends were disrupted, by disease perhaps, it would affect the bone's performance, for example, stiffer 'midshaft bone' located nearer the shaft's end could lead to destructive forces being transmitted to the cartilage/joint each time the bone were loaded. In other situations where the whole bone adapted to new loading conditions, e.g. muscle wastage, the regional mineralisation pattern could possibly change too. If the bone material became highly mineralised in some regions in order to alter localised strains, those regions could suffer reduced toughness and thus become more susceptible to microcracks and/or fracture. These ideas are expanded in the general discussion below.

5.5 Conclusions from Chapter Five

The bone material found at the ends of the long bones has a lower density and different mechanical properties to that found near mid-shaft. Its mineral to collagen ratio, as measured with Raman spectroscopy, is not the same either. Raman analyses of ovine femur bone, and of the equine metacarpal bone, show mineral to collagen ratio-variations occurring in the same anatomical regions as the lower density. The variations may be due to the bone material being less than fully mineralised (i.e. younger bone material) because it is nearer to the growth plate or because more remodelling occurs near the ends of long bones. It could also be that the bone material near the ends of the shaft has adapted to the loads placed on it during life, or it could be that the cortical bone material has been adapted through evolution to have different mechanical properties in certain anatomical areas. If this final explanation is true, if the metaphyseal bone material would never reach the level of mineralisation of diaphyseal bone, then it is adapted to mechanical function in a similar manner to the antler bone material and a tympanic bulla material of the previous chapter but the adaptations that are occurring are less pronounced and occur in more localised regions.

Whatever the reason, the bone material near the ends of the long bones has lower mineral to collagen ratio (as measured by Raman) and has different mechanical properties (as reported in the cited literature). These findings affect the central thesis that the mechanical properties of bone material adapted in differently loaded regions by a subtle tuning of the collagen chemistry which controls the mineral to collagen ratio. It was already shown in Chapter Four how Raman spectroscopy can be used to study this adaptation of bone material mechanical properties, it has now been shown that it can be used to study localised differences within bone organs. The next question to look at is:

- Is mechanical property tuning controlled by the collagen chemistry?

The mechanisms controlling the mineral to collagen ratio of bone material are poorly understood. If it were that some aspect of the collagen chemistry is *causing* the variation in mineralisation, and thus the materials mechanical properties, some evidence for it could be present in Raman spectra (since chemical information can be obtained from both the collagen and mineral phases). The next chapter will be concerned with this collagen chemistry and with the mineralisation mechanisms.

6. What Factors Might Determine the Ratio of Mineral/Collagen?

6.1 Introduction

It has been discussed in previous chapters how the mechanical properties of bone material can vary considerably as a function of mineralisation and can be sensitive to even small variations.[198,216,237] It has also been stated that nature varies the level of mineralisation to create bone material that is suited to its particular function. However, the mechanisms that control the level of mineralisation are not understood. This chapter explores the hypothesis that the bone mineral volume fraction is guided by some feature of the collagen chemistry and this chemistry can be elucidated with Raman spectroscopy. In order to probe the collagen chemistry the amide I band is closely analysed (this band is especially sensitive to collagen secondary structure).[92] The elucidation of the control mechanism, apart from being interesting from a biochemical point of view, could provide therapeutic targets for the management of bone conditions i.e. enabling the control of bone material's mechanical properties.

The starting point for the investigation is the inspection of the Raman collagen band *profiles* from bone materials that have been adapted through evolution to perform different functions in different species. In order to investigate whether similar collagen chemistry changes are ubiquitous whenever nature must tune the mechanical properties of bone (i.e. whenever the collagen to mineral ratio is adapted) and to demonstrate the differences were not related to genetic differences between species, the study was extended to different samples of functionally adapted bone material from a single individual (a 1 year old red deer stag). It was shown in the previous chapter that cortical diaphyseal bone has larger mineral to collagen ratio than metaphyseal bone, it was also discussed how this may be an adaptation to deal with different loading regimes analogous the functional adaptation at the skeleton level. In order to investigate if the compositional difference along the proximodistal axis is mediated by collagen chemistry the amide I band profiles of an equine metacarpal bone were analysed.

A second series of experiments were performed using cortical bone material from different strains of chickens, broilers and layers. Broilers and layers have different phenotypes, broilers are larger than layers and have denser bones; they are bred for their meat whereas layers are bred to lay eggs. Raman analysis was performed in order to investigate if the differences in bone mineral density had an associated difference in collagen chemistry.

6.2 Materials and Methods

Bone Samples

Functionally Adapted Bones

The first sample-set used in this study comprised the functionally adapted bone materials from different species which were discussed in from Chapter Four above: antler (from a red deer – *Cervus elaphus)*, 'standard' bone material from the femur of a sheep (it was from the mid diaphysis of the femur of a skeletally mature Welsh Mule domestic sheep - *Ovis aries*) and the highly mineralised tympanic bulla bone material (from a Fin Whale - *Balaenoptera physalus*), metacarpal bone from a thoroughbred racehorse (*Equus callabus*), both the dentine and cementum from the tusk (incisor tooth) of a narwhal (*Monodon monoceros*) and rostrum bone from the skull of a Beaked Whale (*Mesoplodon densirostris*). There was one sample (n=1) of each.

In order to test the hypothesis that amide I band profile differences are due to species variation rather than functional adaption, three types of bony material from an individual (n=1) red deer were analysed. They were antler bone, standard (metacarpal) bone and highly mineralised tympanic part of the skull from a one year old red deer stag (*Cervus elaphus)*. The density of these three types of bone materials were measured with the pQCT instrument and found to be 864 mg cm^{-3}, 1318 mg cm^{-3} & 1568 mg cm^{-3} respectively. A thorough inspection of amide I regions of the spectra discussed in the Chapter Five (the spectra taken from different points along the proximodistal axes) was also undertaken.

Chicken Bones

The first set of chicken bones probed comprised 12 chicken humeri; 7 from broiler chickens and 5 from layer chickens. The broilers all came from came from the same batch on a single farm and were slaughtered together. The layers all came from came from the same batch on a different farm and were slaughtered together. The average density of the broiler-humeri bone material (measured with the pQCT machine) was 1323.3 ± 26.2 mg cm^{-3} and the average layer-humeri bone material was 1066.2 ± 40.2 mg cm^{-3}.[XVIII]

[XVIII] The density values are averages ± standard deviations. The density difference between the broiler-bones and layer-bones are statistically significant to a 95% confidence level.

The other sample set was 20 chicken tibiotarsi bones (n = 10 broilers and n = 10 layers). The broilers all came from came from the same batch on a single farm and were slaughtered at the same time. The layers all came from came from the same batch on a different farm and were slaughtered together. The average density of the broiler-tibiotarsi bone material was 1286.4 ± 52.8 mg cm^{-3} and the average density of the layer-bone material 1222.2 ± 42.0 mg cm^{-3}.

Data Collection/Processing

The spectra were recorded for 60 x 1 s exposures (60 s) using the Raman instrument described in Chapter Three. The fluorescence backgrounds of the amide I bands were removed using the Lieber[185] method described above (1585 cm^{-1} - 1730 cm^{-1}, 2nd order polynomial). It was shown in Chapter Four that the collagen bands of the different bone materials have different intensities, hence it was necessary to normalise the collagen bands to discern profile differences. The amide I bands were normalised by setting the height of the first peak (from approx. 1620 cm^{-1} - 1660 cm^{-1}) to 1. This normalisation method meant the heights and the relative positions of the bands were changed but the profiles were not.

For some of the highly mineralised samples (in the first two sets), the collagen bands were very weak and so when they were normalised they were very noisy. These spectra were smoothed using the Savitzky-Golay filtering function in OriginPro 8 (OriginLab, Northampton, Massachusetts, U.S.A.). The Savitzky-Golay filter performed a local polynomial regression (of degree 2) and determined the smoothed value for each data point. All other specimens had easily measurable collagen bands which did not require smoothing.

6.3 Results

Functionally Adapted Bones

The amide I bands of the functionally adapted bone material from the different species are shown in Figure 6.1. The red spectra from the standard bone materials (ovine femur and equine metacarpal bone) show the profile of a standard amide I band which is well known from the literature.

The data show that the amide I band comprises three distinct peaks and that the relative ratio of the three peaks change along with the level ratio of mineral to collagen. The change is consistent, with the central peak much reduced for the highly mineralised bone, increasing for the standard bone and most intense for the less mineralised bony materials. If the normalisation method used was such that middle peaks were set to be equal then a similar, albeit more visually awkward, trend would be seen, with the intensity of the two outer peaks increasing with mineralisation.

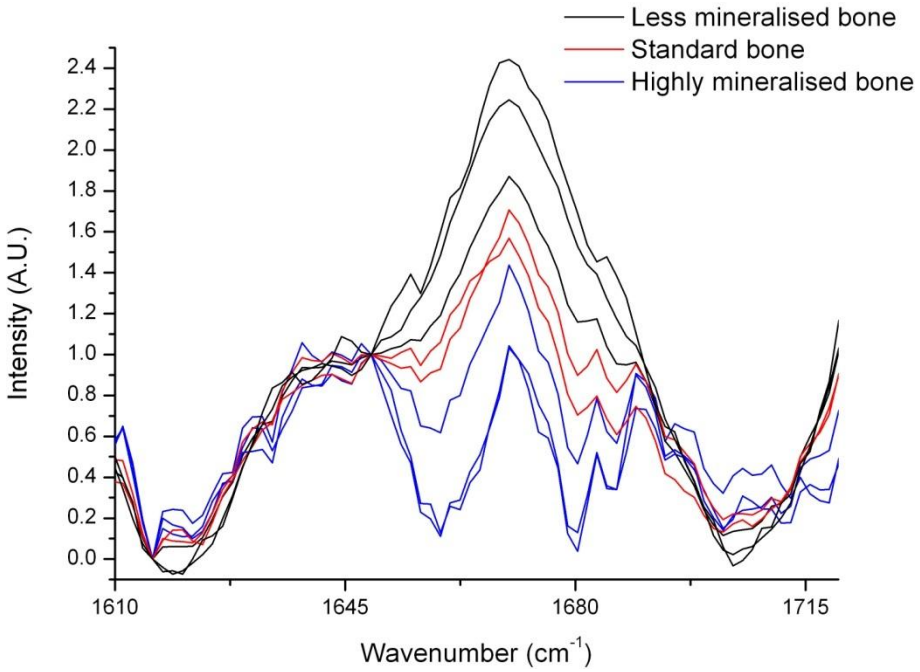

Figure 6.1 The amide I Band; samples are (middle peak - from top) Narwhal Cementum, Narwhal Dentin, Red Deer Antler, Ovine Femur, Equine Metacarpal Bone, Fin Whale Tympanic Bulla and Porpoise Periotic Bone/Beaked Whale Rostrum (same height).

The Raman spectra of antler, metacarpal bone and periotic bone from a one year old red deer are shown in Figure 6.2. The spectra are normalised to the dominant phosphate band and the relative intensity of the collagen bands can be seen to vary. The amide I regions of the three spectra are shown in Figure 6.3, as before the amide I band comprises three distinct peaks and the profile of the band changes along with the level ratio of mineral to collagen. Again, the change is consistent, with the shoulders of the central peak most much reduced for the highly mineralised bone and most intense for the least mineralised antler bone.

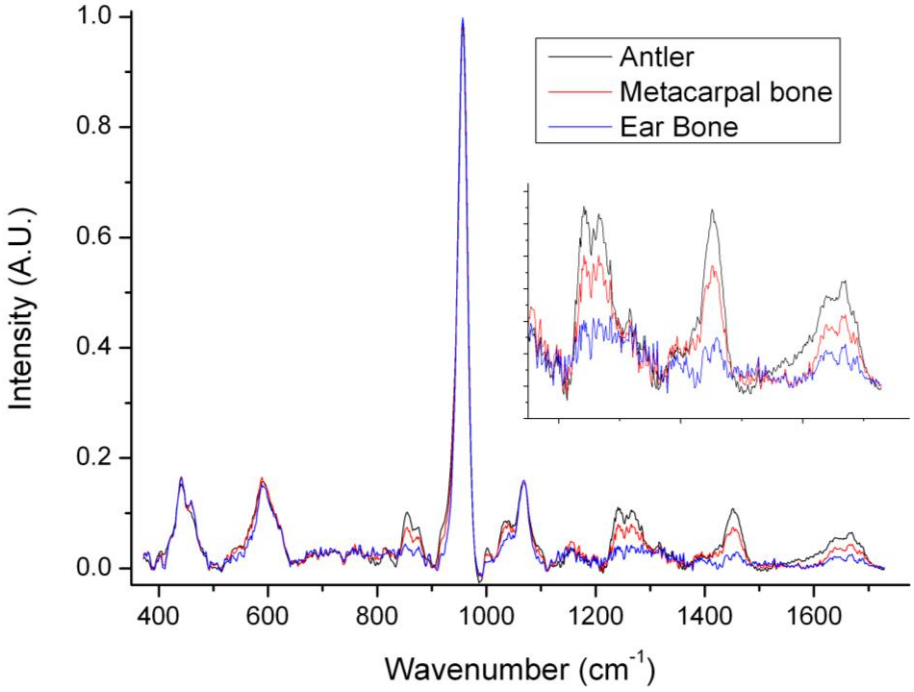

Figure 6.2 Bony materials with widely varying levels of mineralisation from an individual red deer.

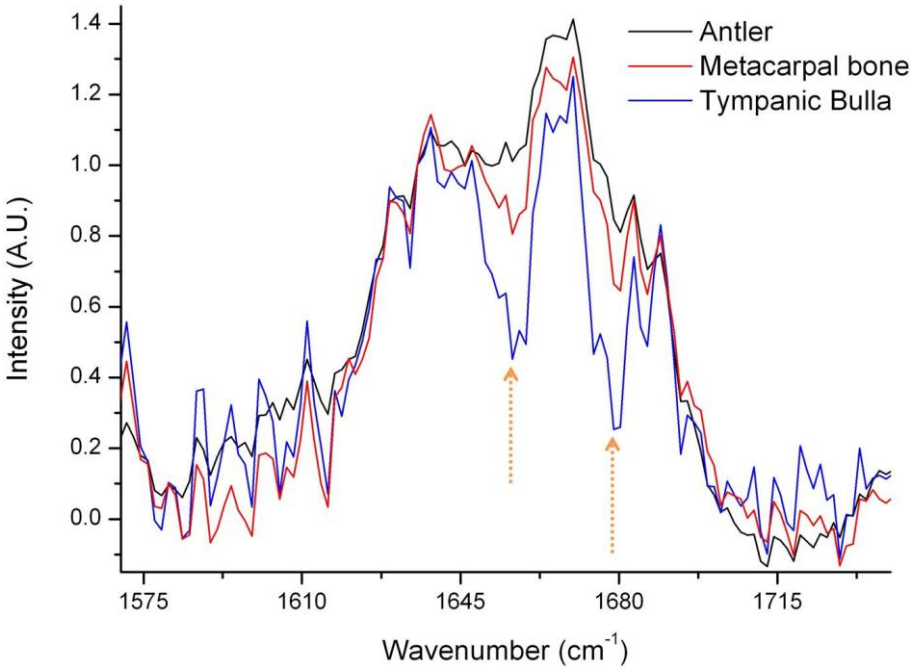

Figure 6.3 Shape of the amide I band shows subtle changes with the shoulders of the middle peak decreasing in relative intensity with increasing mineralisation (i.e. from periotic bone, to standard metacarpal bone, to antler bone).

Figure 6.4 is very similar to Figure 5.3 from Chapter Five; spectrum 1 is from the metaphysis and spectrum 5 is from near the middle of the diaphysis, these particular spectra were chosen because they lay on trend line in Figure 5.3, spectrum 1 lay on the part with large slope (1 cm from the start) and spectrum 5 (5 cm from the start) lay on the flat part of the trend line. Thus they illustrate the difference in the mineral to collagen ratio between metaphysis and diaphysis but are not extreme data points (outliers). The difference in bone material density at these two points is ~120 mg cm^{-3}, about half the difference between broiler humeri/layer humeri or between red deer standard bone/red deer periotic bone (~250 mg cm^{-3}). The amide I band at the two points is shown in Figure 6.5, they are almost identical.

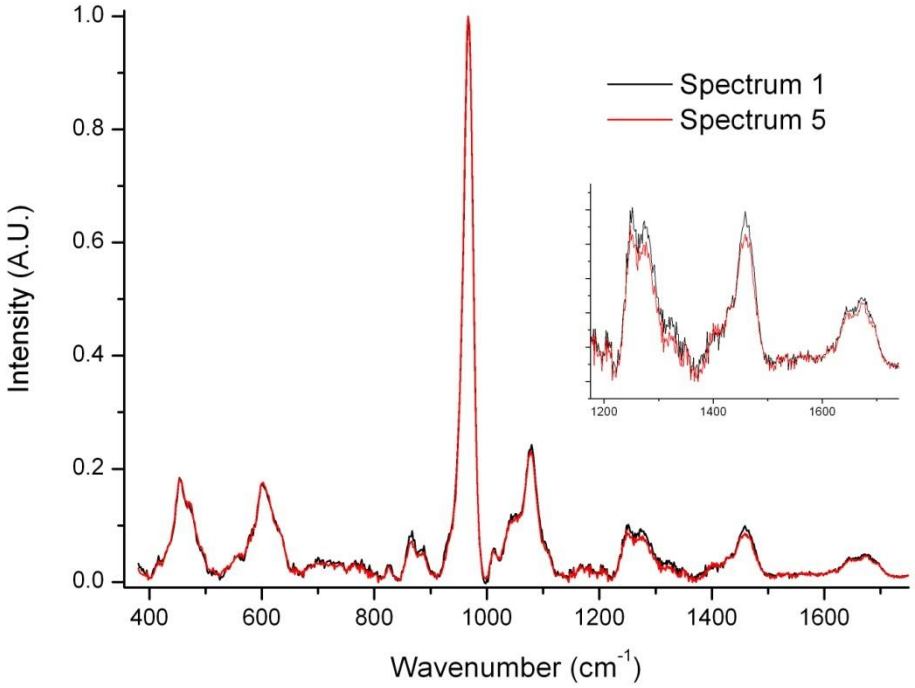

Figure 6.4 Spectra from the diaphysis and metaphysis of the equine metacarpal bone.

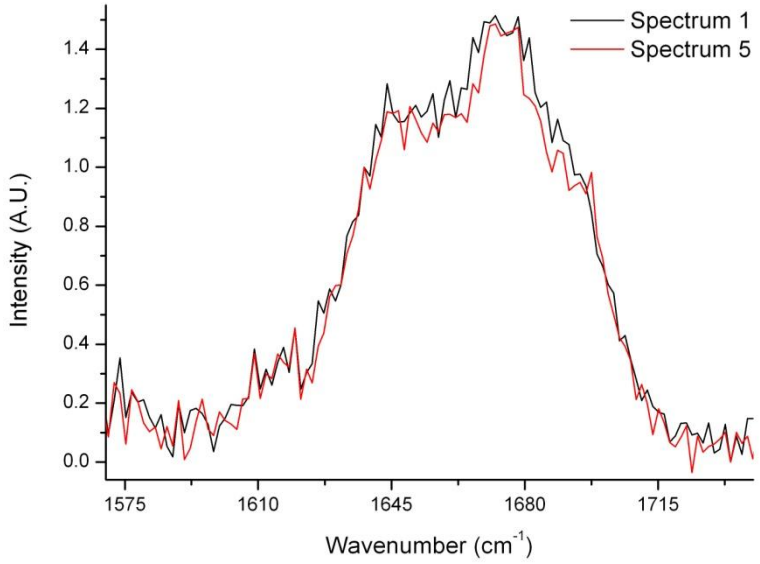

Figure 6.5 The amide I bands of metaphyseal and diaphyseal bone from an equine metacarpal bone.

Broiler and Layer Chickens

The Raman spectra of the 7 broiler humeri and the 5 layer humeri are shown in Figure 6.6 (a) and the average spectra are shown in Figure 6.6 (b). The average mineral to collagen ratio (ν_1 phosphate to ~900 cm^{-1} proline/hydroxyproline) is only slightly larger for the broiler compared to the layers (32 ± 2 versus 29 ± 3, $P < 0.05$) even though the average density difference (~250 mg cm^{-3}) is almost identical to the different between the standard metacarpal bone and the periotic bone in the red deer (~250 mg cm^{-3}). The amide I bands of the broiler and layer humeri are shown in Figure 6.7, the profiles of the bands are almost identical.

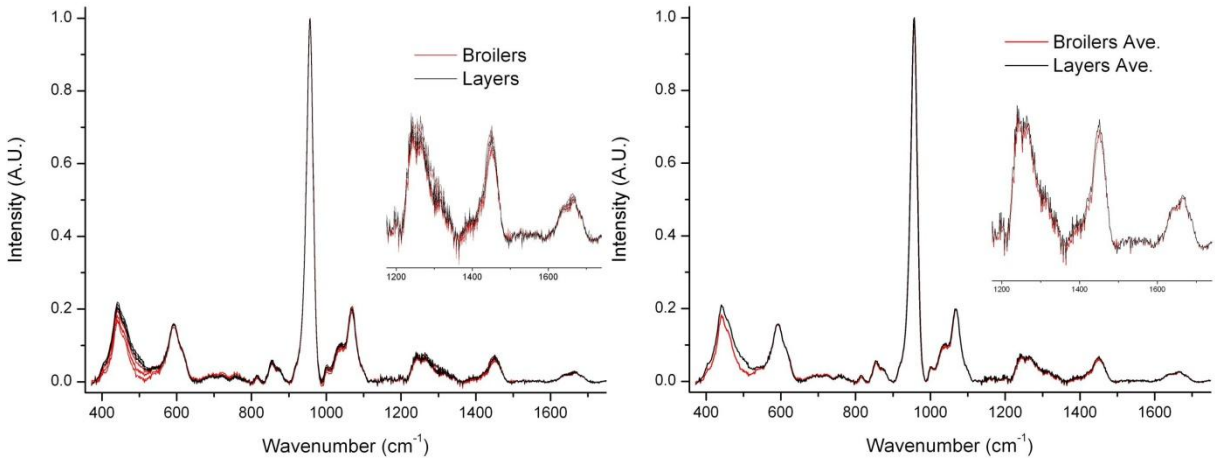

Figure 6.6 (a) on the left shows the spectra all of the broiler humeri and all the layer humeri. Figure 6.6 (b) on the right shows the average of the broiler humeri and the average of the layer humeri. The stand out difference between the Raman spectral profile of the broiler humeri and the Raman spectral profile of the layer humeri occurs near the phosphate band at ~445 cm^{-1}, the symmetric bending (ν_2).

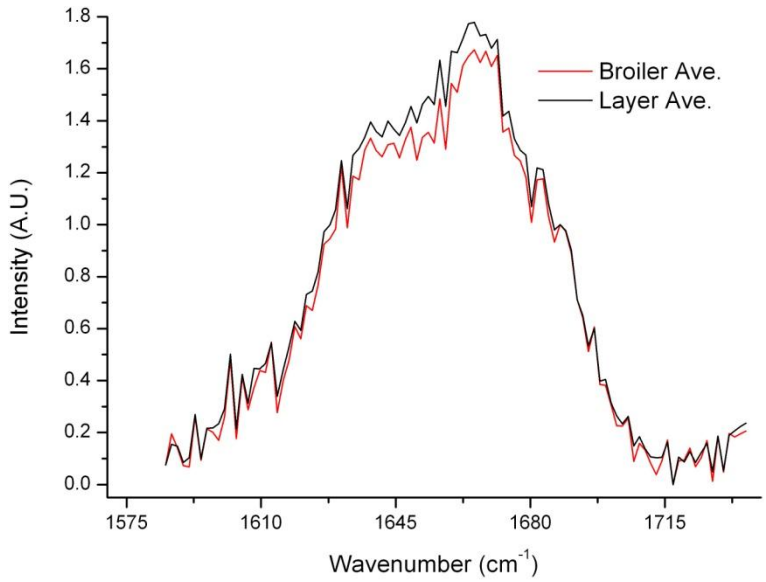

Figure 6.7 shows that the average broiler-humeri amide I band and the average layer-humeri amide I band have almost identical profiles.

The Raman spectra of the 10 broiler tibiotarsi and the 10 layer tibiotarsi are shown in Figure 6.8 (a), the average broiler tibiotarsus spectrum and average layer tibiotarsus is shown in Figure 6.8 (b). The spectra do not show any major differences, there is no statistical difference between the average mineral to collagen band (ν_1 phosphate to ~900 cm^{-1} proline/hydroxyproline) ratios (28 ± 3 versus 29 ± 3). It can be seen in Figure 6.9 that the average broiler tibiotarsus amide I band and the average layer tibiotarsus amide I band are almost identical.

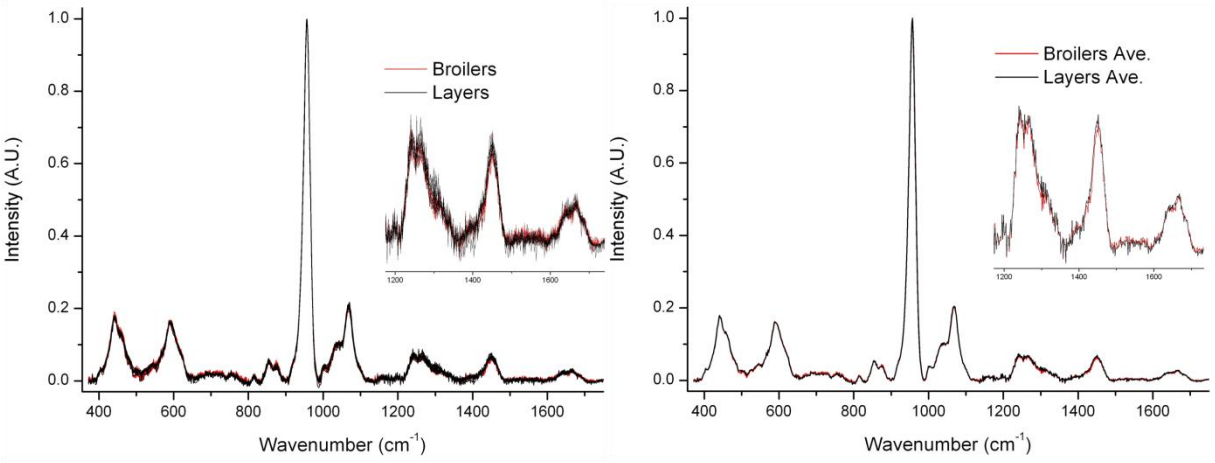

Figure 6.8 (a) on the left shows the spectra all of the broiler tibiotarsi and all the layer tibiotarsi. Figure 6.8 (b) on the right shows the average of the broiler tibiotarsi and the average of the layer tibiotarsi.

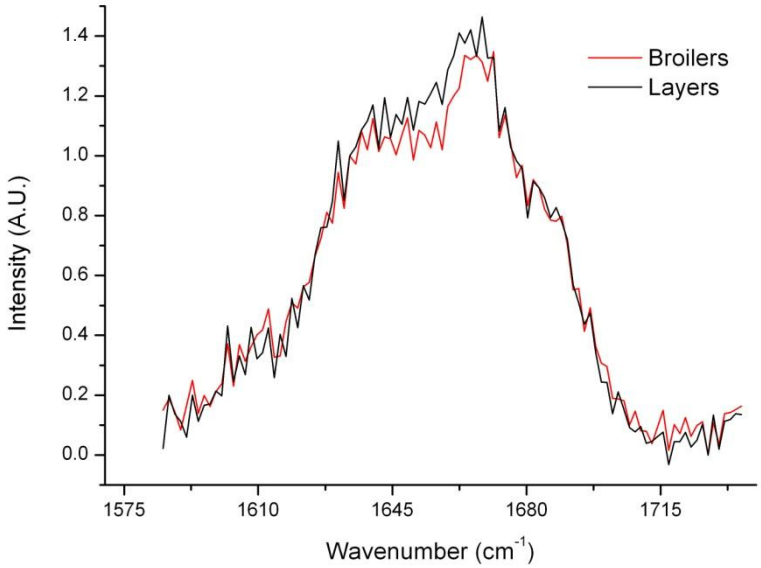

Figure 6.9 shows that the average broiler-tibiotarsus amide I band and the average layer-tibiotarsus amide I band have almost identical profiles.

6.4 Discussion

Functionally Adapted Bones

The spectral profile of the amide I band is dramatically different in the extreme bone materials which have been adapted through evolution to perform different functions. The intensity ratios of the three peaks which comprise the band vary in a systematic way; the relative intensity of the middle peak decreases with increasing mineralisation. It has long been hypothesized in the IR absorption spectroscopy literature (Lazarev et al. - Ref. 238) that the three distinct peaks in the amide I band of collagen are the vibrations of carbonyl stretches in three slightly different chemical environments,

namely three environments along each polytripeptides chains with the period 'Gly-X-Y' (Figure 6.10 and Figure 6.11). The intensity of the O_1, O_2 and O_3 carbonyl-stretches will be affected by their local chemical environment, i.e. by the character of X and Y. The amide I Raman bands in Figure 6.1 also comprise three distinct peaks and it can be hypothesized that the relative intensity differences are caused by the nature of X and Y.

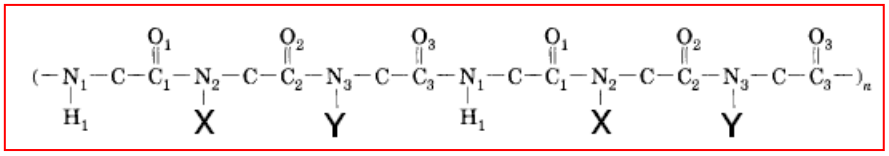

Figure 6.10. Schematic diagram of the three chemical environments of the carbonyl groups in a polytripeptide chain.

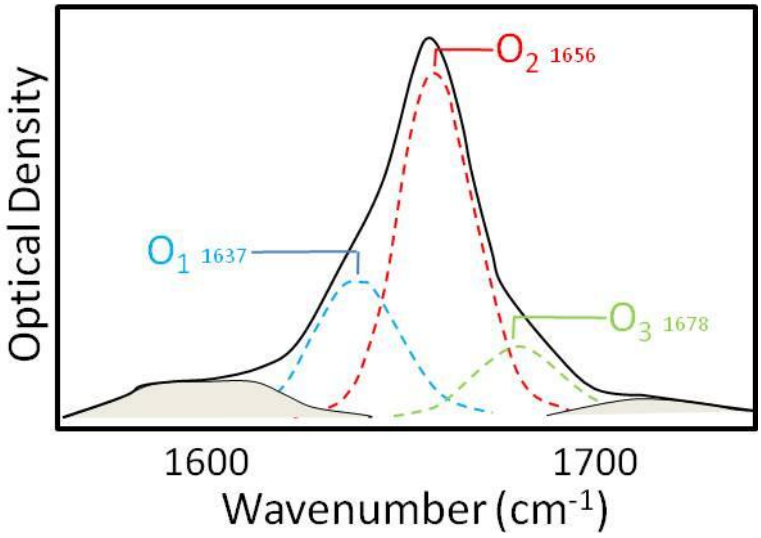

Figure 6.11 shows the components of the amide I band of native collagen from rat skin as described in Lazarev et al. (1985).[238]

The amide I band differences (Figure 6.3) measured for the functionally adapted bone materials from the red deer were not as pronounced as those for the extreme bones (Figure 6.1). The profiles did vary in a systematic way with the relative intensity of the shoulders on the middle peak decreasing with increasing mineralisation. Further analyses of the bands have suggested that this relative change may be caused by a relative variation in the intensity/width of the O_1 band. Again, the intensity of the O_1, O_2 and O_3 carbonyl-stretches will be affected by their local chemical environment, i.e. by the character of X and Y (Figure 6.10. and Figure 6.11).

No differences in the amide I band profile were measured between the metaphyseal and diaphyseal bone (Figure 6.5) from the equine metacarpus. As was shown in Chapter Five, the mineral to collagen ratio and the density do vary along the metacarpal cortex (a differing cortical thickness should not

cause a density differences when a pQCT instrument is used). It is possible that the varying mineralisation along the cortex is associated with variation in collagen chemistry but that the differences are smaller than those in the functionally adapted bone materials (e.g. the density difference was ~120 mg cm^{-3} as opposed to ~250 mg cm^{-3} for the difference between red deer standard bone/periotic bone) and the Raman measurements were not sensitive enough to pick them up.

Broiler and Layer Chickens

The amide I bands of the broiler-humeri and the layer humeri did not show profile changes (Figure 6.7). They also have very similar ν_1 phosphate to ~900 cm^{-1} proline/hydroxyproline ratios (32 ± 2 versus 29 ± 3, $P < 0.05$) even though pQCT readings suggest they have different densities (the density difference between the layer humeri and the broiler humeri was of the same order as the difference between the functionally adapted deer bone material, ~250 mg cm^{-3}). The amide I bands of the broiler-tibiotarsi and the layer tibiotarsi did not show profile changes either (Figure 6.9) though this was not surprise since their mineral to collagen ratios were almost identical and their density difference between the sample sets was not as large (~60 mg cm^{-3}). These results from the phenotypically different strains of chicken are hard to reconcile; if the layers and broilers had the same level of mineralisation (Figure 6.6 (a) & (b), Figure 6.8 (a) & (b)) and if they do not have large differences in the number of resorption cavities (Micrographs - Figure 6.12) then where does the density difference come from?

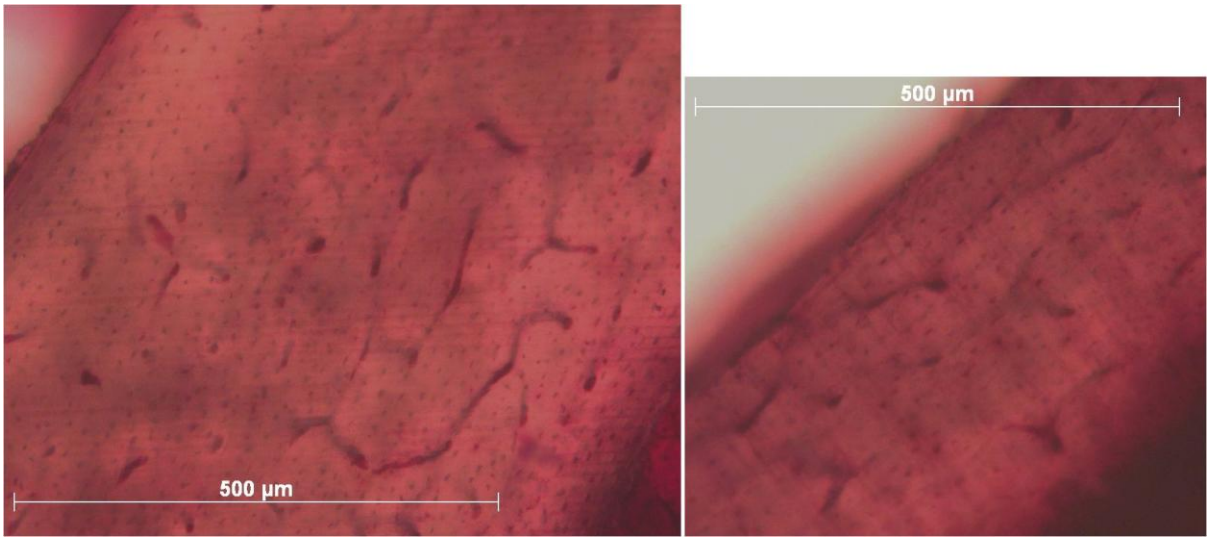

Figure 6.12 Transverse sections (150 µm thick) cut from cortices of a broiler-tibiotarsus (left) and layer-tibiotarsus (right). They were sectioned with a Leica SP 1600 Saw Microtome and stained with Paragon.

If a projection x-ray radiation technique had been used to measure the density, one could hypothesize that the different cortical thicknesses (Figure 6.12) caused a spurious density reading but this should not be the case with a pQCT instrument. Perhaps the Raman spectral profile differences that were measured between the broiler humeri and the layer humeri near the 445 cm^{-1} phosphate band indicate that there is chemical difference in the mineral phase of the bone material in the two strains. Another possibility is that the mineralised collagen fibrils are identical in both strains (identical Raman mineral to collagen ratios) but they are packed more closely together in the broilers and hence the density of their bone material is higher.

These data show that for the large differences in mineral to collagen ratio in the functionally adapted bone materials there is an associated difference in the collagen chemistry (amide I profile changes) though they do not prove that the mineralisation differences are *caused* by the collagen. Though the spectra do contain information about what the profile change means at the molecular level (Figure 6.10 & Figure 6.11), chemical analysis of the collagen from the different bone samples will be needed to confirm what the profile changes actually mean at the molecular level. Further research will be needed to determine if they are related to the chemical mechanism which controls the bone mineral fraction. If it is the case that the mineralisation of bone material, and thus its mechanical properties, are controlled by aspects of the collagen chemistry they will offer new targets for pharmaceutical research.

6.5 Conclusions from Chapter Six

The collagen chemistry is different in bone materials which have been adapted through evolution to perform different functions. The collagen chemistry in standard bone samples which have very different densities may or may not have different collagen chemistry, the Raman measurements presented here did not measure it. What the amide I band profile changes mean at the molecular level will be looked at in future work.

The central thesis is concerned with the collagen mediated adaptation of the mechanical properties of bone material at differently loaded regions (through the tuning of the mineral to collagen ratio); the data presented here did not prove that aspects of the collagen chemistry *cause* the bone mineral volume fraction to vary but they did show that the collagen has some chemical difference in bone materials adapted for different functions. These points will be discussed further in the next chapter.

7. General Discussion & Future Work

7.1 General Discussion

"Clearly then if one wishes to maintain in a great giant the same proportion of limb as that found in an ordinary man he must either find a harder and stronger material for making the bone, or he must admit a diminution of strength in comparison with men of medium stature…"

Galileo Galilei[1]

This thesis explored whether the mechanical properties of bone material are adapted in differently loaded regions by subtle tuning of the collagen chemistry by looking at three related hypotheses. The work led to the findings that Raman spectral features of bone material correlate with mechanical properties over a wide range of mineralisation (the mechanical-property data was from the literature). That the same spectral features vary in a systematic way *within* equine metacarpal bones and ovine femora, and that large differences in mineralisation are associated with changes in collagen chemistry. Some points related to the experimental methodology will be considered before the results are discussed.

Methodology

It is well known that the mechanical properties of bony materials are mostly explained by the weight ratio of mineral component to organic component.[7] It has been described above (pg 40 & pg 58) how selectively damaging the organic phase of the bone, and not the mineral phase, has a deleterious effect on its mechanical properties.[78,79] Raman spectroscopy can be used to measure the mineral/collagen ratio and inspect the state of the collagen non-destructively. It has advantages over many other analytical techniques in that it needs little sample preparation, can be used in the presence of water and uses non-ionizing radiation. The Raman instrument used for this thesis was well suited to the study of bone; the wavelength of the light was short enough to get useable Raman signal (intensity of Raman signal is proportional to the *frequency* of the scattered light to the power four) but not so short that the Raman signal was totally dominated by fluorescence (shorter wavelengths, higher energy and more likely to bridge *electronic* energy gap). The detection system also worked well; usable spectra could be obtained after tens of second's accumulation.

The fluorescence background was removed from each spectrum using semi-automated software; the experimentalist had to choose the parameters of the polynomial curve that was to be subtracted. This adding of subjective values into the experimental method was not ideal but no perfect methods for

removing fluorescence yet exist and the Lieber method is widely used (the paper introducing it has been cited 120 times since 2003).[185]

The data in Chapter Four showed a relationship between Raman spectra and the functionally adapted mechanical properties for a bone samples from a range of species. Though the relationship was strong ($\mathbf{r^2}$ = 0.93) and statistically significant (**p** = 0.0004) it would have been interesting to probe a larger number of extreme samples if they were available.

Chapter Five reported systematic changes in cortex composition along the length of two different long bones. The trends along each bone were illustrated with pQCT scans and hundreds of Raman spectra. When added to the large body of literature reporting mechanical property and density changes along long bones in a large number of long bones (including human, canine and bovine femora, human and bovine tibiae, and equine metacarpal) the evidence indicates that the phenomenon may be universal. New equipment with a large moving sample stage has recently been obtained at our laboratory; it enables the quick collection of many Raman spectra along the proximodistal axes of bones and will allow this question to be investigated further.

The more subtle amide I band *profile* changes that were the subject of Chapter Six show that the molecular environment of the carbonyl stretches is different for collagen chains in eight functionally adapted bones with very different levels of mineralisation. The amide I band profiles were also very different in the functionally adapted bone from the red deer stag although this experiments will need to be repeated for more stag specimens. The experiments showed that at the level of sensitivity of Raman spectroscopy, the chicken bones with very different densities are chemically identical; further work with different experiment modalities will be needed to investigate these samples.

Data

Raman Spectroscopy as a Measure of Mechanical Properties

In Chapter Five, it was stated that the Young's modulus of cortical bone from the limbs of fully grown mammals has a range of 16.7-22.9.[7] If we suppose that the correlation equation from Figure 4.3 holds for bone material in this range, then (for bones with Young's modulus of 17 and 22) the phosphate ν_1/amide I ratio can be calculated to be ~12 (Raman ratio 27.5 and 39.5 respectively). This Raman ratio difference is comparable to that between deer antler and ovine femur and should be measurable. This is important because for bone material Young's modulus is highly correlated with strength and a Young's modulus difference of that order (17 and 22) indicates a bending strength increase of 26% (188 and 237 MPa).[239] This is especially significant because Raman spectroscopy has the potential to be developed as a safe, non-invasive technique for use *in vivo* (Chapter Two); *in vivo* mineral to collagen measurements with < 4% relative error have already been reported (Ref. 172).

Regional Mineral to Collagen Variation

At the very beginning of this thesis it was stated that "the factors which determine whether the bones can fulfil these demands, and withstand the forces put on them, can be divided into two broad categories; structural/architectural properties and material properties." In reality, the properties of the bone material influence the architecture of the bone: e.g. the cortex of an equine metacarpal bone would be thinner if it could be composed of a material that was both tougher *and* stiffer (analogous to the way the properties of metals determine the thicknesses of aircraft fuselages). An example of whole bone structure compensating for material-level mechanical properties has been well documented in the case of young California gulls.[240] Whilst the gulls grow and the bone material comprising their legs and wings matures (increases in stiffness and bending strength) the shape of their bones adapt to compensate. Throughout their development, the gull's legs (which are used from birth) have much larger cross-sectional areas than their wings (which are not used until the gulls are fully grown and ready to fly). The gull's wing bones grow in diameter very quickly just before they start flying.

A possible example of the influence working the opposite way, of anatomical structure influencing the composition of bone material was described in Chapter Five. It was hypothesized that the structure of a horse's foot could mean it is desirable for both the metaphyseal cortical bone material and the cancellous bone material to be less mineralised (i.e. to be more pliant and to absorb more energy).

The interaction between the architecture of whole bones and the mechanical properties of the bone material raises the interesting questions about the bone loss and fragility fractures. If one is losing bone material from a long bone (e.g. due to a remodelling imbalance) the stresses in the long bone will have to increase at certain points (Figure 1.6). Larger stress will result in larger strains. One of the ways strain could be reduced would be if the bones could adapt and change shape.[39] It is known that during aging the cortices of long bones narrow in thickness whilst their diameters widen.[241]

Another method that could be employed to reduce strain would be to increase the stiffness of the bone material (i.e. increase the mineral to collagen ratio). However, whilst 'good' pre-yield properties go up with increased mineral/collagen, 'good' post-yield properties go **down** with increased mineral/collagen (Figure 7.1).[242] This means that the adaptation of bone material (mineralisation) to bone loss may reduce its ability to cope with large (post-yield) forces, e.g. falls.

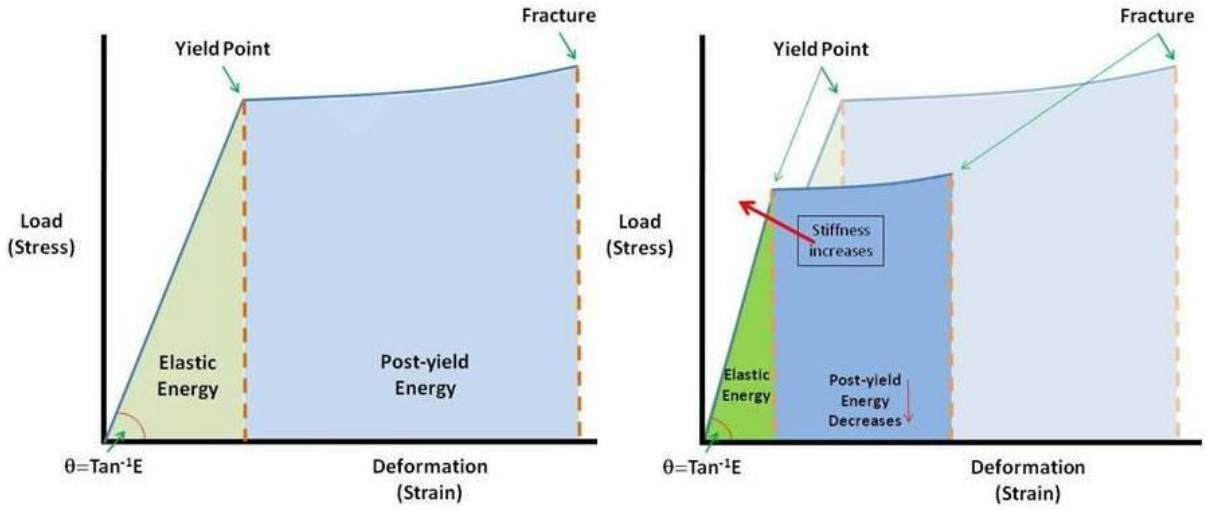

Figure 7.1 shows schematic Stress-Strain plots for two different bony materials. The less stiff material (left) can absorb more energy in the post-yield region before reaching the fracture point. The stiffer material (right) cannot absorb as much energy before fracture.

The localised tuning of mechanical properties (localised tuning of mineral to collagen ratio) within a long bone, like those discussed in Chapter Five, mean that the adaptation of bone material to bone loss may not even be observable in all regions. For instance, a femoral midshaft might increase in diameter to cope with new increased strains (induced by the bone loss) whereas the femoral neck may increase its mineral to collagen ratio. In Chapter Two, a Raman study was described in which cortical bone from the mid-shaft of the femur was homogenized (i.e. milled into small particles) and it was found that the mineralisation (amide I/ phosphate ν_1) did not change with age.[126] It would be interesting to repeat this experiment with bone material from different anatomical regions.

The disruption of the gradual compositional trends by medication, and the relationship between trend disruption and atypical femur fractures may also be interesting to consider.[243] If reduced turnover caused bone material to age and become highly mineralised in regions near the ends of the bone then those regions could suffer reduced toughness and thus become more susceptible to microcracks and/or fracture. It would be interesting to look at the Raman mineral to collagen trend along the femurs of people who have been taking bisphosphonates for a number of years, especially individuals who have suffered low energy femur fractures in the subtrochanteric region.

The adaptation of mineralisation to changes in bone structure/architecture is interesting to consider, so too is the reverse case; the adaptation of whole bone architecture to bone material mechanical properties. For example, it is interesting to consider a situation where the mineral to collagen ratio (and thus Young' modulus) of bone material were therapeutically *reduced*. If the body's natural response to reduced bone material stiffness was to increase the second moment of area (as in the case

of the Californian gulls) then paradoxically the whole bone strength could be *increased* by decreasing the mineral to collagen ratio (since cross-sectional area accounts for a large amount of whole bone strength). For murine femora, variations in cross-sectional geometry account for 2.4 times more than variations in density and 1.8 times more than other factors (bone 'quality').[244] Thus, attempting to engineer the shape of bones may be as worthwhile as attempting to alter the bone material's mechanical properties (this is in addition to the increase in 'good' post-yield properties (i.e. toughness) the less stiff bone material would have).

Understanding Amide I Variation

The results presented in Chapter Six show that the relative intensity of the peaks which comprise the amide I band (i.e. the relative intensity of the O_1, O_2 and O_3 carbonyl-stretches) vary from bones with large differences in mineral to collagen ratio. This means that the local molecular environment the O_1, O_2 and O_3 carbonyl-stretches are different in the different bones. It was discussed that this molecular environment will be influenced by the by the nature of the amino acid side-chains (X and Y in Figure 7.2) but since it is unlikely that the primary protein structure differs for different bone collagens, another candidate must be found. One possible hypothesis is that the post-translational modification of the collagen differs in the different bony materials.

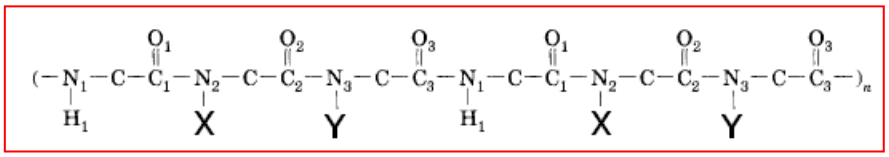

Figure 7.2. Schematic diagram of the three chemical environments of the carbonyl groups in a polytripeptide chain.

The addition of a hydroxyl-group to X or Y, i.e. the hydroxylation of the collagen amino acids in those positions, would change the chemical environment of the O_1, O_2 and O_3 carbonyl-groups (in Figure 7.2) and may be a good candidate for a mineralisation control-mechanism. Figure 7.3 shows a tropocollagen molecule with many hydroxyproline residues in side view and end on.[36] The hydroxyl-groups can be seen to be protruding radially out from the collagen. These tropocollagen molecules group together to form collagen fibres, thus the physiochemical environment inside the fibril (between the molecules) or along the outsides of the fibrils (the out-facing sides of the molecules) would be strongly affected by the presence (or lack) of the polar hydroxyl-groups. Experiments have shown that surfaces covered in hydroxyl-groups are very conducive to nucleating and growing hydroxyapatite crystals; if similar mechanisms occur on the surfaces of the tropocollagen, then it could be implicated in the differing levels of bone mineralisation.[245,246]

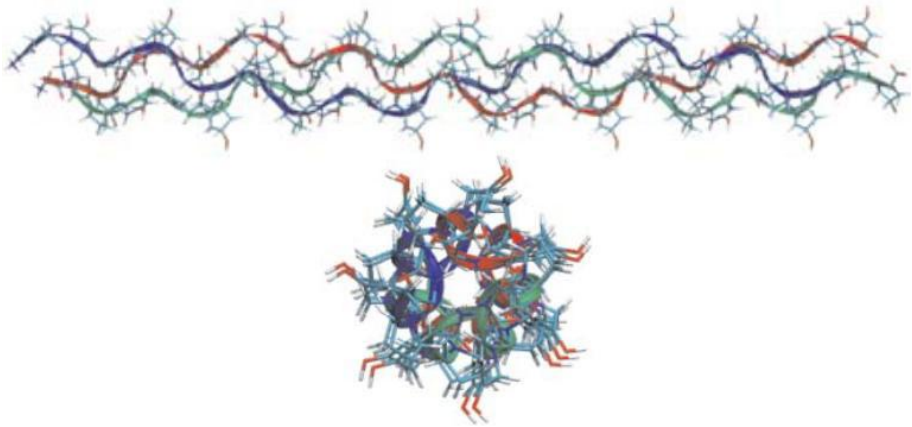

Figure 7.3 a tropocollagen molecule side view and end on; the hydroxyl-groups can be seen protruding out from the molecule. Diagram from ref. 36.

The addition of a hydroxyl-group to proline is not the only way selective hydroxylation can be hypothesized to affect mineralisation. The hydroxylation of lysine is known to be involved in the crosslinking between the tropocollagen molecules in the collagen fibrils. This is illustrated by genetic disorders of collagen such as Ehlers-Danlos syndrome type VI; for sufferers of this disorder the level of hydroxylation is reduced to 17% of normal in bone due to a deficiency in the enzyme lysyl hydroxylase and connective tissue dysfunctions such as osteoporosis follow. Conversely, over-hydroxylation of collagen is seen in several forms of osteogenesis imperfecta, it results from imperfect triple helix formation and means the mineralisation of the bone material is defective.[18]

That the level of mineralisation may be controlled through varying the hydroxylation of lysine, and thus varying the amount of cross-linking, may be in agreement with an older convention from I.R. and Raman spectroscopy. This convention is to use changes in the in the amide I band profile to measure changes in the collagen secondary structure and thus indirectly measure collagen cross-linking.[92]

Chemical analysis will be needed to confirm that the differences in the spectral profile of the amide I band are related to post-translational modifications.

Central Thesis

The data in this thesis begin to build a picture of bone material composition (and thus bone material mechanical properties) as a variable which evolution could act on to deal with local mechanical loading environments. The shape of each bone is evidently a reaction in evolutionary time to the influence of mechanical loading. Since bone material composition can change in evolutionary time (move up and down the red line in Figure 7.4), it is probable that localised composition adaptation is important too. It has been shown that the organic phase is chemically different for bones along the red line; chemical analysis of these bones will need to be added to Raman spectroscopy data presented here in order to ascertain whether these differences *cause* the variation of the mineral to collagen ratio.

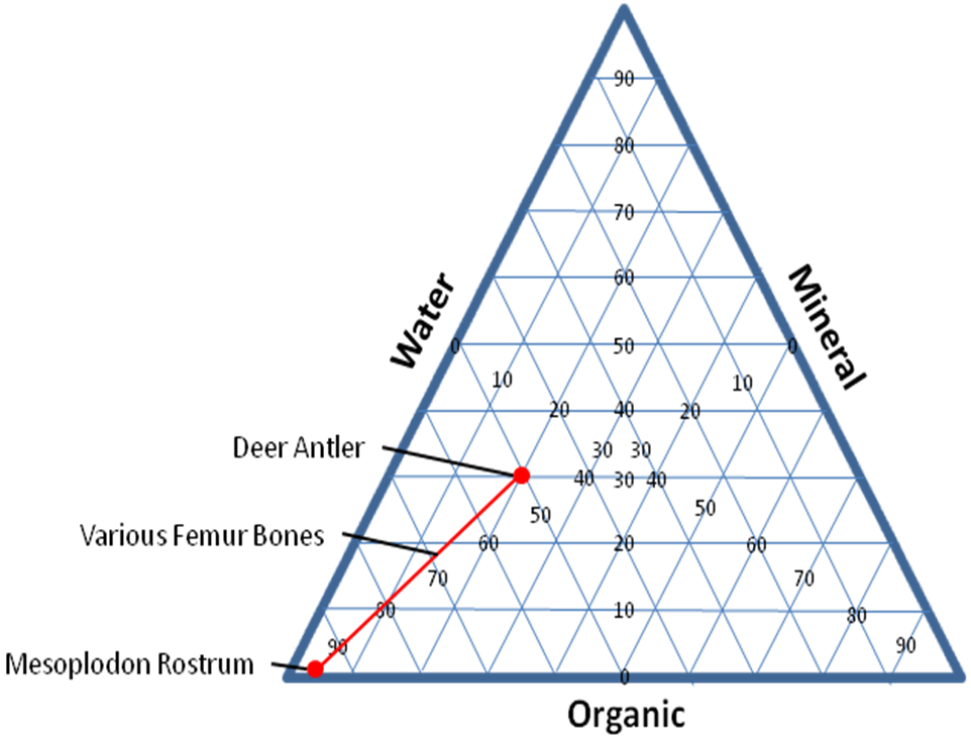

Figure 7.4 This a schematic representation of ternary diagrams adapted from references 2 and 3, the data show the weight fractions of mineral, water and organic material for dozens of bone samples, they all lie along the red line.

7.2 Future Work

A number of interesting questions have been raised during the present research, some of the questions are already being followed up and some will be addressed in the near future.

SORS

Can SORS be used to measure mineral to collagen ratio differences (and hence mechanical property differences) non-invasively *in vivo*? Can SORS be used to measure amide I band profile changes *in vivo* in diseased or aged bones? A pre-clinical trial of SORS which looks to answer these and other questions will begin at the UCL Institute of Orthopaedics and Musculoskeletal Science at the Royal National Orthopaedic Hospital (Stanmore) in 2011.

Beam Enhancer

Can the beam enhancer technique described in Chapter Three be used to enhance SORS signal during those pre-clinical trials? The beam enhancer should increase the depth at which Raman spectra can be retrieved; if a certain number of Raman photons (X) can be retrieved from bone material through Y mm of skin and overlying tissue without the beam enhancer, then $X + \Delta X$ photons should be retrieved with it, and X photons should retrievable through $Y + \Delta Y$ mm. These issues will be investigated in the SORS study.

Change along Proximodistal Axis

Are the local changes of collagen to mineral ratio present in the human femur? Is the pattern changed in diseased, aged or medically altered bone? A Raman instrument has been recently been delivered to the UCL Institute of Orthopaedics and Musculoskeletal Science at Stanmore, it will be used to answer these questions.

Chemistry

What is causing the amide I band profile to change between the highly mineralised bone material, the standard bone material and the less mineralised bone material? Biochemical analysis (High-performance liquid chromatography) of the collagen from antler bone material, metacarpal bone material and tympanic bone material is already underway. The research will look at the ratio of α_1 to α_2, the crosslinking and the hydroxylation of proline/lysine. If the source of the amide band profile change is found, studies will begin to investigate how this could affect mineralisation.

Overall Conclusions

The main conclusions of this thesis are

- A correlation exists between Raman bands (specifically the intensity ratio of the mineral bands to the collagen bands) and the mechanical properties for bony materials that differ widely in mineral volume fraction
- The cortices of long bones have regions where the mineral to collagen ratio vary in a regular way and these variations can be measured with Raman spectroscopy
- There are qualitative differences in the collagen of bony materials with widely differing mineral volume fractions

Taken together these conclusions add weight to the hypothesis that the mechanical properties of bone material are adapted in differently loaded regions by a subtle tuning of the collagen chemistry.

Appendices

Appendix 1.

Technique for Enhancing Signal in Conventional Backscattering Fluorescence and Raman Spectroscopy of Turbid Media

Appendix 2.

Non-invasive Analysis of Turbid Samples using Deep Raman Spectroscopy

Appendix 3.

Recent Advances in the Application of Transmission Raman Spectroscopy to Pharmaceutical Analysis

Anal. Chem. **2008,** *80,* 6006–6009

Technique for Enhancing Signal in Conventional Backscattering Fluorescence and Raman Spectroscopy of Turbid Media

Kevin Buckley,[†,‡] Allen Goodship,[‡] Neil A. Macleod,[†] Anthony W. Parker,[†] and Pavel Matousek*[,†]

Central Laser Facility, Science and Technology Facilities Council, Rutherford Appleton Laboratory, Harwell Science and Innovation Campus, Didcot, Oxfordshire, OX11 0QX, United Kingdom, and Institute of Orthopaedics and Musculoskeletal Science UCL, Stanmore Campus, Royal National Orthopaedic Hospital, Brockley Hill, Stanmore, Middlesex, HA7 4LP, United Kingdom

We demonstrate experimentally, for the first time, the feasibility of passively enhancing fluorescence and Raman signals from diffusely scattering media in a conventional backscattering collection geometry. The method employs transmission of the collimated excitation laser beam through a "unidirectional" dielectric mirror placed directly in front of the sample. This permits laser light that escapes from the sample surface to be reflected back into the sample where it can be more usefully employed in generating Raman and fluorescence signals. This leads to improved Raman signal, higher signal-to-noise ratio, and shorter acquisition times. Feasibility studies performed on standard pharmaceutical tablets and on sheets of Teflon, using a single enhancing element, demonstrate signal enhancement factors of 6 (fluorescence) and 3 (Raman). Potential applications of this simple device include improving quality control of pharmaceutical products, disease diagnosis of biological tissue, forensics, and security screening.

In a number of analytical applications of fluorescence and Raman spectroscopy involving diffusely scattering media, such as living tissue and pharmaceutical products, it is desirable to maximize the signal levels in order to improve the spectral quality, enhance sensitivity, or reduce the acquisition times. When probing diffusely scattering media, a major cause of photon loss, however, occurs at the sample-to-air interface through which the laser radiation is coupled into the sample leading to inefficient generation of desirable signal. Here we demonstrate experimentally, for the first time, a simple method of increasing the coupling of the laser radiation into the sample compatible with conventional collection schemes. The technique (see Figure 1) is applicable when the laser wavelength is not or is only weakly absorbed by the diffusely scattering samples, for example, biological tissue and pharmaceutical tablets using near-infrared excitation wavelengths.

The coupling of laser radiation into turbid samples has been extensively studied using a one-dimensional approximation. It was shown that the photon loss at the coupling sample-to-air interface

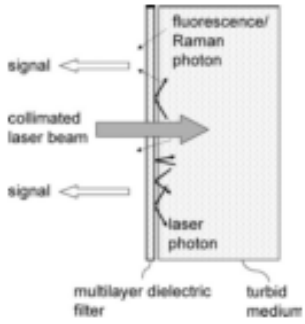

Figure 1. Schematic diagram of the principal for the enhancement of fluorescence and Raman signals in conventional backscattering geometry of turbid samples using a "unidirectional" mirror.

can often represent the dominant loss mechanism of the laser radiation.[1,2] For opaque samples such as powders, over 90% of the incident laser radiation can be scattered backward after traveling through just a few millimeters.[3] This photon loss can be dramatically reduced as a means of enhancing useful signal (specifically fluorescence and Raman signals). This is achieved by inserting a dielectric element into the laser beam path in front of the sample as described in our earlier theoretical and experimental work,[4] where the benefits of such filters were demonstrated using specialized variants of Raman spectroscopy (transmission Raman and spatially offset Raman spectroscopy).[5–7] These studies required the spatial separation of the laser deposition and the collection areas. However, the majority of fluorescence and Raman spectrometers utilize a backscattering geometry where the illumination and collection areas are coincident. Here we demonstrate experimentally the viability of this concept for the backscattering geometry commonly used in Raman and fluorescence spectroscopy. The widening of the applicability of the enhancement concept to conventional backscat-

* To whom correspondence should be addressed: E-mail: P.Matousek@rl.ac.uk.

† Harwell Science and Innovation Campus.

‡ Royal National Orthopaedic Hospital.

(1) Kubelka, P.; Munk, F. *Z. Technol. Phys.* **1931**, *12*, 593–601.
(2) Schrader, B.; Bergmann, G. *Fresenius Z. Anal. Chem.* **1967**, *225*, 230–247.
(3) Schrader, B.; Moore, D. S. *Pure Appl. Chem.* **1997**, *69*, 1451–1468.
(4) Matousek, P. *Appl. Spectrosc.* **2007**, *61*, 845–854.
(5) Matousek, P. *Chem. Soc. Rev.* **2007**, *36*, 1292–1304.
(6) Eliasson, C.; Matousek, P. *J. Raman Spectrosc.* In press.
(7) Matousek, P.; Clark, I. P.; Draper, E. R. C.; Morris, M. D.; Goodship, A. E.; Everall, N.; Towrie, M.; Finney, W. F.; Parker, A. W. *Appl. Spectrosc.* **2005**, *59*, 393–400.

10.1021/ac800700w CCC: $40.75
Published on Web 06/21/2008

tering spectroscopy modes dramatically increases its usefulness and applicability.

The "unidirectional mirror" concept relies on the angular dependence of the transmission of multilayer dielectric optical elements filters on photon incidence angle; the spectral transmission window shifts to shorter wavelength when a photon is incident from an angle greater than zero.[8] The mechanism and the magnitude of this shift are discussed in ref 4. If the filter is designed for high transmittance of the laser wavelength at normal incidence, then it can function as a unidirectional mirror; laser photons scattered from the sample surface with angles of incidence different from normal will be reflected back into the sample with high efficiency. By choosing a suitable dielectric filter, photons shifted to longer wavelength (due to fluorescence or Raman scattering) are able to pass through the filter and onto the detection system (see Figure 2). In addition, broadband mirrors can be used at the other sample−air interfaces to minimize the loss of photons (at all wavelengths) and further enhance the detected signal. This property we also demonstrate experimentally for the first time.

As discussed in our earlier work,[4] the enhancing mirror used in the conventional geometry constrains the usable Raman spectral range to above a certain threshold value (~900-cm^{-1} Raman shift). This limitation stems from the transmission characteristics of the dielectric mirror; the long wavelength edge of the filter must lie a sufficient distance away from the laser line so that it acts effectively as a mirror for laser photons emerging from the sample at non-normal incidence. This is because the spectral profile of the enhancing dielectric mirror that these photons experience is blue-shifted relative to photons that encounter the filter at normal incidence. No such constraint exists on the spectral profile for the transmission geometry where the illumination and collection zones are spatially separated.[4] For fluorescence spectroscopy, this is of lesser importance since the laser and emission wavelengths are typically separated to a much greater degree.

Although conventional mirrors have long been used to redirect transmitted laser light back into the sample as a way of increasing the intensity of Raman signal[9] and to reduce photon loss near the laser radiation coupling zone,[10] such elements do not prevent photon loss at what is often the most critical area, the delivery zone of laser radiation into the sample. This loss becomes more marked in applications where safety or other limits prevent the laser radiation from being concentrated onto a small area. Examples include the illumination of human skin or applications in explosive powder environments in the pharmaceutical industry. The solution presented here is fully compatible with the defocused laser beams used in such conditions.

EXPERIMENTAL SECTION

A schematic diagram of the apparatus used to obtain fluorescence and Raman spectra is shown in Figure 3. For fluorescence measurements, the probe laser was a green HeNe laser (543.5 nm, 0.40 mW, 1.1-mm beam diameter) equipped with a 10-nm band-pass filter centered at the laser wavelength to purify the

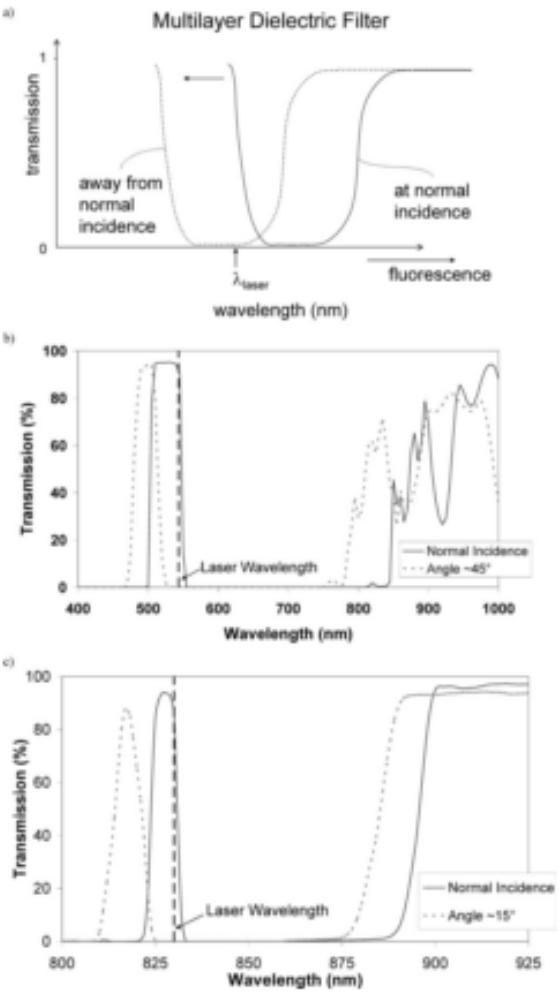

Figure 2. (a) Schematic illustration of the shift of the wavelength dependence of a multilayer dielectric optical element with angle of incidence. (b) Measurement of the wavelength dependence of the unidirectional mirror used to enhance the fluorescence spectra. The nonuniformity of the transmission in the 900−1000-nm range produces artifacts in the enhanced spectra. (c) Measurement of the wavelength dependence of the unidirectional mirror used to enhance the Raman spectra.

spectrum. For the Raman measurements, the laser was a continuous near-infrared diode laser (Process Instruments, model PI-ECL-830-300-FS, 830 nm, 250 mW, 1.0-mm beam diameter). The laser beam was directed through a prism and a dielectric filter (Semrock BrightLine single-band filter (525 nm) for fluorescence and an Iridian Spectral Technologies custom-made filter (with a transmission peak at the lasing wavelength and with full transmission above 900 nm (corresponding to 930-cm^{-1} Raman shift)) for Raman) onto the sample (see Figure 2). The dielectric filter was mounted on a translation stage in order to be able to precisely control its distance from the sample.

Emitted photons were collected by a collimating lens (50-mm diameter and a focal length of 60 mm) and imaged by a second lens, identical to the first, onto the front face of a fiber probe consisting of 22 active optical fibers (numerical aperture of 0.37).

(8) Born, M.; Wolf, E. *Principles of Optics*, 7th ed.; Cambridge University Press: New York, 2005.
(9) Long, D. A. *Raman Spectroscopy*; McGraw-Hill, Inc.: New York, 1977.
(10) Henderson, J. C.; Su, Q.; Grobe, R. *Laser Phys.* **2004**, *14*, 515–520.

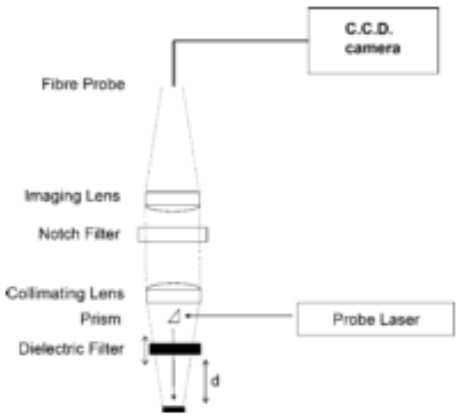

Figure 3. Experimental apparatus used to measure enhanced fluorescence and Raman spectra. The wavelength of the probe laser and the transmission profiles of the filters are different for each experiment.

In this arrangement, the signal is collected from a circle (~1.2-mm diameter) on the sample surface. It should be noted that the fibers are only used to increase the collection efficiency of the Raman system and are not essential for the presence of the enhancement effect, which would also be observed with a more conventional collection system. For fluorescence measurements, an edge filter (Semrock) was used to remove all radiation with a wavelength shorter than 900 nm while a notch filter (Kaiser Optical Systems) was used to remove the laser line scatter in the Raman measurements. The individual fibers were made of silica with a core diameter of 220 μm, a doped silica cladding diameter of 240 μm, and a polyimide coating diameter of 265 μm (CeramOptec Industries, Inc.). The fiber bundle length was ~2 m, and at the output end, the fibers were arranged in a linear shape orientated vertically and placed in the input image plane of a Kaiser Optical Technologies Holospec 1.8i NIR spectrograph equipped with a NIR back-illuminated deep-depletion thermoelectrically cooled charge coupled device camera (Andor Technology, DU420A-BR-DD, 1024 × 256 pixels). The spectra are not corrected for the variation of the filter and detection system's sensitivity across the spectral range. Spectra were obtained by varying the distance between the sample and the dielectric mirror.

In Raman measurements, the sample was a standard 3.9-mm-thick paracetamol tablet. In fluorescence studies, the same tablet was used with a thin coating layer of fluorescent ink applied to its surface using a green highlighter pen to enhance florescence emission in the 900−1000-nm region covered by the detection system. Additional Raman experiments were performed on a 4-mm-thick block of plastic (Teflon) with the dichroic mirror at the illumination site and a second mirror (Aluminum UV protected mirror, reflectivity >90%; 400 nm−10.0 μm, Thorlabs) at the back end of the slab. Raman spectra were taken with no filters present, with the filter at the illumination zone, with the mirror at the back of the sample, and finally with both filter and mirror.

RESULTS AND DISCUSSION

Fluorescence and Raman spectra of a paracetamol tablet are shown in Figure 4 for different distances between the enhancing dielectric filter and the sample; the observed signal decreases rapidly with increasing distance (d) between sample and dichroic

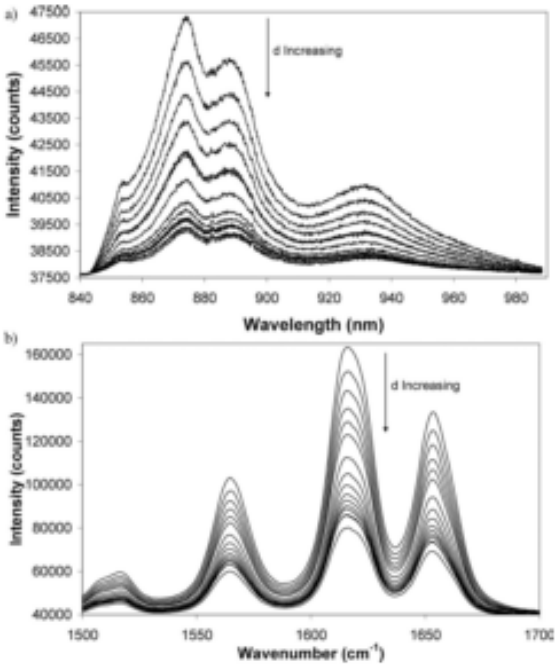

Figure 4. Fluorescence (a) and Raman (b) spectra of a paracetamol tablet recorded at various separations between sample and dielectric mirror. The intensity can be seen to decrease as the filter is moved away from the tablet. The apparent structure in the fluorescence spectra is an artifact of the transmission profile of the mirror. The filter used to enhance the Raman spectra was designed to have a flat transmission profile across the whole active spectral region.

mirror (Figure 5). The apparent structure in the fluorescence spectra is an artifact of the transmission curve of the filter used in the 900−1000-nm range (see Figure 2b). The maximum enhancement is achieved when the filter is in contact with the sample.

The intensity of the fluorescent/Raman signal decreases (approximately exponentially) as the distance between the sample and mirror is increased as can be seen in Figure 5. By normalizing each spectra to the peak height of the least intense spectrum (greatest distance), we see that, at zero separation between the sample and the filter, the signal is enhanced by a factor of 6 (Figure 5a) for fluorescence and by a factor of 3 for Raman (Figure 5b). When the Raman spectra were individually normalized, the spectral features were identical. The enhanced signals were stable with no signs of any undue intensity fluctuations, and the enhancement factors were reproducible upon successive approaches of the filter to the sample.

In some cases, further enhancement can be obtained by the incorporating an additional broadband mirror at the "transmitted side" of the sample. For 4-mm-thick Teflon slabs, a single unidirectional mirror at the illumination zone resulted in an enhancement of the Raman signal by a factor of 1.7. A single broadband mirror at the transmitted side gave an enhancement of 1.5, and the combination of the two gave an enhancement factor of 2.8 (Figure 6). These results suggest that, using suitably selected filters and mirrors, a photon "trap" could be constructed which would be capable of increasing the Raman signal by a

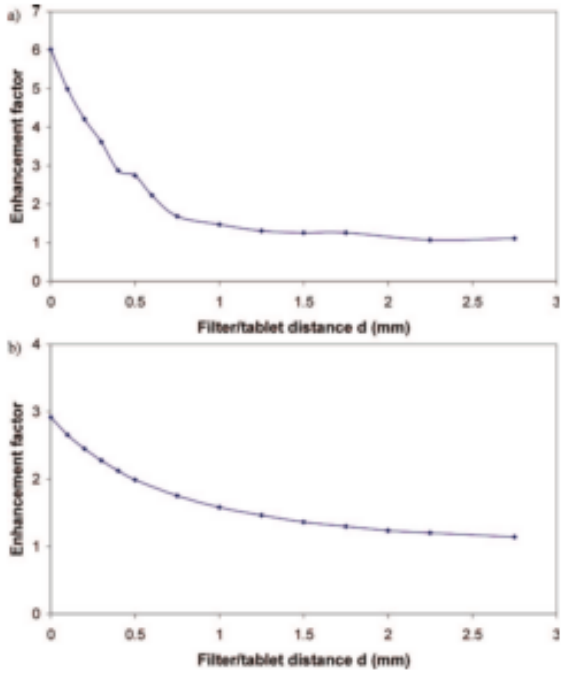

Figure 5. Dependence of (a) fluorescence and (b) Raman signal on the separation between sample (paracetamol tablet) and dielectric filter.

significant and useful amount. The precise enhancement factors achievable in each application will vary depending on the experimental parameters and the scattering/absorption properties of the probed sample. For example, for a standard 3.9-mm-thick paracetamol tablet, a medium of higher turbidity than Teflon, adding an extra mirror at the back, in addition to the beam enhancer at the front, only increased the overall Raman signal by a small fraction (~10%). The efficiency of coupling of laser radiation into turbid media using enhancing elements as a function of sample properties was also discussed in our earlier theoretical study.[11]

In order to achieve an equivalent enhancement using other means, it would be necessary to increase laser power, collection time, detector sensitivity, or collection system/spectrograph throughput[12] by similar factors. However, these alternative measures may not be straightforward (or even possible) to implement since many of these parameters are often already maximized.

(11) Matousek, P. *J. Opt. Soc. Am. B: Opt. Phys.* In press.

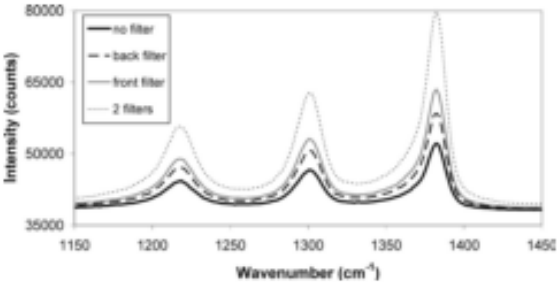

Figure 6. Raman spectra of a plastic slab (Teflon, 4 mm thick) with no filters present (thick line), with a single filter added to the front (dashed line) or back (thin line) of the sample and with filters at both sides of the sample (dotted line).

CONCLUSIONS

A concept for the enhancement of fluorescence and Raman signals from turbid media using a conventional backscattering geometry has been demonstrated. A substantial enhancement in observed signal was achieved using a custom-made dielectric band-pass filter inserted in the proximity of the laser illumination spot. Additional enhancements was achieved by inserting broadband mirrors at the other sample-to-air interfaces. The enhancement contributes to improved signal or permits shortening of applied laser power or acquisition times.

ACKNOWLEDGMENT

The authors thank Dr. Darren Andrews and Dr. Tim Bestwick of CLIK Knowledge Transfer and Professor Mike Dunne of Science and Technology Facilities Council for their support of this work. The support of STFC (Biomedical Network), University College London and EPSRC (EP/D037662/1) are also gratefully acknowledged.

Received for review April 8, 2008. Accepted May 23, 2008.

AC800700W

(12) McCain, S. T.; Gehm, M. E.; Wang, Y.; Pitsianis, N. P.; Brady, D. J. *Appl. Spectrosc.* **2006**, *60*, 663–671.

MINIREVIEW www.rsc.org/analyst | Analyst

Non-invasive analysis of turbid samples using deep Raman spectroscopy†

Kevin Buckley[ab] **and Pavel Matousek**[*abc]

Received 15th September 2010, Accepted 28th October 2010
DOI: 10.1039/c0an00723d

Raman spectroscopy has recently seen major advances in the area of deep non-invasive characterisation of diffusely scattering samples; this progress is underpinned by the emergence of spatially offset Raman spectroscopy and associated renaissance of transmission Raman spectroscopy permitting the characterisation of diffusely scattering samples at depths not accessible by conventional Raman spectroscopy. Examples of emerging research activities include non-invasive diagnosis of bone disease and cancer, rapid quality control of pharmaceutical formulations and security screening of explosives and counterfeit drugs through unopened translucent bottles. This article reviews this field focusing on recent developments with high societal relevance.

Introduction

A number of applications with high societal impact such as non-invasive diagnosis of bone disease and cancer, detection of counterfeit drugs through unopened pill bottles and the security screening of liquid and powder explosives in plastic bottles, require advanced analytical methods capable of accessing deep areas of intact diffusely scattering (turbid) samples. The analytical methods should ideally be fast, safe, highly chemically specific and compatible with aqueous environments. Conventional Raman spectroscopy fulfils these requirements but is not capable of accessing the depths required. For example, the conventional Raman spectroscopy of biological tissues is restricted to depths of several hundred micrometres and conventional Raman spectroscopy of pharmaceutical powders to 1–2 mm. These restrictions stem from the massive dominance of the near-surface signals (Raman and/or fluorescence) over the Raman signals originating from deep in the sample.

Conventional Raman spectroscopy generally utilises a back-scattering collection geometry; the scattered light is collected

[a]*Central Laser Facility, Research Complex at Harwell, Science and Technology Facilities Council, Rutherford Appleton Laboratory, Didcot, Oxfordshire, OX11 0QX, UK. E-mail: Pavel.Matousek@stfc.ac.uk*
[b]*Institute of Orthopaedics and Musculoskeletal Science, University College London, Royal National Orthopaedic Hospital, Stanmore, Middlesex, HA7 4LP, UK*
[c]*Cobalt Light Systems Ltd, Harwell Science & Innovation Campus, The Electron Building, Fermi Avenue, Didcot, Oxfordshire, OX11 0QR, UK*
† This article is part of a themed issue on Grand Challenges.

Kevin Buckley

Kevin Buckley obtained a BSc degree (chemical, mathematical and physical sciences) and a postgraduate diploma (applied physics) from University College Cork, Ireland. He subsequently obtained a MSc degree from the Tyndall National Institute/U.C.C. for his work on novel semiconductor laser devices. He started a PhD at the University College London Institute of Orthopaedics and Musculoskeletal Science in 2007 where the subject of his thesis is the Raman Spectroscopy of Bone Material. Kevin carries out his Raman Spectroscopy research at the Science and Technology Facilities Council's Central Laser Facility at Harwell, Oxfordshire.

Pavel Matousek

Pavel Matousek obtained his MSc and PhD degrees in physics from the Czech Technical University, Prague, Czech Republic. Since 1991, he has worked at the Rutherford Appleton Laboratory, UK. Pavel pioneered the concept of Kerr gated Raman fluorescence rejection, novel pharmaceutical applications of transmission Raman spectroscopy and Spatially Offset Raman Spectroscopy (SORS). Pavel published over 160 peer review articles and filed 10 patents. His honours include 2009 Charles Mann Award for Applied Raman Spectroscopy and shared 2002 and 2006 Meggers Awards. He serves on the boards of Analyst, Applied Spectroscopy *and* Journal of Raman Spectroscopy. *Pavel is a Fellow of the Royal Society of Chemistry, a Fellow of the Science and Technology Facilities Council, a visiting professor of the University College London and the Chief Scientific Officer of Cobalt Light Systems Ltd.*

directly from the laser illumination area (see Fig. 1).[1] In this configuration the Raman signals originating from deep in the sample are diluted due to sideways diffusion of photons within the medium. Recently, a substantial increase of penetration depth was achieved through the development of Spatially Offset Raman Spectroscopy (SORS)[2,3] and its analogues. These methods utilise the diffuse component of light in analogy with techniques used in NIR absorption tomography[4–6] and fluorescence spectroscopy.[7–10] The SORS method was developed from earlier temporal-domain Raman counterparts[11–15] which utilised time-correlated single-photon counting[11] or picosecond Raman Kerr gating (the latter developed originally for fluorescence rejection from Raman spectra[16–18]). A more extensive description of the time gated methods and underlying physical principles can be found in ref. 19. A CCD gated method has also been demonstrated recently for subsurface probing[20] and its potential for combining with SORS has been demonstrated.[21]

These developments have unlocked an array of exciting new opportunities in a wide range of disciplines due to the high chemical specificity of Raman spectroscopy (typically exceeding that of near-infrared absorption (NIR) and terahertz spectroscopy (THz)) and its ability to probe samples containing water. These emerging approaches and applications are reviewed in this paper.

Techniques

SORS concept

SORS can isolate the Raman spectra of *individual sub-layers* within a diffusely scattering medium. Unlike its time-gated predecessors, SORS uses a relatively simple instrumentation and continuous wave lasers. This dramatically enhances the utility of the technique and paves the way for many practical applications. In SORS, Raman spectra are acquired from regions on sample surface which are spatially offset (by a distance Δs) from the laser illumination zone (see Fig. 1). Such spectra contain different contributions from different depths within the sample due to photon diffusion; the photons originating from greater depths are spread further apart as they reach the surface. Typical SORS experimental layout is shown in Fig. 2a. The sample is excited at NIR region of the spectrum (*e.g.* 785 or 830 nm) using a narrow-linewidth laser to minimise sample fluorescence and sample absorption (for maximum penetration depth). The Raman signal is coupled through imaging optics into an optical fibre bundle and brought onto a slit of a low *f*-number spectrograph. The detection of signal is accomplished using a cooled, high

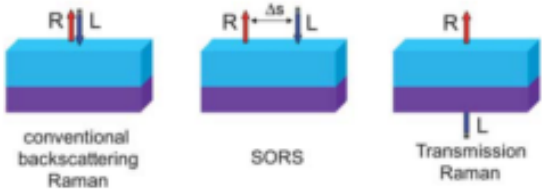

Fig. 1 Raman spectroscopy modalities: conventional backscattering Raman, SORS and Raman transmission geometries. Legend: R—Raman light, L—laser beam, and Δs—spatial offset.

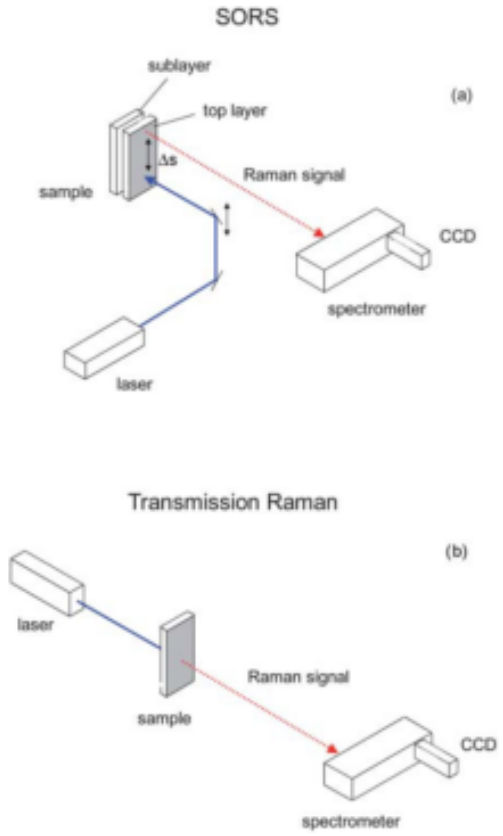

Fig. 2 Experimental arrangement for (a) Spatially Offset Raman Spectroscopy (SORS) and (b) transmission Raman spectroscopy.

performance CCD camera. Typical laser powers used are in a range of 200–600 mW.

Raw spatially offset Raman spectra typically contain residual surface layer Raman signals which can be removed by numerically processing the data. For a two-layer system the processing consists of a scaled subtraction of two SORS spectra acquired at different spatial offsets (*e.g.* at zero and non-zero spatial offsets),[2] cancelling the residual contribution from the surface layer present in the non-zero spectrum. For a multilayer sample or a sample with unknown number of layers processing involves multivariate techniques,[22,2] such as band targeted entropy minimization (BTEM).[23,24] Both the approaches can be automated. It should also be noted that for the separation to be possible the layers do not need to be parallel or of uniform thickness; the spectra from the constituent layers can be separated once they have different relative intensities.

The SORS concept was first demonstrated on a two-layer sample composed of a 1 mm thick PMMA powder on top of a *trans*-stilbene powder sub-layer.[2] SORS spectra obtained in these measurements are depicted in Fig. 3. The zero spatial offset spectrum corresponds to a conventional Raman measurement. The introduction of a non-zero spatial offset leads to a more rapid decrease of the surface Raman component (PMMA)

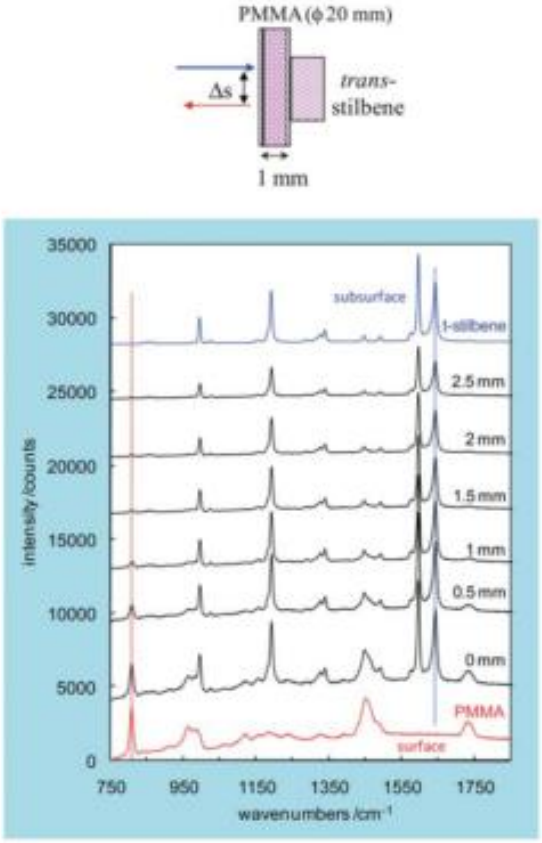

Fig. 3 A set of SORS spectra collected from a two-layer system consisting of 1 mm thick layer of PMMA made of 20 μm diameter spheres followed by a 2 mm layer of *trans*-stilbene powder. The spectra are shown for different spatial offsets. The top and bottom spectra are those of the individual layers obtained in separate measurements. The spectra are offset for clarity. (Reprinted with permission from P. Matousek, I. P. Clark, E. R. C. Draper, M. D. Morris, A. E. Goodship, N. Everall, M. Towrie, W. F. Finney and A. W. Parker, *Appl. Spectrosc.*, 2005, **59**, 393–400. Copyright (2005) The Society for Applied Spectroscopy.)

relative to that of the sub-layer (*trans*-stilbene). This relative intensity change is a key prerequisite for the technique layer separation capability. The relative intensity change between the surface and subsurface Raman signals was approximately an order of magnitude when a spatial offset of 2 mm was introduced.

In order to maximise the collectable Raman intensity and as such the signal-to-noise ratio, the SORS method is typically used in combination with a fibre optic collection scheme developed for conventional Raman spectroscopy by Ma and Ben-Amotz.[25] In this concept, the collection fibres typically arranged in a ring (or disk) pattern, with each ring corresponding to a different spatial offset are re-organised onto the spectrograph slit in a linear pattern matching the slit geometry.[2,3,26–28] The laser beam is typically brought onto sample surface into a small spot centred within the rings.

Further research led to the development of another useful modality of SORS, *inverse SORS*. This concept was developed independently by Matousek *et al.*[29] and Schulmerich *et al.*[30,31] In contrast with conventional SORS, the method switches the roles of Raman collection and laser deposition zones. The laser light is brought onto sample surface in a ring pattern and Raman light is collected through a group of fibres confined within the centre of the ring. The ring-shape laser beam can be generated using a conical lens (axicon)[32] with the radius of the ring being adjustable by altering the distance between the axicon and the sample[29] or by varying the magnification of a telescope inserted between sample and axicon.[30,31] The radius of the ring defines the spatial offset and can be therefore readily optimised to match the dimensions and scattering properties of sample. Inverse SORS is particularly beneficial in cases where sensitive samples are present and illumination intensity limits need to be adhered to. The wider illumination zone available on sample surface permits the deployment of higher overall laser power. This is beneficial, for example, when probing biological tissues *in vivo*, photosensitive samples or formulations in explosive environments.

An added benefit of SORS is its inherent capability to suppress fluorescence emission if it originates from the surface layer of sample (the degree of fluorescence rejection being the same as that achieved for surface Raman signals). Beneficial scenarios include the suppression of fluorescence from containers, from melanin in the skin (when probing tissue) and from coloured shells when probing pharmaceutical capsules.

Although SORS has been primarily developed for probing diffusely scattering samples, it can also be used for probing transparent samples. If the Raman collection zone is set deep in the transparent sample and the beam is angled so as to pass through that point, the Raman signal contributed from the container will be reduced.[33] With transparent samples this configuration also suppresses fluorescence (and Raman signals) originating from surface layers (*e.g.* semi-transparent green glass bottles fluoresce strongly). When this configuration is presented with a diffusely scattering sample the introduced laser beam tilt becomes irrelevant as photons quickly lose the memory about their original direction of travel.

As is the case for conventional Raman spectroscopy and other optical spectroscopies, SORS is unsuitable for metallic, highly absorbing or excessively fluorescing samples. As a consequence it is not suitable, for example, for probing metal beverage containers, brown or black materials such as soil or black packaging materials, or highly impure matrixes such as archaeological artefacts (which are challenging due to a high level of fluorescing and absorbing impurities even with NIR excitation wavelengths). A high or medium degree of sample absorption at the probe and Raman wavelengths (usually NIR part of the spectrum) typically leads to a large reduction of photon migration distances and consequently achievable penetration depths. An important positive feature of SORS is that it does not require *a priori* knowledge of the composition of any of the layers within the sample.

The SORS concept was first substantiated theoretically by Matousek *et al.*[3] using Monte Carlo simulations. The dependence of SORS effect was studied as a function of various experimental and sample variables including sample thickness, absorption, transport length and spatial offset. This provided

useful insights for subsequent development and optimisation of the technique.

The optimum spatial offset to achieve the highest signal-to-noise ratio (*s/n*) within a pure sub-layer Raman spectrum is expected to vary as a function of specific experimental conditions. This is governed by a compromise between the need for suppressing the top layer (more interfering contributions call for a larger spatial offsets) and the need for good signal strength from the sub-layer (which declines with the increasing spatial offset; although more slowly than for the surface layer). This point was investigated recently by Maher and Berger[34] who derived criteria for finding the optimum spatial offset. Bloomfield *et al.*[35] have studied this issue further from a standpoint of screening explosives in diffusely scattering containers. The study also identified that if a fixed total acquisition time is available, a very high fraction of it should be spent acquiring the offset spectrum. For common samples, the best results were obtained where the offset measurement was acquired for 20× longer than the zero offset position. Naturally, it is also possible to optimise the system empirically by acquiring spectra with different spatial offsets and inspecting their quality.

Transmission Raman

Research into deep Raman spectroscopy has also identified several useful properties of transmission Raman spectroscopy (see Fig. 1). It was shown that this optical arrangement exhibits properties well suited for the determination of the *bulk* content of turbid samples such as pharmaceutical capsules and tablets.[36] Transmission Raman can be considered to be a special case of SORS in which the laser beam and the Raman collection zone are separated to the extreme, both being on the opposite sides of sample. Benefits of the technique include the removal of the sub-sampling problem in the *z*-direction (depth)[37] and the related suppression of surface-generated Raman and fluorescence signals.[38] Although the transmission Raman technique was demonstrated in the early days of Raman spectroscopy,[39] its benefits for the non-invasive probing of the bulk content of pharmaceutical samples have not been recognised and exploited until recently.[1] Typical layout of a transmission Raman experiment is shown in Fig. 2b. The sample is excited at NIR region of spectrum (*e.g.* 785 or 830 nm) using a narrow-linewidth laser to minimise sample fluorescence and sample absorption (for maximum penetration depth). The Raman signal is coupled through imaging optics into an optical fibre bundle and brought onto a slit of a low *f*-number spectrograph. The detection of signal is accomplished using a cooled, high performance CCD camera. Typical powers employed are in the range of 200–2000 mW.

The sub-sampling problem associated with conventional Raman spectroscopy can be exacerbated when probing pharmaceutical tablets and capsules, as they are often highly heterogeneous. The sensitivity and accuracy can also be affected by fluorescing surface layers.[37] These issues were partially addressed in the lateral dimensions by Wikstrom *et al.*[40] with a wide-illumination and Raman collection backscattering geometry although a (reduced) sub-sampling problem in the *z*-direction (depth) still remained. This technique and the reduction of sub-sampling were further explored by a group of Chung.[41–44]

The reduction of the sub-sampling problem in transmission Raman was first demonstrated both computationally and experimentally by Matousek and Parker.[36] The results of numerical Monte Carlo simulations are illustrated in Fig. 4. The calculations were performed on a pharmaceutical tablet-like object with a thin 'impurity' layer inserted at different depths and with wide illumination and collection areas (6 mm diameter in both the cases). The results indicated that for conventional backscattering Raman spectroscopy transposing the impurity from the surface to a depth of 3 mm in a 4 mm thick tablet diminishes the signal by 4 orders of magnitude. At these levels, the Raman signal from the impurity layer would typically be overwhelmed by the signal coming from near the surface. In contrast, the transmission geometry yielded a Raman signal which was largely invariant (in this case to within ±50% accuracy) to the depth of impurity layer. These results were in agreement with experimental observations. The Monte Carlo simulations also indicated a weak bias towards signals from deep in the tablet. Further studies of layered pharmaceutical tablets by Townshend *et al.*[45] and Johansson *et al.*[46] have substantiated these predictions experimentally.

Everall *et al.*[47] investigated theoretically the spatial resolution of transmission Raman spectroscopy from a viewpoint of tomographic applications. Apart from looking at the spatial origin of the measured Raman signals, the research investigated the homogeneity of the probing as a function of experimental geometry. The study concluded that the lateral resolution should worsen linearly with sample thickness (typically the spatial resolution reached was about 50% of the sample thickness), and that the lateral resolution was better at the sample surfaces (essentially determined by the probe beam diameter or the collection aperture) than that at the centre of the sample. In line with earlier observations, the signal bias towards the mid-point of thick samples in transmission sampling was also established.

In a subsequent study Everall *et al.*[48] looked experimentally at the spatial resolution and sensitivity of Raman spectroscopy in backscattering and transmission modes in turbid media and for the first time measured the width and intensity of the point

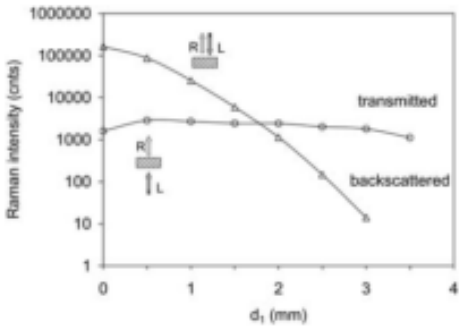

Fig. 4 Plot of the theoretical Raman intensities for the backscattering and transmission geometries *versus* depth (d_1) of the inter-layer (impurity) within a pharmaceutical tablet-like medium. The dependencies are the results of Monte Carlo simulations. (Reprinted with permission from P. Matousek and A. W. Parker, *Appl. Spectrosc.*, 2006, **60**, 1353–1357. Copyright (2006) The Society for Applied Spectroscopy.)

spread function, as a function of sample thickness and depth below the surface. In transmission mode, the lateral resolution for objects in the bulk was shown to degrade linearly with sample thickness. The resolution was also shown to be much better for objects near either surface, being determined essentially by the diameter of the probe beam and collection aperture irrespective of sample thickness. The objects in the bulk yielded higher signals than those located near the surfaces in line with the earlier numerical results[47] and experimental findings.[45–47]

The ability of transmission Raman spectroscopy to access very deep areas of highly turbid pharmaceutical tablets and to deliver measurable Raman signals conveying information on its volumetric content was first demonstrated by Matousek *et al.*[36] The experimental study was performed on a two-layer sample with an overall thickness of 6 mm. The spectra obtained in these measurements both in transmission and conventional backscattering Raman geometries are depicted in Fig. 5. The two-layer sample consisted of a 4 mm thick paracetamol tablet followed by a 2 mm thick layer of *trans*-stilbene powder representing a thick two-layer pharmaceutical tablet. The conventional backscattering Raman spectroscopy was capable of detecting only the top layer of the sample presented to the instrument. In contrast, transmission Raman spectroscopy yielded signal contributions from both the layers.

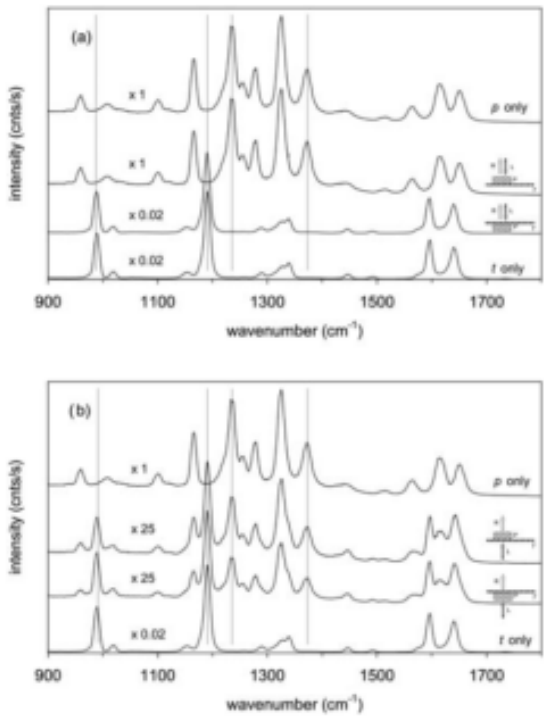

Fig. 5 The Raman spectra obtained from a two-layer sample (3.9 mm thick paracetamol tablet and 2 mm thick *trans*-stilbene powder layer) using (a) conventional backscattering geometry and (b) transmission geometry. The measurements are performed at two sample orientations, with paracetamol at the top and at the bottom of the *trans*-stilbene cell, as indicated in the graphs. The top and bottom spectra are those of paracetamol and *trans*-stilbene, respectively, obtained in separate experiments. The acquisition times were between 0.2 s and 10 s, with a laser power of 80 mW. The spectra are offset for clarity. Legend: *p*—paracetamol, *t*—*trans*-stilbene, R—Raman light, and L—laser beam. (Reprinted with permission from P. Matousek and A. W. Parker, *Appl. Spectrosc.*, 2006, **60**, 1353–1357. Copyright (2006) The Society for Applied Spectroscopy.)

Raman signal enhancement using a 'unidirectional' mirror

As Raman signals can be substantially weaker in transmission Raman spectroscopy than in conventional backscattering Raman spectroscopy, it is often necessary to take careful consideration of instrument configuration and to optimise it specifically for the transmission geometry. Additional measures to boost the quality of retrieved signals include the use of higher laser powers (permitted by considerably larger laser illumination areas in transmission Raman geometry) or longer acquisition times.

Another, unconventional approach for boosting Raman signals by passive means was proposed and demonstrated recently by Matousek.[49] The concept uses a 'unidirectional' mirror ('photon diode') placed in contact with the sample at the laser illumination zone. When probing pharmaceutical tablets the illuminated area is typically large (*e.g.* 4–8 mm in diameter) so as to aid effective averaging of across a larger volume. The key function of this mirror is to prevent the loss of diffusely scattered laser and Raman photons from the sample. This optical element forces both the laser and Raman photons to the other side of the sample towards the Raman collection system and so enhancing the overall detectable Raman signal. The special mirror is formed using an appropriately designed multilayer dielectric optical bandpass or edge filter. The concept relies on the generic angular properties of dielectric filters for which the spectral profile shifts to shorter wavelengths with increasing angles of incidence. As the dielectric filters are typically produced as flat optical elements, the ideal sample should also be flat or at least not excessively curved as the special mirror has to be in near-contact with the sample. This requirement favours flat pharmaceutical tablets or powders. Typical intensity enhancement factors achieved with pharmaceutical tablets can be up to 10 with associated improvement of the signal-to-noise ratio. The concept was also demonstrated to be viable with the SORS[50] and conventional Raman and fluorescence spectroscopy.[51]

Raman tomography

SORS provides information on the chemical composition of individual layers within sample but, when used in its basic form, does not convey information of the spatial distribution of the layers or the presence and location of objects within sample. Schulmerich *et al.*[37,52] have demonstrated that SORS can also be used as an effective tomographic tool capable of forming highly chemically specific images of subsurface sample components with a spatial resolution ultimately limited by photon diffusion (see Fig. 6). Raman tomography progressed rapidly from the initial pilot studies to the demonstration of 3D tomographic imaging-maps of phantoms and of canine hind limb sections (with skin and tissue thickness of up to 45 mm) by Schulmerich *et al.*[52]

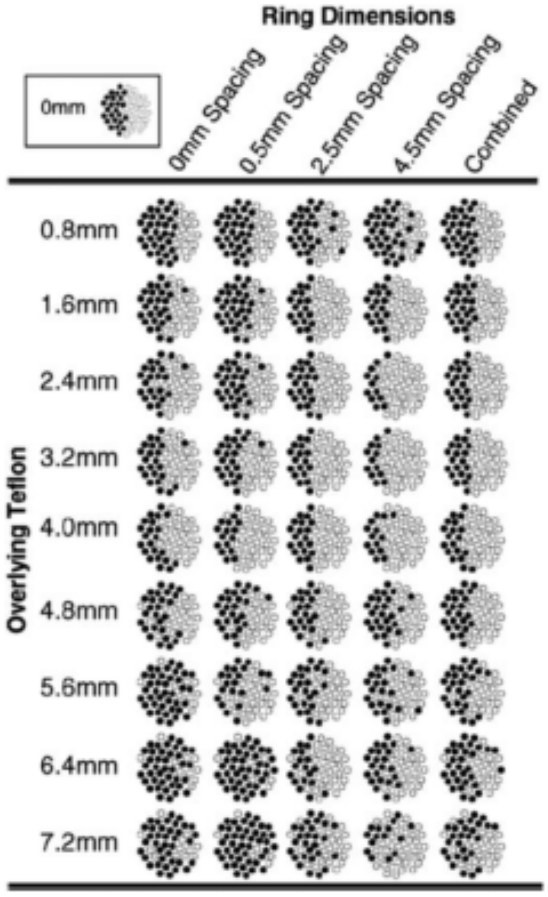

Fig. 6 Fiber maps of the subsurface interface between polyethylene (filled circles) and Delrin (open circles) at different ring/disk spacings. (Reprinted with permission from M. V. Schulmerich, K. A. Dooley, T. M. Vanasse, S. A. Goldstein, and M. D. Morris, *Appl. Spectrosc.*, 2007, **61**, 671–678. Copyright (2007) Society for Applied Spectroscopy.)

Further refinement of the reconstructed images was achieved by Srinivasan *et al.*[53] who introduced image-guided Raman spectroscopy, a technique where X-ray CT images of the tissue are used to guide the numerical recovery.[54] This image-guided Raman yielded a contrast of 145 : 1 between the cortical bone and background.

In a separate study the conceptually much simpler problem of determining the thickness of an over-layer was studied.[55] The assumption of a plane two-layer system with infinite side dimensions greatly simplifies the complexity of the tomographic problem and leads to a more deterministic outcome. This highly simplified situation has a number of potential practical applications including the determination of the penetration of drugs or cosmetic creams through tissue at depths beyond the reach of conventional confocal Raman methods. The technique is straightforward to apply although it can only be used in cases where training sample set containing samples of known layer thicknesses is available to establish appropriate calibration points for the method. No other sample parameters are required. The systems studied included bone with an overlayer of soft tissue and plastic slabs overlain with white paper (giving rise to intense Raman signals and a broad fluorescence background). In both the cases the depth of the overlayer was determined with typical relative accuracies between 5 and 10% to depths of 800 μm (paper) and 5 mm (soft tissue).

Application examples

Since the development of deep probing Raman methods numerous topical applications have emerged across a wide range of disciplines.[56,57]

Biomedical applications

Probing of bones through skin in disease diagnosis. Raman spectroscopy has proven to be an effective technique for analysing excised bone matrix[58] but the difficulty in probing deep through soft tissue has hampered *in vivo* studies. The development of deep sub-surface Raman techniques has provided new opportunities for advancing this field and offers promise for diagnosing bone conditions, such as brittle bone disease (osteogenesis imperfecta) and osteoporosis, noninvasively.[15,58–60] The need for developments in this field can be illustrated with the example of osteoporosis; the current "gold standard" technique Dual-Energy X-ray Absorptiometry (DEXA) only has an accuracy of 60–70% when predicting osteoporotic fractures. This is believed to be, in part, due to its insensitivity to the organic (mainly collagen) component of bone. This organic component is very important in determining the mechanical properties of the bone material, especially its toughness. Recently, both the temporal and spatial deep Raman probing techniques have been applied successfully in this area.

The first non-invasive Raman study of bone matrix was performed by Draper *et al.*[59] using a Kerr gating method. In this study, a defective bone material from OIM/OIM mice (models of the disease *osteogenesis imperfecta*) was detected through 1 mm of overlying skin and soft tissue and identified as such through its having a different ratio of collagen to mineral Raman bands to the wild type controls. Although this was a major breakthrough, several issues still needed to be addressed before the technique could be applied to human subjects *in vivo*. These included the use of very high laser intensities, which were two to three orders of magnitude above the safe levels for illumination of skin and the instrumental complexity.[28]

These issues were resolved with the development of SORS. The first non-invasive SORS bone spectra were obtained by Schulmerich *et al.*[26] who achieved penetration depths of several millimetres in animal and human cadavers using a global illumination geometry, a variant of SORS. Further improvement of signal-to-noise and penetration depth was obtained with a ring illumination geometry (equivalent to inverse SORS).[10] The researchers were able to determine the ratio of the intensities of the phosphate (958 cm^{-1}) and carbonate (1070 cm^{-1}) Raman bands of chicken tibia with an accuracy higher than 8% accuracy through 4 mm of overlaying soft tissue. Typical Raman spectra obtained in these experiments are shown in Fig. 7. The measurements were performed using a laser excitation

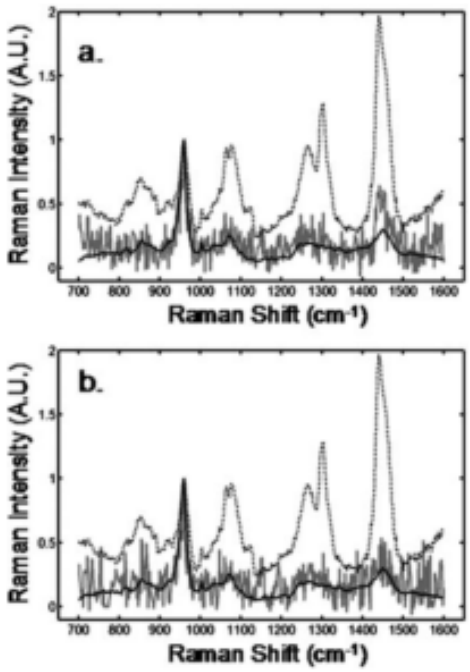

Fig. 7 Measurements made through 4 mm of overlying tissue on a chicken tibia at the mid-diaphysis using SORS approach. Transcutaneous (dotted), recovered bone factor (gray), and exposed bone (black). (a) Recovered bone factor using data from all 50 collection fibers and (b) recovered bone factor using data from the 32 innermost collection fibers. The laser power was 110 mW and the acquisition time 120 s. (Reprinted with permission from M. V. Schulmerich, K. A. Dooley, M. D. Morris, T. M. Vanasse and S. A. Goldstein, Transcutaneous fiber optic Raman spectroscopy of bone using annular illumination and a circular array of collection fibers, *J. Biomed. Opt.*, 2006, **11**, 060502. Copyright (2006) The Society of Photo-Optical Instrumentation Engineers.)

wavelength of 785 nm and laser power of 110 mW. This result is of particular significance as this ratio may be altered in osteoporotic bone.[60] This team also compared different SORS probe designs, tailoring them to smaller samples such as mouse bones matching by the probe size and aspect ratio to particular dimensions of the analysed sample.[61] With such samples standard SORS cannot be directly applied without reducing the technique's effectiveness.

In a parallel research, Matousek *et al.*[28] demonstrated the basic feasibility of obtaining the Raman spectra of bones from humans *in vivo*. Although the recovered Raman spectra were of low quality with some overlaying tissue Raman signals still remaining, the experiments demonstrated that the key bone features can be obtained transcutaneously *in vivo* under safe illumination conditions. These measurements were performed with only 2 mW of laser power at 827 nm, a power comparable to that of a common laser pointer. This level was around an order of magnitude lower than the threshold for a safe illumination of skin. The Raman spectra were collected using a ring fibre probe with zero and 3 mm spatial offsets from the thumb distal phalanx of volunteers through around 2 mm of overlaying soft tissue. The overall acquisition time was 200 s. Considerable prospects exist for further improvement of this method with the inverse SORS approach[29–31] boosting both the sensitivity and penetration depth.

Non-invasive diagnosis of breast cancer. Another rapidly developing application of deep Raman spectroscopy is the non-invasive detection of deep cancer lesions in breast tissue. In this area, two strands of research have been pursued: the detection of cancer lesions through associated calcifications and directly through the detection of abnormalities within soft tissue.

At present, the detection of suspected calcifications by X-ray mammography is typically followed by a needle biopsy to determine whether the lesion is malignant (70–90% of these biopsies give negative results). The detection of the chemical composition of calcifications by non-invasive means opens the prospect for non-invasive identification of the lesions and may provide additional diagnostic power. The potential for the non-invasive characterisation of calcifications within tissue was first demonstrated by Baker *et al.*,[62] Stone *et al.*[63] and Matousek and Stone[64] using the Raman Kerr gated, SORS and transmission Raman methods, respectively, on chicken breast-tissue phantoms. The penetration depths achieved in these earlier studies were 0.9, 8.7 and 16 mm, respectively. The research in this area builds on the work of Haka *et al.*[65] and Baker *et al.*[66] reporting a correlation between the chemical composition of calcifications and the type of lesions, *i.e.* whether malignant or benign.

Presently, the transmission Raman approach has reached the highest penetration depth for these applications. With this method, the signal strength's inherent dependence on the depth of the calcification for a given overall tissue thickness is very low.[64] This provides an added benefit as the method has largely the same sensitivity to the presence of lesions irrespective if their depth. Recognisable chemical signatures have been obtained for two different calcification types (type I, which consists of calcium oxalate dihydrate and type II, which is composed of calcium phosphates, mainly calcium hydroxyapatite) although the sensitivity of the method was below the clinically relevant concentration range. Subsequent combination of chemometric methods with an improved transmission Raman concept led to the recovery of calcification signals in phantom samples reaching 27 mm penetration depth in porcine tissue.[67] The signal was recovered through 20 mm of porcine tissue with calcifications present at clinically relevant concentrations using an 830 nm laser with a spot diameter of around 4 mm and an acquisition time of 50 s (see Fig. 8).

Recently, Keller *et al.*[68] demonstrated the capability of SORS to also identify soft tissue lesions at depths of several mm within healthy soft tissue. Spectral signatures of breast tumours as small as 1–2 mm thick were detected through 2 mm of normal breast tissue. Although a number of questions about its efficacy require further study, this work shows that SORS of soft tissues likely holds promise for biomedical applications previously considered "out of reach" for Raman spectroscopy. The study heralds prospect for a real time diagnostic tool that can be deployed during surgery to aid surgeons in defining the margins of lesions.

A very recent investigation by Stone *et al.*[69] demonstrated a potential of combining SORS with surface enhanced Raman

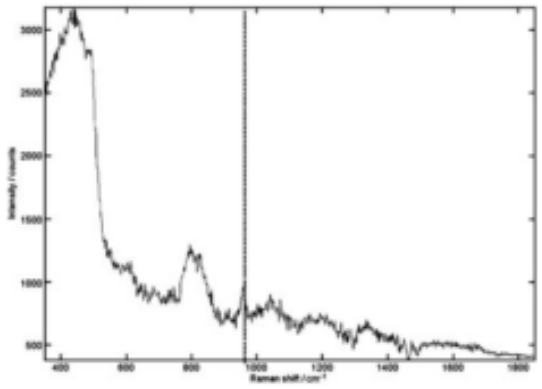

Fig. 8 The recovered signal achieved for 0.125% (relative volume) of HAP (calcium hydroxyapatite) buried within 20 mm of porcine tissue. The 962 cm^{-1} marker band of HAP (marked with a dashed vertical line) has been clearly identified. The acquisition time was 50 s and the laser power 250 mW. (Reproduced from N. Stone and P. Matousek, *Cancer Res.*, 2008, **68**, 4424–4430 with permission from American Association for Cancer Research, Inc.).

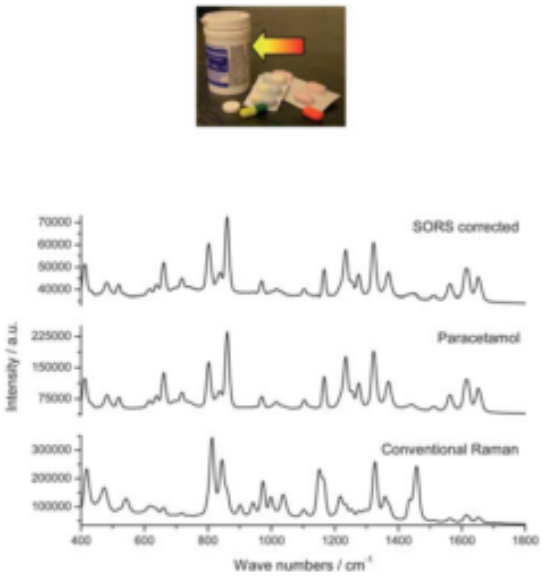

Fig. 9 Non-invasive Raman spectra of paracetamol tablets measured through a white, diffusely scattering 1.7 mm thick plastic container in drug authentication. Conventional Raman and SORS raw data are shown together with the tablets reference Raman spectrum. The acquisition time was 10 s and the laser beam power 50 mW. (Reprinted in part with permission from C. Eliasson and P. Matousek, *Anal. Chem.*, 2007, **79**, 1696–1701. American Chemical Society.)

spectroscopy (SERS) permitting SERS signals to be read from deep within tissue opening thus prospects for multiplexed detection of bioanalytes deep inside the tissue at extremely low concentrations. The method was termed SESORS. Potential future applications of this concept with suitable nanoparticles labelled with antibodies could also include early cancer detection. Although it should be noted that this method is not inherently non-invasive as nanoparticles need to be injected into the sample.

Pharmaceutical applications

The wide occurrence of counterfeit drugs[70] infiltrating pharmaceutical distribution chain represents a major health threat to our society. Recently it was shown[71] that SORS can be used to non-invasively and non-destructively characterise the contents of packaging such as blister packs and translucent plastic bottles without opening them (the inspected drug can then be sold or used as legal evidence that was not tampered with). This capability is conceptually illustrated in Fig. 9 for paracetamol tablets held inside a white translucent plastic bottle. Raman spectra were measured non-invasively using both the conventional Raman and SORS methods. The conventional Raman spectra were dominated by the Raman signal of container wall and were ineffective for characterising the internal content. On the other hand, SORS provided a clear Raman spectrum of the tablets held inside the bottle. The experiments were performed at 827 nm with a 50 mW laser beam and an acquisition time of 10 s. SORS was also used in the detection of counterfeit anti-malarial tablets by Ricci *et al.*[72] As such SORS promises to provide an effective solution to this escalating problem.

Quantification of active pharmaceutical ingredient and excipients in pharmaceutical tablets and capsules. The quantitative analysis of pharmaceutical formulations is traditionally performed using HPLC. However, this technique is time and labour consuming as well as destructive to the sample. In many applications it would be highly advantageous to replace it with a bulk sensing method capable of rapid, non-destructive and non-invasive analysis. This requirement is addressed in some situations by NIR absorption spectroscopy although this method is hampered by its limited chemical specificity and a lack of robustness (due to its high sensitivity to physical properties of sample, *e.g.* formulation particle size). These deficiencies are reduced or removed by transmission Raman spectroscopy.

The first demonstration of the capability to characterise volumetrically thick intact pharmaceutical tablets and capsules with transmission Raman geometry was demonstrated by Matousek and Parker.[36,38] A number of beneficial properties of this sampling geometry were identified. These include the reduction of sub-sampling and the suppression of surface layer fluorescence/surface layer Raman signal. Subsequent research by Johansson *et al.*[73]demonstrated that transmission Raman spectroscopy can provide sufficiently accurate quantitative information on the composition of pharmaceutical formulations. In this study, 20 test tablets (3.3 mm thick) prepared in a laboratory environment were analysed. The quantity of the active pharmaceutical ingredient (API) was determined with a relative root mean square error of ±2.2% (see Fig. 10). The acquisition time in these measurements was 10 s and a laser power of 400 mW (785 nm) was used. The study was also performed in a conventional backscattering Raman geometry which yielded a lower relative accuracy (±2.9%) ascribed to the presence of sub-sampling. The

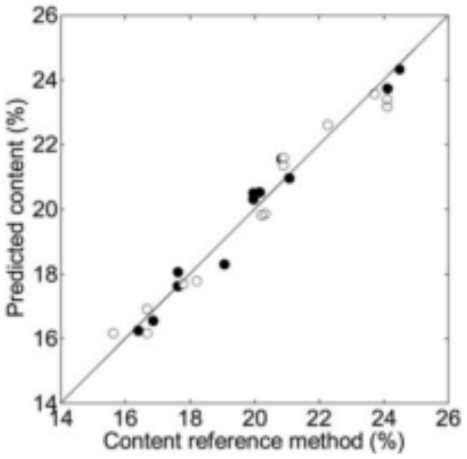

Fig. 10 Prediction of the concentration of propranolol tablets in two independent test sets using Raman transmission (1 PLS component). (Reprinted with permission from J. Johansson, A. Sparen, O. Svensson, S. Folestad and M. Claybourn, *Appl. Spectrosc.*, 2007, **61**, 1211–1218. Copyright (2007) The Society for Applied Spectroscopy.)

transmission Raman method was also applied to pharmaceutical capsules yielding a relative accuracy of ±3.6%. The study indicated that the transmission Raman mode requires a substantially leaner calibration model relative to conventional Raman spectroscopy and was capable of providing reasonably good accuracy even when based on only 2 or 3 calibration spectra.

In another study Eliasson *et al.*[74] used a batch of 150 production line type formulations in white capsules. The investigations demonstrated that intense interfering Raman signals of the capsule shell are suppressed in the Raman transmission mode. This permitted an accurate quantification of the API with a relative root mean square error of ±1.2% with a 5 s acquisition time. In this study the laser power at the sample was 250 mW and the laser wavelength 830 nm. The beam spot diameter on the sample was ~3 to 4 mm.

The two studies above used predominantly binary mixtures. The ability to quantify more complex formulations was studied

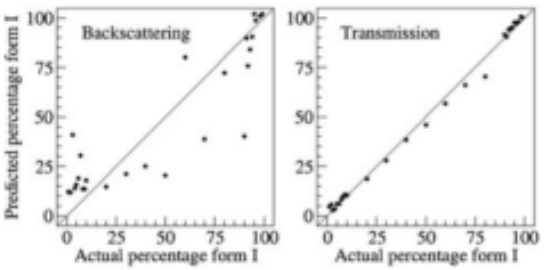

Fig. 11 Results of PLS analysis (validation plot, all data) for two polymorphic mixtures of flufenamic acid collected in backscattering and transmission Raman geometry. (A. Aina, M. D. Hargreaves, P. Matousek and J. C. Burley, Transmission Raman spectroscopy as a tool for quantifying polymorphic content of pharmaceutical formulations, *Analyst*, 2010, **135**, 2328–2333 (http://dx.doi.org/10.1039/c0an00352b). Reproduced by permission of The Royal Society of Chemistry).

by Hargreaves *et al.*[75] In this study pharmaceutical formulations with an active pharmaceutical ingredient (API) and 3 common pharmaceutical excipients were used. For the first time, it was shown that the technique is largely insensitive to the amount of material held within the capsules. A single calibration model was developed using capsules of one fill weight, 100 mg, to a relative error of typically <3%. This model was then used to predict API concentration of capsules with varying fill weights (100–400 mg) and different shell colours. The relative root mean square error of predicted API-concentration (nominal content 75% w/w) was 1.5% with a 5 s acquisition time. The quantity of API was also predicted using the same model for capsules prepared with different generations of API (*i.e.* API manufactured *via* different processes) with a relative error within ~3% indicating a high degree of robustness. This study indicates that there could be significant benefits for the pharmaceutical industry in using this approach; both in terms of resource requirements from method

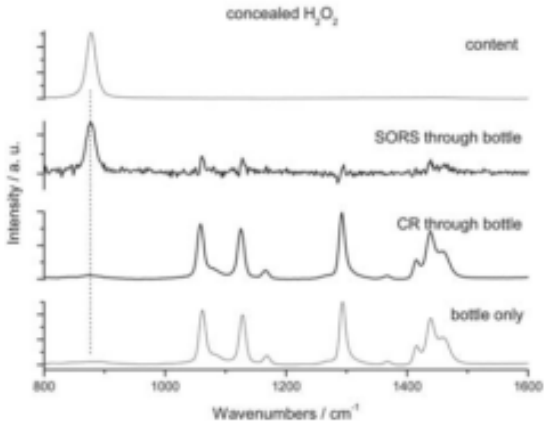

Fig. 12 Conventional (CR) and SORS Raman spectra of an L'Oreal sun lotion bottle, filled with 30% H_2O_2 (aq). The bottle was made of white, translucent semi-soft plastic material with a thickness of 1.1 mm. The dotted line indicates the signature band of H_2O_2 (aq) at 876 cm^{-1}. The bottom trace is the Raman spectrum of the empty jar itself and is essentially identical to the conventional Raman spectrum of the jar containing H_2O_2 with no obvious trace of the Raman signature of H_2O_2. The SORS spectrum, on the other hand, shows clearly the H_2O_2 Raman marker band. The spectra were measured using a probe wavelength of 830 nm, laser power of 250 mW and 1 s acquisition time. (Reprinted with permission from C. Eliasson, N. A. Macleod, P. Matousek, Non-invasive detection of concealed liquid explosives using Raman spectroscopy, *Anal. Chem.*, 2007, **79**, 8185–8189. Copyright (2007) American Chemical Society.)

development and maintenance but also in terms of validation and regulatory activities.

Quantification of polymorphs in pharmaceutical formulations. Recently, Aina *et al.*[76] demonstrated the ability of transmission Raman spectroscopy to also quantify the *polymorphic* content of pharmaceutical formulations. The ability to provide information on polymorphs is of particular significance as HPLC methods rely on dissolution of sample and therefore involve associated loss of information on the polymorphic content. Alternative methods such as X-ray diffraction, NMR or differential scanning calorimetry suffer from long data acquisition times or issues associated with safety management or have limited sensitivity. In the study, flufenamic acid, a non-steroidal anti-inflammatory drug, was used as a model compound. The transmission Raman method was shown to provide a true bulk measurement of the composition, in contrast with conventional backscattering Raman method which provided unsatisfactory results due to severe sub-sampling accentuated by one polymorphic form exhibiting surface segregation. For a model-free fit, the transmission Raman method yielded R^2 of 0.996 compared to the backscattering value of 0.802; for a partial least squares fit with a single component the TRS method accounted for 98.09% of the variance in the data compared to 89.65% for the backscattering method (see Fig. 11). In transmission Raman measurements the wavelength was 830 nm, the laser power 800 mW and acquisition time 10 s.

A key processing step in quantification involves multivariate methods. Fransson *et al.*[77] investigated the accuracy of the quantification of pharmaceutical tablets with transmission Raman spectroscopy as a function of the type of chemometric method used to analyse the data. Several multivariate approaches were investigated: partial least squares (PLS), multivariate curve resolution (MCR), classical least squares (CLS) and curve fitting to derive peak ratios. MCR, CLS and PLS gave comparable results with relative prediction errors for an independent test set in the range of 2.4–3.4%. The curve fitting and peak ratios gave higher prediction errors, typically around 4 and 6%, respectively. The study also noted that the number of samples and concentration levels needed for calibration could be

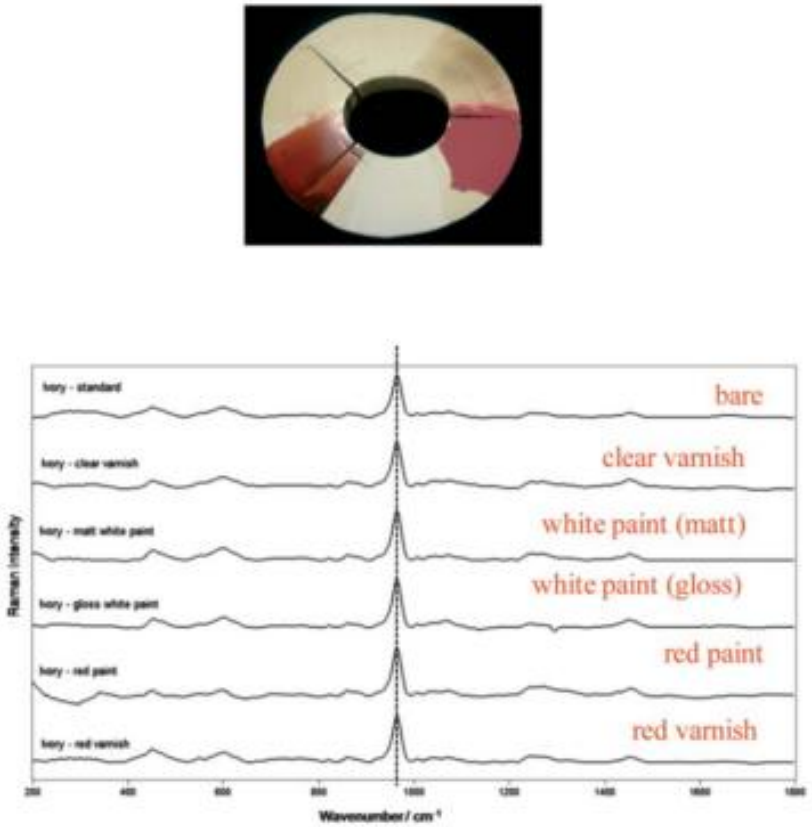

Fig. 13 SORS spectra of an ivory sample (elephant tusk) concealed with various paints and varnishes. The top spectrum is a reference (uncoated) Raman spectrum of the ivory sample. The wavelength was 830 nm, the laser power 250 mW and acquisition time 10 s. A spatial offset of 4 mm was used in the measurements. The spectra are offset for clarity. (Reprinted with permission from M. D. Hargreaves, N. A. Macleod, V. L. Brewster, T. Munshi, H. G. M. Edwards and P. Matousek, Application of portable Raman spectroscopy and benchtop spatially offset Raman spectroscopy to interrogate concealed biomaterials, *J. Raman Spectrosc.*, 2009, **40**, 1875–1880. Copyright (2009). © John Wiley & Sons.)

reduced down to four or even two without any dramatic increase in prediction error. This effect was attributed to the high chemical selectivity of Raman spectroscopy. The number of samples and the low concentration levels used in this study highlight the potential transmission Raman for making lean and rapid calibrations early in the development of pharmaceutical formulations.

Forensic and security screening applications

Non-invasive detection of concealed explosives and illicit drugs. The recent heightened terrorist threat underlines the importance of robust security screening techniques with high chemical specificity. In particular the detection of liquid explosives is of concern as with this class of compounds no adequately effective screening methods are presently available. In a pilot study, Eliasson *et al.*[35] demonstrated the applicability of SORS in the detection of liquid explosives concealed within diffusely scattering plastic bottles. In this work, hydrogen peroxide, a precursor for homemade explosives, was detected through various packaging materials. Fig. 12 shows the results of probing a plastic sun lotion bottle (L'Oreal) containing a 30% aqueous solution of H_2O_2. The bottle was highly diffusely scattering and presented an insurmountable challenge to conventional Raman spectroscopy with the principal marker band of H_2O_2 (876 cm^{-1}) being overwhelmed with the Raman signal of container material. In contrast, SORS, after 'blind' automated data processing using two SORS spectra obtained at two different spatial offsets, clearly revealed the H_2O_2 Raman marker band. The experiments were performed using a continuous wave diode laser (830 nm, 250 mW) with an acquisition time of 1 s. The conclusions were further substantiated by a study of Bloomfield *et al.*[35] in which they looked at a wider range of samples and at factors which determine the optimum spatial offsets and acquisition times.

One the most challenging applications is the interrogation of substances either heavily fluorescing or highly absorbing at the laser or Raman wavelengths. Examples of such a substance are Coca Cola, red wine and milk. A study by Hargreaves *et al.*[78] demonstrated the ability of SORS to detect the presence of hydrogen peroxide solution even when mixed with such highly challenging substances.

In related experiments SORS was also successfully used in the detection of powder samples (chosen to mimic illicit drugs) in envelopes and translucent non-metallic containers, and of cocaine dissolved in rum and concealed in brown glass bottles (a method used by smugglers).[29,79,33,80]

Detection of concealed ivory. Hargreaves *et al.*[81] demonstrated the feasibility of detecting smuggled ivory concealed with a layer of paint or varnish. Whilst conventional Raman spectroscopy was capable of identifying ivory when covered with varnish (clear and red) it was not able to detect its presence when covered with a layer of paint (white and red). In contrast SORS was able to detect the ivory very cleanly in all the cases rendering accurately not only the intense phosphate Raman bands but also more subtle Raman bands of ivory collagen (see Fig. 13). The study also demonstrated the feasibility of detecting ivory through cloth, red card, polyethylene and Delrin blocks using SORS, tasks which defeated the conventional Raman technique.

Conclusions

The extended applicability of Raman spectroscopy to probing deep areas of turbid samples facilitated by SORS and transmission Raman spectroscopy paves the way for a host of new applications across a wide range of fields, often with high societal relevance. Several new exciting potential applications are already emerging including the diagnosis of bone disease and breast cancer, chemically specific tomographic imaging of tissue, quality control and authentication of pharmaceutical products as well as the detection of explosives concealed in bottles. It is envisaged that many other applications will be developed in the coming years. The breadth of these applications is a consequence of the flexibility and straightforward adaptability of these methods to different conditions and different problems.

References

1 *Emerging Raman Applications and Techniques in Biomedical and Pharmaceutical Fields*, ed. P. Matousek and M. D. Morris, Springer, Heidelberg, 2010.
2 P. Matousek, I. P. Clark, E. R. C. Draper, M. D. Morris, A. E. Goodship, N. Everall, M. Towrie, W. F. Finney and A. W. Parker, *Appl. Spectrosc.*, 2005, **59**, 393–400.
3 P. Matousek, M. D. Morris, N. Everall, I. P. Clark, M. Towrie, E. Draper, A. Goodship and A. W. Parker, *Appl. Spectrosc.*, 2005, **59**, 1485–1492.
4 B. B. Das, F. Liu and R. R. Alfano, *Rep. Prog. Phys.*, 1997, **60**, 227–292.
5 J. C. Hebden, A. Gibson, R. Yusof, N. Everdell, E. M. C. Hillman, D. T. Delpy, S. R. Arridge, T. Austin, J. H. Meek and J. S. Wyatt, *Phys. Med. Biol.*, 2002, **47**, 4155–4166.
6 H. Koizumi, Y. Yamashita, A. Maki, T. Yamamoto, Y. Ito, H. Itagaki and R. Kennan, *J. Biomed. Opt.*, 1999, **4**, 403–413.
7 T. J. Pfefer, K. T. Schomacker, M. N. Ediger and N. S. Nishioka, *Appl. Opt.*, 2002, **41**, 4712–4721.
8 N. Ghosh, S. K. Majumder, H. S. Patel and P. K. Gupta, *Opt. Lett.*, 2005, **30**, 162–164.
9 L. Quan and N. Ramanujam, *Opt. Lett.*, 2002, **27**, 104–106.
10 S. C. Gebhart, S. K. Majumder and A. Mahadevan-Jansen, *Appl. Opt.*, 2007, **46**, 1343–1360.
11 J. Wu, Y. Wang, L. Perelman, I. Itzkan, R. Dasari and M. S. Feld, *Appl. Opt.*, 1995, **34**, 3425–3430.
12 P. Matousek, N. Everall, M. Towrie and A. W. Parker, *Appl. Spectrosc.*, 2005, **59**, 200–205.
13 N. Everall, T. Hahn, P. Matousek, A. W. Parker and M. Towrie, *Appl. Spectrosc.*, 2001, **55**, 1701–1708.
14 N. Everall, T. Hahn, P. Matousek, A. W. Parker and M. Towrie, *Appl. Spectrosc.*, 2004, **58**, 591–598.
15 M. D. Morris, P. Matousek, M. Towrie, A. W. Parker, A. E. Goodship and E. R. C. Draper, *J. Biomed. Opt.*, 2005, **10**, 014014.
16 P. Matousek, M. Towrie, A. Stanley and A. W. Parker, *Appl. Spectrosc.*, 1999, **53**, 1485–1489.
17 P. Matousek, M. Towrie, C. Ma, W. M. Kwok, D. Phillips, W. T. Toner and A. W. Parker, *J. Raman Spectrosc.*, 2001, **32**, 983–988.
18 P. Matousek, M. Towrie and A. W. Parker, *J. Raman Spectrosc.*, 2002, **33**, 238–242.
19 P. Matousek, *Chem. Soc. Rev.*, 2007, **36**, 1292–1304.
20 F. Ariese, H. Meuzelaar, M. M. Kerssens, J. B. Buijs and C. Gooijer, *Analyst*, 2008, **134**, 1192–1197.
21 I. Iping Petterson, P. Dvorak, J. Buijs, C. Gooijer and F. Ariese, *Proceedings of the 6th International SPEC Conference, Manchester*, 2010.
22 M. V. Schulmerich, K. A. Dooley, T. M. Vanasse, S. A. Goldstein and M. D. Morris, *Appl. Spectrosc.*, 2007, **61**, 671–678.
23 E. Widjaja, C. Z. Li and M. Garland, *Organometallics*, 2002, **21**, 1991–1997.
24 E. Widjaja, N. J. Crane, T. C. Chen, M. D. Morris, M. A. Ignelzi and B. R. McCreadie, *Appl. Spectrosc.*, 2003, **57**, 1353–1362.

25 J. Y. Ma and D. Ben-Amotz, *Appl. Spectrosc.*, 1997, **51**, 1845–1848.
26 M. V. Schulmerich, W. F. Finney, V. Popescu, M. D. Morris, T. M. Vanasse and S. A. Goldstein, *Proceedings of SPIE: Biomedical Vibrational Spectroscopy III: Advances in Research and Industry*, 2006, vol. 6093, p. 60930O.
27 M. V. Schulmerich, W. F. Finney, R. A. Fredricks and M. D. Morris, *Appl. Spectrosc.*, 2006, **60**, 109–114.
28 P. Matousek, E. R. C. Draper, A. E. Goodship, I. P. Clark, K. L. Ronayne and A. W. Parker, *Appl. Spectrosc.*, 2006, **60**, 758–763.
29 P. Matousek, *Appl. Spectrosc.*, 2006, **60**, 1341–1347.
30 M. V. Schulmerich, K. A. Dooley, M. D. Morris, T. M. Vanasse and S. A. Goldstein, *J. Biomed. Opt.*, 2006, **11**, 060502.
31 M. V. Schulmerich, M. D. Morris, T. M. Vanasse and S. A. Goldstein, *Proceedings of SPIE: Advanced Biomedical and Clinical Diagnostic Systems V*, 2007, vol. 6430, p. 643009.
32 B. Depret, P. Verkerk and D. Hennequin, *Opt. Commun.*, 2002, **211**, 31–38.
33 C. Eliasson, N. A. Macleod and P. Matousek, *Anal. Chem.*, 2007, **79**, 8185–8189.
34 J. R. Maher and A. J. Berger, *Appl. Spectrosc.*, 2010, **64**, 61–65.
35 M. Bloomfield, P. W. Loeffen and P. Matousek, Detection of concealed substances in sealed opaque plastic and coloured glass containers using SORS, *Proc. SPIE*, 2010, **7838**, 783808-1–783808-15.
36 P. Matousek and A. W. Parker, *Appl. Spectrosc.*, 2006, **60**, 1353–1357.
37 J. Johansson, S. Pettersson and S. Folestad, *J. Pharm. Biomed. Anal.*, 2005, **39**, 510–516.
38 P. Matousek and A. W. Parker, *J. Raman Spectrosc.*, 2007, **38**, 563–567.
39 B. Schrader and G. Bergmann, *Fresenius' Z. Anal. Chem.*, 1967, **225**, 230–247.
40 H. Wikstrom, I. R. Lewis and L. S. Taylor, *Appl. Spectrosc.*, 2005, **59**, 934–941.
41 M. Kim, H. Chung, Y. A. Woo and M. S. Kemper, *Anal. Chim. Acta*, 2006, **579**, 209–216.
42 J. Kim, J. Noh, H. Chung, Y. A. Woo, M. S. Kemper and Y. Lee, *Anal. Chim. Acta*, 2007, **598**, 280–285.
43 S. C. Park, M. Kim, J. Noh, H. Chung, Y. Woo, J. Lee and M. S. Kemper, *Anal. Chim. Acta*, 2007, **593**, 46–53.
44 M. Kim, H. Chung, Y. A. Woo and M. S. Kemper, *Anal. Chim. Acta*, 2007, **587**, 200–207.
45 N. Townshend, D. Littlejohn, A. Nordon, M. Myrick, J. Andrews and P. Dallin, *PhAT Raman Analysis of Pharmaceutical Tablets*, 2009, unpublished.
46 J. Johansson, O. Svensson, S. Folestad, A. Sparen and M. Claybourn, *Proceedings of the 36th FACSS, Louisville*, 2009.
47 N. Everall, P. Matousek, N. Macleod, K. L. Ronayne and I. P. Clark, *Appl. Spectrosc.*, 2010, **64**, 52–60.
48 N. Everall, I. Priestnall, P. Dallin, J. Andrews, I. Lewis, K. Davis, H. Owen and M. W. George, *Appl. Spectrosc.*, 2010, **64**, 476–484.
49 P. Matousek, *Appl. Spectrosc.*, 2007, **61**, 845–854.
50 C. Eliasson and P. Matousek, *J. Raman Spectrosc.*, 2008, **39**, 633–637.
51 K. Buckley, A. Goodship, N. A. Macleod, A. W. Parker and P. Matousek, *Anal. Chem.*, 2008, **80**, 6006–6009.
52 M. V. Schulmerich, J. H. Cole, K. A. Dooley, M. D. Morris, J. M. Kreider, S. A. Goldstein, S. Srinivasan and B. W. Pogue, *J. Biomed. Opt.*, 2008, **13**, 020506.
53 S. Srinivasan, M. Schulmerich, J. H. Cole, K. A. Dooley, J. M. Kreider, B. W. Pogue, M. D. Morris and S. A. Goldstein, *Opt. Express*, 2008, **16**, 12190–12200.
54 C. M. Carpenter, B. W. Pogue, S. Jiang, H. Dehghani, X. Wang, K. D. Paulsen, W. A. Wells, J. Forero, C. Kogel, J. B. Weaver, S. P. Poplack and P. A. Kaufman, *Opt. Lett.*, 2007, **32**, 933–935.
55 N. A. Macleod, A. Goodship, A. W. Parker and P. Matousek, *Anal. Chem.*, 2008, **80**, 8146–8152.
56 N. A. Macleod and P. Matousek, *Appl. Spectrosc.*, 2008, **62**, 291A–304A.
57 P. Matousek and N. Stone, *Analyst*, 2009, **134**, 1058–1066.
58 A. Carden and M. D. Morris, *J. Biomed. Opt.*, 2000, **5**, 259–268.
59 E. R. C. Draper, M. D. Morris, N. P. Camacho, P. Matousek, M. Towrie, A. W. Parker and A. E. Goodship, *J. Bone Miner. Res.*, 2005, **20**, 1968–1972.
60 B. R. McCreadie, M. D. Morris, T. Chen, D. S. Rao, W. F. Finney, E. Widjaja and S. A. Goldstein, *Bone*, 2006, **39**, 1190–1195.
61 M. V. Schulmerich, J. H. Cole, J. M. Kreider, F. Esmonde-White, K. A. Dooley, S. A. Goldstein and M. D. Morris, *Appl. Spectrosc.*, 2009, **63**, 286–295.
62 R. Baker, P. Matousek, K. L. Ronayne, A. W. Parker, K. Rogers and N. Stone, *Analyst*, 2007, **132**, 48–53.
63 N. Stone, R. Baker, K. Rogers, A. W. Parker and P. Matousek, *Analyst*, 2007, **132**, 899–905.
64 P. Matousek and N. Stone, *J. Biomed. Opt.*, 2007, **12**, 024008.
65 A. S. Haka, K. E. Shafer-Peltier, M. Fitzmaurice, J. Crowe, R. R. Dasari and M. S. Feld, *Cancer Res.*, 2002, **62**, 5375–5380.
66 R. N. Baker, K. D. Rogers, N. Shepherd and N. Stone, *Br. J. Cancer*, submitted.
67 N. Stone and P. Matousek, *Cancer Res.*, 2008, **68**, 4424–4430.
68 M. D. Keller, S. K. Majumder and A. Mahadevan-Jansen, *Opt. Lett.*, 2009, **34**, 926–928.
69 N. Stone, K. Faulds, D. Graham and P. Matousek, *Anal. Chem.*, 2010, **82**, 3969–3973.
70 R. Mukhopadhyay, *Anal. Chem.*, 2007, **79**, 2622–2627.
71 C. Eliasson and P. Matousek, *Anal. Chem.*, 2007, **79**, 1696–1701.
72 C. Ricci, C. Eliasson, N. A. Macleod, P. Newton, P. Matousek and S. G. Kazarian, *Anal. Bioanal. Chem.*, 2007, **389**, 1525–1532.
73 J. Johansson, A. Sparen, O. Svensson, S. Folestad and M. Claybourn, *Appl. Spectrosc.*, 2007, **61**, 1211–1218.
74 C. Eliasson, N. A. Macleod, L. C. Jayes, F. C. Clarke, S. V. Hammond, M. R. Smith and P. Matousek, *J. Pharm. Biomed. Anal.*, 2008, **47**, 221–229.
75 M. D. Hargreaves, N. A. Macleod, M. R. Smith, D. Andrews, S. V. Hammond and P. Matousek, *J. Pharm. Biomed. Anal.*, 2011, **54**, 463–468.
76 A. Aina, M. D. Hargreaves, P. Matousek and J. C. Burley, *Analyst*, 2010, **135**, 2328–2333.
77 M. Fransson, J. Johansson, A. Sparen and O. Svensson, *J. Chemom.*, 2010, DOI: 10.1002/cem.1330.
78 M. D. Hargreaves and P. Matousek, *Proceedings of SPIE: Optics and Photonics for Counter terrorism and Crime Fighting V*, 2009, **7486**, 74860B-1–74860B-7.
79 C. Eliasson, N. A. Macleod and P. Matousek, *Vib. Spectrosc.*, 2008, **48**, 8–11.
80 C. Eliasson, N. A. Macleod and P. Matousek, *Anal. Chim. Acta*, 2008, **607**, 50–53.
81 M. D. Hargreaves, N. A. Macleod, V. L. Brewster, T. Munshi, H. G. M. Edwards and P. Matousek, *J. Raman Spectrosc.*, 2009, **40**, 1875–1880.

G Model
PBA-7919; No. of Pages 8

ARTICLE IN PRESS

Journal of Pharmaceutical and Biomedical Analysis xxx (2010) xxx–xxx

Contents lists available at ScienceDirect

Journal of Pharmaceutical and Biomedical Analysis

journal homepage: www.elsevier.com/locate/jpba

Review

Recent advances in the application of transmission Raman spectroscopy to pharmaceutical analysis

Kevin Buckley[a,b], Pavel Matousek[a,b,c,*]

[a] Central Laser Facility, Research Complex at Harwell, Science and Technology Facilities Council, Rutherford Appleton Laboratory, Didcot, Oxfordshire, OX11 0QX, UK
[b] Institute of Orthopaedics and Musculoskeletal Science, University College London, Royal National Orthopaedic Hospital, Stanmore, Middlesex, HA7 4LP, UK
[c] Cobalt Light Systems Ltd., The Electron Building, Fermi Avenue, Harwell Science & Innovation Campus, Didcot, Oxfordshire, OX11 0QR, UK

ARTICLE INFO

Article history:
Received 10 September 2010
Received in revised form 27 October 2010
Accepted 29 October 2010
Available online xxx

Keywords:
Transmission Raman
Quantitative analysis
Pharmaceutical formulations
Quality control

ABSTRACT

This article reviews recent advances in transmission Raman spectroscopy and its applications, from the perspective of pharmaceutical analysis. The emerging concepts enable rapid non-invasive volumetric analysis of pharmaceutical formulations and could lead to many important applications in pharmaceutical settings, including quantitative bulk analysis of intact pharmaceutical tablets and capsules in quality and process control.

Contents

1. Introduction

In a number of analytical applications in the pharmaceutical environment it is often desirable to characterise the bulk chemical constituency of intact samples rapidly, non-destructively and non-invasively. Raman spectroscopy holds a particular promise in this area due to its inherently high chemical specificity (substantially higher than that of its competitor: near-infrared absorption (NIR) spectroscopy), its ability to probe samples in the presence of water, and its potential for high penetration depth into non-absorbing or weakly absorbing turbid samples (similar to NIR absorption spectroscopy), such as those typically present within pharmaceutical formulations.

The higher chemical specificity of Raman spectroscopy compared with NIR absorption spectroscopy stems from the fact that NIR spectra consist of broad and overlapping bands which are typically high frequency overtone and combination bands of fundamental vibrational modes; the fundamental modes themselves are invisible to the technique. As NIR only detects combinations/overtones, it is only sensitive to anharmonic vibrations, i.e. predominantly *X*–H bonds. This is another reason for the lack of chemical information compared with MIR or Raman. In contrast, Raman spectroscopy permits the direct monitoring of fundamental vibrational modes (within the important finger print and phonon mode spectral regions) and exhibits much sharper bands [1]. Although the other main optical counterparts of Raman scattering

* Corresponding author at: Central Laser Facility, Research Complex at Harwell, Science and Technology Facilities Council, Rutherford Appleton Laboratory, Didcot, Oxfordshire, OX11 0QX, UK. Tel.: +44 0 1235 445377; fax: +44 0 1235 445693.
E-mail address: Pavel.Matousek@stfc.ac.uk (P. Matousek).

0731-7085/$ – see front matter.
doi:10.1016/j.jpba.2010.10.029

Please cite this article in press as: K. Buckley, P. Matousek, Recent advances in the application of transmission Raman spectroscopy to pharmaceutical analysis, J. Pharm. Biomed. Anal. (2010), doi:10.1016/j.jpba.2010.10.029

G Model
PBA-7919; No. of Pages 8
ARTICLE IN PRESS
2 K. Buckley, P. Matousek / Journal of Pharmaceutical and Biomedical Analysis xxx (2010) xxx–xxx

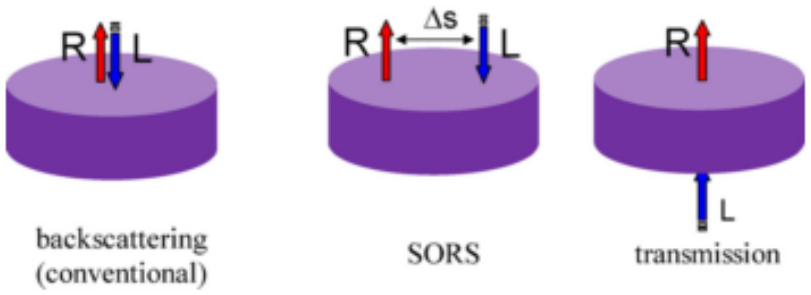

Fig. 1. Raman spectroscopy variants: conventional backscattering Raman, spatially offset Raman spectroscopy and transmission Raman spectroscopy. Legend: *R* – Raman light, *L* – laser beam and Δ*s* – spatial offset.

(mid-infrared (MIR) and to some extent terahertz (THz) spectroscopy) also offer high chemical specificity, their applications are typically restricted to dry samples, due to strong water absorption impeding their applicability. In addition, MIR spectroscopy is in general only applicable to very thin layers of samples unless the samples are substantially diluted. On the other hand, the Raman technique suffers from sensitivity to fluorescence which can sometime swamp the much weaker Raman signal. This problem can, however, often be circumvented by using near-infrared excitation [1].

Until recently the volumetric analysis of pharmaceutical samples such as tablets and capsules with Raman spectroscopy was hampered by severe sub-sampling [2,3]. This limitation stems from the widely used backscattering Raman collection geometry in which most Raman instruments operate. In this mode Raman signal is collected from the sample directly at the laser illumination zone. This geometry is widely used for its instrumental simplicity and ease of deployment.

Recently, a range of Raman techniques capable of penetrating substantially deeper into the sample than possible with the conventional Raman backscattering approach have emerged. These developments permitted new important applications in a number of disciplines [4]. This review focuses on one of these methods, transmission Raman spectroscopy, as it has considerable potential to become a particularly important tool in pharmaceutical analysis.

1.1. Transmission Raman spectroscopy

The development of transmission Raman spectroscopy for pharmaceutical applications was a spin out from the recent development of spatially offset Raman spectroscopy (SORS) [5,6], a method for isolating Raman signals from chemically distinct layers deep within turbid media. It stems from earlier research into deep Raman ultrafast methods and Raman photon migration research and is finding applications across a wide range of disciplines [7–16]. Although the transmission Raman technique was demonstrated in the early days of Raman spectroscopy [17], until recently its benefits for the non-invasive probing of the bulk content of samples had not been recognised and exploited in pharmaceutical settings. Transmission Raman spectroscopy can be considered a special modality of SORS, in which the laser beam and the Raman collection zone are separated to the extreme, both being on opposite sides of the sample. It was shown that this configuration exhibits special properties compared with conventional Raman spectroscopy that are well suited for the determination of the bulk content of turbid samples such as pharmaceutical capsules and tablets [18]. Crucially, one can also effectively suppress the sub-sampling in the *z*-direction (depth) [3] which plagues conventional Raman spectroscopy (extreme oversensitivity to the signals from within the vicinity of the laser illumination zone on sample surface) as well as any surface-generated Raman and fluorescence signals to which conventional backscattering Raman spectroscopy is overly sensitive [19].

The sub-sampling problem presents a severe limitation to the applicability of conventional Raman spectroscopy to probing pharmaceutical tablets (and capsules) as these samples are often highly heterogeneous and can also contain surface coatings or layers giving rise to strong Raman and fluorescence signals that reduce technique's sensitivity to the inner content of the sample [3]. The problem of sub-sampling was partially addressed in lateral dimensions by Wikstrom et al. [20] who used a wide-illumination with a conventional Raman collection backscattering geometry although the sub-sampling problem in the *z*-direction (depth), albeit reduced, still remained. This technique and the reduction of sub-sampling was further explored by a group of Chung [21–24]. The transmission Raman geometry addresses the sub-sampling problem further in the *z*-direction (depth) permitting a rapid and effective monitoring of the bulk content of pharmaceutical formulations (Fig. 1).

The reduction of the sub-sampling problem in the transmission Raman geometry was first demonstrated computationally by Matousek and Parker [18]. Numerical Monte-Carlo simulations were performed of a pharmaceutical tablet like object with a thin 'impurity' layer inserted at different depths and with wide illumination and collection areas (6 mm diameter in both the cases). The results (illustrated in Fig. 2) indicate that transposing the impurity from surface to a depth of 3 mm within a 4 mm thick tablet diminishes the signal in conventional backscattering Raman spectroscopy by 4 orders of magnitude. At this point, such signal would be typically overwhelmed by the surface Raman signal preventing the detection of this impurity layer by conventional means. In contrast, the transmission geometry yields a Raman signal level largely invariant (in this case, to within ±50% accuracy) to the depth of impurity layer. This result was in agreement with experimental observations. The Monte Carlo simulations also indicated a weak bias towards signals from the inner part of the tablet (see Fig. 2a). Experimental studies of layered pharmaceutical tablets have confirmed these predictions e.g., Townshend et al. [25] and Johansson et al. [26].

Everall et al. [27] further investigated theoretically the spatial resolution of transmission Raman spectroscopy in both lateral and depth dimensions from a standpoint of tomographic applications. Apart from looking at the spatial origin of the measured Raman signals, the research investigated homogeneity of the probing as a function of experimental geometry. The study examined the effect of incident beam size, Raman collection aperture, sample thickness and transport length. In this study it was predicted that the lateral resolution should worsen linearly with sample thickness (typically the spatial resolution was about 50% of the sample thickness). The lateral resolution was better at the sample surfaces (essentially

Please cite this article in press as: K. Buckley, P. Matousek, Recent advances in the application of transmission Raman spectroscopy to pharmaceutical analysis, J. Pharm. Biomed. Anal. (2010), doi:10.1016/j.jpba.2010.10.029

G Model
PBA-7919; No. of Pages 8
ARTICLE IN PRESS
K. Buckley, P. Matousek / Journal of Pharmaceutical and Biomedical Analysis xxx (2010) xxx–xxx

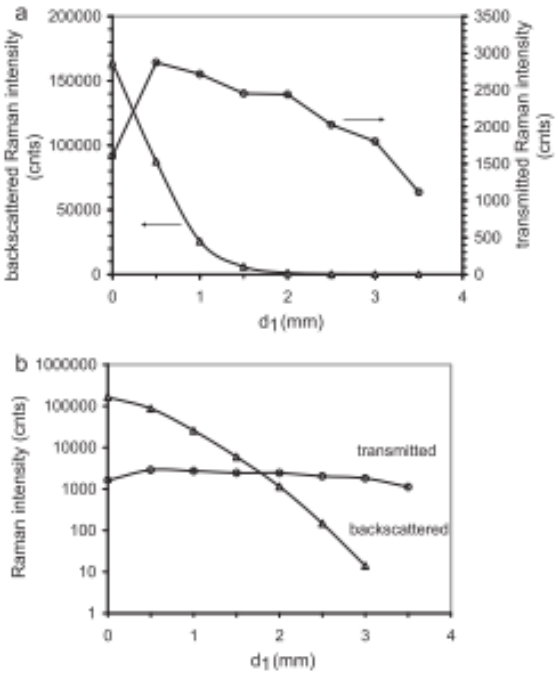

Fig. 2. Plot of calculated Raman intensities for the backscattering and transmission geometries versus depth (d_1) of the inter-layer (impurity) within a pharmaceutical tablet-like medium. The dependencies are the results of Monte Carlo simulations. The results are presented in (a) linear and (b) $\log_{10}$ plots.
Reprinted with permission from Matousek and Parker [18]. Copyright (2006). The Society for Applied Spectroscopy.

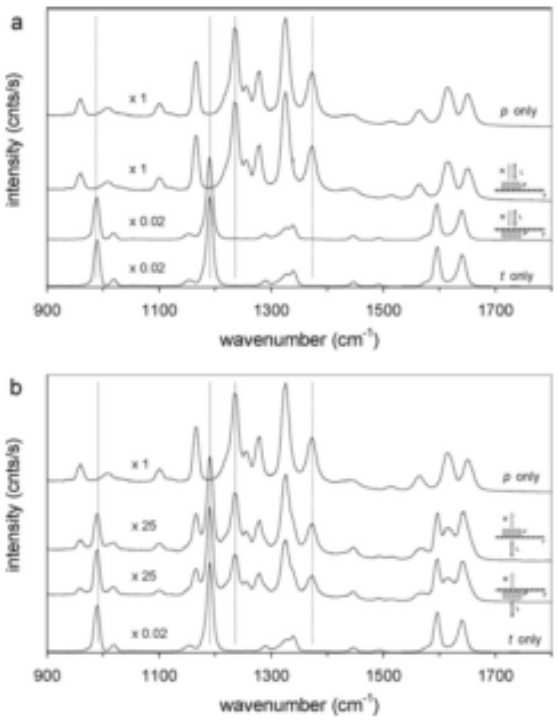

Fig. 4. The Raman spectra obtained from a two-layer sample (3.9 mm thick paracetamol tablet and 2 mm thick trans-stilbene powder layer) using (a) conventional backscattering geometry and (b) transmission geometry. The measurements are performed at two sample orientations, with paracetamol at the top and at the bottom of the trans-stilbene cell, as indicated in the graphs. The top and bottom spectra are those of paracetamol and trans-stilbene, respectively, obtained in separate experiments. The acquisition times were between 0.2 s and 10 s, with a laser power of 80 mW. The spectra are offset for clarity. Legend: p – paracetamol, t – trans-stilbene, R – Raman light, L – laser beam.
Reprinted with permission from Matousek and Parker [18]. Copyright (2006) The Society for Applied Spectroscopy.

determined by the probe beam diameter or the collection aperture) than that for objects buried deeply in the sample. In line with earlier observations the signal biased towards the mid-point of thick samples in transmission sampling was also established. This effect is depicted in Fig. 3 showing the Monte Carlo simulated Raman signal intensity as a function of depth of its origin.

In a subsequent study Everall et al. [28] looked experimentally at the spatial resolution and sensitivity of Raman spectroscopy in backscatter and transmission modes in turbid media. For the first time under such conditions the width and intensity of the point spread function has been accurately measured as a function of sample thickness and depth below the surface. In transmission mode,

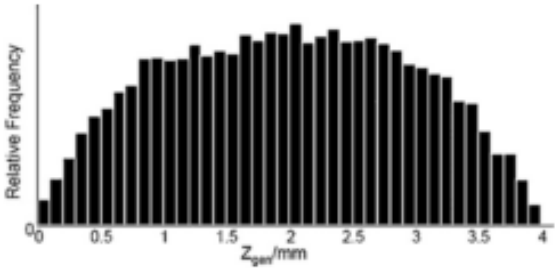

Fig. 3. Computed distribution of generation depths for all detected Raman photons assuming 4 mm thick sample, 0.5 mm probe beam, 1 mm collection zone and 80 μm transport length; the detected photons tended to be generated near the middle of the sample.
Reprinted with permission from Everall et al. [28]. Copyright (2010). The Society for Applied Spectroscopy.

the lateral resolution for objects in the bulk was shown to degrade linearly with sample thickness. The resolution was also shown to be much better for objects near either surface, being determined by the diameter of the probe beam and collection aperture irrespective of sample thickness. The objects in the bulk yielded higher signals than those at the surfaces in line with the preceding numerical simulations [27] and experimental findings [25–27]. The observations were also shown to be insensitive to the choice of transport length in the studied deep diffusion regime implying that a simple model can be used to predict instrument performance for given experimental conditions.

The ability of transmission Raman spectroscopy to access very deep areas of highly turbid samples and convey information on its bulk content was experimentally demonstrated by Matousek et al. [18] on a two-layer tablet-like sample of overall thickness ~6 mm. This is demonstrated in Fig. 4 where conventional backscattering and transmission Raman results are depicted. They were performed on a 3.9 mm thick tablet of paracetamol followed by a 2 mm thick layer of trans-stilbene powder. Whilst conventional backscattering Raman spectroscopy was capable of seeing only the surface layer presented to the instrument transmission Raman spectroscopy yielded signal contributions from both the layers within this thick and highly turbid sample. For a paracetamol tablet of 3.9 mm thickness the overall Raman signal strength was lower by a factor of 12 in transmission Raman geometry compared to the backscattering

Please cite this article in press as: K. Buckley, P. Matousek, Recent advances in the application of transmission Raman spectroscopy to pharmaceutical analysis, J. Pharm. Biomed. Anal. (2010), doi:10.1016/j.jpba.2010.10.029

G Model
PBA-7919; No. of Pages 8
ARTICLE IN PRESS
4 K. Buckley, P. Matousek / Journal of Pharmaceutical and Biomedical Analysis xxx (2010) xxx–xxx

measurement. Despite the reduced intensity of the signal, the transmission Raman configuration still permitted high quality Raman spectra to be acquired within seconds.

1.2. Raman signal enhancement using a 'photon diode'

Since signals can be substantially weaker in transmission Raman spectroscopy than in conventional backscattering Raman spectroscopy, it is often necessary to take steps to increase the signal-to-noise level and/or reduce the concentration detection threshold (limit of detection). These measures can include the optimisation of Raman collection system specifically for the transmission Raman geometry, the use of higher laser powers (permitted by considerably larger laser illumination areas in transmission Raman spectroscopy) or using longer acquisition times.

Another, more unconventional approach for boosting Raman signals by passive means, which is suitable for use with transmission Raman spectroscopy, was proposed and recently demonstrated by Matousek [29]. This concept uses a 'unidirectional' mirror placed in a close proximity of sample within the laser illumination zone to enhance the Raman signal. The role of this optical element is to prevent the loss of diffusely scattered photons lost from the sample at the laser coupling interface whilst permitting the laser beam to be transmitted through the optical element on the other side. The special mirror is effectively a multilayer dielectric optical bandpass or edge filter. The concept relies on the generic angular properties of dielectric filters for which the spectral profile shifts to shorter and shorter wavelengths as photons impact them at angles further from normal incidence. The increased coupling of laser radiation into the sample leads to a substantial boost of overall Raman signal generated within the sample. As the dielectric filters are typically produced as flat optical elements and the filters need to be in near-contact with the sample the sample should also be ideally flat, or at least not excessively curved. Ideal samples are therefore flat pharmaceutical tablets or powders. Although some curvature is acceptable its presence typically leads to the diminishment of the enhancement effect. Fig. 5 shows the performance of the enhancer with 6–7 mm thick powder formulation of paracetamol. An enhancement factor of 8.5 was achieved in this particular situation. The associated benefits to the signal-to-noise ratio is evidenced from the figure. The concept was also demonstrated to be viable with the SORS concept [30] as well as with conventional Raman and fluorescence spectroscopy [31].

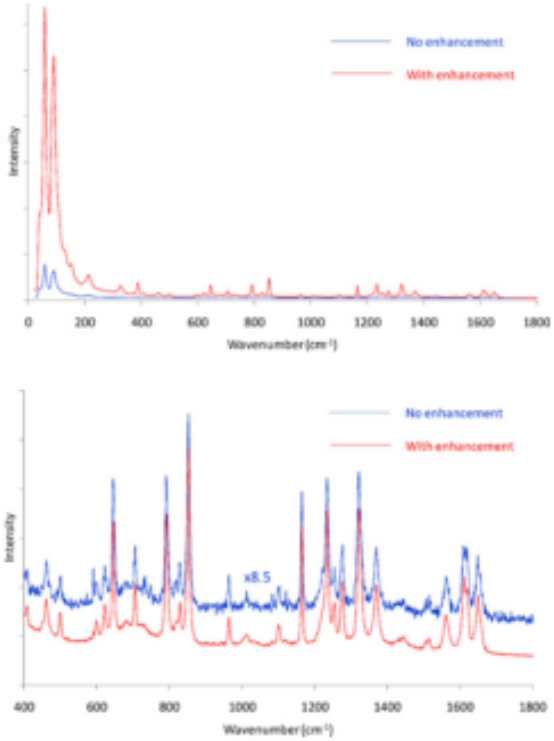

Fig. 5. The experimental demonstration of the enhancement of transmission Raman signal using a 'unidirectional' mirror ('photon diode') on a 6–7 mm thick powder sample of paracetamol. The Raman spectra were measured with and without the enhancing mirror. The acquisition time was 1 s.

2. Examples of pharmaceutical applications

2.1. Quantification of active pharmaceutical ingredients and excipients in pharmaceutical tablets and capsules

The quantitative analysis of pharmaceutical formulations is traditionally performed using HPLC. However, this technique is time and labour consuming as well as destructive to the sample. In many applications it would be highly advantageous to replace it with a bulk sensing method capable of rapid, non-destructive and non-invasive analysis. This requirement is addressed in some situations by NIR absorption spectroscopy although in a number of applications this method is hampered by technique's limited chemical specificity and a lack of robustness due to its high sensitivity to the physical properties of the sample (e.g., formulation particle size). Many of these deficiencies are largely suppressed or removed by Raman and, in particular, transmission Raman spectroscopy.

A complete displacement of HPLC methods by transmission Raman spectroscopy is unlikely to occur, as HPLC has a much lower concentration detection threshold and is capable of reaching trace level sensitivity. In contrast, Raman spectroscopy in general can typically detect species at concentrations of ~0.1% at best. However, the key advantages of Raman spectroscopy are that it is rapid and non-destructive, and is capable of providing information that is lost during the HPLC preparation process (e.g., information on the polymorphic content), it can also detect insoluble excipients. These factors can be crucially important in a number of quality control applications. These features are also likely to lead to a number of niche applications in the process control area.

The ability of transmission Raman spectroscopy to provide quantitative information on sample constitution was demonstrated experimentally by Johansson et al. [32]. In this study, 20 test tablets (3.3 mm thick) prepared in a laboratory environment were analysed. The quantity of the active pharmaceutical ingredient (API) was determined with a relative root mean square error of ±2.2% (see Fig. 6). The acquisition time in these measurements was 10 s and a laser power of 400 mW (785 nm) was used. The study was also performed in a conventional backscattering Raman geometry which yielded a lower relative accuracy (±2.9%) ascribed to the presence of sub-sampling. The transmission Raman method was also applied to pharmaceutical capsules yielding a relative accuracy of ±3.6%. The study indicated that the transmission Raman mode requires a leaner calibration model relative to conventional Raman spectroscopy and was capable of providing reasonably good accuracy even when based on only 2 or 3 calibration spectra (see Fig. 6).

In a parallel study Eliasson et al. [33] used a batch of 150 production line type formulations contained within white capsules prepared in a laboratory environment. The investigations showed that intense interfering Raman signals from the capsule shell were

Please cite this article in press as: K. Buckley, P. Matousek, Recent advances in the application of transmission Raman spectroscopy to pharmaceutical analysis, J. Pharm. Biomed. Anal. (2010), doi:10.1016/j.jpba.2010.10.029

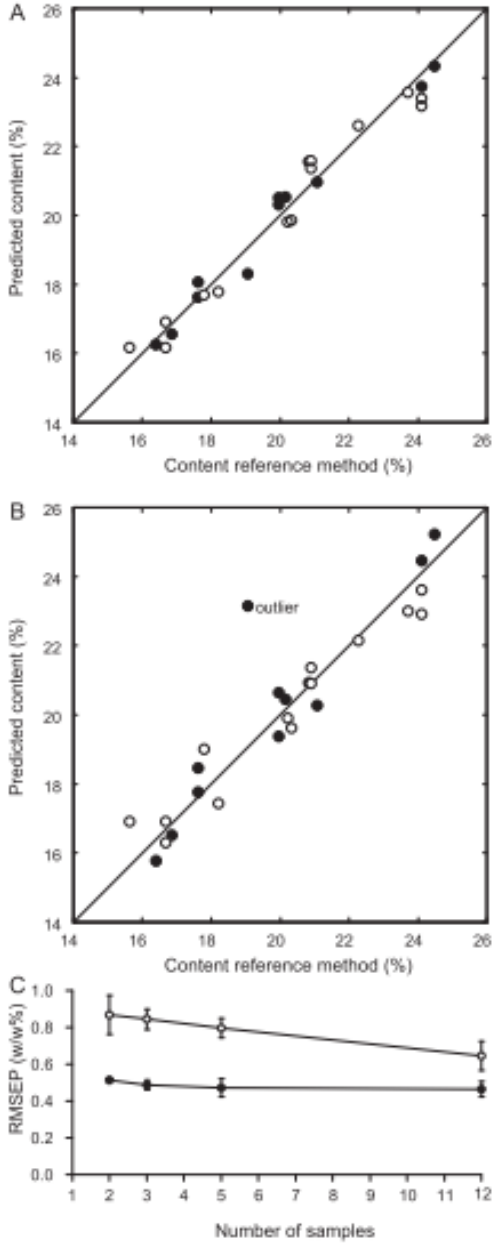

Fig. 6. Prediction of the concentration of propranolol tablets in two independent test sets; the original test sets (solid circles) and the exchanged test sets (open circles). Comparison of (A) Raman transmission (1 PLS component) and (B) Raman backscatter (1 PLS component). (C) Model robustness: the effect of reducing the number of samples in calibration models on the prediction errors for independent test sets. Solid circles represent the transmission mode while open circles represent the backscatter mode. The figure shows mean values of RMSEP for reduced models built on the original and the exchanged models, and the error bars show max and min values of RMSEP. The same test set was used for all reduced models originating from the same full model.
Reprinted with permission from Johansson et al. [32]. Copyright (2007) The Society for Applied Spectroscopy.

suppressed in the Raman transmission mode by a factor of 33 relative to conventional Raman measurement. This permitted the accurate quantification of the API with a relative root mean square error of ±1.2% with 5 s acquisition time. In this study the laser power at the sample was 250 mW and the laser wavelength 830 nm. The beam spot diameter on the sample was ~3–4 mm.

The ability to use widely defocused beams in transmission Raman spectroscopy also permits to increase the laser power without risking sample damage compared with traditional Raman microscopy setups. This property is useful in situations demanding further improvement of Raman signal-to-noise ratio or where reduction of exposure time is desirable. An additional Raman signal boost can also be achieved with the aforementioned 'photon diode' mirror. The larger illumination and collection areas also dramatically reduce requirements for the alignment of the sample in front of the instrument and further contribute to the effective averaging of the signals throughput the sample.

The two studies above used predominantly binary mixtures. The ability to quantify more complex formulations was studied by Hargreaves et al. [34]. This study focused on a detailed characterisation of transmission Raman spectroscopy from the standpoint of rapid quantitative analysis of pharmaceutical capsules using production relevant formulations; these comprised active pharmaceutical ingredient (API) and 3 common pharmaceutical excipients. For the first time, it was shown that the technique is largely insensitive to the amount of material held within the capsules. A single calibration model was developed using capsules of one fill weight, 100 mg, to a relative error of typically <3%. This model was then used to predict API concentration of capsules with varying fill weights (100–400 mg) and different shell colours. The relative root mean square error of prediction of the concentration of API for the main sample set (nominal content 75% (w/w)) was 1.5% with a 5 s acquisition time. The quantity of API was also predicted using the same model for capsules prepared with different generations of API (i.e., API manufactured via different processes) with a relative error within ~3% indicating a high degree of robustness. The study suggests that there could be significant benefits for the pharmaceutical industry to using this approach; both in terms of resource requirements from method development and maintenance but also in terms of validation and regulatory activities.

2.2. Quantification of polymorphs in pharmaceutical formulations

Recently, Aina et al. [35] demonstrated the ability of transmission Raman spectroscopy to quantify the polymorphic content of pharmaceutical formulations. This study represents another step on the way to establishing this emerging analytical technique as a practical tool in the area of process and quality control, as the quantification of polymorphs (crystalline structure) is of particular importance. It cannot be accomplished using traditional HPLC methods that rely on dissolution of sample and therefore involve associated loss of information on the polymorphic form within the original formulation. Alternative methods such as X-ray diffraction, NMR or differential scanning calorimetry suffer from limited sensitivity, complexity with safety management or long data acquisition times. In the study, flufenamic acid, a non-steroidal anti-inflammatory drug, was used as a model compound. The transmission Raman method was shown to provide a true bulk measurement of the composition, in a sharp contrast with conventional backscattering Raman method which provided unsatisfactory results due to a severe sub-sampling problem. For a model-free fit, the transmission Raman method yielded R^2 of 0.996 compared to the backscattering value of 0.802; for a partial least squares fit with a single component the TRS method accounted

Please cite this article in press as: K. Buckley, P. Matousek, Recent advances in the application of transmission Raman spectroscopy to pharmaceutical analysis, J. Pharm. Biomed. Anal. (2010), doi:10.1016/j.jpba.2010.10.029

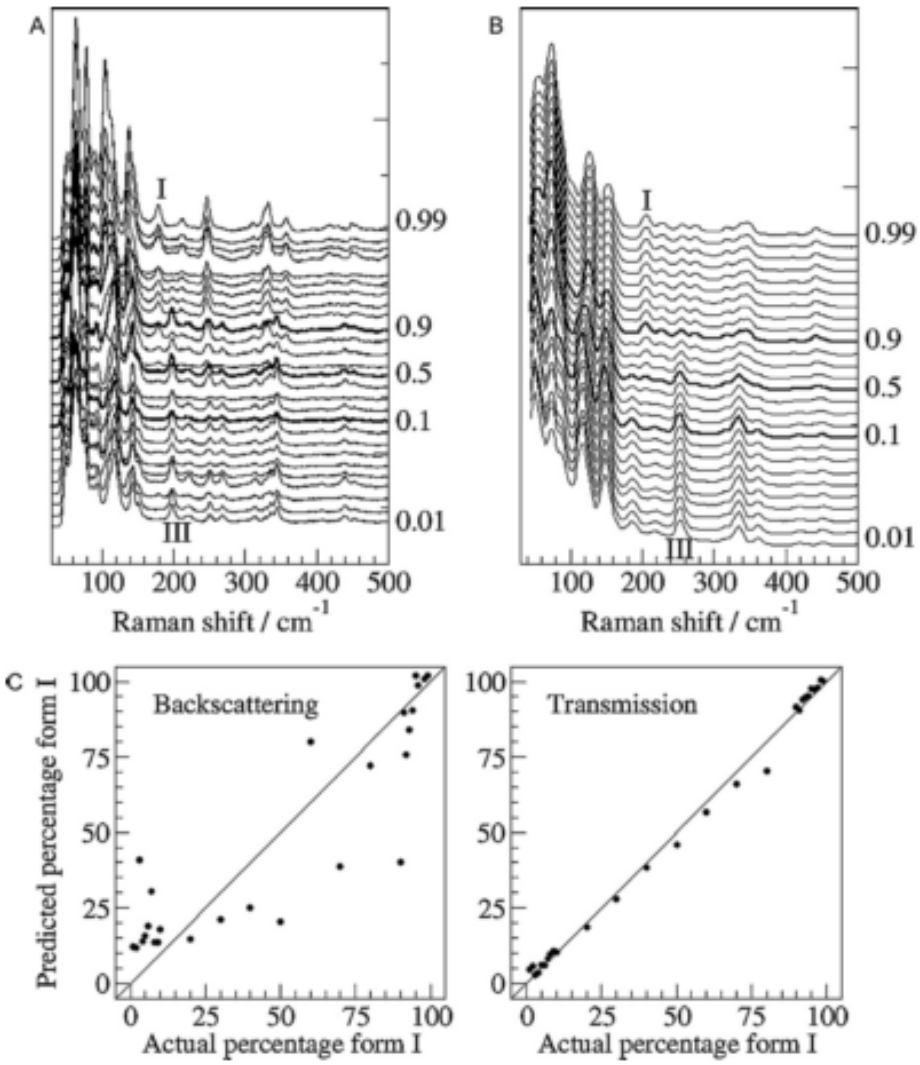

Fig. 7. Raman spectra of two polymorphic mixtures of flufenamic acid collected in (A) backscattering and (B) transmission geometry. Signature peaks for forms I and III are labelled. Composition (mole fraction of form I) is given on the right, spectra for 0.1, 0.5, 0.9 mixtures are in bold. The Raman spectra were recorded on different instruments with different spectral resolutions; full width at half maximum of the phenyl peak is 7 cm^{-1} for transmission mode and 4 cm^{-1} for backscattering). (C) Results of PLS analysis (validation plot, all data) for transmission and backscattering data.
Aina et al. [35]. /http://dx.doi.org/10.1039/C0AN00352B – reproduced by permission of The Royal Society of Chemistry).

for 98.09% of the variance in the data compared to 89.65% for the backscattering method (see Fig. 7).

The study also looked at the likely cause of the variability of the backscattering spectra associated with a sub-sampling issue. A series of 20 spectra were recorded on different areas of polymorphic form I, form III and the 50:50 mixture using conventional Raman spectroscopy. For mixtures, the reproducibility of the measurement was expected to be considerably lower and the standard deviation of the measurement higher. Indeed much higher standard deviation was observed for the 50:50 mixture compared with the pure forms clearly indicating the presence of a sub-sampling problem. It was therefore concluded that the use of a Raman microscopy in conventional backscattering geometry, and the associated small sample volume, is not appropriate for accurately measuring the composition of bulk samples, even when great care is taken to reduce lateral sub-sampling problems, e.g. by co-milling samples prior to measurement to facilitate thorough sample mixing and by rastering the laser over a 50 μm × 50 μm area.

Further scrutiny of the Raman spectra also revealed a systematic trend in which more of the spectra captured using the backscattering geometry resembled form III than form I. This systematic over-sampling of form III was suggestive of surface segregation of the mixed samples. Such surface segregation was confirmed by scanning electron microscopy (SEM) demonstrating that co-milling led to a greater size reduction of form III than form I. Crucially, the transmission Raman spectroscopy overcame all these issues by more effectively sampling the volume of the tablets.

In a recent study Fransson et al. [36] investigated the accuracy of the quantification of pharmaceutical tablets with transmission Raman spectroscopy as a function of the type of chemometric

Please cite this article in press as: K. Buckley, P. Matousek, Recent advances in the application of transmission Raman spectroscopy to pharmaceutical analysis, J. Pharm. Biomed. Anal. (2010), doi:10.1016/j.jpba.2010.10.029

method used to analyse data. Several multivariate approaches were investigated including partial least squares (PLS), multivariate curve resolution (MCR), classical least squares (CLS), curve fitting and peak ratios were included for comparison. MCR, CLS and PLS gave comparable results with relative prediction errors for an independent test set in the range of 2.4–3.4%. Curve fitting and peak ratios gave higher prediction errors, typically around 4 and 6%, respectively. The study also noted that the number of samples and concentration levels needed for calibration could be reduced down to four or even two without any major increase in prediction error. This effect was attributed to a higher chemical selectivity of Raman spectroscopy. For PLS, MCR and CLS, the use of very few samples and concentration levels shows the potential for making lean and rapid calibrations, using transmission Raman, early in the development of pharmaceutical formulations. With PLS data processing there is the added benefit that the selective Raman spectra coupled to a calibration model with few components results in easy to interpret loadings. For CLS, MCR and the curve-fitting methods, the interpretation is always straightforward since they use, or obtain, spectral components of pure drug substance and excipients.

2.3. Sample presentation and calibration transfer

Sample presentation can be a critical issue when applying spectroscopic techniques to solid formulations. This is a well studied issue with NIR spectroscopy [37]. In this context, the robustness towards sample presentation was investigated for both transmission and backscatter Raman geometries by tilting a tablet in the sample well by Sparen et al. [38]. The results demonstrate that a slight or moderate tilt does not have any significant effect on the predicted concentration, nor does turning the tablet upside down. However, when a heavy tilt is imposed the predictions can be severely affected. Similar results were obtained for backscattering mode concluding that the sample presentation can be considered to be robust in both the transmission and backscatter geometries.

Calibration transfer has also been extensively studied for NIR absorption spectroscopy [39–43]. With this method elaborate means are often needed to ensure accurate and precise performance after transferring a qualitative or quantitative calibration from one instrument to another. This desire is driven by global nature of manufacturing where a single drug can be manufactured at several sites across the world. In a feasibility study performed by Sparen et al. [38], the effect on the accuracy of quantification was investigated when transferring a calibration developed on one Raman instrument to another. Predictions from spectra measured on the second instrument, using a calibration developed on the first device, gave large prediction errors, mainly consisting of a bias. Applying a spectral pre-treatment, however dramatically reduced the prediction error. The feasibility study indicates that calibration transfer techniques, which are well established for NIR spectroscopy, may be directly applicable to Raman spectroscopy although more work is needed in this area.

3. Conclusions

A combination of the benefits of transmission Raman spectroscopy: the ability to yield highly chemical specific information, the ability to probe water containing samples and the ability to obtain quantitative volumetric data from thick and highly turbid samples, unlocks a range of new applications in pharmaceutical settings. These include rapid volumetric quantification of API/excipients and of polymorphs within intact tablets and capsules or powders. Perhaps most importantly, the technique is experimentally straightforward and can be combined with the existing multivariate techniques.

References

[1] M.J. Pelletier, Analytical Applications of Raman Spectroscopy, Blackwell Science, Oxford, 1999.
[2] H. Wang, C.K. Mann, T.J. Vickers, Effect of powder properties on the intensity of Raman scattering by crystalline solids, Appl. Spectrosc. 56 (2002) 1538–1544.
[3] J. Johansson, S. Pettersson, S. Folestad, Characterization of different laser irradiation methods for quantitative Raman tablet assessment, J. Pharm. Biomed. Anal. 39 (2005) 510–516.
[4] P. Matousek, M.D. Morris, Emerging Raman Applications and Techniques in Biomedical and Pharmaceutical Fields, Springer, Heidelberg, 2010.
[5] P. Matousek, I.P. Clark, E.R.C. Draper, M.D. Morris, A.E. Goodship, N. Everall, M. Towrie, W.F. Finney, A.W. Parker, Subsurface probing in diffusely scattering media using spatially offset Raman spectroscopy, Appl. Spectrosc. 59 (2005) 393–400.
[6] P. Matousek, M.D. Morris, N. Everall, I.P. Clark, M. Towrie, E. Draper, A. Goodship, A.W. Parker, Numerical simulations of subsurface probing in diffusely scattering media using spatially offset Raman spectroscopy, Appl. Spectrosc. 59 (2005) 1485–1492.
[7] J. Wu, Y. Wang, L. Perelman, I. Itzkan, R. Dasari, M.S. Feld, Three-dimensional imaging of objects embedded in turbid media with fluorescence and Raman spectroscopy, Appl. Optics 34 (1995) 3425–3430.
[8] P. Matousek, N. Everall, M. Towrie, A.W. Parker, Depth profiling in diffusely scattering media using Raman spectroscopy and picosecond kerr gating, Appl. Spectrosc. 59 (2005) 200–205.
[9] N. Everall, T. Hahn, P. Matousek, A.W. Parker, M. Towrie, Picosecond time-resolved Raman spectroscopy of solids: capabilities and limitations for fluorescence rejection and the influence of diffuse reflectance, Appl. Spectrosc. 55 (2001) 1701–1708.
[10] N. Everall, T. Hahn, P. Matousek, A.W. Parker, M. Towrie, Photon migration in Raman spectroscopy, Appl. Spectrosc. 58 (2004) 591–597.
[11] P. Matousek, M. Towrie, A. Stanley, A.W. Parker, Efficient rejection of fluorescence from Raman spectra using picosecond kerr gating, Appl. Spectrosc. 53 (1999) 1485–1489.
[12] M.V. Schulmerich, W.F. Finney, R.A. Fredricks, M.D. Morris, Subsurface Raman spectroscopy and mapping using a globally illuminated non-confocal fiber-optic array probe in the presence of Raman photon migration, Appl. Spectrosc. 60 (2006) 109–114.
[13] M.V. Schulmerich, K.A. Dooley, M.D. Morris, T.M. Vanasse, S.A. Goldstein, Transcutaneous fiber optic Raman spectroscopy of bone using annular illumination and a circular array of collection fibers, J. Biomed. Opt. 11 (2006) 060502.
[14] P. Matousek, Deep non-invasive Raman spectroscopy of living tissue and powders, Chem. Soc. Rev. 36 (2007) 1292–1304.
[15] N.A. Macleod, P. Matousek, Deep noninvasive Raman spectroscopy of turbid media, Appl. Spectrosc. 62 (2008) 291A–304A.
[16] P. Matousek, N. Stone, Emerging concepts in deep Raman spectroscopy of biological tissue, Analyst 134 (2009) 1058–1066.
[17] B. Schrader, G. Bergmann, Die Intensitat Des Ramanspektrums Polykristalliner Substanzen. I. Strahlungsbilanz Von Substanz Und Probenanordnung, Zeitschrift fur Analytische Chemie Fresenius 225 (1967) 230–247.
[18] P. Matousek, A.W. Parker, Bulk Raman analysis of pharmaceutical tablets, Appl. Spectrosc. 60 (2006) 1353–1357.
[19] P. Matousek, A.W. Parker, Non-invasive probing of pharmaceutical capsules using transmission Raman spectroscopy, J. Raman Spectrosc. 38 (2007) 563–567.
[20] H. Wikstrom, I.R. Lewis, L.S. Taylor, Comparison of sampling techniques for in-line monitoring using Raman spectroscopy, Appl. Spectrosc. 59 (2005) 934–941.
[21] M. Kim, H. Chung, Y.A. Woo, M.S. Kemper, New reliable Raman collection system using the wide area illumination (WAI) scheme combined with the synchronous intensity correction standard for the analysis of pharmaceutical tablets, Anal. Chim. Acta 579 (2006) 209–216.
[22] J. Kim, J. Noh, H. Chung, Y.A. Woo, M.S. Kemper, Y. Lee, Direct, non-destructive quantitative measurement of an active pharmaceutical ingredient in an intact capsule formulation using Raman spectroscopy, Anal. Chim. Acta 598 (2007) 280–285.
[23] S.C. Park, M. Kim, J. Noh, H. Chung, Y. Woo, J. Lee, M.S. Kemper, Reliable and fast quantitative analysis of active ingredient in pharmaceutical suspension using Raman spectroscopy, Anal. Chim. Acta 593 (2007) 46–53.
[24] M. Kim, H. Chung, Y.A. Woo, M.S. Kemper, A new non-invasive, quantitative Raman technique for the determination of an active ingredient in pharmaceutical liquids by direct measurement through a plastic bottle, Anal. Chim. Acta 587 (2007) 200–207.
[25] N. Townshend, D. Littlejohn, A. Nordon, M. Myrick, J. Andrews, P. Dallin, PhAT Raman analysis of pharmaceutical tablets, 2009, unpublished study.
[26] J. Johansson, O. Svensson, S. Folestad, A. Sparen, M. Claybourn, Transmission Raman Spectroscopy for Robust Tablet Assessment, FACSS Conference Proceedings, (abstract 300) Louisville, Kentucky, 2009, p. 131.
[27] N. Everall, P. Matousek, N. Macleod, K.L. Ronayne, I.P. Clark, Temporal and spatial resolution in transmission Raman sectroscopy, Appl. Spectrosc. 64 (2010) 52–60.
[28] N. Everall, I. Priestnall, P. Dallin, J. Andrews, I. Lewis, K. Davis, H. Owen, M.W. George, Measurement of spatial resolution and sensitivity in transmission and backscattering Raman spectroscopy of opaque samples: impact on pharmaceutical quality control and Raman tomography, Appl. Spectrosc. 64 (2010) 476–484.

Please cite this article in press as: K. Buckley, P. Matousek, Recent advances in the application of transmission Raman spectroscopy to pharmaceutical analysis, J. Pharm. Biomed. Anal. (2010), doi:10.1016/j.jpba.2010.10.029

[29] P. Matousek, Raman signal enhancement in deep spectroscopy of turbid media, Appl. Spectrosc. 61 (2007) 845–854.
[30] C. Eliasson, P. Matousek, Passive signal enhancement in spatially offset Raman spectroscopy, J. Raman Spectrosc. 39 (2008) 633–637.
[31] K. Buckley, A. Goodship, N.A. Macleod, A.W. Parker, P. Matousek, Technique for enhancing signal in conventional backscattering fluorescence and Raman spectroscopy of turbid media, Anal. Chem. 80 (2008) 6006–6009.
[32] J. Johansson, A. Sparen, O. Svensson, S. Folestad, M. Claybourn, Quantitative transmission Raman spectroscopy of pharmaceutical tablets and capsules, Appl. Spectrosc. 61 (2007) 1211–1218.
[33] C. Eliasson, N.A. Macleod, L.C. Jayes, F.C. Clarke, S.V. Hammond, M.R. Smith, P. Matousek, Non-invasive quantitative assessment of the content of pharmaceutical capsules using transmission Raman spectroscopy, J. Pharm. Biomed. Anal. 47 (2008) 221–229.
[34] M.D. Hargreaves, N.A. Macleod, M.R. Smith, D. Andrews, S.V. Hammond, P. Matousek, Characterisation of transmission Raman spectroscopy for rapid quantitative analysis of intact multi-component pharmaceutical capsules, J. Pharm. Biomed. Anal. (2010).
[35] A. Aina, M.D. Hargreaves, P. Matousek, J.C. Burley, Transmission Raman spectroscopy as a tool for quantifying polymorphic content of pharmaceutical formulations, Analyst 135 (2010) 2328–2333.
[36] M. Fransson, J. Johansson, A. Sparen, O. Svensson, Comparison of multivariate methods for quantitative determination with transmission Raman spectroscopy in pharmaceutical formulations, J. Chemometr. (2010), doi:10.1002/cem.1330.
[37] A. Sparen, M. Malm, M. Josefson, S. Folestad, J. Johansson, Light leakage effects with different sample holder geometries in quantitative near-infrared transmission spectroscopy of pharmaceutical tablets, Appl. Spectrosc. 56 (2002) 586–592.
[38] A. Sparen, J. Johansson, O. Svensson, S. Folestad, M. Claybourn, Transmission Raman spectroscopy for quantitative analysis of pharmaceutical solids, Am. Pharm. Rev. (2009).
[39] H. Leion, S. Folestad, M. Josefson, A. Sparen, Evaluation of basic algorithms for transferring quantitative multivariate calibrations between scanning grating and FT NIR spectrometers, J. Pharm. Biomed. Anal. 37 (2005) 47–55.
[40] E.L. Bergman, H. Brage, M. Josefson, O. Svensson, A. Sparen, NIR News 14 (2003) 10–11.
[41] E.L. Bergman, H. Brage, M. Josefson, O. Svensson, A. Sparen, Transfer of NIR calibrations for pharmaceutical formulations between different instruments, J. Pharm. Biomed. Anal. 41 (2006) 89–98.
[42] O.E. de Noord, Multivariate calibration standardisation, Chemom. Intell. Lab. Syst. 25 (1994) 85–97.
[43] T. Fearn, Standardisation and calibration transfer for near infrared instruments: a review, J. Near Infrared Spectrosc. 9 (2001) 229–244.

Please cite this article in press as: K. Buckley, P. Matousek, Recent advances in the application of transmission Raman spectroscopy to pharmaceutical analysis, J. Pharm. Biomed. Anal. (2010), doi:10.1016/j.jpba.2010.10.029

References

1. Galilei G., *Dialogues Concerning Two New Sciences*, (1638) [Translated – Crew H. & De Salvio A. (1914)], (Dover Publications Inc., New York, N.Y., U.S.A., **1954**)

2. Lees S., Considerations regarding the structure of the mammalian mineralized osteoid from viewpoint of the generalized packing model, *Connective Tissue Research*, **16(4)**:281-303, (1987)

3. Zioupos P., Currey J.D. & Casinos A., Exploring the effects of hypermineralisation in bone tissue by using an extreme biological example, *Connective Tissue Research*, **41(3)**:229-248, (2000)

4. Vose G.P. & Kubala A., Bone Strength - Its Relationship to X-Ray Determined Ash Content, *Human Biology*, **33**:261, (1959)

5. Currey J.D. The Mechanical Consequences of Variation in the Mineral Content of Bone, *Journal of Biomechanics*, **2**:1-11, (1969)

6. **Buckley K.,** Goodship A., Macleod N.A., Parker A.W. & Matousek P., Technique for Enhancing Signal in Conventional Backscattering Fluorescence and Raman Spectroscopy of Turbid Media. *Analytical Chemistry*, **80**:6006-6009, (2008)

7. Currey J.D., *Bones: Structure and Mechanics, 2nd ed.*, (Princeton University Press, Princeton, N.J., U.S.A., **2006**)

8. Biewener A.A., Thomason J., Goodship A.E. & Lanyon L.E., Bone stress in the horse forelimb during locomotion at different gaits: a comparison of two experimental methods, *Journal of Biomechanics*, **16**:565-576, (1983)

9. Boivin G., & Meunier P. J., Changes in Bone Remodeling Rate Influence the Degree of Mineralization of Bone, *Connective Tissue Research*, **43(2-3)**:535-537, (2002)

10. Viguet-Carrin S., Garnero P. & Delmas P.D., The role of collagen in bone strength, *Osteoporosis International*, **17**:319-336, (2006)

11. Veis A., Collagen fibrillar structure in mineralized and nonmineralised tissues, *Current Opinion in Solid State & Materials Science*, **2:**370-378, (1997)

12. Huerre C., Junien C., Weil D., Chu M.L., Morabito M., Van Cong N., Myers J.C., Foubert C., Gross M.S., Prockop D.J., Boué A., Kaplan J.C., De la Chapelle A., & Ramirez F., Human type I

procollagen genes are located on different chromosomes, *Proceedings of the National Academy of Sciences of the United States of America*, **79**:6627-6630, (1982)

13. Glanville R.W., Breitkreutz D., Meitinger M. & Fietzek P.P., Completion of the amino acid sequence of the alpha 1 chain from type I calf skin collagen. Amino acid sequence of alpha 1(I)B8, *The Biochemical Journal*, **215**:183-189, (1983)

14. Lees S. & Davidson C.L., The role of collagen in the elastic properties of calcified tissues, *Journal of Biomechanics,* **10**:473-486, (1977)

15. Smith J., Molecular pattern in native collagen, *Nature,* **219**, 157-158, (1968)

16. Thurner P.J., Atomic force microscopy and indentation force measurement of bone, *Engineering,* **1(6)***:*624-649, (2009)

17. Hulmes D.J., Wess T.J., Prockop D.J. & Fratzl P., Radial packing, order, and disorder in collagen fibrils, *Biophysical Journal*, **68(5)**:1661-1670, (1995)

18. Knott L. & Bailey A.J., Collagen cross-links in mineralizing tissues: a review of their chemistry, function, and clinical relevance, *Bone*, **22**:181-187, (1998)

19. Bailey A.J. & Knott L., Molecular changes in bone collagen in osteoporosis and osteoarthritis in the elderly, *Experimental Gerontology*, **34:**337-351, (1999)

20. Fratzl P., Gupta H.S., Paschalis E.P. & Roschger P., Structure and mechanical quality of the collagen-mineral nano-composite in bone, *Journal of Materials Chemistry,* **14**:2115, (2004)

21. Boskey A.L., Bone mineralization, Chapter **5** of Cowin S.C. (ed.) *Bone Mechanics Handbook, 2nd ed.*, (CRC Press, Boca Raton, FL., U.S.A., **2001**)

22. Jager I. & Fratzl P., Mineralized Collagen Fibrils: A Mechanical Model with a Staggered Arrangement of Mineral Particles, *Biophysical Journal,* **79**:1737-1746, (2000)

23. Fratzl P. & Weinkamer R., Nature's hierarchical materials, *Progress in Materials Science,* **52**:1263-1334 (2007)

24. Gupta H.S. & Zioupos P., Fracture of bone tissue: The 'hows' and the 'whys', *Medical Engineering & Physics*, **30**:1209-1226, (2008)

25. Wilson E.E., Awonusi A., Morris M.D., Kohn D.K., Tecklenburg M.M.J. & Beck L.W., Three structural roles for water in bone observed by solid-state NMR, *Biophysical Journal* **90**:3722-3371, (2006)

26. Cowin S.C., Bone Poroelasticity, *Journal of Biomechanics,* **32**, 217-238, (1999)

27. Sedlin E.D. & Hirsch C., Factors affecting the determination of the physical properties of femoral cortical bone, *Acta Orthopaedica Scandinavica,* **37**:29-48, (1966)

28. Fratzl P., Fratzl-Zelman N. & Klaushofer K., Collagen packing and mineralization; An x-ray scattering investigation of turkey leg tendon, *Journal of Biophysics,* **64**:260-266, (1993)

29. Wilson E.E., Awonusi A., Morris M.D., Kohn D.H., Tecklenburg M.M.J. & Beck L.W., Highly ordered interstitial water observed in bone by nuclear magnetic resonance, *Journal of Bone and Mineral Research*, **20**:625-634, (2005)

30. Young M.F., Bone matrix proteins: their function, regulation, and relationship to osteoporosis, *Osteoporosis International,* **14(3):**S35-S42, (2003)

31. Alford A.I., Terkhorn S.P., Reddy A.B. & Hankenson K.D., Thrombospondin-2 regulates matrix mineralization in MC3T3-E1 pre-osteoblasts, *Bone,* **46**:464-471, (2010)

32. Hankenson K.D., Bain S.D., Kyriakides T.R., Smith E.A., Goldstein S.A. & Bornstein P., Increased marrow-derived osteoprogenitor cells and endosteal bone formation in mice lacking thrombospondin 2, *Journal of Bone and Mineral Research*, **15(5)**, 851-862, (2000)

33. Buckley K. & Matousek P., Recent Advances in the Application of Transmission Raman Spectroscopy to Pharmaceutical Analysis, *Journal of Pharmaceutical and Biomedical Analysis*, **55**:645-652, (2011)

34. Wagermaier W., Gupta H.S., Gourrier A., Burghammer M., Roschger P. & Fratzl P., Spiral twisting of fiber orientation inside bone lamellae, *Biointerphases*, **1(1)**:1-5, (2006)

35. Weiner S. & Traub W., Bone structure: From angstroms to microns, *The FASEB Journal*, **6**:879-885, (1992)

36. Ritchie R.O., Buehler M.J. & Hansma P., Plasticity and Toughness in Bone, *Physics Today,* **June**:41-47, (2009)

37. Weiner S. & Wagner H.D., The Material Bone: Structure-Mechanical Function Relations, *Annual Review of Materials Science*, **28(1)**:271-298, (1998)

38. Webster S.S.J., Integrated Bone Tissue Physiology, Chapter **1** of Cowin S.C. (ed.) *Bone Mechanics Handbook, 2nd ed.*, (CRC Press, Boca Raton, FL., U.S.A., **2001**)

39. Goodship A.E., Lanyon L.E. & McFie H., Functional adaptation of bone to increased stress - An experimental study, *The Journal of Bone and Joint Surgery - American*, **61(4)**:539-546, (1979)

40. Turner C.H. & Burr D.B., Basic biomechanical measurements of bone: a tutorial, *Bone*, **14**:595-608, (1993)

41. Mahesh M., The AAPM/RSNA physics tutorial for residents - Search for isotropic resolution in CT from conventional through multiple-row detector, *Radiographics*, **22(4)**:949-962, (2002)

42. Blake G.M. & Fogelman I., Technical principles of dual energy x-ray absorptiometry, *Seminars in Nuclear Medicine*, **27(3)**:210-228, (1997)

43. Kalender W.A., Effective dose values in bone mineral measurements by photon absorptiometry and computed tomography, *Osteoporosis International*, **2(2)**:82-87, (1992)

44. Heaney R.P., BMD: The problem, *Osteoporosis International*, **16(9)**: 1013-1015, (2005)

45. Rizzoli R., & Ammann P., Bone strength and its determinants, *Osteoporosis International*, **14(3)**:13-18, (2003)

46. Gregg E.W., Kriska A.M., Salamone L.M., Roberts M.M., Aderson S.J., Ferrell R.E., Kuller L.H., & Cauley J.A., The epidemiology of quantitative ultrasound: a review of the relationships with bone mass, osteoporosis and fracture risk, *Osteoporosis International*, **7(2)**:89-99, (1997)

47. Danese R.D. & Licata A.A., Ultrasound of the skeleton: review of its clinical applications and pitfalls, *Current Rheumatology Reports*, **3(3)**:245-248, (2001)

48. Hendrick R.E., The AAPM/RSNA Physics Tutorial for Residents - Basic Physics of Mr-Imaging - An Introduction, *Radiographics*, **14(4)**:829-846, (1994)

49. Pooley R.A., The AAPM/RSNA physics tutorial for residents - Fundamental physics of MR imaging, *Radiographics*, **25(4)**:1087-1099, (2005)

50. Branch M.V., Murray R.C. & Dyson S.J. & Goodship A.E., Magnetic Resonance Imaging of the Equine Tarsus, *Clinical Techniques in Equine Practice*, **6(1)**:96-102, (2007)

51. Genant H.K., Lang T.F., Engelke K., Fuerst T., Gluer C.C., Majumdar S. & Jergas M., Advances in the noninvasive assessment of bone density, quality, and structure, *Calcified Tissue International*, **59**:S10-S15, (1996)

52. Kvistad K.A., Bakken I.J., Gribbestad I.S., Ehrnholm B., Lundgren S., Fjosne H.E. & Haraldseth O., Characterization of neoplastic and normal human breast tissues with in vivo H-1 MR spectroscopy, *Journal of Magnetic Resonance Imaging*, **10(2)**:159-164, (1999)

53. Kurhanewicz J., Vigneron D.B., Hricak H., Narayan P., Carroll P. & Nelson S.J., Three-dimensional H-1 MR spectroscopic imaging of the in situ human prostate with high (0.24-0.1-cm^3) spatial resolution, *Radiology*, **198(3)**:795-805, (1996)

54. Allen J.R., Prost R.W., Griffith O.W., Erickson S.J. & Erickson B.A., In vivo proton (H1) magnetic resonance spectroscopy for cervical carcinoma, *American Journal of Clinical Oncology-Cancer Clinical Trials*, **24(5)**:522-529, (2001)

55. Wang C.K., Li C.W., Hsieh T.J., Chien S.H., Liu G.C. & Tsai K.B., Characterization of bone and soft-tissue tumors with in vivo H-1 MR spectroscopy: Initial results, *Radiology*, **232(2)**:599-605, (2004)

56. Price R.R., The AAPM/RSNA physics tutorial for residents - MR imaging safety considerations, *Radiographics*, **19(6)**:1641-1651, (1999)

57. Votaw J.R., The AAPM/RSNA Physics Tutorial for Residents. Physics of PET, *Radiographics*, **15(5)**:1179-1190, (1995)

58. Miller T.R., Clinical aspects of emission tomography, *Radiographics*, **16(3)**:661-668, (1996)

59. Installe J., Nzeusseu A., Bol A., Devogelaer J.P. & Lonneux M., ^{18}F-Fluoride PET for Monitoring Therapeutic Response in Paget's Disease of Bone, *Journal of Nuclear Medicine*, **46(10)**:1650-1658, (2005)

60. Kindt J.H., Thurner P.J., Lauer M.E., Bosma B.L., Schitter G., Fantner G.E., Izumi M., Weaver J.C., Morse D.E. & Hansma P.K., In situ observation of fluoride-ion-induced hydroxyapatite–collagen detachment on bone fracture surfaces by atomic force microscopy, *Nanotechnology*, **18(13)**:135102, (2007)

61. Donnelly E., Boskey A.L., Baker S.P. & van der Meulen M.C.H., Effects of tissue age on bone tissue material composition and nanomechanical properties in the rat cortex, *Journal of Biomedical Materials Research. Part A*, **92(3)**:1048-1059, (2010)

62. Tai K., Qi H.J. & Ortiz C., Effect of mineral content on the nanoindentation properties and nanoscale deformation mechanisms of bovine tibial cortical bone, *Journal of Materials Science: Materials in Medicine,* **16(10)**:947-959, (2005)

63. Boivin G., Anthoine-Terrier C., & Obrant K.J., Transmission electron microscopy of bone tissue. A review, *Acta Orthopaedica Scandinavica*, **61(2)**:170-180, (1990)

64. Boyde A. & Jones S.J., Scanning electron microscopy of bone: instrument, specimen, and issues, *Microscopy Research and Technique*, **33(2)**:92-120, (1996)

65. Bloebaum R.D., Skedros J.G., Vajda E.G., Bachus K.N. & Constantz B.R., Determining mineral content variations in bone using backscattered electron imaging, *Bone*, **20(5)**:485-490, (1997)

66. Fratzl P., Schreiber S. & Klaushofer K., Bone mineralization as studied by small-angle x-ray scattering, *Connective Tissue Research,* **34(4)**:247-254, (1996)

67. Fratzl P., Small-angle scattering in materials science - a short review of applications in alloys, ceramics and composite materials, *Journal of Applied Crystallography*, **36(3)**:397-404, (2003)

68. Hiller J. & Wess T., The use of small-angle X-ray scattering to study archaeological and experimentally altered bone, *Journal of Archaeological Science*, **33(4)**:560-572, (2006)

69. Bonar L.C., Lees S. & Mook H.A., Neutron diffraction studies of collagen in fully mineralized bone, *Journal of Molecular Biology*, **181(2)**:265-270, (1985)

70. Skakle J.M.S. & Aspden R.M., Neutron diffraction studies of collagen in human cancellous bone, *Journal of Applied Crystallography*, **35(4)**:506-508, (2002)

71. Banwell C.N. & McCash E.M., *Fundamentals of Molecular Spectroscopy, 4th ed.,* (McGraw-Hill, London, U.K., **1983**)

72. Carden A. & Morris M.D., Application of vibrational spectroscopy to the study of mineralized tissues (review), *Journal of Biomedical Optics*, **5**:259-268, (2000)

73. Morris M.D. & Finney W.F., Recent developments in Raman and infrared spectroscopy and imaging of bone tissue, *Spectroscopy*, **18(2)**:155-159, (2004)

74. Stringer M.R., Lund D.N., Foulds A.P., Uddin A., Berry E., Miles R.E. & Davies A.G., The analysis of human cortical bone by terahertz time-domain spectroscopy, *Physics in Medicine and Biology*, **50(14)**:3211-3219, (2005)

75. Yiwen S., Fischer B.M. & Pickwell-MacPherson E., Effects of formalin fixing on the terahertz properties of biological tissues, *Journal of Biomedical Optics*, **14(6)**:064017, (2010)

76. Lakshmi R.J., Alexander M., Kurien J., Mahato K.K. & Kartha V.B., Osteoradionecrosis (ORN) of the mandible: A laser Raman spectroscopic study, *Applied Spectroscopy*, **57(9)**:1100-1116, (2003)

77. Polomska M., Kubisz L., Kalawski R., Oszkinis G., Filipiak R. & Mazurek A., Fourier Transform Near Infrared Raman Spectroscopy in Studies on Connective Tissue, *Acta Physica Polonica A*, **118(1)**:136-140, (2010)

78. Barth H.D., Launey M.E., MacDowell A.A., Ager J.W. & Ritchie R.O., On the effect of X-ray irradiation on the deformation and fracture behavior of human cortical bone, *Bone*, **46(6)**:1475-1485, (2010)

79. Currey J.D., Foreman J., Laketic I., Mitchell J., Pegg D.E. & Reilly G.C., Effects of Ionizing Radiation on the Mechanical Properties of Human Bone, *Journal of Orthopaedic Research*, **15(1)**:111-117, (1997)

80. Raman C.V., A New Radiation, *Indian Journal of Physics*, **(2)**:387-398, (1928)

81. Krishnan R.S. & Shankar R.K. Raman effect: History of the discovery, *Journal of Raman Spectroscopy*, **10**:1-8, (1981)

82. Raman C.V., A New type of Secondary Radiation, *Nature*, **121(3048)**:501-502, (1928)

83. Singh R.C., V. Raman and the Discovery of the Raman Effect, *Physics in Perspective*, **4**:399-420, (2002)

84. Carey P.R., *Biochemical Applications of Raman and Resonance Raman Spectroscopies*, Chapter **1** (Academic Press, New York, NY., U.S.A. **1982**)

85. Smith E. & Dent G., *Modern Raman Spectroscopy: A Practical Approach* (John Wiley & Sons, Chichester, U.K., **2005**)

86. Long D.A., *The Raman Effect: A Unified Treatment of the Theory of Raman Scattering by Molecules*, (John Wiley and Sons, Chichester, U.K., **2002**)

87. Walton A., Deveney M. & Koenig J., Raman spectroscopy of Calcified Tissue, *Calcified Tissue International*, **167**:162-167, (1970)

88. Dendramis A.L., Poser J.W. & Schwinn E.W., Laser Raman Spectroscopy of Calf Bone Gla Protein, *Biochimica et Biophysica Acta.*, **742(3)**:525-529, (1983)

89. De Mul F.F.M., Hottenhuis M.H.J., Bouter P., Greve J., Arends J. & Ten Bosch J.J., Micro-Raman Line Broadening in Synthetic Carbonated Hydroxyapatite, *Journal of Dental Research*, **65**: 437, (1986)

90. Walters M.A., Leung Y.C., Blumenthal N.C., Konsker K.A. & R. Z. LeGeros, A Raman and infrared spectroscopic investigation of biological hydroxyapatite, *Journal of Inorganic Biochemistry*, **39**:193-200, (1990)

91. Walters M.A., Blumenthal N.C., Leung Y., Wang Y., Ricci J.L. & Spivak J.M., Molecular structure at the bone-implant interface: a vibrational spectroscopic characterization, *Calcified Tissue International*, **48(5)**:368-369, (1991)

92. Morris M.D., Raman Spectroscopy of Bone and Cartilage, Chapter **14** of Matousek P. & Morris M.D. (Eds.) Emerging Applications of Raman Spectroscopy in Pharmaceutical and Biomedical Fields, (Springer, Berlin, Germany, **2010**)

93. Bazin D., Chappard C., Combes C., Carpentier X., Rouziere S., Andre G., Matzen G., Allix M., Thiaudiere D., Reguer S., Jungers P. & Daudon M., Diffraction techniques and vibrational spectroscopy opportunities to characterise bones, *Osteoporosis International*, **20**:1065–1075, (2009)

94. Krafft C., Steiner G., Beleites C. & Salzer R., Disease recognition by infrared and Raman spectroscopy, *Journal of Biophotonics*, **2**:13–28, (2009)

95. Krafft C. & Sergo V., Biomedical applications of Raman and infrared spectroscopy to diagnose tissues, *Spectroscopy*, **20**:195–218, (2006)

96. Boskey A.L. & Mendelsohn R., Infrared spectroscopic characterization of mineralized tissues, *Vibrational Spectroscopy*, **38**:107–114, (2005)

97. Awonusi A., Morris M.D. & Tecklenburg M.M.J., Carbonate assignment and calibration in the raman spectrum of apatite, *Calcified Tissue International*, **81(1)**:46-52, (2007)

98. Sauer G.R., Zunic W.B., Durig J.R. & Wuthier R.E., Fourier-Transform Raman Spectroscopy of Synthetic and Biological Calcium Phosphates, *Calcified Tissue International*, **54(5)**:414-420, (1994)

99. Rehman I., Smith R., Hench L.L. & Bonfield W., FT-Raman spectroscopic analysis of natural bones and their comparison with bioactive glasses and hydroxyapatite, *Bioceramics*, **7**:79-84 (1994)

100. Tsuda H. & Arends J., Orientational Micro-Raman Spectroscopy on Hydroxyapatite Single Crystals and Human Enamel Crystallites, *Journal of Dental Research*, **73**:1703 (1994)

101. Rehman I., Smith R., Hench L.L. & Bonfield W., Structural evaluation of human and sheep bone and comparison with synthetic hydroxyapatite by FT-Raman spectroscopy, *Journal of Biomedical Materials Research*, **29(10)**:1287-1294 (1995)

102. Penel G., Leroy G., Cournot G. & Bres E., Characterization of synthetic and biological calcium phosphate materials by micro-Raman spectrometry, *Bioceramics*, **10**:571-574, (1997)

103. Joschek S., Nies B., Krotz R. & Gopferich A., Chemical and physicochemical characterization of porous hydroxyapatite ceramics made of natural bone, *Biomaterials*, **21(16)**:1645-1658, (2000)

104. Johnson G.S., Mucalo M.R. & Lorier M.A., The processing and characterization of animal-derived bone to yield materials with biomedical applications - Part 1: Modifiable porous implants from bovine condyle cancellous bone and characterization of bone materials as a function of processing, *Journal of Materials Science - Materials in Medicine*, **11(7)**:427-441, (2000)

105. Penel G., Pottier E.C. & Leroy G., Raman investigation of calcium carbonate bone substitutes and related biomaterials, *Bulletin du Groupement International pour la Recherche Scientifique en Stomatologie & Odontologie*, **45(2-3)**:56-59, (2003)

106. Taylor M.G., Parker S.F., Simkiss K. & Mitchell P.C.H., Bone mineral: evidence for hydroxy groups by inelastic neutron scattering, *Physical Chemistry Chemical Physics*, **3(8)**:1514-1517, (2001)

107. Pasteris J.D., Wopenka B., Freeman J.J., Rogers K., Valsami-Jones E., van der Houwen J.A.M. & Silva M.J., Lack of OH in nanocrystalline apatite as a function of degree of atomic order: implications for bone and biomaterials, *Biomaterials*, **25(2)**:229-238, (2004)

108. Ou-Yang H., Paschalis E.P., Boskey A.L. & Mendelsohn R., Two-dimensional vibrational correlation spectroscopy of in vitro hydroxyapatite maturation, *Biopolymers*, **57(3)**:129-139, (2000)

109. Kazanci M., Fratzl P., Klaushofer K. & Paschalis E.P., Complementary information on in vitro conversion of amorphous (precursor) calcium phosphate to hydroxyapatite from Raman microspectroscopy and wide-angle X-ray scattering, *Calcified Tissue International*, **79(5)**:354-359, (2006)

110. Crane N.J., Popescu V., Morris M.D., Steenhuis P. & Ignelzi M.A., Raman spectroscopic evidence for octacalcium phosphate and other transient mineral species deposited during intramembranous mineralization, *Bone*, **39(3)**:434-442, (2006)

111. Ohsaki K., Shibata A., Yamashita S., Oe M., Wang K.Q., Cui P.C. & Ye Q., Demonstrations of de-and remineralization mechanism as revealed in synthetic auditory ossicle (Apaceram) of rats by laser-Raman spectrometry, *Cellular and Molecular Biology (Noisy-le-grand)*, **41(8)**:1155-1167, (1995)

112. Chen J.L., Burger C., Krishnan C.V., Chu B., Hsiao B.S. & Glimcher M.J., In vitro mineralization of collagen in demineralized fish bone, *Macromolecular Chemistry and Physics*, **206(1)**:43-51, (2005)

113. van Apeldoorn A.A., Aksenov Y., Stigter M., Hofland I., de Bruijn J.D. & Koerten H.K., Parallel high-resolution confocal Raman SEM analysis of inorganic and organic bone matrix constituents, *Journal of the Royal Society - Interface*, **2(2)**:39-45, (2005)

114. Gajjeraman S., Narayanan K., Hao J.J., Qin C.L. & George A., Matrix macromolecules in hard tissues control the nucleation and hierarchical assembly of hydroxyapatite, *Journal of Biological Chemistry*, **282(2)**:1193-1204, (2007)

115. Pouget E., Dujardin E., Cavalier A., Moreac A., Valery C., Marchi-Artzner V., Weiss T., Renault A., Paternostre M. & Artzner F., Hierarchical architectures by synergy between dynamical template self-assembly and biomineralisation, *Nature Materials*, **6(6)**:434-439, (2007)

116. Tarnowski C.P., Ignelzi M.A. & Morris M.D., Mineralization of developing mouse calvaria as revealed by Raman microspectroscopy, *Journal of Bone and Mineral Research*, **17(6)**:1118-1126, (2002)

117. Stewart S., Shea D.A., Tarnowski C.P., Morris M.D., Wang D., Franceschi R., Lin D.L. & Keller E., Trends in early mineralization of murine calvarial osteoblastic cultures: a Raman microscopic study, *Journal of Raman Spectroscopy*, **33(7)**:536-543, (2002)

118. Tarnowski C.P., Ignelzi M.A., Wang W., Taboas J.M., Goldstein S.A. & Morris M.D., Earliest mineral and matrix changes in force-induced musculoskeletal disease as revealed by Raman microspectroscopic imaging, *Journal of Bone and Mineral Research*, **19(1)**:64-71, (2004)

119. Balooch M., Habelitz S., Kinney J.H., Marshall S.J. & Marshall G.W., Mechanical properties of mineralized collagen fibrils as influenced by demineralization, *Journal of Structural Biology*, **162(3)**:404-410, (2008)

120. Kontoyannis C.G. & Vagenas N.V., FT-Raman spectroscopy: A tool for monitoring the demineralization of bones, *Applied Spectroscopy*, **54(11)**:1605-1609, (2000)

121. Freeman J.J., Wopenka B., Silva M.J. & Pasteris J.D., Raman spectroscopic detection of changes in bioapatite in mouse femora as a function of age and in vitro fluoride treatment, *Calcified Tissue International*, **68(3)**:156-162, (2001)

122. Akkus O., Adar F. & Schaffler M.B., Age-related changes in physicochemical properties of mineral crystals are related to impaired mechanical function of cortical bone, *Bone*, **34(3)**:443-453, (2004)

123. Farlay D., Panczer G., Rey C., Delmas P.D. & Boivin G., Mineral maturity and crystallinity index are distinct characteristics of bone mineral, *Journal of Bone and Mineral Metabolism*, **28(4)**:433-445, (2010)

124. Ager J.W., Nalla R.K., Breeden K.L. & Ritchie R.O., Deep-ultraviolet Raman spectroscopy study of the effect of aging on human cortical bone, *Journal of Biomedical Optics*, **10(3)**:034012, (2005)

125. Ager J.W., Nalla R.K., Balooch G., Kim G., Pugach M., Habelitz S., Marshall G.W., Kinney J.H. & Ritchie R.O., On the increasing fragility of human teeth with age: A deep-UV resonance Raman study, *Journal of Bone and Mineral Research*, **21(12)**:1879-1887, (2006)

126. Akkus O., Polyakova-Akkus A., Adar F. & Schaffler M.B., Aging of microstructural compartments in human compact bone, *Journal of Bone and Mineral Research*, **18(6)**:1012-1019, (2003)

127. Kohn D.H., Sahar N.D., Wallace J.M., Golcuk K. & Morris M.D., Exercise Alters Mineral and Matrix Composition in the Absence of Adding New Bone, *Cells Tissues Organs*, **189(1-4)**:33-37, (2009)

128. Shen J., Fan L., Yang J., Shen A.G. & Hu J.M., A longitudinal Raman microspectroscopic study of osteoporosis induced by spinal cord injury, *Osteoporosis International*, **21(1)**:81-87, (2010)

129. Pezzotti G., Raman piezo-spectroscopic analysis of natural and synthetic biomaterials, *Analytical and Bioanalytical Chemistry*, **381**:577-590, (2005)

130. Xu J.W., Gilson D.F.R., Butler I.S. & Stangel I., Effect of high external pressures on the vibrational spectra of biomedical materials: Calcium hydroxyapatite and calcium fluoroapatite, *Journal of Biomedical Materials Research*, **30(2)**:239-244, (1996)

131. De Carmejane O., Morris M.D., Davis M.K., Stixrude L., Tecklenburg M., Rajachar R.M. & Kohn D.H., Bone chemical structure response to mechanical stress studied by high pressure Raman spectroscopy, *Calcified Tissue International*, **76(3)**:207-213, (2005)

132. Carden A., Rajachar R.M., Morris M.D. & Kohn D.H., Ultrastructural changes accompanying the mechanical deformation of bone tissue: A Raman imaging study, *Calcified Tissue International*, **72(2)**:166-175, (2003)

133. Morris M.D., Finney W.F., Rajachar R.M. & Kohn D.H., Bone tissue ultrastructural response to elastic deformation probed by Raman spectroscopy, *Faraday Discussions*, **126**:159-168, (2004)

134. Dooley K.A., McCormack J., Fyhrie D.P. & Morris M.D., Stress mapping of undamaged, strained, and failed regions of bone using Raman spectroscopy, *Journal of Biomedical Optics*, **14(4)**:044018, (2009)

135. Kubisz L. & Polomska M., FT NIR Raman studies on gamma-irradiated bone, Spectrochimica Acta Part A-Molecular and Biomolecular, *Spectroscopy*, **66(3)**:616-625, (2007)

136. Polescu V., Steenhuis P., Morris M.D. & Ignelzi M.A., Osteopontin and bone mineral expression during intramembranous ossification, *Journal of Bone and Mineral Research*, **21**:S344-S344, (2006)

137. Kavukcuoglu N.B., Denhardt D.T., Guzelsu N. & Mann A.B., Osteopontin deficiency and aging on nanomechanics of mouse bone, *Journal of Biomedical Materials Research Part A*, **83A(1)**:136-144, (2007)

138. Kavukcuoglu N.B., Arteaga-Solis E., Lee-Arteaga S., Ramirez F. & Mann A.B., Nanomechanics and Raman spectroscopy of fibrillin 2 knock-out mouse bones, *Journal of Materials Science*, **42(21)**:8788-8794, (2007)

139. Kavukcuoglu N.B., Patterson-Buckendahl P. & Mann A.B., Effect of osteocalcin deficiency on the nanomechanics and chemistry of mouse bones, *Journal of the Mechanical Behaviour of Biomedical Materials*, **2(4)**:348-354, (2009)

140. Morris M.D., Tarnowski C.P., Dreier J.L. & Ignelzi M.A., Raman microscopy of de novo woven bone tissue, *Proceedings of the SPIE - Biomedical Diagnostic, Guidance, and Surgical-Assist Systems III*, **2(11)**:90-96, (2001)

141. Uthgenannt B.A., Kramer M.H., Hwu J.A., Wopenka B. & Silva M.J., Skeletal self-repair: Stress fracture healing by rapid formation and Densification of woven bone, *Journal of Bone and Mineral Research*, **22**:1548-1556, (2007)

142. Timlin J.A., Carden A. & Morris M.D., Chemical microstructure of cortical bone probed by Raman transects, *Applied Spectroscopy*, **53(11)**:1429-1435, (1999)

143. Carden A., Timlin J.A., Edwards C.M., Morris M.D., Hoffler C.E., Kozloff K. & Goldstein S.A., Raman imaging of Bone Mineral and Matrix: Composition and Function, *Proceedings of the SPIE - Biomedical Applications of Raman Spectroscopy*, **3608**:132-138, (1999)

144. Timlin J.A., Carden A., Morris M.D., Bonadio J.F., Hoffler C.E., Kozloff K.M. & Goldstein S.A., Spatial distribution of phosphate species in mature and newly generated mammalian bone by hyperspectral Raman imaging, *Journal of Biomedical Optics*, **4(1)**:28-34, (1999)

145. Gourion-Arsiquand S., Havill L.M. & Boskey A. L., Within Osteons Infrared Parameters Linked to Specific Bone Properties Vary as a Function of Tissue and Animal Age, *Journal of Bone and Mineral Science*, **22**:S258-S258, (2007)

146. Hofmann T., Heyroth F., Meinhard H., Franzel W. & Raum K., Assessment of composition and anisotropic elastic properties of secondary osteon lamellae, *Journal of Biomechanics*, **39(12)**:2282-2294, (2006)

147. Marotti G., A New Theory of Bone Lamellation, *Calcified Tissue International*, **53(1)**:S47-S56, (1993)

148. Kazanci M., Roschger P., Paschalis E.P., Klaushofer K. & Fratzl P., Raman spectral mapping of bone osteonal tissues, *Bone*, **39(5)**:S16-S16, (2006)

149. Kazanci M., Roschger P., Paschalis E.P., Klaushofer K. & Fratzl P., Bone osteonal tissues by Raman spectral mapping: Orientation-composition, *Journal of Structural Biology*, **156(3)**:489-496, (2006)

150. Kazanci M., Wagner H.D., Manjubala N.I., Gupta H.S., Paschalis E., Roschger P. & Fratzl P., Raman imaging of two orthogonal planes within cortical bone, *Bone*, **41(3)**:456-461, (2007)

151. Gamsjaeger S., Masic A., Roschger P., Kazanci M., Dunlop J.W.C., Klaushofer K., Paschalis E.P. & Fratzl P., Cortical bone composition and orientation as a function of animal and tissue age in mice by Raman spectroscopy, *Bone*, **47:**392-399, (2010)

152. Falgayrac G., Facq S., Leroy G., Cortet B. & Penel G., New Method for Raman Investigation of the Orientation of Collagen Fibrils and Crystallites in the Haversian System of Bone, *Applied Spectroscopy*, **64(7)**:775-780, (2010)

153. Bonifacio A. & Sergo V., Effects of sample orientation in Raman microspectroscopy of collagen fibers and their impact on the interpretation of the amide III band, *Vibrational Spectroscopy*, **53(2)**:314-317, (2010)

154. Raghavan M., Sahar N.D., Wilson R.H., Mycek M., Pleshko N., Kohn D.H. & Morris M. D., Quantitative polarized Raman spectroscopy in highly turbid bone tissue, *Journal of Biomedical Optics*, **15**:037001, (2010)

155. Penel G., Delfosse C., Descamps M. & Leroy G., Composition of bone and apatitic biomaterials as revealed by intravital Raman microspectroscopy, *Bone*, **36(5)**:893-901, (2005)

156. Matousek P., Deep non-invasive Raman spectroscopy of living tissue and powders, *Chemical Society Reviews*, **36(8)**:1292-1304, (2007)

157. Eliasson C. & Matousek P., A Noninvasive method for deep Raman Spectroscopy of living tissue and Powders, *American Laboratory*, **39(14)**:42-44, (2007)

158. Matousek P., Towrie M. & Stanley A. & Parker A.W., Efficient Rejection of Fluorescence from Raman Spectra Using Picosecond Kerr Gating, *Applied Spectroscopy*, **53:**1485-1489, (1999)

159. Morris M.D., Goodship A.E., Draper E.R.C., Matousek P., Towrie M. & Parker A.W., Kerr-gated picosecond Raman spectroscopy and Raman photon migration of equine bone tissue with 400-nm excitation, *Proceedings of the SPIE - Biomedical Vibrational Spectroscopy and Biohazard Detection Technologies*, **5321**:164-169, (2004)

160. Morris M.D., Matousek P., Towrie M., Parker A.W., Goodship A.E. & Draper E.R.C., Kerr-gated time-resolved Raman spectroscopy of equine cortical bone tissue, *Journal of Biomedical Optics*, **10(1)**:014014, (2005)

161. Morris M.D., Draper E.R.C., Goodship A.E., Matousek P., Towrie M., Parker A.W. & Camacho N.P., Picosecond time-gated Raman spectroscopy for transcutaneous evaluation of bone composition, *Proceedings of the SPIE - Optical Tomography and Spectroscopy of Tissue VI*, **5693**:344-350, (2005)

162. Draper E.R.C., Morris M.D., Camacho N.P., Matousek P., Towrie M., Parker A.W. & Goodship A.E., Novel assessment of bone using time-resolved transcutaneous Raman spectroscopy, *Journal of Bone and Mineral Research*, **20(11)**:1968-1972, (2005)

163. Matousek P. & Stone N., Emerging concepts in deep Raman spectroscopy of biological tissue, *Analyst*, **134(6)**:1058-1066, (2009)

164. Matousek P., Clark I.P., Draper E.R.C., Morris M.D., Goodship A.E., Everall N., Towrie M., Finney W.F. & Parker A.W., Subsurface probing in diffusely scattering media using spatially offset Raman spectroscopy, *Applied Spectroscopy*, **59(4)**:393-400, (2005)

165. Schulmerich M.V., Finney W.F., Popescu V., Morris M.D., Vanasse T.M. & Goldstein S.A., Transcutaneous Raman spectroscopy of bone tissue using a non-confocal fiber optic array probe, *Proceedings of the SPIE - Biomedical Vibrational Spectroscopy III: Advances in Research and Industry*, **6093**:O930-O930, (2006)

166. Schulmerich M.V., Dooley K.A., Morris M.D., Vanasse T.M. & Goldstein S.A., Transcutaneous fiber optic Raman spectroscopy of bone using annular illumination and a circular array of collection fibers, *Journal of Biomedical Optics*, **11(6)**:060502, (2006)

167. Matousek P., Draper E.R.C., Goodship A.E., Clark I.P., Ronayne K.L. & Parker A.W., Noninvasive Raman Spectroscopy of human tissue in vivo, *Applied Spectroscopy*, **60(7)**:758-763, (2006)

168. Schulmerich M.V., Cole J.H., Kreider J.M., Esmonde-White F., Dooley K.A., Goldstein S.A. & Morris M.D., Transcutaneous Raman Spectroscopy of Murine Bone In Vivo, *Applied Spectroscopy*, **63(3)**:286-295, (2009)

169. Schulmerich M.V., Finney W.F., Fredricks R.A. & Morris M.D., Subsurface Raman spectroscopy and mapping using a globally illuminated non-confocal fiber-optic array probe in the presence of Raman photon migration, *Applied Spectroscopy*, **60(2)**:109-114, (2006)

170. Schulmerich M.V., Morris M.D., Vanasse T.M. & Goldstein S.A., Transcutaneous Raman spectroscopy of bone global sampling and ring/disk fiber optic probes, *Proceedings of the SPIE - Advanced Biomedical and Clinical Diagnostic Systems V*, **6430**:43009-43009, (2007)

171. Cole J.H., Schulmerich M.V., Dooley K.A., Kreider J.M., Daley E., Goldstein S.A. & Morris M.D., Measurement protocols for the non-invasive assessment of bone constituent properties by Raman Spectroscopy, *Journal of Bone and Mineral Research*, **22**:S257-S257, (2007)

172. Schulmerich M.V., Dooley K.A., Vanasse T.M., Goldstein S.A. & Morris M.D., Subsurface and transcutaneous Raman Spectroscopy and mapping using concentric illumination rings and collection with a circular fiber-optic array, *Applied Spectroscopy*, **61(7)**:671-678, (2007)

173. Schulmerich M.V., Cole J.H., Dooley K.A., Morris M.D., Kreider J.M. & Goldstein S.A., Optical clearing in transcutaneous Raman spectroscopy of murine cortical bone tissue, *Journal of Biomedical Optics*, **13(2)**:021108, (2008)

174. Srinivasan S., Schulmerich M., Cole J.H., Dooley K.A., Kreider J.M., Pogue B.W., Morris M.D. & Goldstein S.A., Image-guided Raman spectroscopic recovery of canine cortical bone contrast in situ, *Optics Express*, **16(16)**:12190-12200, (2008)

175. Schulmerich M.V., Cole J.H., Dooley K.A., Morris M.D., Kreider J.M., Goldstein S.A., Srinivasan S. & Pogue B.W., Noninvasive Raman tomographic imaging of canine bone tissue, *Journal of Biomedical Optics*, **13(2)**:020506, (2008)

176. Schulmerich M.V., Srinivasan S., Kreider J., Cole J.H., Dooley K.A., Goldstein S.A., Pogue B.W. & Morris M.D., Raman tomography of tissue phantoms and bone tissue, *Proceedings of the SPIE - Biomedical Optical Spectroscopy*, **6853**:V8530-V8530, (2008)

177. Kavukcuoglu N.B., Denhardt D.T., Guzelsu N. & Mann A.B., Osteopontin deficiency and aging on nanomechanics of mouse bone, *Journal of Biomedical Materials Research Part A*, **83A(1)**:136-144, (2007)

178. Schrader B., *Raman/Infrared Atlas of Organic Compounds, 2nd ed.*, (VCH mbH, Weinheim, Germany, **1989**)

179. Smith R. & Rehman I.U., Fourier transform Raman spectroscopic studies of human bone, *Journal of Materials Science: Materials in Medicine*, **5**:775-778, (1995)

180. Shea D.A. & Morris M.D., Bone tissue fluorescence reduction for visible laser Raman spectroscopy, *Applied Spectroscopy*, **56(2)**:182-186, (2002)

181. Golcuk K., Mandair G.S., Callender A.F., Finney W.F., Sahar N., Kohn D.H. & Morris M.D., Rapid Raman spectroscopy of musculoskeletal tissue using a visible laser and an electron-multiplying CCD (EMCCD) detector, *Proceedings of the SPIE - Biomedical Vibrational Spectroscopy III: Advances in Research and Industry*, **6093**:9314-9314, (2006)

182. Golcuk K., Mandair G.S., Callender A.F., Sahar N., Kohn D.H. & Morris M.D., Is photobleaching necessary for Raman imaging of bone tissue using a green laser? *Biochimica et Biophysica Acta-Biomembranes*, **1758(7)**:868-873, (2006)

183. Freeman J.J. & Silva M.J., Separation of the Raman spectral signatures of bioapatite and collagen in compact mouse bone bleached with hydrogen peroxide, *Applied Spectroscopy*, **56(6)**:770-775, (2002)

184. Chen T.C., Shea D.A. & Morris M.D., Effect of hydrogen peroxide bleaching on bone mineral/matrix, *Applied Spectroscopy*, **56(8)**:1035-1037, (2002)

185. Lieber C.A. & Mahadevan-Jansen A., Automated method for subtraction of fluorescence from biological Raman spectra, *Applied Spectroscopy*, **57**:1363-1367, (2003)

186. Pienkowski D., Doers T.M., Monier-Faugere M.C., Geng Z., Camacho N.P., Boskey A. & Malluche H.H., Calcitonin Alters Bone Quality in Beagle Dogs, *Journal of Bone and Mineral Research*, **12**:1936-1943, (1997)

187. Matousek P., Raman Signal Enhancement in Deep Spectroscopy of Turbid Media, *Applied Spectroscopy*, **61**:845-854, (2007)

188. Eliasson C. & Matousek P., Passive signal enhancement in spatially offset Raman spectroscopy, *Journal of Raman Spectroscopy*, **39(5)**:633-637, (2008)

189. Kubelka P. & Munk, F., Ein Beitrag zur Optik der Farbanstriche, *Zeitschrift fur Technischen Physik*, **12**:593-601(1931)

190. Schrader B. & Bergmann G., Die Intensität des Ramanspektrums polykristalliner Substanzen, *Fresenius' Journal of Analytical Chemistry*, **225**:230-247, (1967)

191. Schrader B. & Moore D.S., Laser-Based Molecular Spectroscopy for Chemical Analysis-Raman Scattering Processes, *Pure and Applied Chemistry*, **69**:1451-1468, (1997)

192. Born M. & Wolf E., *Principles of Optics, 7th ed.*, (Cambridge University Press, Cambridge U.K., **2005**)

193. Long D.A., *Raman Spectroscopy*, (McGraw-Hill International, New York, N.Y., U.S.A., **1977**)

194. Henderson J.C., Su Q. & Grobe R., Mirror Assisted Imaging in One-Dimensional Turbid Media Using Photon Density Waves, *Laser Physics*, **14(4)** :515-520, (2004)

195. Matousek P., Enhancement of laser radiation coupled into turbid media by using a unidirectional mirror, *Journal of the Optical Society of America B: Optical Physics*, **25(7)**:1223-1230, (2008)

196. McCain S.T., Gehm M.E., Wang Y., Pitsianis N.P. & Brady D.J., Coded Aperture Raman Spectroscopy for Quantitative Measurements of Ethanol in a Tissue Phantom, *Applied Spectroscopy*, **60(6)**:663-671, (2006)

197. Currey J.D., Mechanical properties of bone with greatly differing functions, *Journal of Biomechanics*, **12(4)**:313-319, (1979)

198. Currey J.D., The evolution of the mechanical properties of amniote bone, *Journal of Biomechanics*, **20**:1035-1044, (1987)

199. Currey J.D., The design of mineralised hard tissues for their mechanical functions, *The Journal of Experimental Biology*, **202**:3285-3294, (1999)

200. Gourion-Arsiquaud S., Burket J.C., Havill L.M., DiCarlo E., Doty S.B., Mendelsohn R., van der Meulen M.C.H. & Boskey A.L., Spatial variation in osteonal bone properties relative to tissue and animal age, *Journal of Bone and Mineral Research*, **24**:1271–1281, (2009)

201. Goodyear S.R., van't Hof R., Gibson I.R., Skakle J.M.S., Wells R.P.K. and Aspden R.M., The mechanical material and chemical properties of cortical bone form NNOS null mice, *Journal of Biomechanics*, **41(1)**:S261-S261, (2008)

202. Wallace J.M., Golcuk K., Morris M.D. & Kohn D.H., Inbred strain-specific response to biglycan deficiency in the cortical bone of C57BL6/129 and C3H/He mice, *Journal of Bone and Mineral Research*, **24**:1002-1012, (2009)

203. Yerramshetty J.S. & Akkus O., The associations between mineral crystallinity and the mechanical properties of human cortical bone, *Bone*, **42**:476-482, (2008)

204. Tsuda H., Ruben J. & Arends J., Raman spectra of human dentin mineral, *European Journal of Oral Sciences*, **104(2)**:123-131, (1996)

205. Wentrup-Byrne E., Armstrong C.A., Armstrong R.S. & Collins B.M., Fourier transform Raman microscopic mapping of the molecular components in a human tooth, *Journal of Raman Spectroscopy*, **28(2-3)**:151-158, (1997)

206. Fattibene P., Carosi A., De Coste V., Sacchetti A., Nucara A., Postorino P. & Dore P., A comparative EPR, infrared and Raman study of natural and deproteinated tooth enamel and dentin, *Physics in Medicine and Biology*, **50(6)**:1095-1108, (2005)

207. He G., Dahl T., Veis A. & George A., Nucleation of apatite crystals in vitro by self-assembled dentin matrix protein, *Nature Materials*, **2(8)**:552-558, (2003)

208. Brody R.H., Edwards H.G.M. & Pollard A.M., Chemometric methods applied to the differentiation of Fourier-transform Raman spectra of ivories, *Analytica Chimica Acta*, **427(2)**:223-232, (2001)

209. Zhou C.X. & Pasteris J., Preliminary study of fish bone using Raman spectroscopy, *Geochimica et Cosmochimica Acta*, **69(10)**:A75-A75, (2005)

210. Coman V., Grecu R., Baciut M., Baciut G., Prodan P. & Simon V., Investigation of different bone matrices by vibrational spectroscopy, *Journal of Optoelectronics and Advanced Materials*, **9(11)**:3372-3375, (2007)

211. Kreith F., (Ed.), *CRC Handbook of Mechanical Engineering*, (CRC Press, Boca Raton, Fl., U.S.A., **1998**)

212. Les C., Stover S., Keyak J., Taylor K. & Willits N., The distribution of material properties in the equine third metacarpal bone serves to enhance sagittal bending, *Journal of Biomechanics*, **30(4)**:355-361, (1997)

213. Zylberberg L., Traub W., De Buffrenil V., Allizard F., Arad T. & Weiner, S., Rostrum of a toothed whale: ultrastructural study of a very dense bone, *Bone*, **23**:241-247, (1998)

214. Zioupos P., Currey J.D. & Casinos A., Mechanical properties of the rostrum of the whale Mesoplodon densirostris, a remarkably dense bony tissue, *Journal of Zoology (London)*, **241**:725-737, (2001)

215. MacLeod C.D., Possible functions of the ultradense bone in the rostrum of Blainville's beaked whale (Mesoplodon densirostris), *Canadian Journal of Zoology*, **80**:178–184, (2002)

216. Currey J.D., Ontogenic Changes in Compact Bone Material Properties, Chapter **19** of Cowin S.C., (Ed.) *Bone Mechanics Handbook, 2nd ed.* (CRC Press, Boca Raton, FL., U.S.A., **2001**)

217. Boivin G., Chavassieux P., Santora A., Yates J. & Meunier, PJ., Alendronate increases bone strength by increasing the mean degree of mineralization of bone tissue in osteoporotic women, *Bone*, **27**:687-694, (2000)

218. Boivin G. & Meunier P.J., The Degree of Mineralization of Bone Tissue Measured by Computerized Quantitative Contact Microradiography, *Calcified Tissue International*, **70**:503-511, (2002)

219. Macleod N.A. & Matousek P., Deep Noninvasive Raman Spectroscopy of Turbid Media, *Applied Spectroscopy*, **62**:291A-304A, (2008)

220. Guo X.E. & Goldstein S.A., Is trabecular bone tissue different from cortical bone tissue? *Forma*, **12:**185–196, (1997)

221. Gong J.K., Arnold J.S. & Cohn S.H., Composition of trabecular and cortical bone, *The Anatomical Record*, **149(3)**:325-331, (1964)

222. Hodgskinson R., Currey J.D. & Evans G.P., Hardness, an indicator of the mechanical competence of cancellous bone, *Journal of Orthopaedic Research*, **7(5)**:754-758, (1989)

223. Goodyear S.R., Gibson L.R., Skakle J.M.S., Wells R.P.K. & Aspden R.M., A comparison of cortical and trabecular bone from C57 Black 6 mice using Raman spectroscopy, *Bone*, **44(5)**:899-907, (2009)

224. Biewener A.A., Bone strength in small mammals and bipedal birds: do safety factors change with body size? *Journal of Experimental Biology*, **98**:289-301, (1982)

225. Evans F.G. & Lebow M., Regional Differences in Some of the Physical Properties of the Human Femur, *Journal of Applied Physiology*, **3**:563-572, (1951)

226. Pope M.H. & Outwater J.O., Mechanical properties of bone as a function of position and orientation, *Journal of Biomechanics*, **7**:61-66, (1974)

227. Ashman R.B., Cowin S.C., Van Buskirk W.C. & Rice J.C., A continuous wave technique for the measurement of the elastic properties of cortical bone, *Journal of Biomechanics*, **1(5)**:349-361, (1984)

228. Kim H.D. & Walsh W.R., Mechanical and ultrasonic characterization of cortical bone, *Biomimetics*, **1**:293-310, (1992)

229. Atkinson P.J. & Weatherell J.A., Variation in the density of the femoral diaphysis with age, *Journal of Bone and Joint Surgery - British Volume*, **49**:781–788, (1967)

230. Burr D.B., Patterns of variability in mineralization of the primate femoral diaphysis, *American Journal of Physical Anthropology*, **51(2)**:219-232, (1979)

231. Jansonsa E., Tatarinovb A., Dzenisb V. & Kregersc A., Constructional peculiarities of the human tibia defined by reference to ultrasound measurement data, *Biomaterials*, **5(4)**:221-226, (1984)

232. Mechanic G.L., Arnaud S.B., Boyde A., Bromage T.G., Buckendahl P., Elliott J.C., Katz E.P. & Durnova G.N., Regional Distribution of Mineral and Matrix in the Femurs of Rats Flown on Cosmos 1887 Biosatellite, *The FASEB Journal*, **4**:34-40, (1990)

233. Wong F.S.L., Elliott J.C., Anderson P. & Davis G.R., Mineral concentration gradients in rat femoral diaphyses measured by X-ray microtomography, *Calcified Tissue International*, **56(1)**:62-70, (1995)

234. Capozza R.F., Feldman S., Mortarino P., Reina P.S., Schiessl H., Rittweger J., Ferretti J.L. & Cointry G.R., Structural analysis of the human tibia by tomographic (pQCT) serial scans, *Journal of Anatomy*, **216**:470-481, (2010)

235. Ramasamy J.G. & Akkus O., Local variations in the micromechanical properties of mouse femur: The involvement of collagen fiber orientation and mineralization, *Journal of Biomechanics*, **40(4)**:910-918, (2007)

236. Marotti G., Quantitative Data on Bone Formation Rate Throughout the Skeletal System, *CISM Bone cell and tissue mechanics*, Udine, July 19-23, **2010**

237. Chalmers J. & Weaver J.K., Cancellous Bone: Its Strength and Changes with Aging and an Evaluation of Some Methods for Measuring Its Mineral Content: II. An Evaluation of some Methods for Measuring Osteoporosis, *Journal of Bone and Joint Surgery - American Volume*, **48**:299-308, (1966)

238. Lazarev Yu. A., Grishkovsky B.A. & Khromova T.B., Amide I band of IR spectrum and structure of collagen and related polypeptides, *Biopolymers*, **24(8)**:1449-1478, (1985)

239. Currey J.D., What Determines the Bending Strength of Compact Bone? *The Journal of Experimental Biology*, **202**:2495-2503, (1999)

240. Carrier D. & Leon L.R., Skeletal growth and function in the California gull, *Journal of Zoology*, **222**:375-389, (1990)

241. Seeman E., Invited Review: Pathogenesis of osteoporosis, *Journal of Applied Physiology*, **95(5)**:2142-2151, (2003)

242. Currey J., Composition-Mechanical property-function relations in bone tissue, *CISM Bone Cell and Tissue Mechanics*, Udine, July 19-23, **2010**

243. Masoodi N.A., Bisphosphonates and atypical femur fractures, *British Journal of Medical Practitioners*, **3(1)**:311-312, (2010)

244. Wergedal J.E., Sheng M.H.-C., Ackert-Bicknell C.L., Beamer W.G. & Baylink D.J., Genetic variation in femur extrinsic strength in 29 different inbred strains of mice is dependent on variations in femur cross-sectional geometry and bone density, *Bone*, **36(1)**:111-122, (2005)

245. Tanahashi M. & Takehisa M., Surface functional group dependence on apatite formation on self-assembled monolayers in a simulated body fluid, *Journal of Biomedical Materials Research*, **34(3)**:305-315, (1997)

246. Toworfe G.K., Composto R.J., Shapiro I.M. & Ducheyne P., Nucleation and growth of calcium phosphate on amine-, carboxyl- and hydroxyl-silane self-assembled monolayers, *Biomaterials*, **27(4)**:631-642, (2006)